Towards implementing lattice structures into load-bearing lightweight components

Vom Fachbereich Maschinenbau
an der Technischen Universität Darmstadt
zur
Erlangung des Grades eines Doktor-Ingenieurs (Dr.-Ing.)
genehmigte

D i s s e r t a t i o n

vorgelegt von

Dipl.-Ing. Guillaume Meyer

aus Mulhouse (Frankreich)

Berichterstatter:	Prof. Dr.-Ing. habil. Christian Mittelstedt
Mitberichterstatter:	Prof. Dr. rer. nat. Oliver Weeger
Tag der Einreichung:	18.10.2023
Tag der mündlichen Prüfung:	13.12.2023

Darmstadt 2023

Meyer, Guillaume Bertrand Thibaut : Towards implementing lattice structures into load-bearing lightweight components
Darmstadt, 2023

Shaker-Verlag
ISSN 2702-4075
ISBN 978-3-8440-9414-5
zugl.: Darmstadt, Technische Universität Darmstadt, Dissertation

Vorwort

Diese Arbeit ist im Rahmen meiner Tätigkeit als wissenschaftlicher Mitarbeiter am Fachgebiet Leichtbau und Strukturmechanik (ehem. Konstruktiver Leichtbau und Bauweisen) der Technischen Universität Darmstadt entstanden.

Zunächst möchte ich meinem Doktorvater Herrn Prof. Dr.-Ing. habil. Christian Mittelstedt, Leiter des Instituts, danken. Sein Betreuungsstil aus Unterstützung jeglicher Art, gewährter Freiheit und Vertrauen trug wesentlich zum Erfolg meiner Arbeit bei.
Weiterhing möchte ich mich bei Herrn Prof. Dr. rer. nat. Oliver Weeger, Leiter des Fachgebiets Cyber-Physische Simulation, für seine fachliche Unterstützung und die Übernahme des Korreferats bedanken.

Weiterhin möchte ich meinen herzlichen Dank an alle meine aktuellen und ehemaligen Kollegen von der Werkstatt bis hin zu den Büros aussprechen. Die zahlreichen intensiven fachlichen Gespräche aus unterschiedlichen Blickwinkeln haben mir dabei geholfen, meine Arbeit und mich persönlich durch die Jahre zu entwickeln. Ein besonderer Dank geht an Herrn Dadak, der Leiter des FVK-Technikums, für seine stets lösungsorientierte technische Unterstützung.

Ebenso möchte ich mich bei allen von mir betreuten Studierenden bedanken, die im Rahmen von Abschlussarbeiten oder Tätigkeiten als studentische Hilfskräfte dieses Projekt durch ihr Vertrauen, Engagement und Fleiß maßgeblich mitgestaltet haben.

Letztendlich möchte ich den größten Dank meinen Töchtern und meiner Frau widmen.

Heppenheim, Oktober 2023 Guillaume Meyer

Kurzfassung

Die Luft- und Raumfahrtindustrie strebt nach einem Optimum zwischen Nachhaltigkeit, Kosten und Effizienz. In diesem Kontext hat sich die additive Fertigung durch die angebotene konstruktive Flexibilität als disruptive Technologie etabliert. Jüngere Forschung hat nachgewiesen, dass das Leichtbaupotential lasttragender struktureller Komponenten durch diese Technologie signifikant erweitert werden kann. Trotz möglicher Verringerungen von Masse und Materialverbrauch, die durch topologieoptimierte Strukturen erreicht werden können, hindern in den meisten Fälle der Herstellungs- und Nachbearbeitungsaufwand die additive Fertigung daran, eine wettbewerbsfähige Alternative zu den herkömmlichen Herstellungsverfahren zu sein. Tatsächlich wird die additive Fertigung oft im Rahmen vom Rapid Prototyping angewendet, während ihr Einsatz in der Serienproduktion, aufgrund hoher Kosten und Fertigungszeiten, noch eingeschränkt ist.

Eine erhöhte Wettbewerbsfähigkeit kann durch die Realisierung innovativer Strukturen, die anhand der additiven Fertigung hergestellt werden können, erreicht werden. Auf der Mesoskala bieten additiv gefertigte zelluläre Strukturen und insbesondere Gitterstrukturen zusätzliche Designfreiheit und somit neue Konstruktionsmöglichkeiten, die durch konventionelle Verfahren nicht realisierbar sind. Neben dem erhöhten Leichtbaupotential können zelluläre Strukturen die Fertigungszeit drastisch reduzieren und die additive Fertigung hinsichtlich Time-to-Market ökonomisch rentabler machen. Dennoch finden Gitterstrukturen nur eingeschränkte Anwendungen in der Serienproduktion und werden derzeit noch nicht in lasttragenden Leichtbaukomponenten angewendet. Dies liegt an einer fehlenden Standardisierung auf mehreren Ebenen, vom Initialdesign bis hin zur Produktzertifizierung, was der Hauptgrund ist, warum das volle Potential solcher Strukturen noch nicht genutzt wird.

Diese Arbeit betrachtet die konzeptuellen und herstellungsbedingten Herausforderungen der Implementierung von Gitterstrukturen in Leichtbaukomponenten. Im ersten Teil dieser Arbeit werden Konzepte für eine Krafteinleitung ohne lokale Spannungserhöhung an den Schnittstellen zwischen Vollkörper und Gitterstrukturen und zwischen Gitterzellen entwickelt und numerisch verifiziert. Im zweiten Teil dieser Arbeit werden sowohl die zuverlässige additive Fertigung von Gitterstrukturen im Sub-Millimeter Bereich im Rahmen des selektiven Strahlschmelzens als auch Ansätze für deren Implementierung in Vollkörperteilen untersucht. Einblicke in den Einfluss der Fertigung auf die strukturelle Integrität von Gitterstrukturen und deren mechanischen Eigenschaften werden im Rahmen der experimentellen Validierung der entwickelten Konzepte gegeben.

Die vorliegende Arbeit schlägt ein Rahmenwerk für eine standardisierte Konzipierung und zuverlässige Herstellung von Zugproben für die Charakterisierung mechanischer Eigenschaften von Gitterstrukturen vor. Demnach kann dieser Beitrag als erster Meilenstein auf dem Weg zu einfachen Designrichtlinien über die Implementierung von Gitterstrukturen

in Leichtbaukomponenten in der täglichen Ingenieurpraxis betrachtet werden. Die entwickelten Konzepte sind nicht spezifisch auf das untersuchte AlSi10Mg Pulvermaterial zugeschnitten und sind somit auf weitere Materialklassen übertragbar.

Abstract

The aerospace industry strives for an optimum between sustainability, cost and resource efficiency. In this frame, additive manufacturing has established itself as a disruptive technology by offering increased constructive flexibility. Recent research demonstrated that the lightweight potential of load-carrying structural components could be further enhanced using this technology. Despite the reduction of weight and resource consumption that can be achieved through topology optimised structures, the efforts involved in both manufacturing and post-processing hinder in most cases additive manufacturing at being a competitive contender against conventional manufacturing processes. As a matter of fact, additive manufacturing is often employed for rapid prototyping while its use in serial production is rather restrained due to high costs and production times.

An improved competitiveness can be achieved with the realisation of innovative structures through additive manufacturing. At the meso-scale, additively manufactured cellular structures and, in particular, lattice structures offer supplementary design freedom and, thus, new engineering opportunities that cannot be realised by conventional means of manufacturing. In addition to the increased lightweight potential they offer, cellular structures can drastically reduce the printing time and therefore make additive manufacturing more viable in terms of Time-to-Market. However, lattice structures find restricted fields of application for serial production and are still not implemented into load-carrying lightweight components. This is due to lacks of standard on several levels, from the initial design to the final product certification, which hold back exploiting their potential.

This work explores the challenges met by the implementation of lattice structures into bulk parts from both design and manufacturing points of view. In the first part of this work, concepts for load introduction designs avoiding local stress concentration at both lattice-to-bulk and lattice-to-lattice interfaces are developed and numerically verified. In the second part of this work, the reliable additive manufacturing of sub-millimetre lattice structures in the framework of laser powder-bed fusion and manufacturing approaches for their implementation into bulk parts are investigated. Insights into the influence of manufacturing on the structural integrity of lattice structures and their inherent mechanical properties are provided in the frame of experimental validations as well.

The present work proposes a framework for both standardised design and reliable manufacturing of test specimens for the mechanical characterisation of lattice structures under tensile loading. Furthermore, this contribution can be considered as a first milestone towards straightforward design guidelines on the implementation of lattice structures in lightweight components for daily engineering practice since the developed concepts are not specific and therefore not restricted to the employed AlSi10Mg powder material.

Table of contents

Nomenclature

Abbreviations

AM	Additive Manufacturing
AR	Aspect Ratio
BC	Boundary Conditions
BESO	Bi-directional Evolutionary Structural Optimisation
CAD	Computer Aided Design
CT	Computer Tomography
DFAM	Design for Additive Manufacturing
DoE	Design of Experiment
EBM	Electron Beam Melting
FE	Finite Element
FGM	Functionally Graded Material
HIP	Hot Isostatic Pressing
KLuB	Konstruktiver Leichtbau und Bauweisen
LB-PBF	Laser Beam Powder-Bed Fusion
LHD	Latin Hypercube Design
LSM	Leichtbau und Strukturmechanik
N/A	Not applicable / no data
NURBS	Non-Uniform Rational B-Splines
PBF	Powder-Bed Fusion
RVE	Representative Volume Element
RUC	Representative Unit Cell
SCF	Stress Concentration Factor
SIMP	Solid Isotropic Material with Penalisation
SKO	Soft Kill Option
SLM	Selective Laser Melting
SLS	Selective Laser Sintering
STL	Standard Tessellation Language
TO	Topology Optimisation
TPMS	Triply Periodic Minimal Surface

Greek symbols		Unit
α	Inclination angle	°
γ	Curvature factor	-
ϵ	Strain	-
Θ	Polar angle	°
θ	Curvature factor	-
θ_h	Hatch vectors rotation angle	°

Greek symbols		Unit
ρ	Density	g/cm³
σ	Stress	MPa
Φ	Azimuth angle	°

Latin symbols		Unit
A	Area	mm²
a	Cell size	mm
A_{eH}	Maximum compressive strain	-
AR	Aspect ratio	-
bo	Beam offset	μm
b	Width	μm
C	Circularity measure for roundness	-
D	Diameter (stepped bar)	mm
d	Diameter (bore hole)	mm
d_h	Hatch distance	μm
d_L	Laser beam diameter	μm
d_s	Hatch stripe width	μm
E_l	Line energy density	J/mm
E_a	Surface energy density	J/mm²
E_V	Volumetric energy density	J/mm³
F	Force	N
f	Scaling factor	-
h	Height	mm
IF_i	Interface	-
k	Contour	-
K_t	Stress concentration factor	-
L	Lightweight grade	-
l	Length	μm
l_s	Layer thickness	μm
M	Maxwell number	-
m	Mass	g
m_{minmem}	Minimum member size	mm
m_{maxmem}	Maximum member size	mm
n	Number of nodes in a RUC (Maxwell number)	-
n_h	Hatch vectors number	-
$n_{RUC,x}$	Number of RUC in the x-direction	-
$n_{RUC,xy}$	Number of RUC in the xy-plane	-
$n_{RUC,y}$	Number of RUC in the y-direction	-
$n_{RUC,z}$	Number of RUC in the z-direction	-
P	Laser power	W
P_i	Panel	-

Latin symbols		Unit
p	Perimeter	mm
r	Radius	mm
R_a	Surface roughness	μm
R_{plt}	Plateau stress	MPa
R_{eH}	Maximum compressive strength	MPa
s	Number of struts in a RUC (Maxwell number)	-
T	Temperature	°C
T_{bp}	Build platform temperature	°C
t	Thickness, strut thickness / diameter	μm
v	Laser scanning speed	mm/s
U	Displacement	mm
V_f	Volume fraction	-
w	Waviness	μm

Indices	
*	Effective (cellular structure)
$\bar{}$	Relative
$+$	Compression
$-$	Tension
ana	Analytical
CAD	As-designed
c	Contour
$centre$	Centre
$cone$	Cone
$crit$	Critical
$diff$	Difference
D	Design space
$down$	Lower, downskin
eff	Effective
eq	Equivalent
$g, graded$	Graded
h	Hatch
i	Iteration number
in	Inner
$Lattice$	Lattice structure
max	Minimum
$mean$	Mean
min	Maximum
MTE	Multiple track exposure
n	Iteration number
out	Outer

Indices

p	Point exposure strategy
ref	Reference
RUC	Representative unit cell
S	Solid material
s	Specimen
SCE	Single contour exposure
SPE	Single point exposure
STE	Single track exposure
$Strut$	Strut
t	Thickness
Tr	Transition
top	Top / Upper
$u, ungraded$	Ungraded
up	Upper / upskin
var	Variation
VM	Von-Mises
$water$	Water

Coordinate systems

x, y, z	Cartesian coordinate system
I, II, II	Principal coordinate system

1 Introduction

1.1 Motivation

The sixth assessment report of the Intergovernmental Panel on Climate Change documents thoroughly human-induced climate change and justifies increasing concerns. The emissions of greenhouse gases, primarily carbon dioxide and methane from fossil fuels, further accelerate global warming and have far-reaching consequences for human beings and nature [1]. For example, according to the World Health Organization, an annual amount of 4.2 million deaths worldwide is reported to be caused by ambient air pollution and 96 % of European urban residents were exposed to a harmful concentration of particulate matter in 2020 [2]. It has been estimated that current emissions need to be reduced by 45 % by 2030 and reach net zero by 2050 to slow down climate change [3]. The industrial manufacturing sector is directly affected by this environmental challenge since rising temperatures have been attributed to industrial practices, which account for about 15 % of global energy consumption and for roughly 35–40 % of global material consumption [4]. Both scarcity of natural resources and resultant ecological impact cannot be ignored anymore and future industrial development is deemed to lean towards global sustainability and eco-friendly manufacturing. This means that the industry does not only have to achieve its economic goals but also to commit safeguarding the environment through a reduction of resource consumption all over the product life cycle [5]. This applies especially to the aerospace industry, where numerous technical and economic objectives such as functional performance, lead time reduction or cost management may appear to be contradictory to each other [6].

Lightweight design can contribute to achieving this goal by significant mass reductions while simultaneously maintaining the required mechanical performance [6, 7]. As a consequence, the fuel consumption in non-stationary applications in fields such as aerospace and automotive industries can be indirectly reduced [8]. As a matter of fact, 30 % weight saving results in more than 10 % fuel efficiency improvement in the example of the Boeing 787 aircraft [9].

The additive manufacturing technology is a prime example and a driving force of new directions taken by mechanical engineering in the field of lightweight design. Over the past decades, it has established itself as a disruptive technology [4, 10, 11]. The main advantage of additive manufacturing resides in the unique component complexity available without increasing manufacturing costs due to the reduction of material usage compared to conventional manufacturing technologies [5, 6]. These typical traits are known under the concepts of *individualisation and complexity for free* [12, 13]. Additive manufacturing offers the possibility to produce components that cannot be realised by conventional manufacturing processes [14]. In some cases, an increase of both productivity and quality can be achieved. For example, integrating close contour channels into additively manufac-

tured injection moulding heads leads to a 15% cycle-time-reduction compared to conventionally manufactured heads while a more homogeneous temperature distribution is obtained, reducing warping in the produced plastic parts [15]. In the production of lighter components, additive manufacturing enables merging several lightweight concepts in the development phase of a part or a component. Typical examples are, on the one hand, the replacement of standard steel belts by additively manufactured titanium ones which enables 55 % mass saving per part i.e., 72.5 kg per aircraft, which ends up in 2 M€ fuel economy [16], and, on the other hand, additively manufactured aircraft brackets that bring upon 30 % weight-saving due to the reduction of parts number through the notable absence of fasteners while offering a plug-and-play solution [17].

Thanks to its nature of employing material only where it is needed, additive manufacturing naturally opens the door to load-driven design via topology optimisation [18], which is therefore offered to play a major role in the process chain [19] in the framework of optimisation of tooling [20] or end-product as in the above-mentioned examples. That is why additive manufacturing has the potential to take a non-negligible place in a manufacturing landscape motivated by the ecological responsibility of engineers to use fewer amounts of resources and diminish the produced emissions of machines throughout their life cycles [21, 22]. However, despite a revenue growth in service and products of 19.5 % in 2021 [23] and the increasing involvement of end-part products in the portfolio of additive manufacturing companies (from 10 % of the production in 2019 [24] to 33.7 % in 2022 [23]), additively manufactured end-parts are not well-established in the industrial landscape yet and the tools available to assess their sustainability are still to be adapted to the life cycle of additive manufacturing [5, 24, 25]. The common point of the manifold drawbacks of additive manufacturing for serial production is its rentability [23]. The main issues here are the operating costs for a rather low time-to-market compared to conventional means of manufacturing. Reasons for this can be found in build rates, process-dependent part quality [26] and consequent certification issues [6] as well as manufacturing restrictions [27] and needed post-processing steps. As indicated in the Wohlers Report, *complexity for free* is a myth [23, 28]. The question is then, how can the technology become economically competitive compared to other manufacturing technologies?

The first answer provided by recent research lies in the full control of the additive manufacturing process. Exhausting the potential of additive manufacturing can only be achieved by a complete understanding of the relationships between a product and its manufacturing process [29]. An extensive and certainly expensive but necessary process parameter optimisation can overcome or, at least, alleviate the challenges inherent to manufacturing restrictions and, thus, to reduce post processing steps [26]. Moreover, build rates can be increased while maintaining good part quality. Several examples can be found in the frame of additive manufacturing by means of Laser Beam Powder-Bed Fusion (LB-PBF). Buchbinder showed that build rates can be increased by 400 % by changing laser power, hatch distance and scanning speed while achieving part densities of 99.5 % [22]. Furthermore, Metelkova et al. could increase the productivity by 840 % by means of laser defocus [30]

and Sow et al. obtained moderate built rate increase up to 50 % with changes in the beam diameter for comparable bulk part density [31]. Moreover, Großmann et al. showed that controlling the melt pool width, which depends on material and process parameters, leads to either high precision or increased build rates with the help of dimensionless numbers validated by Yang et al., who demonstrated in their work that scaling laws have the potential to become effective tools in the framework of industrial resource-efficient additive manufacturing [32, 33].

"When modern man builds large load-bearing structures he uses dense solids: steel, concrete, glass. When nature does the same, she generally uses cellular materials: wood, bone, coral. There must be good reasons for it".

M.F. Ashby [34]

The aforementioned compatibility between additive manufacturing and topology optimisation in mechanical engineering is not only restricted to the load-driven design that characterises the so-called *bionic structures* but pushes also towards more specific and direct inspiration from nature through biomimicry [35, 36]. Among the evolutionary topology optimised load-bearing features found in nature, wood, coral or bones are often cited as ultimate lightweight engineering features [34]. The latter consists of an external shell, called *compacta*, preventing the functionality of the *medullar cavity* from outer damages. In between an inner filigree structure of varying density, the *spongiosa*, ensures a proper load distribution [37].

Additive manufacturing enables the realisation of such complex structures thanks to multi-scale manufacturing. At the meso-scale, additively manufactured cellular structures and, in particular lattice structures as one of their sub-categories, offer an extreme degree of lightweight design that cannot be reached by conventional means of manufacturing [38, 39]. These highly periodic structures not only provide some of the highest mechanical strength and stiffness relatively to their weight or volume [40] but also promise to reduce the build rates up to 80 % [41], which results in material, time and energy saving during their fabrication and all along the product life cycle. Furthermore, the direct relationship between geometry and mechanical properties enables engineers to predict their mechanical properties by means of analytical models [42, 43]. In the frame of structural design, the variety of available representative unit cells opens the doors of an even more efficient and load-driven design through a predictable tailoring of their mechanical specific properties, which in turns offers to expand and fill gaps in the material property space [44].

The future of lattice structures shines bright in many industrial fields such as aerospace [6] or medicine [45]. These structures can reveal themselves as game changer for different applications like fatigue [46], energy absorption [47], crashworthiness [48], or dynamic impact [49]. However, when it comes to their involvement into structural parts, lattice structures are often integrated as in-fill for lightweighting or thermal exchanger rather than for mechanical purposes [39, 50]. Similar to additively manufactured end-products

issued from mechanical engineering, which are involved in secondary structures only [6, 14], the deployment of lattice structures in primary and, thus, safety relevant structures has still not reached high technology readiness level. It remains at the level of "*trends*" [48] or "*perspectives*" [49].

The implementation of lattice structures into lightweight load-bearing components requires complex hierarchical structures, as is the case for natural structures [45]. Based on the example of bone structures, lattice structures have the potential to replicate its working principle and, thus, let arise a new generation of lightweight structures [51]. This raises the questions of both load introduction and load path monitoring while designing lightweight components with integrated lattice structures. One of the most promising approach is the use of gradient lattice structures [51, 52]. However, the development of complex graded structures occurs exclusively though computationally expensive numerical topology optimisation algorithms [18, 51] and therefore leads to case specific optimised solutions, which compromises a desirable systematic methodology.

In the framework of LB-PBF, the integration of lattice structures into lightweight components pose not only design but also manufacturing challenges due to the absence of concrete guidelines and disparate knowledge, which is highlighted by the lack of systematic reporting of the chosen manufacturing approaches, especially at small scale [50, 53]. As for bulk material, the emergence of defects can strongly impact both geometric accuracy and mechanical performance and, thus, hampers the establishment of reliable and robust design and manufacturing methods [46, 54]. These variations may lead to imperfect geometries and material connections that alter the loading conditions and, thus, influence the overall mechanical performance of lattice structures [46]. This issue prevents from integrating lattice structures into serial parts and explains the low number of industrial use cases [39].

The absence of standards even reaches the mechanical characterisation of lattice structures [55], which leads to a high diversity of sample design and manufacturing approaches, and, to a greater extent, may jeopardise the certification process of lightweight load-bearing components with integrated lattice structures [6, 56]. Engineers have the need for straight-forward and convenient approaches to generate a comprehensive design of additively manufactured lightweight components utilising their full potential. To derive such approaches and create accurate and repeatable output, reproducible design and manufacturing methods specific to additively manufactured lattice structures need to be developed, from which general rules for their integration into load-bearing components can be extracted and established.

1.2 Scope of this work

This work takes place in the conceptional framework of *laser-driven lightweight design* initiated by my former colleague Alexander Großmann [57] that has been further developed at the institute. This vision consists in the melt pool controlled additive manufacturing of

macro-scale topology optimised parts with implemented meso-scale lattice structures for simultaneous quality and productivity increases. This *multi-scale design for additive manufacturing* therefore combines the two aforementioned solutions of process control and cellular structures in order to address the concerns on the competitiveness of additive manufacturing by exploiting the correlation between robust design concepts, deep process control and predictable mechanical properties.

The aim of this work is to propose simple and generic approaches that could offer practitioners, designers, and researchers straightforward guidelines specific to lattice structures in order to rapidly design robust lightweight structures, e.g. sandwich panels with embedded lattice structures in aircraft primary structures, without requiring any specific background knowledge. The practical example of testing specimens for the mechanical characterisation of cubic truss lattice structures under tensile loading is employed as recurring theme throughout this thesis, where corresponding design methodologies for a normalised sample design and reliable manufacturing are investigated. To a further extent, this work opens the door to general design guidelines and certification methods and, therefore, to exhaust the potential of additive manufacturing in lightweight structural design.

Chapter 1 introduces both framework and motivation of this work. Chapter 2 sets up the employed background knowledge and develops identified challenges in the context of the implementation of lattice structures into load-bearing lightweight components with the precise example of tensile test specimens. Chapter 3 describes the methodology employed in the different investigation stages. Chapter 4 deals with developed material independent design concepts and their numerical verification. It is divided into three sub-chapters. The first two sub-chapters investigate the load introduction at the interface between bulk material and lattice structure. Two distinct solutions for a transition region are proposed: on the one hand, the structural grading of lattice unit cells and, on the other hand, a topology-optimised transition region avoiding high samples potentially involved by structural grading. The third part of chapter 4 covers the transition between single lattice unit cells. Here, particular attention is given to the junction centre of lattice struts since identified as the most critical area in terms of design induced notches in truss-based lattice structures. Chapter 5 deals, on the one hand, with the reliable AlSi10Mg LB-PBF manufacturing of sub-millimetre lattice structures and, on the other hand, with the realisation of the interface between bulk material and lattice structure through different manufacturing approaches. Chapter 6 develops the experimental validation of the developed concept by means of mechanical testing as well as assessments on the structural integrity of the manufactured structures. Based on the obtained results, the relevance of the proposed design solutions is evaluated in a benchmark analysis. Chapter 7 provides a summary of the achieved milestones while addressing the different challenges encountered throughout the realisation of this work, from which further research needs are deduced. The discussion is extended to the transferability to other structures and to potential guidelines or design rules for the reliable implementation of additively manufactured lattice structures into lightweight component as well.

2 Background

This chapter reflects the current state of the art and sets the framework of the present work by providing background knowledge on additive manufacturing with focus on the LB-PBF of metal parts, load-driven design and lattice structures. Current technological challenges met by the implementation of lattice structures in lightweight load-bearing structures are highlighted and research needs are extracted.

2.1 Additive manufacturing

Additive manufacturing, also commonly called *3D-printing* or, to a lesser extent, *generative manufacturing*, is a manufacturing process that has been given different names in the past. Terms that were historically employed include *additive fabrication*, *additive processes*, *additive techniques*, *additive layer manufacturing*, *layer manufacturing*, *solid freeform fabrication,* and *freeform fabrication* [58]. Additive manufacturing belongs to the category of *primary shaping* manufacturing processes, which consists in the creation of a product from shapeless material such as powder or fluid [59]. In the industrial landscape, additive manufacturing is listed among the three manufacturing pillars [60]. It is characterised by the layer-wise addition of raw material, which is bound to a given shape by energy input, and differs from subtractive manufacturing such as boring, turning or milling, where the end geometry is obtained from semi-finished products through material removal, or from formative production processes like casting or forging, where the end geometry follows the conservation of volume while being produced.

Additive manufacturing encompasses different technologies using a broad bandwidth of materials and, thus, products yielding distinctive properties [61]. The numerous additive manufacturing process variants differ in the type of the employed raw material, the type of energy input and the layer binding approach [28, 62]. They are divided into seven processes according to the DIN ISO EN/ASTM 52900 standard: binder jetting, directed energy deposition, material extrusion, material jetting, powder-bed fusion, sheet lamination, and VAT photopolymerization [58, 63]. Independently from the employed technologies, the additive manufacturing process can be divided into three stages: pre-process, in-process and post-process [62]. During pre-processing, hard- and software preparative operations such as the digital definition of the part end geometry are undertaken. Post-process operations are conducted after the in-process stage, i.e., manufacturing. They mostly consist in separating the additively manufactured part from the system, where a prime example is the removal of support structures.

The antecedents of the concept of additive manufacturing are manifold and can be found in the ancient past with examples of the construction of pyramids or cathedrals, the first three-dimensional topology maps or even layered cakes [28, 63]. One well-spread milestone in the pre-history of additive manufacturing is the three-dimensional recording and

reproduction of François Willème, who recorded his silhouette by means of 24 cameras under different angles and created a physical three-dimensional model of himself [64]. The additive manufacturing technology really ignited in the early 1980s with the development of computers, lasers and electronical controlling systems [65]. In 1984, Charles (Chuck) Hull developed stereolithography as the first manufacturing process. Further patented additive technologies followed [65]. However, a significant industrial expansion of additive manufacturing can only be seen from the 2000s on, thanks to the rapid technological development of machine and computer components [66].

Nowadays, additive manufacturing is applied in several industries thanks to its layer-wise approach that enables a theoretically limitless design freedom and, thus, flexibility and versatility. Application-specific designed structures with tailored properties can be generated. They are comparably impossible to manufacture by means of subtractive or formative processes on similar economic basis [21, 67]. Tailored designs based on optimised geometries as an integral product can not only offer similar or significant higher mechanical performance but also a simplification of the process chain through a reduction of the number of parts or tooling, and manufacturing steps involved in comparison to classical construction methods [29, 68]. These traits are widely known as the concepts of *individualisation for free* and *complexity for free*. These concepts, schematically shown in Figure 1, are particularly relevant for the lightweight industry, where weight, mechanical performance and, most importantly, costs are the driving selection criteria. Depending on the involvement of additive manufacturing in the process chain, these advantages are employed in the framework of *rapid manufacturing* for an end product or *rapid prototyping* for intermediary development stages [13, 60]. However, the main challenge of the additive manufacturing technology lies in achieving serial production maturity while accounting for manufacturing approach dependencies i.e., reliable and reproducible provision of subsequently mechanically loaded parts with little rework; the latter being a time and cost consuming factor [69].

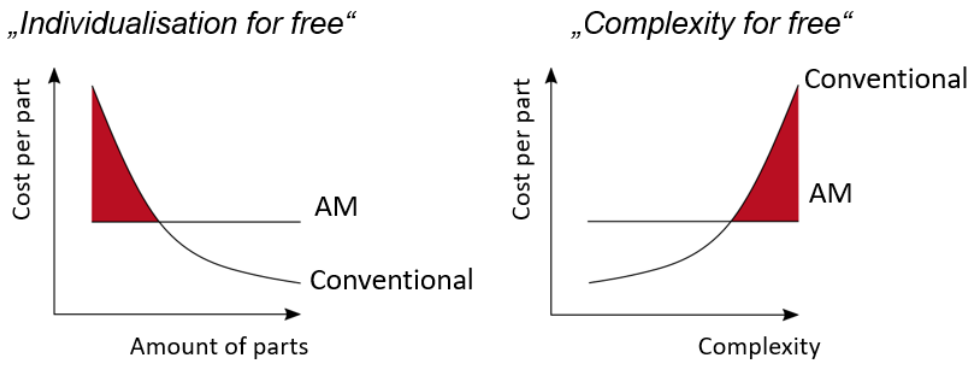

Figure 1: Advantages of additive manufacturing in terms of industrial application as compared to conventional manufacturing.

2.1.1 Laser beam powder-bed fusion

From the different processes that have arisen over the last decades, *Powder-Bed Fusion* (PBF) based processes have become the most dominating additive manufacturing technology in the framework of the industrial production of metal parts [28, 63]. The main advantage of PBF processes lies in the pre-alloyed state of the employed powder material [70] that allows producing parts of similar or even higher density and mechanical properties compared to raw base material or conventionally machined parts [12]. While alloys such as steel-, titanium- or aluminium-based alloys are commonly employed [61], current research focuses on the development of new PBF-compatible compositions for potentially better properties or different applications [71].

Among the three major PBF sub-categories *Selective Laser Sintering* (SLS), *Electron Beam Melting* (EBM), and *Laser Beam Powder-Bed Fusion* (LB-PBF), which was also known as *Selective Laser Melting* (SLM) before standardisation [58], the latter is the most widely employed process [66, 72]. LB-PBF consists in the layer-wise two-dimensional local melting of metal powder particles by a laser source to create a three-dimensional solid part [67]. Figure 2 shows a sketch of a LB-PBF setup. A portion of the *feedstock*, which is stored in the *feed region*, is repeatedly conveyed with a coater to the *powder bed* in the *build space* along different *build cycles* until the part is completely printed. Any excess of powder is collected in the *overflow region* [58]. Typical layer thicknesses range between 30 μm and 100 μm [66]. The *build chamber* is sealed hermetically and flowed by inert gas, e.g. argon, order to avoid contamination and oxidation of the employed powder [73]. Moreover, the *build platform* can be held at a specified temperature to avoid temperature gradients and resultant eigenstresses in the final part [12, 69].

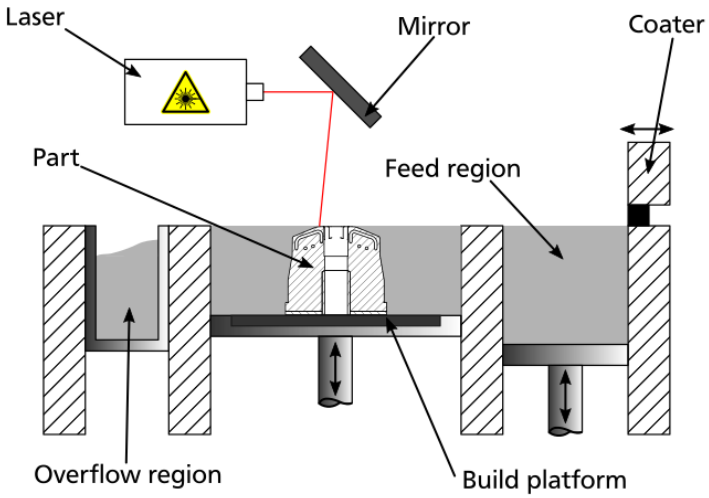

Figure 2: Example of LB-PBF setup.

As mentioned in section 2.1, the LB-PBF workflow consists of three stages and is depicted in Figure 3 [62].

Its specific pre-processing stage is divided into two sub-stages. The one stage consists in a physical pre-processing that takes place to condition the printing environment. Main steps in the machine preparation are managing the powder feedstock, adjusting both build platform height and temperature as well as inert gas flowing. The other stage deals with digital pre-processing. It starts with the preparation of a facet model made of approximated surfaces of the part to be printed, which is specifically necessary from machine specific software. This boundary model can be obtained by either a Computer Aided Design (CAD) model issued from commercial software or by reverse engineering, e.g., by optical scanning methods such as Computer Tomography (CT). In the first case, the three-dimensional CAD model is reduced to a facet model by polygonization or triangulation. The most employed format of such model is the Standard Tessellation Language (STL) format. Then comes the preparation of the manufacturing approach. Firstly, the part to be printed is positioned and oriented in the virtual build space while designed and, if necessary, process- and design-specific support structures have to be applied. Secondly, the virtual part and its supports are distributed into layers along the height of the build space in a process that is commonly called *slicing*. Finally, the identified process strategies and parameters are assigned. The in-process stage takes places, the part is printed in a layer-wise manner described above and the process stops until the part is completely manufactured.

LB-PBF specific post-processing starts with the removal from the machine of the built platform with the additively manufactured part on it and is further divided into two sub-stages too. On the one hand, preparative steps for the next print such as machine cleaning or powder recycling need to be performed. On the other hand, part specific actions need to be undertaken. Among them, separation from the build platform, powder and support structures removal and part-specific finishing operations, which are out of the scope of the additive manufacturing process chain but can account for the main production costs of the part [12].

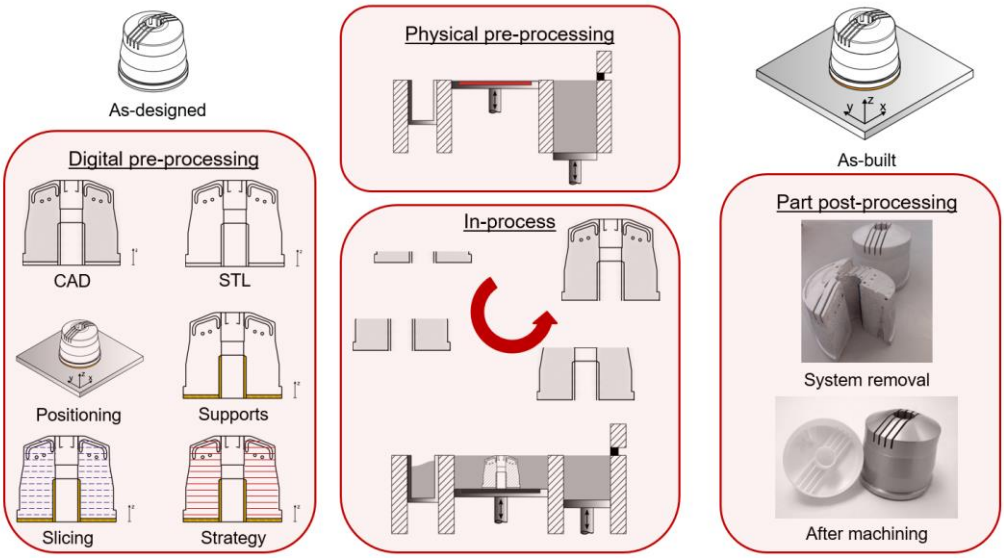

Figure 3: Schematic example of the LP-PBF workflow in the framework of the additive manufacturing of an injection moulding tool head [15].

2.1.2 Manufacturing approaches

In this section, LB-PBF manufacturing approaches are described with the representative example of truss lattice struts with cylindrical blank as in the VDI3405 norm [74].

Within the LP-PBF workflow described in the previous section, the two digital pre-processing sub-stages that are part positioning and manufacturing strategy assignment are decisive for manufacturing time, part quality and properties. Part positioning on the build platform, as depicted in Figure 4, is described by two angles. On the one hand, the *azimuth angle* Φ is defined as the part inclination relative to the coater i.e., powder application direction, on the build platform (xy-plane). An azimuth angle of 0° corresponds to a part aligned with the coating direction (x-axis) while 90° stands for a part perpendicular to the coater direction (y-axis). On the other hand, the *polar angle* Θ is defined as the inclination of the part in relation to the build direction (z-axis). A polar angle of 90° corresponds to an upright part while 0° stands for a horizontally printed part [74]. Moreover, independently from the part inclination, the so-called *up-* and *down-skin areas* can be identified. They correspond to the part surfaces oriented up- or downwards, respectively [27].

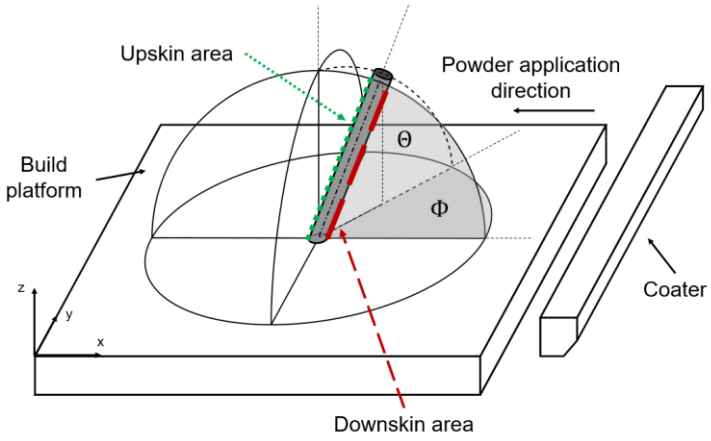

Figure 4: Positioning on the build platform according to [27, 74].

Three exposure strategies are available in the frame of LB-PBF manufacturing, each of them having its own dimensionality and corresponding features. The best-known strategy, namely the *hatch exposure strategy*, consists of a two-dimensional scanning strategy made of assembled single melt tracks, which can vary between 130 μm and 250 μm [32]. It is suited for the additive manufacturing of massive bulk parts. Another exposure strategy is the *contour exposure strategy*, which consists of a one-dimensional scanning of the contour lines of a given part. This strategy is not only employed for an in-situ finishing of big parts such as improving their surface roughness [75] but is also suited for the additive manufacturing of small features with circular cross-sections such as truss lattice structures. Non-hollow struts of diameters ranging from 220μm to 500μm can be printed [76, 77]. The least known and least employed strategy is the *point exposure strategy*, which can be described as a dimensionless scanning approach. It enables the manufacturing of extremely

thin-walled features with wall thicknesses below 200 μm [77-79]. However, this strategy is not standard in every commercial machine or software [77]. In this case, workarounds using either contour or hatch exposure strategies are mandatory to reach thicknesses in a similar order of magnitude. The standard manufacturing approach for commercial machines is a combined exposure made of one hatch exposure followed by two successive contour exposures with scanning paths offset from each other.

In daily practice, the AM software end-user is confronted with a variety of input parameters, from which the most relevant ones are shown in Figure 5 for one given manufacturing layer. Among them, the most important parameters are directly linked with the energy source, i.e., the laser. These are the *laser beam diameter* d_L, the *laser scanning speed* v and the *laser power* P. With further material constants, they directly influence the *melt pool width* b specific to each exposure strategy [32]. Another melt pool sizing feature is the *layer thickness* l_s, which is employed by the AM software to assign parameters to both up- and downskin areas. These parameters are generally different from the ones assigned the inner region. Furthermore, the outer part contour to be exposed is obtained by considering both *beam offset* bo and outer CAD contour or, in the context of trusses, *as-designed diameter* t_{CAD}. The assignment of exposure vectors directly depends on both *hatch distance* $d_h$and the *number of hatch vectors* n_h. Two successive hatch layers are generally rotated by an *angle* θ_h to tackle the fact that the hatch exposure strategy leads to two distinct diameters for one given manufacturing layer. As mentioned in section 2.1.1, global temperature gradients can be influenced by the *build platform temperature* T_{bp}. Another way to alleviate these temperature gradients is to assign specific pattern strategies governed to the hatch exposure. Figure 6 depicts the example of the standard AM strategy for commonly employed separation patterns of the hatch vectors for one given manufacturing layer. Alternative pattern, such as stripe and checker-board, offer shorter scanning vectors governed by the *hatch stripe width* d_s. This results in a more homogenous local temperature redistribution of the exposed area and a subsequent reduction of the local temperature gradient [75].

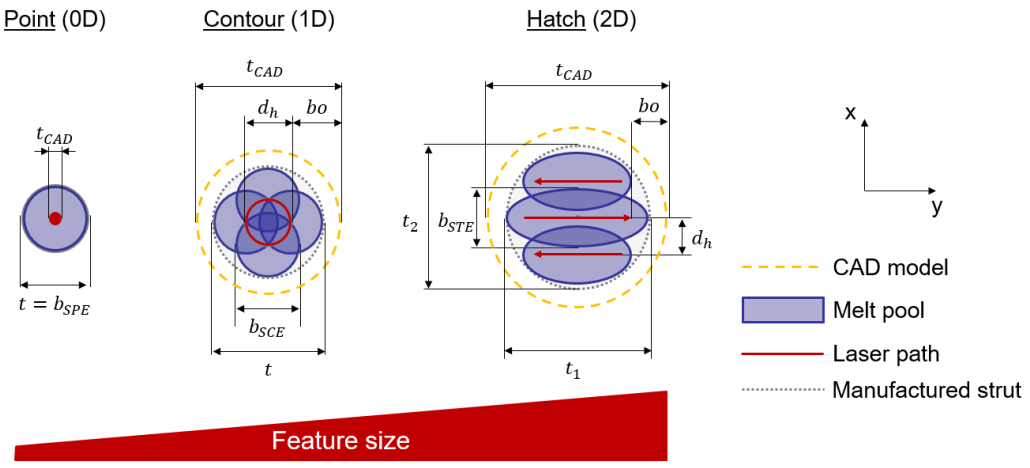

Figure 5: LB-PBF exposure strategies and most relevant parameters for a given layer.

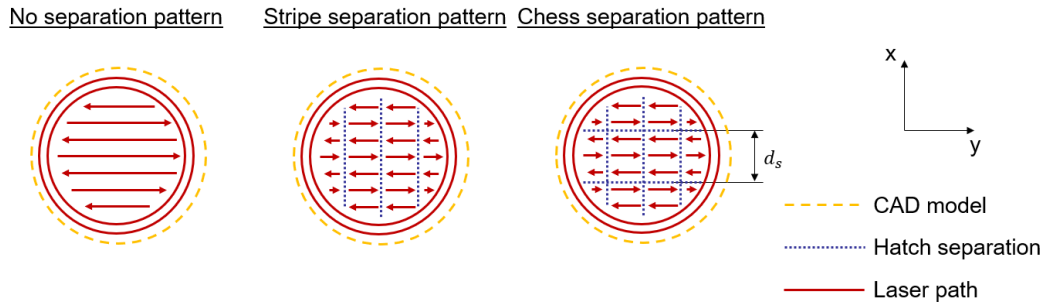

Figure 6: Hatch separation patterns in the context of standard exposure (double contour + hatch) for a given layer.

A commonly employed fast sizing criterion for the printability of additively manufactured parts is the energy density formulation. Depending on the size and strategy of the concerned feature, the energy density is expressed as *volumetric energy density* (Eq.1) or is reduced to either a *surface* (Eq.2) or a *line energy* (Eq.3) *density* in the case of thin-walled features [28, 80, 81]. However, these expressions neglect the influence of laser-material interactions on the resulting properties as well as machine dependencies [57, 82].

$$E_V = \frac{P}{v l_s d_h} \tag{1}$$

$$E_a = \frac{P}{v l_s} \tag{2}$$

$$E_l = \frac{P}{v} \tag{3}$$

2.1.3 Influences and consequences

The quality of LB-PBF manufactured parts has manifold influencing factors that are commonly depicted in an Ishikawa (or fishbone) diagram. These influencing factors are generally organised into the following categories: user, pre-process, part, machine, material processing and post-processing [82, 83]. This section is restricted to the direct impact of the manufacturing approaches and process parameters described in the previous section. The involved phenomena and their impact on additively manufactured structures at different scales are introduced.

Process parameters do not only influence productivity through built rates [22, 30, 31] but also strongly impact part properties, where process-induced defects such as porosity or surface roughness play a major role in the deterioration of their structural integrity and, thus, their mechanical performance [54]. Furthermore, the manufacturability of LB-PBF metal parts depends on process parameters as well [70]. The manufacturability is generally mapped by so-called *process windows* based on the most influential parameters such as laser power and scanning speed. Figure 7 shows an example of process window in the framework of manufacturability investigations on lattice structures performed by

Großmann et al. [76]. These process windows are material and machine specific and, thus, require extensive experimental campaigns [84-88].

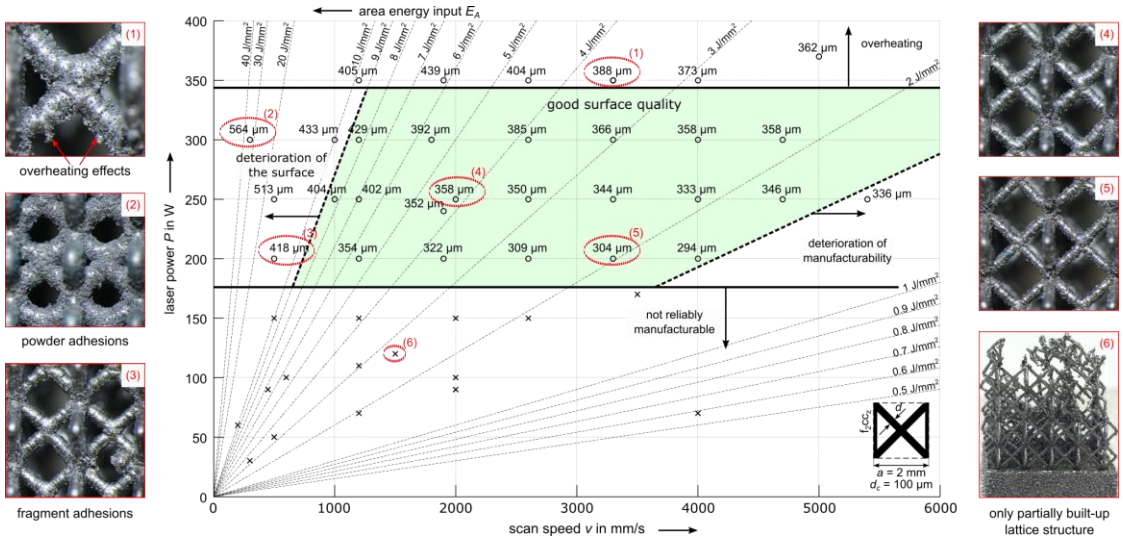

Figure 7: Process window at the example of the processability of lattice structures by means of contour exposure strategy [76].

The processability of LB-PBF metal parts is driven by the *melt pool*. This key feature is directly linked to the process parameters since it depends on both energy input and resulting temperature. It is responsible for distinct phenomena.

The *balling* phenomenon occurs when the molten material fails to wet the underlying substrate and conglomerates due to surface tension [84]. At high energy density input (top left corner of the process window of Figure 7), balling follows *material swelling*, which is defined as the rise of molten solid material above the plane of powder distribution and hints at overheating [70, 89]. Powder particles conglomerate into either ellipsoidal or spherical particles depending on the length-to-width ratio of the melt pool. The aggregation of powder particles creates *denudation zones* surrounding the melt track [70, 90]. This kind of balling is more likely to be observed at the contours of LB-PBF parts because material swelling jeopardises their manufacturing before balling. At low energy input (bottom right corner of the process window of Figure 7), balling is associated to both melt track discontinuity and *plateau Rayleigh instability*. The latter is defined as capillary instability of the melt pool aiming at the reduction of surface energy [91, 92] and can induce *lack-of-fusion pores* i.e., unmolten powder particles trapped between melt regions, between layers [93]. Balling is further responsible for geometric inaccuracies such as *waviness* or *surface roughness*, which add up to the natural volume reduction during the transition from liquid to solid phase. These potential interlayer connection issues and, in the worst cases, manufacturability issues explain the boundaries of established process windows.

The melt pool influences the heat conduction mode [94]. Two convection modes schematically depicted in Figure 8 can be observed, depending on the ratio between the melt pool depth and its width. The first mode is called *conductive mode* and is described by a melt pool depth less than half of its width. This mode is rarely observed since the low

energy input it involves may not be enough to melt powder particles, which would then simply absorb it. The second heat conduction mode, in which the majority of investigated melt pools in literature fall, is called *keyhole* [87, 95]. It is characterised by a melt pool depth much higher than its width. According to Khairallah et al., keyhole formation can be explained by the interaction between two intimately coupled phenomena, the *recoil force* from the laser impulse and the *surface tension* issued from local temperature gradients between the melt pool centre and its borders [91, 96]. The high local energy input of the laser impulse creates a topological depression similar to a keyhole due to high recoil pressure. The high temperatures trigger metal evaporation and, thus, the development of a vapor cavity that enhances laser absorption [94, 95]. The *Marangoni effect* takes place: the surface tension drives the melt flow from the hot laser spot toward the cold rear. This effect creates spattering as liquid metal with low viscosity is ejected away from the surface. In this configuration, two different kinds of denudation zones leading to lack-of-fusion pores and partially molten particles take place depending on the inert gas pressure. At high pressure, adjacent particles and spatters are attracted by the *Bernoulli effect* induced by the recoiled metal vapor and create denudation zones in the vicinity of the melt pool, whereas they are ejected from the melt pool under low gas pressure [97]. Upon cooling, the surface tension increases and overcomes the recoil effect, which was keeping the depression open [91, 94]. Keyhole dimensions, temperature gradients and corresponding melt pool turbulence are proportional to the energy input density [96]. High energy input tends to lead to deep keyholes and may involve an abrupt collapse of the cavity material, creating so-called *keyhole pores* [91, 94].

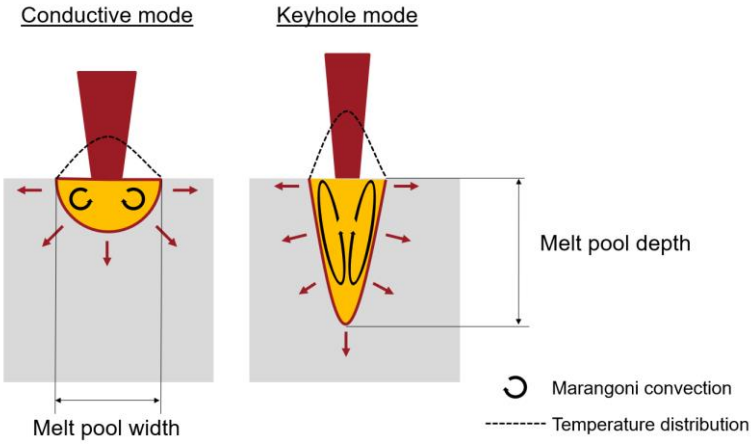

Figure 8: Schematic representation of heat conduction modes in LB-PBF.

The different pore formation phenomena explain that different gas particles such as inert gas [98], hydrogen [98, 99] or vaporised metal [84] can be enclosed. Beside the melt pool, porosity emergence is directly related to manufacturing approaches and, in particular, to hatch distances (Figure 5), rotation angles and scanning patterns (Figure 6) [93, 100, 101]. The term of *overlapped areas* i.e., repeatedly or constantly exposed areas, is often used. Literature has proven that the *overlap* has a non-negligible influence on porosity. For

example, Yadroistev et al. [102] and Han et al. [103] stated that reducing the hatch distance, i.e., increasing the overlap for similar line energy, results in increased keyhole porosity while using a too wide hatch distance, thus, the absence of overlap, increases the number of lack-of-fusion pores [93].

Moreover, manufacturing strategies not only result in local temperature gradients at melt pool scale but also in temperature gradients at both layer and part scales. These temperature gradients occur upon cooling and are directed towards the build platform as the colder spot with respect to the exposed layer. They depend on energy input, build platform temperature, employed material and part geometry. They are due to the difference in heat conduction between powder and bulk material, meaning that the current scanning path and already exposed paths i.e., surrounding structures, impact the mechanical properties of LB-PBF manufactured parts [22, 93].

Melt pool and temperature gradients affect the solidification process upon cooling. For different alloys, process parameters have been identified as the dominant factors for the melt pool solidification front, the evolution of microstructure, the resulting grain morphology and, thus, macro-scale part properties [86, 104-106]. For example, it is possible to directly influence properties by establishing strongly anisotropic microstructures with grains of increased size oriented in the direction parallel to the build direction, which leads to a decrease of mechanical properties [107, 108]. Solidification is not only governed by the cooling rate but also by the direction of the temperature gradient, which, in turn, depends on the melt pool shape, part geometry and part inclination. A notable example is the strong dependency of both temperature gradient direction and consequent texturing on wall-thickness [109, 110] in a phenomenon that can be called *miniaturisation* [111, 112] (Figure 9). Consequently, the influence of both design and exposure strategy is non-negligible as well. Functionally graded microstructures offer further promising insights on laser-driven part properties for different applications such as tailored properties [113] or part labelling [114].

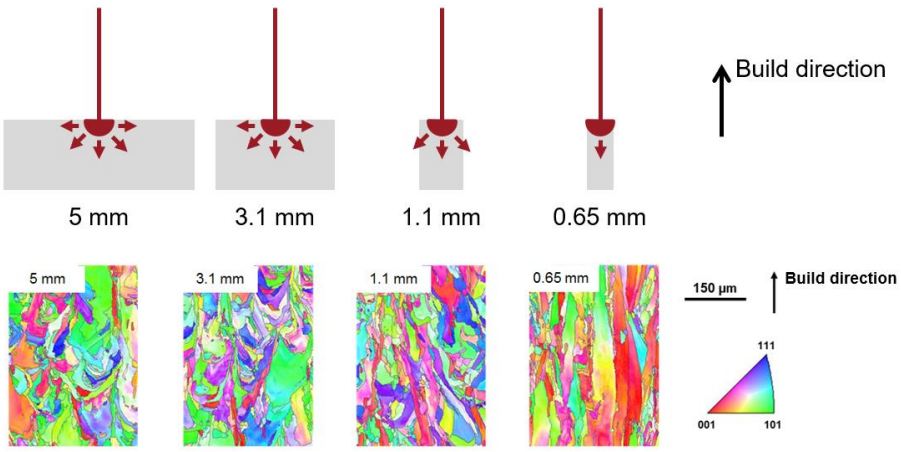

Figure 9: Schematic example of the miniaturisation effect, in which increasing texture and elongated grain size along the build direction can be observed for decreasing wall thickness [111, 112].

Another effect of temperature gradients is the presence of thermally induced *residual stresses* or *eigenstresses* i.e., inner part constraints not originated by the application of external force, in LB-PBF manufactured parts. They originate from thermal strain differences between top layer and substrate material, which can be made of one or more layers. The top layer experiences thermal strains upon powder melting and cooling. During the cooling phase, occurring material shrinkage induces bending stresses (Figure 10). Therefore, residual stresses depend on material properties, surrounding temperature and temperature gradient [80,84]. They further depend on scanning vectors and scanning patterns. Residual stresses are aligned with the scanning direction, creating a non-uniform anisotropic stress field in which temperature oscillates with a frequency dependent on the scanning vector length: the local temperature is inverse proportional to the scanning path length [84, 115, 116]. Here again, this effect can be emphasised by differences in heat conduction of surrounding structures or the presence of pores in sublayers and, thus, is closely related to the part design. It predominantly occurs when large areas are melted due to higher cooling times or when thin-walled parts, small cross-sections, and part borders with inclined or overhanging downskin surfaces are subject to high local temperature [117, 118]. The latter case is generally accompanied by particle aggregation and, in particular, leads to the formation of dross due to the aforementioned melt pool phenomena [119, 120].

If residual stresses exceed yield stress, plastic deformation takes place. They may induce the *curl effect*, which is defined as a geometric distortion characterised by a warping of the upper substrate surface as shown in Figure 10. This effect is likely to occur in the framework of AlSi10Mg LB-PBF because of the high shrinkage ratio of its melt pool during solidification [93]. When the deformation is higher than the layer thickness, it comes to a collision with the coater. This is particularly the case at high energy density input combined with material swelling [22, 121]. In the case of multiple local exposure distributed in a time frame sufficient for intermittent cooling, the concerned layers are subject to a local fatigue cycle prone to crack initiation and delamination. This adds up to with the detrimental effects of pores and surface roughness on the fatigue life of LB-PBF parts [46, 122]. Therefore, temperature gradients can lead to damage in the finished part or to the abortion of the entire manufacturing process, which in turn may lead to significant financial losses.

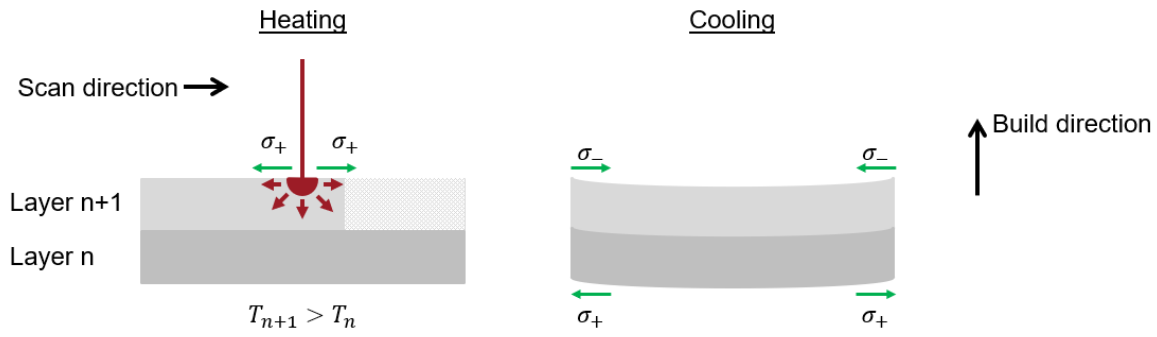

Figure 10: Schematic example of the formation of residual stresses responsible for the curl effect.

Part design not only plays a major role in shaping temperature gradients and the subsequent solidification process but also involves the creation of overhangs in the frame of digital pre-processing (Figure 3). *Overhanging or downward facing areas* belong to the extreme case of downskin areas since they are characterised by a polar angle of 0° combined with an abrupt change in design due to bore holes or a shaft. During slicing the CAD model of the part to be additively manufactured is fragmented into layers with respect to the build direction, as already mentioned in section 2.1.1. This triggers the so-called *staircase effect* (Figure 11), which manifests itself in discontinuous contours depending on the layer thickness [27]. A higher layer thickness leads to a bigger staircase effect, which increases the overhanging surface. The staircase effect leads practically to all aforementioned issues (particle aggregation, dross formation, surface roughness, curling, swelling…) since the melt pool depth is generally higher than the layer thickness and, thus, heat conduction issues are emphasised [67, 117, 123].

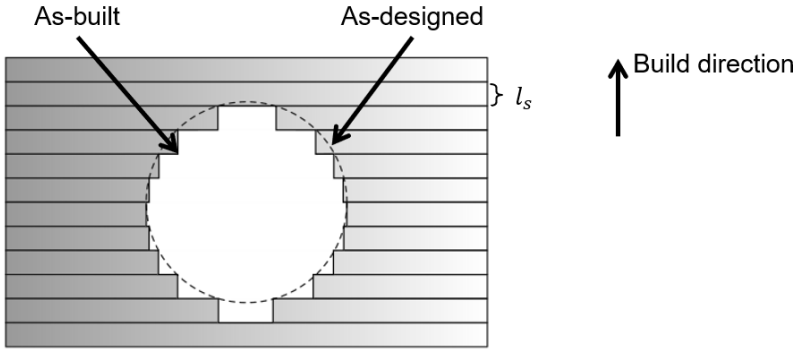

Figure 11: Schematic example of the staircase effect in a bore hole with the difference between as-designed and as-built parts.

2.1.4 Towards controlling process dependencies

As reported in the previous section, process dependent induced defects lead to a part quality deterioration and a subsequent decrease of mechanical performance and, thus, describe a major issue for serial production competitiveness. This section covers the developed solutions to tackle process dependencies, from established and commercialised industrial measures to recent research topics.

The most widely-known and established solutions as part of the additive manufacturing workflow (Figure 3) are, on the one hand, the use of *support structures* and, on the other hand, *part post-processing*.

Support structures are described as temporary design features in an additively manufactured part. They are attached to downskin areas below a *critical polar angle* Θ_{crit} and directed towards the build platform or adjacent design parts. Their main role is to keep the molten material from sinking into the powder bed underneath by fixing the part on the building platform and to avoid, or at least reduce, thermal gradients through the pro-

vided additional heat transfer, compensating residual stresses and all aforementioned induced effects [27, 124]. Several support structure configurations of different dimensionality are available in commercial LB-PBF software. Among them, the so-called *block support* i.e., a three-dimensional shell-like support, is the most widely employed because of its versatility, ease of use and capacity to cover large areas. Although the concept of support structures is well established, recent research shows interest in the role of support features and their influence on both heat transfer behaviour and mechanical properties of additively manufactured parts for a better efficiency [125-127]. As a matter of fact, supports are seen as technological restriction due to the involved supplementary volume, the reduced part accessibility and the supplementary efforts in post-processing they involve, i.e., more resources, time and, therefore, higher costs [12, 60, 69].

Part post-processing, although being often reduced to support removal, covers all necessary steps until the additively part is ready for employment. On the one hand, it includes actions related to the separation of the part from the LB-PBF system. These actions are related to the separation of the structure from the build platform or the removal of support structures and of residual powder. On the other hand, part-post processing consists of part finishing measures such as hot isostatic pressure (HIP), heat or chemical treatment for property homogenisation (e.g. reducing pore size), mechanical machining such as milling to fulfil tolerances, turning or surface treatments such as colouring or coating for an increased surface quality [128, 129, 130]. These various possibilities explain why post-processing costs are nowadays still the driving factor hindering the market competitiveness of additively manufactured parts [23, 63]. It has to be noted that costs can be weighed in cost-effective approach consisting in reducing manufacturing efforts based on the efficiency of a post-processing step that would have been employed anyway. For example, the machine time cost can be reduced by compensating an increased part porosity involved by higher build rates through HIP [131].

In the context of reducing supports and subsequent post-processing costs, the concept of *design for additive manufacturing* (DFAM) has been developed. It can be described as an AM-specific design approach accounting for process dependencies and consists in design measures that can be undertaken at early steps of the digital pre-processing workflow, namely at both CAD and part positioning levels according to Figure 3. DFAM is broadly established in the industrial landscape since standardised specific manufacturing restrictions and design rules based on research results are available for daily practice [27, 124]. Typical design rules aim at reducing thermal gradients while minimising downksin areas and, thus, the amount of support structures. Two approaches are possible: keep the original design intact or perform a part redesign [125]. Both are therefore linked with the way parts are positioned and oriented.

The main DFAM rules are briefly presented and illustrated in Figure 12 below. It is advised to avoid exposed areas that are either large or narrow. In the case of a part with one dimension much bigger than the other ones, it should be positioned so that a fatal collision with the coater ($\Phi \neq 90°$) or an issue with powder distribution ($\Phi \neq 0°$) are both

avoided while supports are minimised ($\Theta \neq 0°$) or avoided as well ($\Theta \geq \Theta_{crit}$). In the typical study-case of bore holes, several alternatives to a drilling axis perpendicular to the build direction, and its involved support structures, are offered. Positioning the drilling axis parallel to the build direction not only avoids support structures but also significantly improves surface roughness due to the absence of the aforementioned staircase effect (Figure 11). If an alignment with the build direction is not possible, a redesign of the bore hole itself is recommended. If possible, the hole should be redesigned so that its diameter d remains below an effective bore hole diameter d_{eff}, under which support structures can be avoided. Alternatively, redesigning the hole's circular cross-section into an ellipse or droplet shaped one results in a support-free design as well by accounting for powder sinking [67, 121]. The latter approach is widely known as *compensation*, which consists in a reverse engineering design accounting for process dependent geometric deviations in as-built parts [132-134].

DFAM is therefore not only restricted to parts but is also applicable to support structures. Since the best support structure is the one which does not exist, the most cost-effective approach is to generate a support free design, i.e., *self-supporting structures* [135, 136]. In the case of non-avoidable support structures, recent research proposes beam-like thin-walled support structures leaning towards cellular structures, and particularly lattice structures, as alternative to the aforementioned commercialised support structures [136-139]. Even more recent trends lean towards the use of so-called *contact-free support structures* [140-142]. This approach consists in thermal support structures without direct contact while being manufactured in the vicinity of the part. The main geometric variables are the downskin angle, the gap width and the thickness of the considered support.

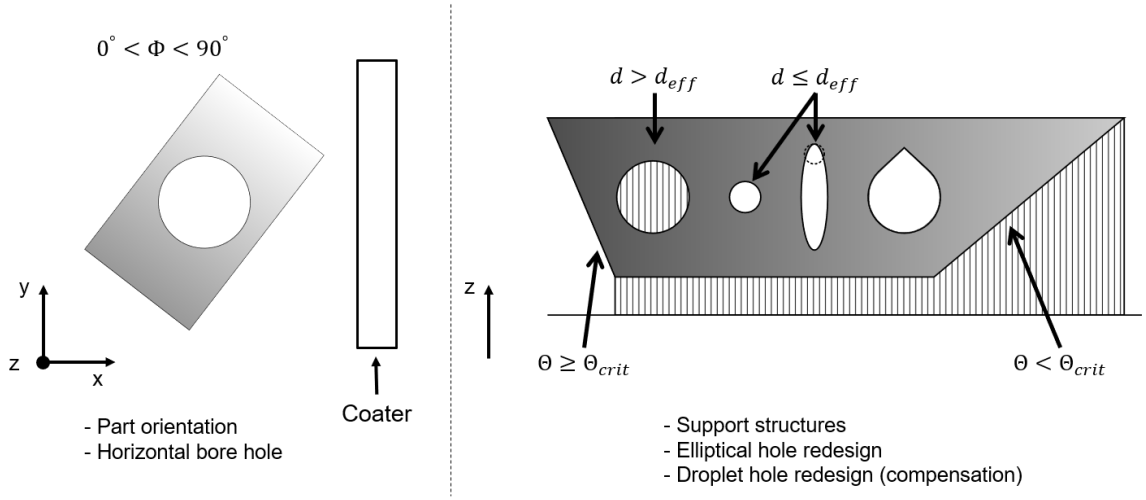

Figure 12: DFAM rules for part orientation, overhanging structures and bore holes in accordance with [67, 121].

However, DFAM proposes "only" general design guidelines while the influence of process parameters is only briefly mentioned. In the abovementioned DFAM examples, the critical polar angle Θ_{crit} is material and machine dependent. This is why norms only indicate a critical range from 30° to 45° [27, 124] based on literature for tolerable surface roughness

[136, 143]. Depending on material and parameters, narrower polar angles are possible but often at costs of decreased downskin surface quality [67, 121, 144, 145].

In a similar way to DFAM, manufacturing rules could theoretically be extracted from literature findings on the investigation of the influence of process parameters on both part quality and performance (see section 2.1.3). It is nowadays common knowledge that enhancing the temperature of the build platform can help reducing temperature gradients and, thus, warping [22, 72]. When it comes to critical features such as part borders, downskin areas or overhang, a reduction of the energy density helps reducing keyhole pore formation and particle aggregation [146, 147]. In this case, scanning patterns need to be adapted, too. In order to minimise the anisotropy and thermal stresses in one direction of the built part, shorter scanning vectors avoid temperature gradients in big areas [148, 149] while the assigned energy input density needs to be decreased at the scanning vector's rotation centre [91] and the orientation of the melt track needs to be changed as much as possible [115]. The latter helps to further reduce lack-of fusion pores thanks to overlapping regions [150]. This explains the commercially employed combination of a chess pattern (Figure 6) and a hatch rotation angle of 67°, for which the same orientation is reiterated only after 12060 layers [63]. The correct overlap between melt pools issued from scanning paths needs to be considered as well [119, 150]. In the case of overhanging areas, so-called *transition layers* with optimised parameters can achieve parts with lesser or no supports [149]. For example, Cloots et al. showed that 20 critical downskin layers with adapted process parameters only require local point support of 2 mm distance [144]. Furthermore, it is possible to once again expose the already exposed area to homogenise both powder bed and cooling rates for denser material and enhanced mechanical properties. This leads to material re-melting, more homogeneous hardness and reduction of both lack-of-fusion and, in a lesser extent, keyhole pores [151]. This explains the widespread use of the standard combination of hatch and double contour exposures. The part is hatched in the beginning, then a first contour exposure is applied to reduce particle aggregation and, finally, a second contour of lesser energy density and different offset is employed to guarantee a smooth transition in terms of porosities and local properties at the interface between the first two exposures.

However, these manufacturing rules may be contradictory to each other since they aim at fulfilling the opposite needs of an energy input high enough to properly melt metal powder, i.e., avoiding lack-of-fusion, without generating instabilities i.e., keyhole pores, dross, and thermal gradients, induced by too high energy input. This explains the role of process windows, the first intuitive tools for finding optimal parameters for better processability. It therefore remains in the hands of the end-user to decide on the use-case specific manufacturing strategy, based on part requirements, critical design features, parameters and costs. This involves of course supplementary research and development costs due to the broad parameter space offered by the additive manufacturing technology [26].

In order to control these various dependencies, *holistic multi-scale predictive models* are in the focus of current research [18]. These models rely on the concept of *physical and digital twins* [152-154].

In the frame of additive manufacturing, the *physical twin* consists in a heuristic database related to the employed machine and manufacturing strategy as well as to the considered part. Gathered data are issued from in-situ monitoring, which is generally performed with sensors or optical and thermal cameras [155-157], and part monitoring using destructive or non-destructive testing [54]. Gathered data are hence ranging from the nano-scale (melt pool, solidification, texture, local mechanical properties) to the macro-scale (porosity, roughness, part mechanical properties).

Its counterpart, the *digital twin*, is defined as a virtual equivalent recreated from initial CAD models or non-destructive test data. Based on the data obtained from the physical twin and modelling approaches at different scales, from melt pool and solidification modelling to macro-scale mechanical simulation, so-called *multi-scale surrogate models* are generated [26, 158]. These data-driven models are the core of the digital twin concept since they offer an approximation of parameter-structure-properties correlations that takes the complete additive manufacturing workflow into account. Combined with multi-objective optimisation, optimal part-specific manufacturing approaches can be identified [18]. Furthermore, employing machine learning approaches based on artificial neuronal networks allow a real-time adaptation of the manufacturing strategy through an interaction between live monitoring and property predictions [26, 159]. This enables the detection and correction of present or upcoming build failures during manufacturing. Recent literature provides the examples of crack mitigation in LB-PBF parts [160], fatigue properties improvement of stainless-steel parts [161] or even the applicability to thin-walled structures such as multi-material metamaterial [162].

One major drawback of holistic multi-scale models is their computational costs and the size of generated data. The two ways current research is proposing to foster the computational efficiency of such models while maintaining their efficiency are *reduced-order models* and *scaling laws*.

Reduced-order modelling consists in a simplification of the mathematical model employed in the framework of numerical simulations. The most known approach is *homogenisation*, which consists in a part-scale mapping of approximated meso-scale properties that are smeared into volume elements [16]. Due to the multi-physics involved by additive manufacturing, the most promising reduced-order modelling approach to achieve computational efficiency is, here again, machine learning [18].

Scaling laws offer a simplified framework to predict process property correlations. They rely on dimensionless numbers and offer an excellent compromise between reliability and accuracy [57, 164]. Several scaling laws can be found in literature. They quantify either process phenomena such as melt pool width [32, 33, 165] and melt pool depth [165], or their consequences such as warping [166] or porosities [164, 167 168]. Their diversity can be once again explained by the broad parameter space offered by the additive manufacturing technology. Therefore, their efficiency and consequent relevance highly depend on both considered variables and resulting benefits for end-users.

According to the current state of research, it can be concluded that the most promising way to foster the economic competitiveness, the sustainability and the reliability of additively manufactured parts is to combine models, machine learning and scaling laws. Based on holistic multi-scale predictive models, machine learning algorithms could extract the most influencing variables from parameter-structure-properties correlations and combine them into easy-to-handle dimensionless scaling laws for industrial use [167].

2.2 Load-driven design in additive manufacturing

Due to the nature of employing material only where it is necessary as described in section 2.1, the additive manufacturing technology unlocks an immense potential for new applications that have not, or only with extreme effort, been possible to manufacture with classical methods. It opens the door to mechanical designs directly inspired from nature and has therefore set a milestone with regard to lightweight engineering.

This section first explains in which extent natural evolution is a key-enabler for load-driven design. Then, its implementation into industrial process development is described and the resulting benefits are illustrated with selected industrial examples. Finally, the main pillar of load-driven design, namely topology optimisation (TO), is introduced and its role in exploiting the full potential of additively manufactured lightweight structures is discussed.

2.2.1 Bionic design

Nature has always been a source of inspiration for inventors, designers or engineers. Years of evolution led to creative processes such as natural selection, recombination and mutation that produced optimised complex structures adapted to the needs of an organism in a given external environment [169]. Bio-inspired designs have been employed in a wide range of fields such as medicine, sport, or aeronautics [35, 47]. To mimic and enhance these designs, the field of *bionics* researches nature's examples and tries to derive manufacturable designs for technical products by transferring the observed principles [170]. On the one hand, the growing interest for bio-inspired structures aligns with the need for preserving natural resources in the current ecological context, and, on the other hand, the emergence of the additive manufacturing technology. As a matter of fact, the number of bio-inspired grants, research and patents increased by five time since 2000 [171], starting point of the industrial expansion of additive manufacturing (see section 2.1).

Natural structures offer remarkable lightweight design features resulting in high *specific mechanical properties*, i.e. properties related to their mass, such as the combination of low density and high energy absorption capacities [34, 47]. A prominent example in the regime of bionics is the human bone, which main grow paths align with the principal directions of endured stresses [172, 173]. Furthermore, smooth transitions between functional areas, e.g. the head of the femoral bone, can be considered as design features issued from

a natural shape optimisation to prevent from notch stresses and therefore to increase their fatigue life [174, 175]. This kind of design is called *load-driven* or *generative* since material is placed where needed to sustain any applied constraints. In the field of lightweight engineering, the term *bionic design* is commonly employed instead, although no direct biological input is present [35].

Aiming at reducing the amount of mechanically unsolicited material is of utmost importance from both engineering and economical points of view. Consequently, the compatibility between additive manufacturing and bio-inspired structures is natural [35, 176]. Figure 13 provides an example of bio-mimicry enabled by additive manufacturing with the extreme lightweight example of an additively manufactured maple seed of total weight of about 0.2 g after coating. The corresponding investigation not only pushes the limits of a commercial LB-PBF system to its lower limits in terms of least reliably manufacturable wall thickness (approx. 100 μm) but also demonstrates the flying ability of the additively manufactured seed. In their work, Großmann et al. speculated on a potential upscale of this design for an improved flight performance of lightweight rotor wings and reduced fuel consumption [79].

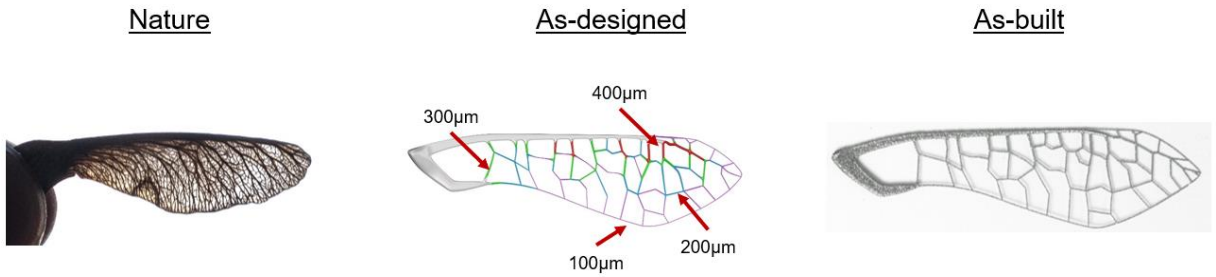

Figure 13: Bio-inspired example of extreme lightweight structures enabled by AM. From left to right: maple seed in nature, design principles and manufactured part [79].

2.2.2 Bionic design and product development

In order to achieve these bio-inspired structures, the industrial process chain and, in particular, the product development process need to be adapted. The main concept behind the product development process for bio-inspired structures remains the same as for other industrialised products. It consists of the three main stages that are the establishment of a product requirement list, the search for design solutions, and the verification of the final design [177]. The main difference lies in the depth of interaction between each stage. While the design development process for conventionally manufactured products can be represented by means of plain sequential diagrams, the product development process in additive manufacturing needs to account for more than one "*design for X*" [178]. The manifold influences of additive manufacturing force rethinking conventional design to comply to manufacturing restrictions (see sections 2.1.2 and 2.1.4). The additive design process is nowadays highly simulation-driven, with topology optimisation (see section 2.2.3) as its most cost-effective approach [35, 63].

Generative design involves a generative process chain. This leads to specific phases providing different possible design scenarios, emphasising the highly interactive and iterative nature of this process [179]. For example, the added value of the additive manufacturing process needs to be checked at several process steps, in particular for its lightweight potential and rentability [121, 179]. Several models for cost analysis are available in the literature [65, 121, 180, 181]. The influencing factors are related to the different stages of the considered additive manufacturing process (see section 2.1.1) and can be related to the part, e.g. build time per batch, consumables, post processing, or to the AM system, e.g. utilisation rate, maintenance or repair costs.

The different phases of the product development process of additively manufactured bio-inspired parts are depicted in Figure 14 [19, 182]. The first step in designing additively manufactured bio-inspired structures is the *concept phase*, which consists in describing the component needed with the help of a requirement list. For each requirement, design solutions are proposed. They can stem from concept researches by means of screening, catalogue and morphological box [183] or holistic data (see section 2.1.4). Subsequently, a first design draft is proposed during the *design phase*. In case topology optimisation is employed at this step, the requirement list is translated into boundary conditions or optimisation objectives (see section 2.2.3). A pool of solutions is generated and design features are derived from the obtained shapes, resulting in different designs and various manufacturing scenarios. Then comes the *analysis phase*, which consists in evaluating the proposed design for its performance, compliance with the additive manufacturing process and its costs. The following *optimisation phase* consists of an iterative design enhancement of the design draft. It primarily takes places if the initial design does not fulfil requirements but can be employed to exhaust the AM-potential of the part as well. Different levels of redesign are possible, from local design change after parametric analysis to new design based on alternative designs and manufacturing scenarios issued, for example, from topology optimisation. As mentioned above, the optimisation phase can include already available data from existing parts such as CT scans or test results [63]. Furthermore, it is possible to exploit and include process parameter dependency, e.g. by using scaling laws [79]. Design, analysis and optimisation phases are reiterated until the proposed design meets all requirements and, thus, leads to the final design.

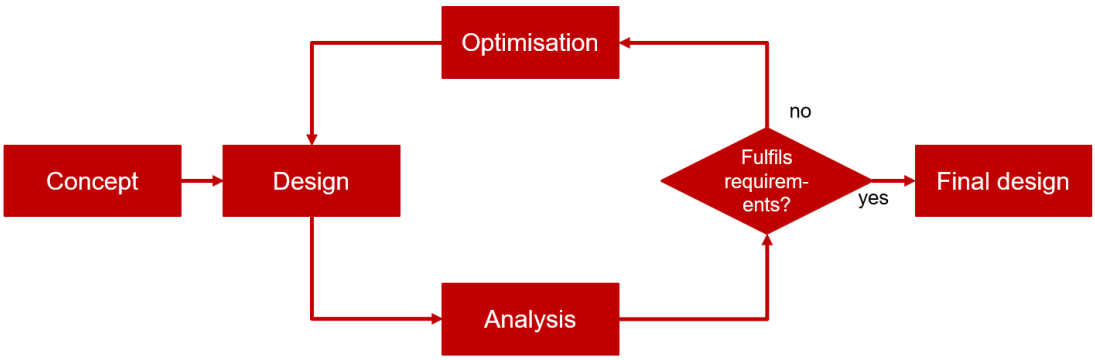

Figure 14: Product development process of additively manufactured bio-inspired parts, in accordance with [19, 182].

Figure 15 illustrates examples of industrial use-cases employing additively manufactured parts issued from optimised bio-inspired design as well as their main benefits, which cannot be achieved by optimising the conventional part.

The part on the left hand-side comes from the injection moulding industry and is employed in the manufacturing process for thermoplastic parts with complex geometries [15]. This additively manufactured injection moulding tool head consists of an innovative helix-shaped close contour cooling system replacing conventionally drilled cooling baffles. Close contour cooling is a direct inspiration of the thermal management system as found in nature, e.g. blood vessels [184]. The final design of internal cooling channels stems from shape optimisation and parametric studies. In the frame of a comparative study with conventionally manufactured injection moulding tools, the additively manufactured part brings two major advantages. On the one hand, the quality of manufactured thermoplastic parts is increased as warping is reduced thanks to a 24 % decrease of the peak temperature along with a reduction by 77 % of the standard deviation of the temperature distribution within the part. On the other hand, an increased productivity is achieved through a reduction of the cooling time by 24 %, which leads to a reduction of the complete cycle time by 15 %. In a fictional example employing values close to the real case (mass of the moulded part 70 g, material costs 2.50 €/kg, revenue per part 0.50 €), a non-negligible yearly revenue increase of 42 k€ was estimated considering only one machine.

The middle example covers a typical bracket as used in the aerospace industry [17, 185]. The bionic design of this part (section 2.2.1) was achieved by topology optimisation. The main benefits of combining topology optimisation and additive manufacturing in this example are a plug-and-play solution, i.e. a conservation of the functional interfaces with other components, and a reduction of the number of components from thirty to a single one. The latter results in an integral design, enabling a reduction of the manufacturing time by 90 % and, at the same time, a weight reduction of 30 %.

The example on the right hand-side deals with the bionic design of a rivet tool as used in the automotive industry [20, 186], for which topology optimisation was employed as well. In this example, a 21 % weight saving was achieved in parallel to a reduction by 11 % of the critical dimensioning stress. Furthermore, the reduction of material waste was estimated to be higher than 98 % when compared to subtractive manufacturing.

Figure 15: Benefits of additively manufactured optimised bio-inspired parts. From left to right: industrial use cases of an injection moulding head [15], a parking bracket [17, 185] and a riveting tool [20, 186].

2.2.3 Bionic design and topology optimisation

Optimisation is a process aiming at bringing the best possible added-value to components in a given system so that this system is able to fulfil a given targeted functionality under given constraints. Depending on the relevance of one considered component with respect to this given functionality, its potential may not be fully exhausted [187]. Optimisation algorithms are employed to solve a wide range of multi-physics problems spanning from basic structural mechanics to fluid dynamics, heat transfer, photonics, acoustics, or electromagnetism.

From the perspective of structural design, optimisation is an active field of research that can propose new counterintuitive designs [188, 189]. There are different levels of structural optimisation occurring at different scales. *Part sizing*, or *dimensioning*, consists in changing local *design variables* in a defined part, generally geometric dimensions such as wall thickness, in the framework of parametric studies. Part-scale design modifications can occur employing *shape optimisation*, which aims at a reduction of stress concentrations and results in smoother contour avoiding sharp edges. *Topology optimisation* (TO) can completely change the appearance of a part and, thus, has been recognised as one of the most powerful design tools since the pioneering works of Bendsøe and Kikuchi [16] and of Rozvany et al. [190]. Topology optimisation seeks the best material distribution within a design domain, the *design space*, while extremising a given performance criterion, called *objective*, and fulfilling a set of constraints, i.e., *restrictions* of *design variables* and *boundary conditions* (BCs). Resulting designs range from discrete grid-like structures to continuum structures [187, 188, 191]. The iterative nature of topology optimisation makes it an enabler of generative design in a process analogous to biological evolution (see section 2.2.1), i.e. with an improvement in every iteration [35, 63].

According to Yago et al. [189], there are two main categories of TO. On the one hand, probabilistic methods based on trial-and-error schemes, e.g. genetic or ant colony algorithm, and, on the other hand, mathematical methods relying on gradient computation. The latter category is the most widespread due to the exponential dependence of computational costs on the number of unknowns involved by the former.

The most established methods among gradient computation based TO approaches are *density-based approaches*. In this kind of approach, TO is performed by distributing continuously varying materials in a discretised design space to comply with objective function and explicit BCs. The elements within the discretised design space are assigned one of the two following distinct states: full and void. This results in a black and white pixel- or voxel-like representation of the optimised volume, for two- and three-dimensional cases, respectively [192-194].

Most of density-based approaches rely on the *homogenisation theory* introduced by Bendsøe and Kikuchi [16]. Rozvany et al. describe homogenisation as the process of replacing an inhomogeneous structural element, containing an infinite number of discontinuities in material or geometric properties by a homogeneous continuum element [190].

This enables employing classical linear elasticity and therefore drastically simplifies calculations [195, 196].

In the framework of TO employing homogenisation, varying densities are allocated to discrete elements according to the optimisation objective [197]. In order to assign elements of intermediate densities one of the two aforementioned status, several approaches are possible. The *Solid Isotropic Material with Penalisation* (SIMP) method introduces an exponential penalty function of varying potency to create a physically interpretable material distribution. Different topologically optimised structures can be extracted depending on the obtained density mapping. Further design solutions can be obtained after regularisation schemes such as density filtering, leaving room to interpretation and engineering judgment [188, 189, 196]. The *Bi-directional Evolutionary Structural Optimisation* (BESO) method, which is also known as *Soft Kill Option* (SKO), offers topology or shape optimisation by mimicking the principle of bone growth [175, 182]. It relies on a simple heuristic criterion, generally stress-based, to gradually remove inefficient material. Elements below a determined threshold are considered as not contributing to the load carrying behaviour of the structure and, thus, are eliminated [189, 198, 199].

Alternative to density-based approaches, *level-set approaches* belong to the mainstream of employed TO. In this kind of approach, an implicit description of boundaries implicitly defined by a scalar function, called *level-set function*, is used to parametrise the geometry. The structural boundary of the design is represented by so-called *zero level isocontour* (or *iso-surface*) of the level-set function [200-202]. The evolving structural boundaries involved by level-set methods allow a convenient treatment of topological changes since they do not involve mesh-dependent spatial oscillations of the interface geometry such as staircasing (similar to slicing as described in section 2.1.3). This results in optimal designs with sharp and smooth edges, avoiding elements of intermediate densities involved by density-based approaches [189, 191, 194].

The efficiency of the abovementioned main topology optimisation approaches was compared in the framework of a study performed by Yago et al. [189]. Although level-set approaches lead to better accuracy in the vicinity of the boundaries, involving less post-processing to smooth design, they involve higher computational costs. Density-based approaches allow to obtain more complex structure while the SIMP approach is slightly more effective. Furthermore, BESO approaches encounter difficulties in obtaining convergent solutions. In the framework of lightweight engineering, an optimal distribution of material is more important than looking for the most suitable surface. This explains why SIMP has become the most popular topology optimisation and been embedded in commercial software to solve engineering problems. As mentioned in section 2.2.2, the generated forms and shape can barely be manufactured by conventional technologies. Therefore, TO can be used to its full industrial potential only in combination with the additive manufacturing technology [203, 204].

In the framework of additive manufacturing, structural TO can be leveraged for various optimisation objectives and restrictions [18, 203]. In order to generate AM compliant robust designs (see section 2.1.4), optimisation approaches take manufacturing restrictions

into account by incorporating build orientation and support structure into the optimisation process [205]. Overhanging surfaces can be reduced [206, 207], support structures can be optimised [138, 208, 209] or even erased in the framework of self-supporting parts [210]. It is further possible to avoid cavities in which powder can be trapped [211] or to account for the manufacturing process itself, with the optimisation of machine-linked process variables (see section 2.1.3) such as the deposition path of the material [212] or control of the microstructure via process parameters [213].

Recent research aims at exploiting the fact that density-based approaches enable to optimise simultaneously the topology and the geometry of grid-type structures [193] in order to exhaust the lightweight potential of topology optimised structures to its greatest extent [203, 213]. With the combined emergent trends of bionic design, bio mimicry and additive manufacturing, distance is nowadays taken with the initial vision of aiming at a removal of porous regions [190], allowing the generation of grey-scale pattern enabled by elements of intermediate densities instead of purely black and white ones [192]. These elements of intermediate densities can be interpreted as *representative volume elements* (RVEs) idealising *representative unit cells* (RUCs) of a given cellular structure (see section 2.3) of corresponding density [51, 214, 215]. The most intuitive case is to idealise the unit cell as homogeneous continuum element and, thus, to exploit the homogenisation process at its full potential [195, 216].

However, this approach raises length scale issues because of the influence of the meso-scale design on the macroscopic response when the unit cell is homogenised. Current research tries to solve these issues by uncoupling the problem of combined material and layout optimisation as a local and a global problem [217], with approaches accounting for meso-scale effects [218] such as notch stresses [219] or anisotropic behaviour [220, 221]. This requires modelling and solving approaches at meso-scale such as de-homogenisation, which consists in translating back the homogeneous continuum element along with its surrounding boundary conditions [222]. This therefore creates the need for new product design methods [223] with implemented multi-scale topology optimisation methods [224, 225] in combination with multi-physics multi-scale materials and process modelling [18] (see section 2.1.4).

2.3 Lattice structures

As highlighted in previous sections, the consideration of grid-like structures and grey scale topologies obtained by optimisation (see section 2.2.3) in the context of bionic design (see section 2.2.1) inevitably leads to cellular design features. *Cellular structures* of the most varied types and forms can be found almost everywhere in nature, e.g., wood, bone structures, or animal shells, and at different scales (nano-, meso- and macro-scales). Consequently, the term of multi-scale metamaterials is often employed to describe cellular structures [34, 36, 47].

This section deals with one subclass of cellular solids, *lattice structures*. The growing interest for lattice structures is explained in general. Then, the structural design of lattice structures as considered in this work is introduced. Furthermore, the link between design and mechanical properties of lattice structures is demonstrated, based on which it is explained why tailoring their mechanical properties and employing structural grading can unleash their lightweight potential. Finally, additive manufacturing approaches and resulting process induced defects are introduced as well.

2.3.1 General notes

According to Gibson, cellular solids consist of an assembly of cells with solid edges or faces, packed together so that they fill space, in which cells are described as an interconnected network of solid struts or plates. They are distributed in two main categories: *stochastic*, e.g. foam or sponge, or *periodic*, e.g. honeycomb (two-dimensional periodicity), lattice structures (three-dimensional periodicity). Cellular structures can further be categorised among *open-cells* or *closed-cell* depending on the shape of their *representative unit cell* (RUC), i.e., the interconnected network they are made of. They are characterised by their relative density $\bar{\rho}$, which is the ratio between their effective density ρ^* and the density of their constituent solid material ρ_S (Eq.4) [34, 42]. In the case of relative densities above 30 %, cellular structures are no longer considered as such but as porous material.

$$\bar{\rho} = \frac{\rho^*}{\rho_S} \tag{4}$$

Over the past decades, the lightweight potential of cellular structures has been recognised as one of the most promising engineering features to design load-bearing structures since their properties may differ from those of their constituent base material [34, 226, 227]. Historically, the use of simple or natural cellular structures, such as cork and honeycomb structures, was one of the first steps into lightweight design [42]. More recently, despite the introduction of metallic foams in engineering fields [228], architected *cellular lattice structures* have been gaining increasing interest. They not only offer controllable superior specific properties [229], but also enable multi-functional design in the context of biomimicry, e.g. heat transfer and load-bearing, by exploiting real biological inputs [35, 36]. Furthermore, they can even surpass natural functions with features not found in nature, e.g. tuneable compliant, chiral or auxetic behaviours [227].

Lattice structures find numerous applications in fields where high structural performances are necessary, such as automotive and aerospace engineering [6, 53, 230]. One of the most interesting properties of lattice structures for engineering practice is the energy absorption capacity [47-49, 52]. Lattice structures can be employed in the mechanical design of wings [79, 231], turbine blades [232], car engine hood [233], anti-icing [234] or shielding systems [235]. They can be involved in the consolidation of parts as well, e.g. as a joint for interfaces between structures, leading to integral design solutions [236, 237].

Lattice structures are also used in other applications as thermal or fluid exchangers [173, 238-240], or for orthopaedic implants [241-243] thanks to their specific surface.

Conventional methods of manufacturing of lattice structures, such as investment casting [226, 244], expanded metal sheet [245] and metallic wire assembly [246] have been progressively replaced by additive manufacturing. The promised design freedom (section 2.1) to mimic natural structures at different scales offers to realise a large number of shapes and topologies with much less effort and, thus, offers the possibility to generate lattice structures according to specific design requirements [38, 230, 247 248].

In the framework of additive manufacturing, lattice structures can drastically reduce the printing time in addition to the increased lightweight potential they offer and, consequently, improve its competitiveness [38, 39, 40]. One major drawback of additively manufactured products is their low time-to-market and high costs due to the high manufacturing time. In the example of the riveting tool of section 2.2.2, an increase of both manufacturing costs and time of 164 % and 1,300 %, respectively, can be observed [20]. Employing lattice structures and, thus, reducing exposed surfaces thanks to their smaller cross-sections would not only lead to lightweighting but also to improved build rates [41] as well as a further waste reduction [36, 50]. In this context, lattice structures can be employed as support structures as well [209].

2.3.2 Why truss-based lattice structures?

According to Gibson's definition (see section 2.3.1), lattice structures can be distributed in two subcategories: *truss-based* and *plate-based* lattice structures. Although plate-based lattice structures and, in particular, *triply periodic minimal surface* (TPMS) lattice structures [229, 249] offer theoretical higher specific properties, truss-based lattice structures of cubic periodicity are in the focus of the present work since they benefit from a well-established scientific background knowledge. This offers more advantages in the establishment of systematic and general design rules, which can be backed by high degrees of comparability and accuracy of results between theoretical properties, numerical simulation and experimental validation.

Firstly, the direct relationship between geometry and mechanical properties (see section 2.3.3) enables engineers to predict their mechanical properties by means of closed-formed analytical models employing for example, the beam theory [42, 43, 250]. Secondly, despite its apparent simplicity, the conception of lattice structures is time-consuming and prone to errors for small scale features, which may result in geometric inaccuracy. Although a broad panel of lattice structures are nowadays computed with the help of established commercial software, modelling approaches for complex lattice structures are focus of current research [227, 251]. This is the case of the most promising plate-based lattice structures, TPMS lattice structures. TPMS lattice structures require mathematical formulations that compromise the quality of explicit modelling methods, such as the *non-uniform rational B-Splines* (NURBS) method employed for truss-based lattice structures [252, 253].

As alternative to B-spline, implicit modelling is employed for complex structures by means of level-set approaches similar to the ones employed in the framework of topology optimisation [227, 254, 255] (see section 2.2.2). This saves a large amount of processing time and computational power, e.g. triangulating and repairing the facet model of complex geometries [256], but, in turn, may results in RUC specific modelling approaches [251, 257, 258]. This explains the recent emergence of commercial or open-source software specialised in the creation of parts for additive manufacturing with specific features, own library and coding for lattice structures [227, 259-261]. Thirdly, similar argumentation can be used in terms of numerical simulation efforts. Finally, the additive manufacturing of truss-based lattice structures is better established (see section 2.3.4) than plate-based lattice structures, which offers a better database for benchmarking.

2.3.3 Structural design of truss-based lattice structures

The representative unit cells of truss-based lattice structures are directly inspired from the *Bravais lattice concept* as employed in crystallography [262]. Among the seven available crystallographic systems, lattices of cubic periodicity are commonly investigated due to the simplicity of the geometric relationships involved by the cubic system [247]. Among the three Bravais lattice cubic systems, the two commonly employed basis RUC are *face-centred cubic fcc* and *body-centred cubic bcc* lattices (Figure 16, left). The former consists of struts positioned diagonally with respect to the RUC faces while the latter is constituted of struts positioned diagonally with respect to the RUC centre of gravity. The corresponding strut inclination angles α are 45° and 35.2°, respectively. Constituent of primitive Bravais lattices, struts in the x- y- or z-directions are used as reinforcements in the respective corresponding directions (Figure 16, bottom centre). Further strut combinations are possible, increasing the complexity of the RUC (Figure 16, right).

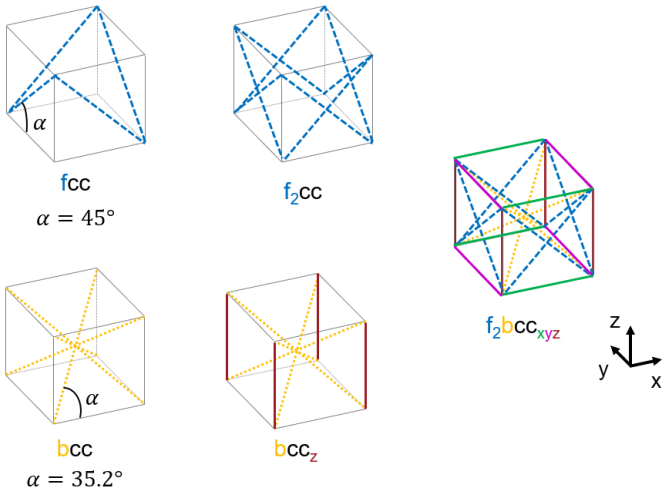

Figure 16: Different kinds of lattice RUC as inspired from Bravais lattices.

From a constructive point of view, the design space of the RUC can be seen as a cloud of nodes of different types: corner nodes, edge nodes, face nodes, and body nodes (Figure

17). Therefore, the region where struts join is commonly called the *nodal region*. This results in different representations of the same unit cell, which main advantage is to avoid representing partial struts at the RUC's edges or faces.

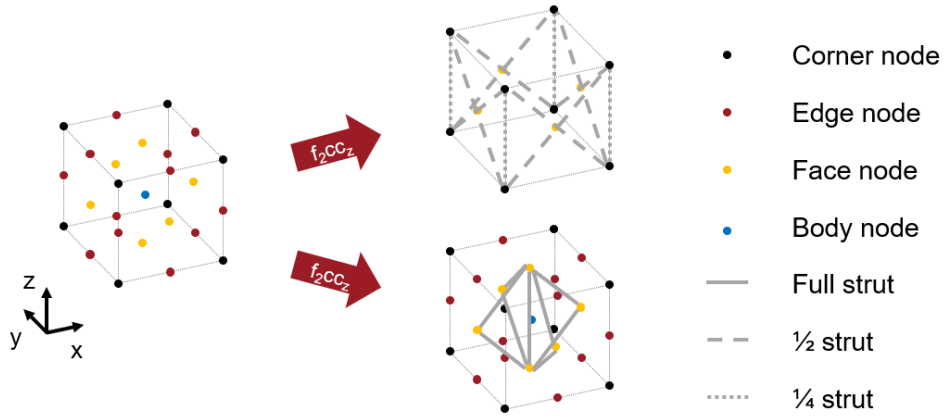

Figure 17: Example of different representations of the same unit cell (f_2cc_z).

The aspect ratio *AR* (Eq.5) of a truss-based lattice structure is a slenderness ratio defined as the relationship of the cell size a and the strut thickness t of a given RUC (see Figure 18, left). Its lower bound, the so-called *critical AR*, is achieved when the RUC not only stops being a framework, i.e., cannot be interpreted as a truss-based lattice structure. This happens when two neighbouring struts are so thick that their overlapping region takes up more than half of the RUC's length [247], resulting in relative densities far above the limit of 30 % (see section 2.3.1 and Figure 22 and Figure 23).

$$AR = \frac{a}{t} \tag{5}$$

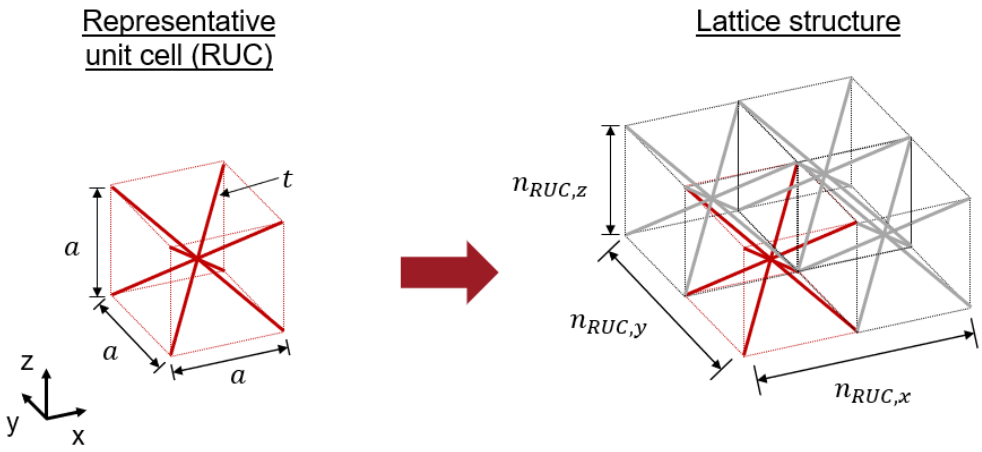

Figure 18: From a representative unit cell to a lattice structure.

Lattice structures are obtained by tessellating the RUC [44] (see Figure 18, right). The total amount of RUCs within a lattice sample is denoted as shown in Eq.6, with n being the number of RUCs in the x-, y- or z-directions, respectively.

$$n_{RUC,x} \times n_{RUC,y} \times n_{RUC,z} \tag{6}$$

2.3.4 Design dependent mechanical properties

Truss-based lattice structures exhibit two distinct types of behaviour depending on the alignment of the struts with respect to the loading direction: a lattice structure exhibiting struts aligned with the loading direction is considered as *stretching dominated* while the absence of alignment with the loading direction leads to a *bending-dominated* behaviour [42].

In literature, the *Maxwell number M* for three-dimensional trusses (Eq.7) is used as indicator of the degree of compliance of a given RUC. It depends on the number of struts s and the number of nodes n involved in the RUC. According to this criterion, $M < 0$ corresponds to a bending-dominated behaviour, whereas $M \geq 0$ means that the lattice structure is stretch-dominated [53, 247, 263]. However, this criterion is not sufficient to predict the mechanical behaviour of lattice RUC since it is purely based on geometric assessments and, thus, ignores the influence of the loading direction. As a result, the only lattice RUC denoted as stretching-dominated is f_2bcc_{xyz} with $M = 5$ [263]. In order to highlight this statement, Table 1 reports the Maxwell numbers obtained for different bending-dominated RUCs and their respective corresponding stretching-dominated counterpart according to the definition provided by Gibson [42]. Therefore, employing the Maxwell number is not advised.

$$M = s - 3n + 6 \tag{7}$$

Table 1: Maxwell number for truss-based lattice structures.

Bending-dominated RUC	*M*	Stretching-dominated equivalent RUC	*M*
fcc	-2	fcc_z	-7
f_2cc	-14	f_2cc_z	-10
bcc	-13	bcc_z	-9
f_2bcc	-9	f_2bcc_z	-5

Figure 19 depicts typical stress-strain diagrams of both bending- and stretching dominated truss-based lattice structures under compressive load. Both are characterised by three regions: the *elastic region* until *yield strength* identified by a first *peak stress* is reached, the *plastic region* identified by a so-called *stress plateau*, and a *densification region* recognizable through a sudden increase of stress.

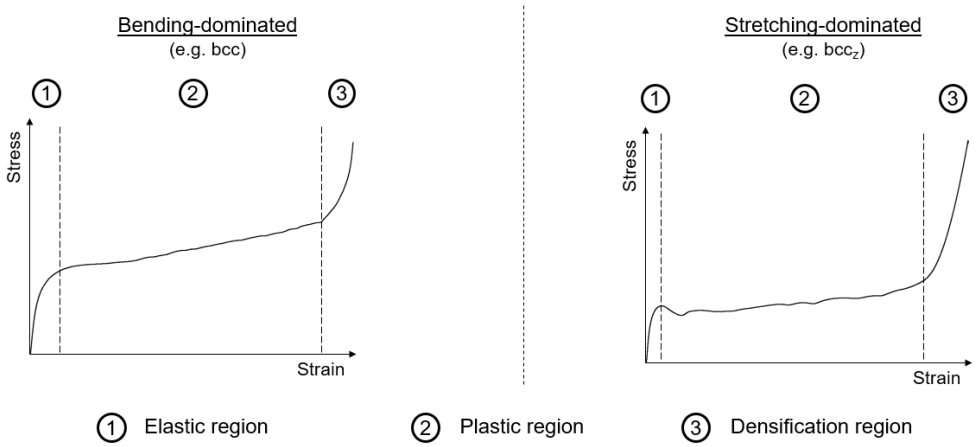

Figure 19: Schematic examples of bending- (left) and stretching-dominated (right) behaviours of lattice structures under compression loading. Recompiled from [264].

However, the diagrams in Figure 19 are not representative for a potential brittle as-built state. This is the case for additively manufactured lattice structures made of AlSi10Mg, which can only achieve this kind of ductile behaviour after heat treatment [265-267]. Figure 20 and Figure 21 show examples of stress-strain diagrams for bending- and stretching-dominated lattice structures under compression loading, namely bcc and f_2cc_z, respectively. In the as-built state, few to no plateau stress is observed. Abrupt brittle failures are present in both cases and, in the case of f_2cc_z, successive load bearing intervals corresponding to new load redistribution within the lattice structure after each collapse [266, 267]. The curve corresponding to a heat treatment ($T = 350°C$ for 2 h) for same AR highlights the improved ductility with higher achieved strains and the presence of a plateau stress. It can be noted that the peak stresses in f_2cc_z do not necessarily completely disappear [265].

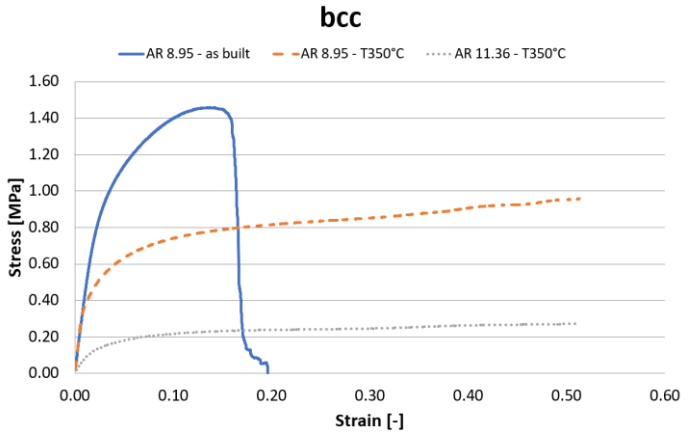

Figure 20: Comparison of stress-strain diagrams for the bending-dominated bcc lattice structure under compression loading (AlSi10Mg). Recompiled from [265].

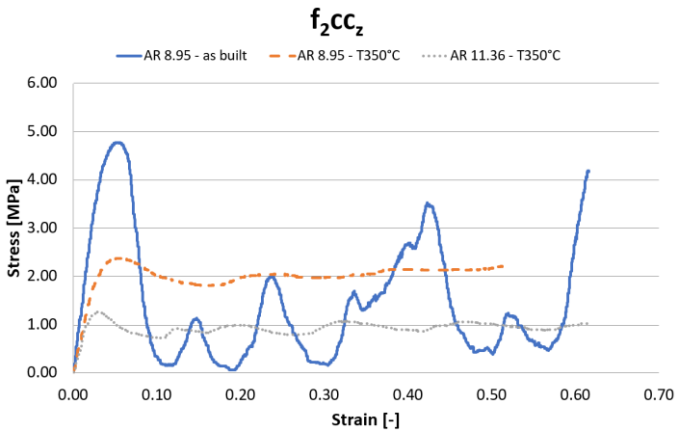

Figure 21: Comparison of stress-strain diagrams for the stretching-dominated f_2cc_z lattice structure under compression loading (AlSi10Mg). Recompiled from [265].

Figure 20 and Figure 21 also provide a comparison of two different ARs (8.95 and 11.36) of the same lattice RUC. It can be observed that different properties are achieved. This is due to the fact that the properties of lattice structures are intimately linked to the configuration of their RUC [34]. Therefore, it is possible to tailor the mechanical properties of lattice structures through their topology (see section 2.3.1). The widely used power law describing the relationship between relative density ρ^*/ρ_S and a given specific property K^*/K_S established the framework of the Gibson-Ashby model is shown in Eq.8 [42, 228, 268].

$$\frac{K^*}{K_S} = C\left(\frac{\rho^*}{\rho_S}\right)^{t_e} \tag{8}$$

Therein C and t_e are experimental variables. According to the model for open-celled aluminium foam in low relative density regions, $t_e = 1$ corresponds to a stretching-dominated behaviour while $t_e = 2$ corresponds to a bending-dominated behaviour.

The Gibson-Ashby model usually depicts property relationships in a logarithmic scale, which can be misleading regarding the decrease of properties. Figure 22 and Figure 23 highlight the dependency of mechanical properties on the configuration of the RUC in a linear scale for bending- and stretching-dominated lattice structure representant, bcc and f_2cc_z, respectively. The correlations between aspect ratio, relative density and effective compressive stiffness E^* were generated based on data extracted from the work of Souza et al. for the AlSi10Mg material [43]. In their work, Souza et al. obtained accurate calculations of both aspect ratio and relative density by a Monte Carlo analysis as well as analytical formulations of mechanical properties based on the Timoshenko beam theory. Moreover, both diagrams depicted in Figure 22 and Figure 23 account for the RUC specific critical aspect ratio (see section 2.3.3), the limit of cellular material corresponding to a relative density of 30 % (see section 2.3.1), and the limit of $AR = 5$, golden rule for slenderness ratio in lightweight design for which the simplification of beams for calculations is no longer valid [269].

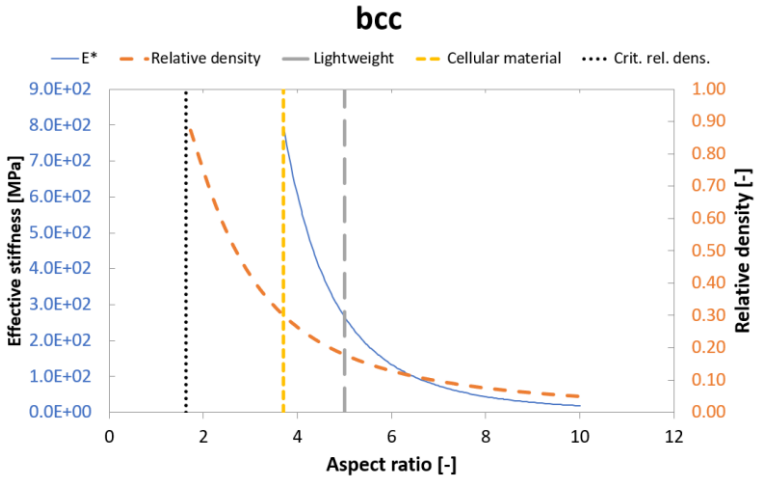

Figure 22: Correlations between aspect ratio, relative density and effective stiffness for the bending-dominated bcc lattice structure (AlSi10Mg). Recompiled from [43].

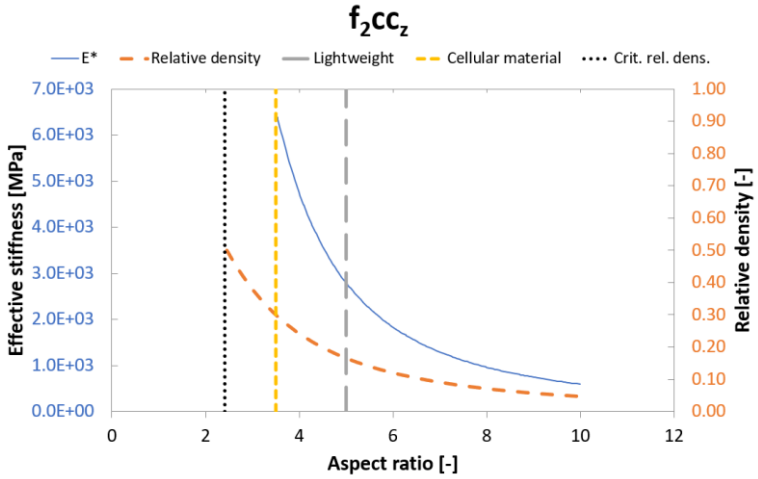

Figure 23: Correlations between aspect ratio, relative density and effective stiffness for the stretching-dominated f_2cc_z lattice structure (AlSi10Mg). Recompiled from [43].

In order to emphasise the importance of lightweight design, Figure 24 shows the lightweight grade L^* of truss-based lattice structures based on the data of Figure 22 and Figure 23. The lightweight grade is calculated as the difference between normalised slopes of both effective stiffness and relative density for a given aspect ratio (Eq.9). The normalisation is performed with initial values K^*_{ini} obtained at the limit of cellular material. A positive lightweight grade means that the gain in effective stiffness is higher that the gain in mass, i.e., leads to increased specific stiffness. This highlights the lightweight potential of lattice structures of aspect ratios higher than 5. However, above an aspect ratio of 10, the effective stiffness of the considered lattice structures starts to flatten at low level (see Figure 22 and Figure 23). It can be concluded from Figure 22, Figure 23 and Figure 24 that the area of interest for lightweight lattice structures is between aspect ratios of 5 and 10.

$$L^* = \frac{(E^*_n - E^*_{n-1})/E^*_{ini}}{(AR_n - AR_{n-1})/AR_{ini}} - \frac{(\rho^*_n - \rho^*_{n-1})/\rho^*_{ini}}{(AR_n - AR_{n-1})/AR_{ini}} \tag{9}$$

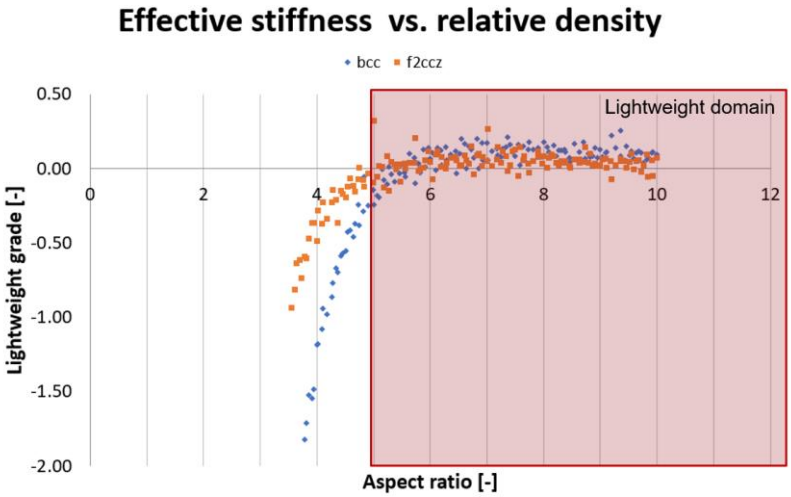

Figure 24: Lightweight grade in truss-based bcc and f_2cc_z lattice structures.

2.3.5 The potential of structural grading

Functionally graded materials (FGMs) are defined by a spatial gradation in microstructure and/or composition in order to offer locally tailored properties [270]. According to Saleh et al., the scientific interest for FGM was raised in the early 1980s while dedicated research has been actually launched in the 1990s, thanks to the technological development of suitable manufacturing processes. Since then, the continuous increase in publications shows the potential of FGM and additive manufacturing is considered as a game changer for their industrial application [271].

In the context of load-driven design enabled by the tailoring of additively manufactured lattice structures and by topology optimisation (see sections 2.2.1, 2.2.3 and 2.3.4), structural grading appears like a natural solution. As for all load-driven design features, numerous examples of structural grading approaches can be found in nature, e.g. bamboo trees or human bones [35, 36, 271]. In the example of the bone discussed in the introduction chapter, the total bone weight consists of 75 % *compacta*, i.e. bulk material, and of 25 % structurally graded *spongiosa*, which makes up to 10% of the total human body weight (against 40 % for muscles) [272, 273]. Inspired from this example, medical implants adapted to the patient's need are made of graded lattice structures [45, 50, 274]. Therefore, a structural grading of truss-based lattice structures can be employed as lightweight design solution for load introduction problems, as highlighted by the precursor works on frame structures of Rankine [275], Maxwell [276, 277]and Michell [278].

More recent works demonstrate the applicability of structural grading and their resulting enhanced lightweight potential [51, 52, 214]. The results obtained in the framework of these investigations are promising as far as lightweight design is concerned. Depending on the structural grading approaches, great improvements in mechanical properties have been observed compared to uniformly distributed unit-cell of equivalent relative density. Grading approaches involving one or more RUCs have already been investigated [279-282] and showed an increase of 80 % of the energy absorption capacity [283] or

drastic improvement of the fatigue life [284]. Saldívar et al. proved that employing functional grading in the framework of bio-inspired hard-soft interfaces leads to mechanical strengths approaching the upper theoretical limit and to an improvement in toughness up to 50 % [285].

The different approaches employed for the structural grading of additively manufactured lattice structures are depicted in Figure 25. The most widely used approach is a structural grading over the wall thickness or, in the context of truss-based RUCs, over the strut thickness t. The majority of examples found in literature consider a constant strut thickness within the RUC [279, 286-288] while continuous grading approaches are less investigated [281]. This is due, on the one hand, to the novelty of such approaches and, on the other hand, to the ease of computing, which enables straightforward design and manufacturing to assess the potential of such structures. Alternatively, structural grading can be achieved by varying the cell size a [230, 289] or a combination of RUC [290, 291]. Again, these grading approaches are less employed due to the compatibility conditions at the RUC's boundaries, restricting the design freedom and, in the case of the latter, leaving potentially unexploited material. Furthermore, Bai et al. have proven in the framework of a comparative study that a structural grading of the strut diameter yields superior energy absorption capacities compared to the other approaches while avoiding critical strength and stability issues of the thinnest and, thus, weakest struts [292].

More complex structures can be achieved by combining the aforementioned approaches, i.e. combining structurally graded RUCs, under the condition that material is aligned to the main load path [293]. A typical example of smart design employing this approach lies in exploiting the constructive vision of a RUC being a cloud of nodes (see Figure 17) to derive different RUCs from a basis one, assuming that the absence of a strut is equivalent to a structural grading of $t = 0$ mm (Figure 25, right) [294, 295]. Doing so enables load path monitoring and offers promising applications in the context of load introductions. In order to realise structurally graded structures of higher order of complexity, topology optimisation is typically employed and coupled with sigmoid formulations to fulfil compatibility conditions at the RUC's boundaries [282, 291].

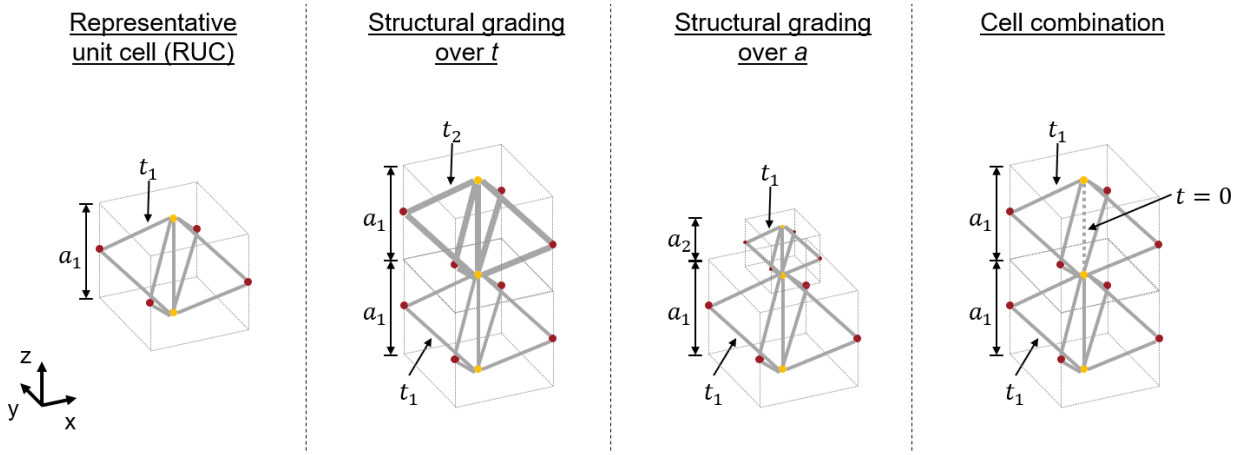

Figure 25: Structural grading approaches. From left to right: initial representative unit cell, structural grading over *t*, structural grading over *a*, cell combination.

2.3.6 Additive manufacturing of truss-based lattice structures

The manufacturability of lattice structures at sub-millimetre range is of utmost interest because it reveals itself as a decisive sizing feature for lattice structures. As the smallest manufactured feature in lightweight components, the smallest manufacturable lattice strut thickness sets the lowest cell size for a unit cell of given relative density and, thus, the lower limit of the design space for targeted specific properties.

Table 2 sums up strut thickness ranges as reported in the available literature dealing with the LB-PBF manufacturing of lattice structures. This table solely accounts for their manufacturability for the different exposure strategies introduced in section 2.1.2, ignoring considerations on resulting quality or printing time. The standard manufacturing approach consisting of a hatch exposure followed by two contour exposures (Figure 6) provides stable manufacturing down to strut thicknesses of about 900 μm [296-298]. Depending on machine and used material, this lower limit can be further reduced to 400 μm [77, 279 280, 299-302]. This proves that the standard exposure strategy was developed for the effective manufacturing of massive bulk parts and is not necessarily suited for submillimetre thin-walled structures [41, 303]. Alternative combinations of exposure strategies leading to reliable manufacturing of lattice structures ranging between 500 μm to 1 mm are the multiple contour exposure [301, 304] and the combination of contour and single-track exposures [298, 305]. For strut thicknesses below 500 μm, single manufacturing approaches (Figure 5) have to be employed. The contour exposure delivers lattice structures of good surface quality with thicknesses often ranging between 200 μm and 450 μm [41, 76, 301]. Strut thicknesses of similar range of order can be achieved by the hatch exposure too, but at cost of geometric accuracy [306]. In the domain of low-resolution LB-PBF manufacturing, i.e. for thicknesses below 250 μm, the point exposure is employed and can produce lattice structures of thicknesses ranging from 100 μm to 500 μm [77-79]. In the case manufacturing by means of point exposure is not available as standard [77], both contour and hatch exposures can theoretically be employed under the condition of performing workarounds. For example, the hatch exposure can be employed at all scales under the condition of manipulating the number of hatch vectors. In the context of low-scale manufacturing, the hatch exposure can be reduced to a single-track exposure, which leads to thicknesses between 100 μm and 250 μm [32].

Table 2: Manufacturability ranges of lattice structures for different exposure strategies based on literature findings. Range have been simplified for clarity.

Exposure type	$t < 250\mu m$	$250\mu m < t < 500\mu m$	$500\mu m < t < 1mm$	$t \geq 1mm$
Point	✓	✓	×	×
Contour	✓*	✓	×	×
Hatch	✓*	✓	✓	✓
Multiple contour	×	×	✓	✓
Contour + hatch	×	×	✓	✓
Double contour + hatch	×	×	✓	✓

*workaround

Recent research focuses on the reliable manufacturing of lattice structures as non-optimal process parameters lead to defects that have detrimental impact on the mechanical behaviour of lattice structures, especially at large deformations [46, 307, 308]. It has been shown for different materials that the mechanical performance of lattice structures is intrinsically linked with their structural integrity [296-299, 309-311]. As for the additive manufacturing of bulk material, appropriate process windows have to be established for the selected manufacturing strategy [76, 296, 312, 313] (Figure 7).

In the context of lattice structures, the role of phenomena involved by AM and the impact of their resulting defects (see section 2.1.3) are emphasised due to their higher relative dimensionality at meso-scale. Both topology and dimensions of lattice structures involve a supplementary amount of surrounding less conductive powder, which in turn leads to magnified heat conduction issues and, thus, temperature gradients. Furthermore, the small cross-sections involved by lattice structures may lead to reduced time intervals between melting of two layers, which results in strongly directed heat flux. Therefore, thin-walled specific effects such as miniaturisation (Figure 9) cannot be neglected [109-112, 314, 315, 316]. Furthermore, resulting texture depend on the employed manufacturing strategy. Figure 26, left, shows exemplarily the texture obtained after employing the contour exposure strategy. Melt pool instabilities induced by strong heat flux not only result in texturing issues but also in a significant increase of eigenstresses and porosities (Figure 26, centre) as well as deviations from the initial design (Figure 26, right). The latter is the most-widely reported issue in the literature. Geometric inaccuracies at strut level are the absence of *roundness* of the strut's cross section, *surface roughness*, *strut diameter variation*, *strut diameter difference*, and *strut waviness* [263, 296, 298, 304, 317-319]. Extreme deviations may lead to local strut failures or may even destroy the complete lattice during manufacturing.

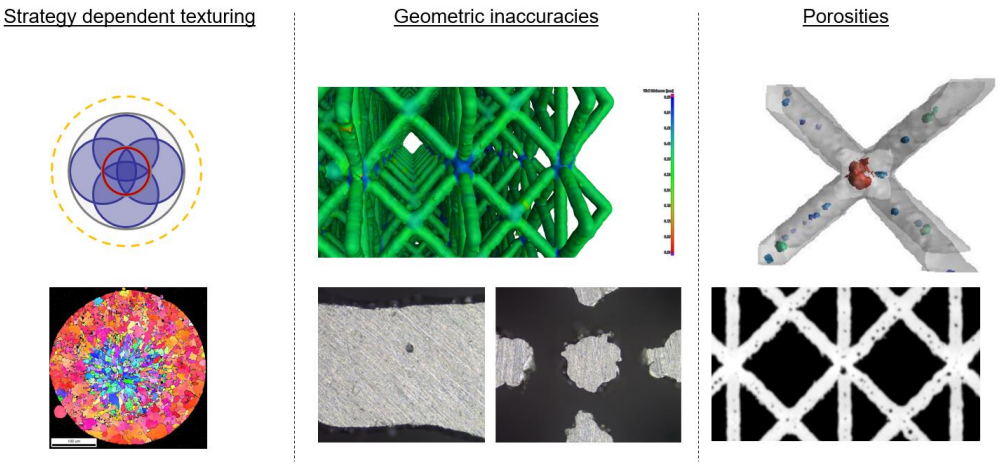

Figure 26: Defects in truss-based lattice structures manufactured by contour exposure: texturing (left), geometric inaccuracies (centre) and porosities (right). Recompiled from [265, 320].

The topology of lattice structures, i.e. their RUC, contains critical areas, i.e. areas more likely to be subject to defects. These are inclined struts and the nodal area (see section 2.1.4). Independently from the build layout, most lattice structures exhibit at least one type of strut in their RUC, which inclination lies in the range of order of the critical downskin angle. Downskin areas are especially subject to porosities, surface roughness and different textures as highlighted in section 2.1.3 [305, 306, 321-324]. Therefore, investigating only vertical struts is not representative of the whole lattice structure. The nodal area is the most complex feature in a truss-based RUC since the generation of defects in this area is further influenced by surrounding struts and, ultimately, other RUCs. This results in potentially different local texturing [322, 324], a drastic local porosity increase [76], necking of surrounding struts [76], or other geometric inaccuracies such as the deviation of its centre of gravity [317, 325].

It can be concluded here that defects impact the complete product process chain of additively lattice structures. Firstly, they do not allow to consider lattice as a perfect truss framework anymore or may lead to different load carrying diameters, which prevents from predicting effective properties and, thus, robust designs. Then, defects hamper the reliable realisation of potentially robust designs. Finally, they may lead to sub-optimal parts, which in turn prevent their competitiveness in spite of their promising properties.

2.4 Research needs

2.4.1 Identified challenges

As explained throughout the previous sections, the nature of additively manufactured products and the means used to exploit their potential lead to specific solutions, whose relevance is questioned at each stage of the process chain. Therefore, the specific efforts required by both manufacturing and post-processing stages prevent this technology from being a competitive contender against conventional manufacturing processes, despite the possible reductions of weight and resource consumption. As a matter of fact, additive manufacturing is often employed for rapid prototyping and rapid manufacturing or complex applications with small batch size while its use in serial production is rather limited [50, 53].

The main concern is related to the process dependent performance of additively manufactured components due to the large parameter space offered by additive manufacturing. This impacts all stages of the process chain, from design and manufacturing approaches to part certification. This aspect highlights the prevailing lack of control over the additive manufacturing technology, being a major roadblock to its widespread use [6, 14, 56]. It can be deduced that *complexity for free* is a myth [23, 28]. This degree of complexity further results in comparability issues between case-specific design solutions and, thus, results in a lack of harmonised standards at every level. *Individualisation* is not free either.

This statement is particularly true for lattice structures. Although they may offer reduced printing time, the knowledge gathered around them is not as deep as for bulk material. Despite extensive research for more than a decade, the literature on the relationships between process parameters, microstructure and mechanical properties of lattice structures is still fragmented due to issues involved by their length scale.

Due to the current issues encountered for bulk materials, lattice structures are not in industrial focus as they still require extensive and expensive research, a hindering argument for profit-based companies. Consequently, lattice structures are employed in industrial structural parts in the case of a straight-forward integration with standard parameters, under the condition to bring immediate benefits without further improvements. Lattice structures are often integrated as in-fill for lightweight purposes or thermal exchangers rather than for mechanical purposes [39, 50]. In the worst case, they are implemented as fancy item for eye-catching in a nice-to-have showcase product issued from rapid prototyping. When it comes to their involvement into structural parts, lattice structures are only involved in secondary, i.e. non-safety relevant, structures such as topology optimised brackets [6, 14, 53]. Similar to additively manufactured end-products issued from mechanical engineering, the deployment of lattice structures in primary structures has still not reached high technology readiness level [48, 49].

As for bulk material, the main challenge lies in understanding and predicting the mechanical performance of additively manufactured lattice structures. Such input is of utmost importance for daily engineering practice since it could open the door to a *laser-driven lightweight design*. This concept relies on the control over the manufacturing defects in a given structure, based on property tailoring and reliable predictions of the mechanical performance. For example, it can be speculated that the undesired roughness [46], if tailored so that no fatigue issues are encountered, could be beneficial to the implementation of lattice structures as design features in bone implants.

The mechanical performance of lattice structures can be predicted by analytical descriptions based on beam theories [43, 250, 268, 326, 327], holistic modelling employing semi-empirical probabilistic finite element models [312, 317, 325, 328-330] resulting in design approaches accounting for process induced defects [331-333], or scaling law using dimensionless numbers specific to lattice structures [32, 79, 167]. However, each approach has its own downsides. Available analytical models are still rarely applied since they are subject to relatively high deviations from experiments. This is due to the fact that modelling assumptions do not systematically consider manufacturing defects or rely on slender structures [43, 326, 334] and, thus, do not address the reliability and reproducibility issues raised by process dependencies. Up to 300 % deviation could be observed for lattice structures of aspect ratio lower than 5 [269], whereas higher aspect ratio lead to 10 % and 20 % deviation from analytical values in the best cases of compression and tension loading, respectively [43, 326]. Scaling laws depend on input parameter variables and influencing parameters, which implies either initial knowledge on the most influencing parameters or educated guesses. The lack of available holistic models with reasonable computing effort hampers the implementation and optimisation of lattice structures at

industrial level. Moreover, the still low number of expensive and time-consuming empirical investigations for other cases than compression [46, 55, 286] further challenges the establishment of lattice structures in a precise niche of technical products.

The intricate problematic of meso-scale parameter-structure-properties correlations leads to missing specific standardisation procedures towards design and certification guidelines geared towards lattice structures. The absence of standardised characterisation and failure criteria highlights the very limited understanding of the impact of microstructural effects on the macroscopic mechanical behaviour and, more particularly, on the stiffness of lattice structures. It is the role of current research to find straightforward and efficient design rules, universal design criteria, and reliable and reproducible manufacturing approaches gathering the different length scales involved in additively manufactured components with implemented lattice structures in order to provide a framework that allows the development of optimal metamaterial for a specific application and, thus, to exhaust their lightweight potential to its greatest extent [335, 336].

2.4.2 The example of tensile specimen

The reliable mechanical characterisation of the mechanical properties of additively manufactured lattice structures is crucial to assess the influence of process parameters on their mechanical properties and, thus, to identify a precise niche of technical products. After numerous investigations of their compression behaviour, an interest for their properties under tensile loading arises as the question of their fatigue properties is raised [46]. However, tensile tests are scarcely investigated because of the higher complexity of the sample design of tensile specimens [53, 77]. No norm nor publication covers a systematic and standardised tensile testing guideline for additively manufactured lattice structures. A norm on the tensile testing of metallic cellular materials does exist but was developed in the frame of the mechanical testing of honeycomb structures [337]. Therefore, it does not address any explicit methodological specimen design for the reliable and reproducible characterisation of additively manufactured lattice structures.

Designing tensile specimen has been recognised as a "*considerable challenge*" [46] with, in particular, the difficulties encountered by the present edge effects that hinder failure at the centre of the considered samples. In the case of an inappropriate design, a local stress concentration occurs at the transition between lattice and bulk material needed for the connection to the testing machine, which results in an undesirable fracture at this location [338, 339]. The aforementioned absence of standards leads to a big room for interpretation and, thus, a high diversity of sample design and manufacturing approaches, which are still in current research's focus.

The history of the main features in tensile specimen design found in the currently available literature allow to retrace their evolution and to witness the growing awareness on the need to mitigate the edge effect. Very first tensile specimens dealt with lattice structures of cubic periodicity consisting of rectangular or quadratic cross-sections, i.e. a description of their configuration in the cartesian coordinate system as shown in Eq.6. Initial tensile

specimen designs consisted of a straightforward application of a bulk part onto the investigated lattice structure for the connection to the test rig [77, 247, 338-341]. These designs were further developed with the presence of a transition region as first issues with stress concentrations were encountered [300, 329, 342-344]. Parallel to this development, lattice structures of circular cross-sections, i.e. structure configurations defined in a polar coordinate system, were developed to directly mitigate edge effects for straightforward designs [345, 346] and samples with a transition region [286, 347, 348]. It can be noted that all the aforementioned references employ the same unit cell for both the transition and investigated regions as advised by Bai [292] (see section 2.3.5) while other load introduction configurations remain theoretically possible.

However, the diversity of tensile specimen, especially in size, and the lack of corresponding justification of such designs do not contribute to the proper comparability and transferability of results between the reported investigations [46, 55]. This results in unreliable holistic databases. Moreover, despite the noticeable growing awareness for size and edge effects, it is not guaranteed that the proposed solutions offer a pure tensile stress state and, thus, that the investigated cells are representative for the investigated lattice RUC in continuum, i.e. that theoretical tensile properties can be retrieved.

The lack of systematic development and concrete design guidelines is further emphasised by the lack of justification for the chosen manufacturing approaches [46, 50, 53]. Challenges at two specific levels can be identified.

On the one hand, the transition between bulk part and lattice structure is not only a considerable challenge in terms of design but also regarding its realisation because of manufacturing restrictions specific to LB-PBF [124]. Both parameter and inclination dependencies of the manufacturability of both lattice struts [299¸303, 311, 349] and bulk parts [145, 247, 350] add up to the initial design issues implied by the cross-section change at the bulk-to-lattice interface [338]. As a matter of fact, a cross-section change does not only result in local stress concentrations but also in inhomogeneous temperature gradients and, thus, in manufacturing issues linked with heat dissipation and eigenstresses [144¸247]. The available literature on test samples and sandwich structures involving lattice structures develops two main design approaches: *integral* and *modular designs*. *Modular designs* can be found in the standard for tensile testing of metallic cellular materials [337], which aligns with the standard for sandwich structures made of honeycomb cores [351]. The bulk part is manufactured separately from the lattice structure and, as for honeycomb cores, both parts are bonded to each other [247, 339, 352]. While this approach overcomes most of the DFAM challenges, the effectiveness of the employed load introduction has still to be questioned. *Integral designs* consist in printing the sample monolithically. The easiest approach is to print the bulk part (or skin) vertically, i.e. parallel to the build direction [247, 324, 353, 354]. In order to account for the inclination dependency of the manufacturability of both lattice and skin, the sample can be inclined [345, 347, 355]. However, this measure may require support structures and subsequent machining. Literature reports different cases of horizontally printed skin panels of sandwich structures with lattice cores. Nevertheless, all of them rely on the same principle without explicitly

mentioning it: lattice structures are employed as support structure of the skin. To overcome manufacturability issues, DFAM compliant design features such as cones can be employed in order to increase the manufacturing surface. They can be used as space filler [77, 356] or as load introduction feature, considering them as a special case of structural grading. In the case of classical structural grading, lattice structures are graded either over the cell length [247] or over the strut diameter [293, 300, 344, 348] as described in section 2.3.5. If lattice structures are dense enough or their diameters are big enough to offer a smooth temperature gradient, the overhanging area can be successfully printed without structural grading [338, 357, 358]. In some cases, an overlay of one or two layers between lattice structure and skin ensures good connection at the interface [77, 324]. Other sources report parameter and/or scanning strategy optimisation of transition layers (see section 2.1.4), i.e. the first skin layers in the vicinity of the interface [77, 144, 349, 350]. Precise indications about the reasons for the chosen design and printing approaches are rarely provided and manufacturability issues with corresponding workarounds are not systematically mentioned. This shows that manufacturing is rather a background information for current research reporting, which hampers the development of robust approaches and guidelines for reliable and reproducible manufacturing of lattice structures implemented into bulk parts.

On the other hand, design and manufacturing challenges are posed at lattice level, especially in the case of structural grading. The aforementioned references employing structural grading consider either a straightforward and arbitrary grading, in most cases a single grading aligned with the loading direction, or complex configurations issued from numerical topology optimisation algorithms, which therefore lead to case specific optimised solutions [221, 359-363]. In both cases, the low comparability with other design solutions compromises desirable normalised design rules. Another design issue concerns the transition between unit cells. While recent research focuses on the influence of process parameters on the mechanical behaviour of truss-based lattice structures, less attention is given to geometric notches issued from sharp edges induced by the structural design. The nodal area is not only critical for manufacturing (see section 2.3.6) but also for design [328, 364-366] since they lead to fatigue issues that may even be present after using optimisation routines [360, 367, 368]. Notches often appear for big changes in cross-sections as is the case for tree branches under different loading scenarios [174, 175]. Avoiding design notches is by definition a form optimisation task, which is mainly addressed by the single universal solution of a form or shape optimisation by means of circular fillet radius in literature [134, 328, 344, 347, 366, 369]. General construction guidelines allowing further complex shapes for this particular case are not available while load case specific optimisation solutions can always be developed [370].

Depending on the targeted manufacturing scale, lattice struts can be realised in different ways (see section 2.3.6). However, the lack of systematic reporting often prevents from comparability studies in this case too. While straightforward manufacturing guidelines are desirable for the reliable and reproducible manufacturing of lattice structures, the reasons for the chosen printing approach are not explained in spite of raised manufac-

turability issues. In most cases, one single manufacturing strategy is considered. It is supposed that, when the manufacturing strategy is not reported in research papers, the standard approach is used. Although current research tries to raise the question of the right scanning strategy and design guidelines for small scale features [76, 78, 298, 301, 303, 304, 316, 331, 371], parameter variations without strategy change are commonly explored while comparisons of strategies do not include parameter optimisation. This statement is particularly surprising knowing that the manufacturability of downskin surfaces depends on both parameters employed and part design, and that DFAM rules for bulk material not necessarily applicable to the specific case of lattice structures [299, 311, 349] (see sections 2.1.3 and 2.1.4).

3 Methods

This chapter describes the methodology employed in the different investigation stages of this work. Firstly, the investigated unit cells and the sample design for tensile specimen developed to address the issues raised in section 2.4.2 are introduced. Secondly, theoretical and numerical approaches as employed for the verification of the proposed designs (see chapter 4) are described. Finally, both manufacturing and experimental frameworks are introduced in the context of the subsequent validation of the proposed designs (see chapters 5 and 6, respectively). Further details specific to each investigation are described in the corresponding chapters. All generated data and created scripts are available at the institute on demand.

3.1 Design

In this work, explicit modelling is employed (see section2.3.2). All relevant features were manually created and parametrised using the CAD software package *Siemens NX12*. The parametrisation of lattice structures enables the simple and fast variation of their design as described in section 2.3.3 and, thus, of their mechanical properties (see section 2.3.4).

3.1.1 Considered unit cells

In order to limit the scope of the investigations, the body-centred cubic RUC *bcc* and the double-face-centred cubic RUC with vertical reinforcements f_2cc_z were selected as the representative of both bending-dominated and stretching-dominated categories of truss lattice structures, respectively (Figure 27). The former yields high fatigue [345] and high energy absorption [39, 46, 247] properties despite its low specific stiffness when compared to other lattice RUCs. Furthermore, bcc lattice structures exhibit the highest nodal stress concentration among truss-based lattice structures [296], shorter build time [279] and their isotropic behaviour [43] facilitates modelling approaches based on homogenisation thanks to their strut configuration. The f_2cc_z RUC exhibits the highest specific stiffness and the highest specific strength compared to other truss-based lattice structures and is therefore frequently examined in the literature [43, 77, 296].

The representation of the selected unit cells was chosen so that the strut junctions are located in the centre of their upper and lower faces, i.e. no half or quarter struts are present. This simplifies numerical simulations and ensures reliable manufacturing.

The lowest investigated aspect ratio of the considered RUCs is $AR = 6$. This enables to remain in the vicinity of the lightweight limit of $AR = 5$ (Figure 24) even after a structural grading based on strut diameter variation and, thus, guarantees the validity of the employed beam theory (see section 3.2.1). The lowest investigated aspect ratio of the considered RUCs is $AR = 10$ as upper limit of realistic use-cases for load carrying components.

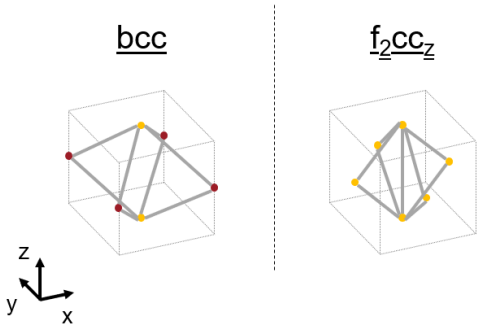

Figure 27: Selected unit cells.

3.1.2 Tensile sample design

Figure 28 depicts the principle of the proposed tensile specimen design. It furthermore highlights the comparability to existing norms for bulk materials. The two norms used for comparison purposes are the norm for the determination of plastics tensile properties [372] and the norm for tensile testing of metallic materials [373]. The proposed tensile specimen design consists of three distinct zones: the *target region*, in which the desired homogeneous tensile stress state is to be ensured for the specific unit cell under investigation, the *bulk region*, which stands for the sample bulk grip area that is used for the primary load introduction, and the *transition region*, which acts as a design space to guarantee a homogeneous tensile stress state at its interface to the target region. The quadratic cross-section of the bulk region in the xy-plane is directly extracted from the cubic periodicity of the selected unit cells. While the sample dimensions are based on units of length in the existing norms for bulk materials, dimensions based on lattice structures rely on the number of unit cells in each direction, which indirectly leads to final samples dimensions through the size of the unit cell (see section 2.3.3).

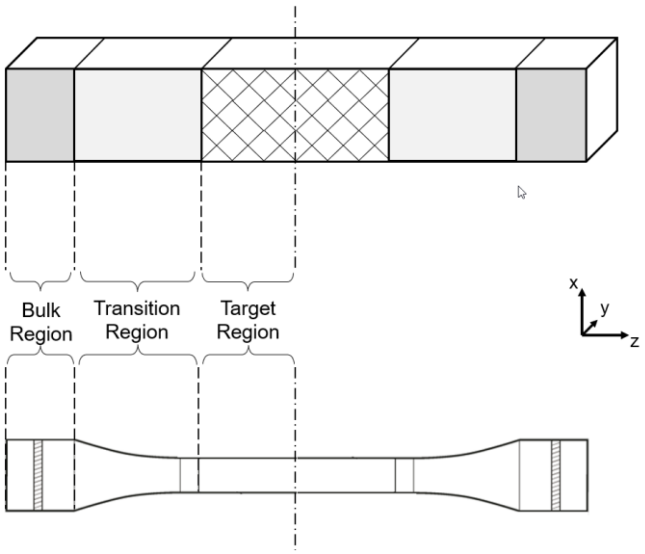

Figure 28: Proposed tensile specimen design (top) and comparison with sample design for bulk material (bottom). Recompiled from sample 1B [372].

The aspect ratio of the specimen (AR_s) is introduced (Eq.10). It describes the slenderness of the sample through the relationship between the number of RUCs in the vertical, i.e. loading direction, $n_{RUC,z}$, and the number of RUCs in the transverse directions, $n_{RUC,x}$.

$$AR_s = \frac{n_{RUC,z}}{n_{RUC,x}} \tag{10}$$

3.2 Modelling

This work focuses on the elastic domain as both design and sizing of the majority of load-bearing parts are meant to withstand loads without entering the plastic domain, with exception of energy absorption purposes. Therefore, both geometrical and material linearities are assumed as only static calculations are performed.

The analytical model is coded in *MATLAB* while numerical simulations employ the software packages *ABAQUS CAE 2017* and *Altair Hyperworks v14.0*. Topology optimisation analyses were performed using the software the *Optistruct* solver from the software package *Altair Hyperworks v14.0.* Model generation, post processing and plot generation were monitored using *MATLAB* and *PYTHON* scripts.

3.2.1 Analytical model

The analytical model developed by Souza et al. [43] is used for comparison purposes in the framework of the predictability of the mechanical properties of lattice structures. Moreover, the analytical yield strength is used to determine the limit of the elastic domain to assess elastic properties in the framework of experimental investigations.

It determines the theoretical relationship between aspect ratio, strut diameter, and mechanical properties of a given cellular structure, whereby the cell struts are considered as Timoshenko beams [374]. Furthermore, this model relies on a Monte Carlo density integration for a precise estimation of the relative density of the considered lattice structures.

The analytical model consists of a strain energy-based homogenisation scheme in the linear elastic domain [16]. The RUC is idealised as an ideally homogeneous orthotropic RVE, whose macroscopic strain energy density is determined through an integration of microscopic stresses and strains throughout its complete volume. In order to assess the effective elastic properties, the cell geometry is parametrised and the structural periodicity is granted through the application of periodic boundary conditions. By means of the Castigliano's 2nd theorem and local transformation matrices, the macroscopic strains and stresses can be deducted based on the displacements and forces applied to the RVE. Young's moduli and Poisson's ratios can be obtained as scalar from the uniaxial load case, where a single axial unitary load is considered. The shear modulus is extracted from six

load cases (three normal stresses and three shear stresses) to account for the assumed orthotropic behaviour of the cellular material. The yield strength is then derived from maximum applied loads.

3.2.2 Numerical simulations

Although different software packages were employed to fulfil different purposes, they rely on similar modelling approaches.

1D beam finite elements were employed for a direct comparison with the analytical model described above and for load path monitoring in the context of load introduction. 3D finite elements were employed in case details on the local stress distribution in a given structure were required or in case design features need to be extracted in the framework of topology optimisation.

In the present work, numerical simulations cover two length scales of the structure (Figure 29). The finite element model consists of either a single RUC or a lattice structure. In the latter case, lattice structures can be idealised as an eighth model thanks to symmetry considerations. To do so, applied boundary conditions were defined according to the compatibility conditions involved by the symmetry planes. In all cases, the load introduction occurs at the top section of the modelled structures. In the framework of numerical investigations, it is assumed that the load introduction from the bulk region into the transition region is homogeneously distributed over the bulk grip material surface (see Figure 28).

The reported results diagrams exploit the symmetry of lattice structures too. Two-dimensional plots of selected view cuts are sufficient to offer a representative assessment of the whole structure.

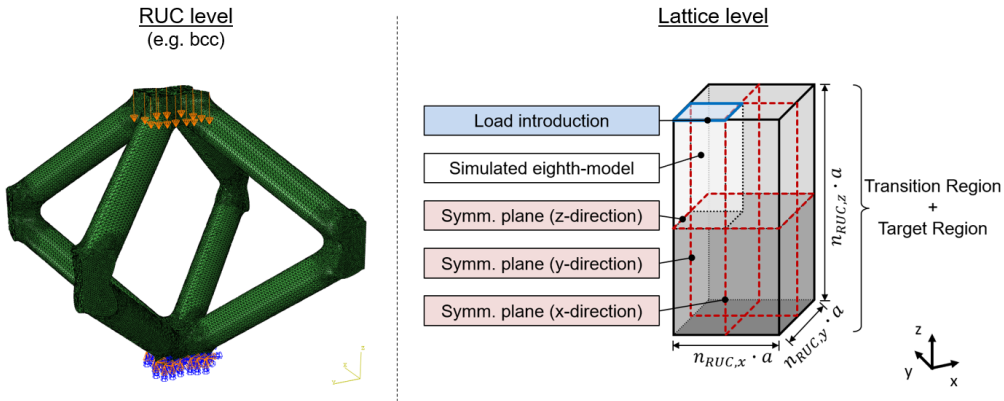

Figure 29: Two modelling scales: representative unit cell (left), lattice structure under symmetry conditions (right).

3.3 Manufacturing

The software packages *Materialize Magics v23.1* and *EOS PRINT v2.6* were employed in the framework of digital pre-processing (Figure 3). All investigated specimens were produced in AlSi10Mg by an *EOS M290* laser powder bed fusion system equipped with a Yb-

fibre laser of an 80 μm beam diameter. The AlSi10Mg powder [375] was identified as ideal for research in additively manufactured lightweight design because of its low density compared to other metallic alloys and its relative low costs compared to other alloys. Direct post-processing steps consisted of the separation of samples from the build platform. To do so, the initially designed lattice structures were assigned supplementary sacrificial layers in the build direction, which were sawn off and subsequently grinded with tools especially manufactured for this purpose (Figure 30). There were two types of grinding tools: a grinding tool of variable size machined so that its walls are moveable and different lattice structures can be clamped by a holder, and additively manufactured tools of fixed size employed in the case of high number of samples of the same size for comparable grinding.

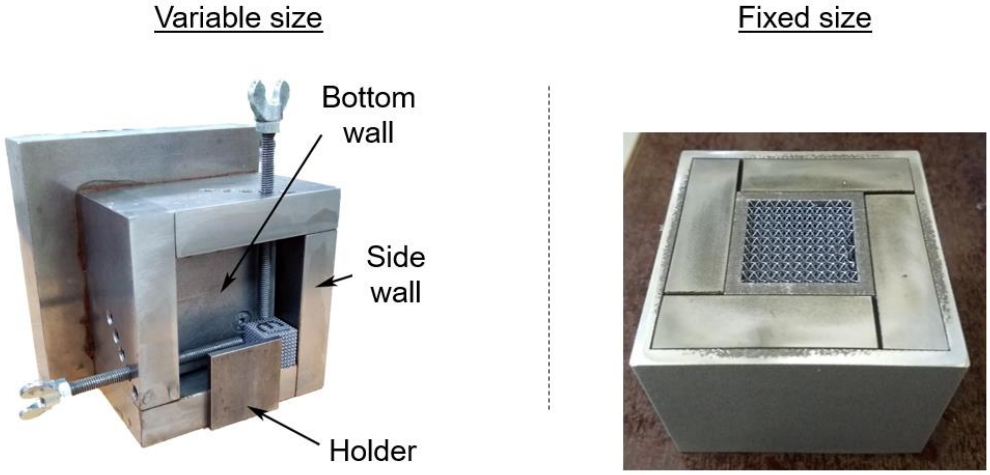

Figure 30: Grinding tools for lattice structures: tool of variable size (left) and tool of fixed size (right).

3.4 Experimental setup

The experimental setup is divided into two parts: the assessment of the mechanical properties of additively manufactured lattice structures and their structural integrity. In the present work, mechanical testing, density measurement and optical microscopy are deemed sufficient to effectively provide clues on the potential and challenges of lattice structures for load-bearing applications as this work focuses on the elastic domain (see section 3.2). Therefore, post-processing methods such as heat treatment [264, 265] or investigations by means of CT [311, 320] and EBSD [265] as performed in other studies were not performed and the manufactured samples were investigated in their as-built state. Defects can be considered as stochastically distributed and can be therefore expected to have a less to insignificant impact on the elastic properties compared to their geometric configuration [265, 317, 329, 330, 376].

3.4.1 Mechanical testing

Mechanical investigations were performed using a *Zwick/Roell Z100* testing machine. Uniaxial static compression tests were conducted in accordance with the corresponding German engineering norm DIN50134 [377] while uniaxial tensile tests were carried out according to the standard DIN 50099 [337] (Figure 31, a & b).

In the case of compression loading investigations, the determination of the plateau stress deviated from the standard, similarly to Großmann et al. [76] and Weidmann et al. [378]. This is due to the brittleness of the AlSi10Mg alloy in its as-built state, which yields a stochastic mechanical behaviour after reaching the compressive failure strain (Figure 20 and Figure 21). The calculation of the plateau stress R_{plt}, which is assessed through a preliminary test, is based on the first maximum compressive strength R_{eH} corresponding to the first local maximum in the stress-strain curve (Eq.11). The effective Young's modulus is determined within the advised range between 20 % and 70 % of R_{plt}, conformly to the norm. In all cases, the stiffness of both machine and load introduction were considered by correcting the measured displacement of the crosshead (Figure 31, c).

$$R_{plt} = \frac{1}{2} R_{eH} \tag{11}$$

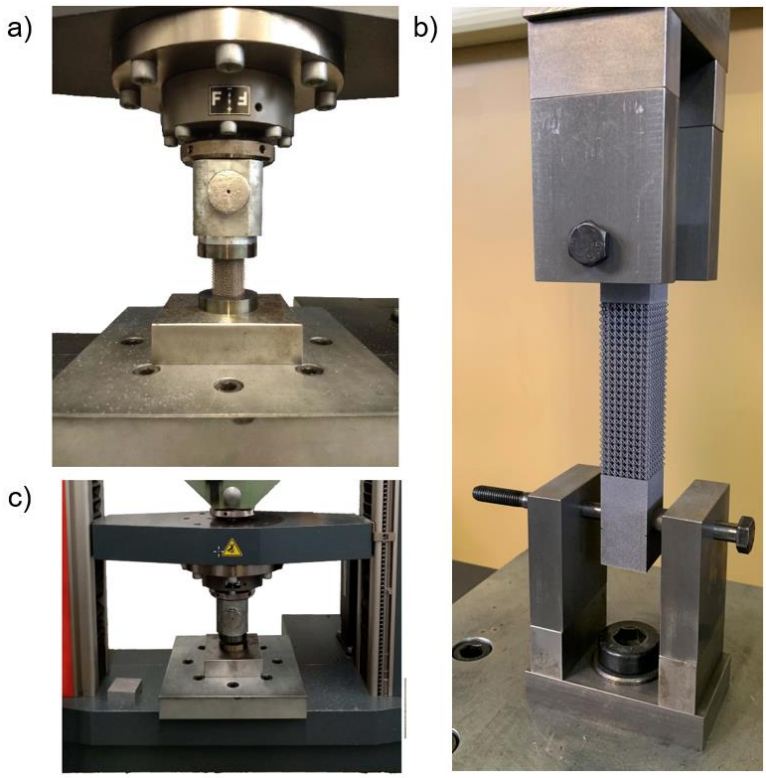

Figure 31: Mechanical testing setup: compression (a), tension (b), stiffness investigation for compression loading (c).

3.4.2 Density measurements

Archimedean density measurements were carried out based on the German engineering norm DIN 3369 [379] to assess the presence of process-induced porosities. The effective density of the lattice structure ρ^* is obtained by measuring the mass difference between two measures, $m_{measure1}$ and $m_{measure2}$, accounting for the density of water ρ_{water} and the ambient temperature. Data for ρ_{water} was taken from [380]. The corresponding relative density is calculated according to Eq.4 and Eq.12 with an assumed solid density $\rho_S = 2.67\ g/cm^3$ [375]. A *Sartorius 1702* scale ranging from 0 g to 200 g with a precision of 0.1 mg was employed (Figure 32, a).

$$\rho^* = \frac{m_{measure1} \cdot \rho_{water}}{m_{measure1} - m_{measure2}} \tag{12}$$

Before density measurements, lattice samples are cleaned from aggregated powder in an ultrasonic bath (Figure 32, b) and then embedded in distilled water. A combination of two methods, one chemical and one physical, is employed to eliminate air bubbles entrapped in the water surrounding the specimens. Detergent droplets are used for their ability to break hydrogen bonds of water and, thus, to reduce the surface tension, which allows to release entrapped air bubbles. Since this approach does not guarantee to eliminate all the air bubbles, a vacuum desiccator (Figure 32, c) is used as well.

Figure 32: Archimedean density measurements: setup (a), ultrasonic bath (b) and vacuum desiccator (c).

3.4.3 Geometric accuracy

All investigated specimens for structural integrity were analysed with a *ZEISS Axioskop A1 HAL 100* microscope and subsequent pictures were recorded with an *AxioCam ICc5* camera.

Investigations were performed at several scales: at strut scale, at single RUC scale, for small lattice samples (less than 4 RUCs), or for large lattice samples (more than 5 RUCs). The design of test specimens for both strut and single RUCs scales deployed in the framework of this work is inspired from the German norm on test features for limiting geometric elements [381]. It consists of an inclinable pot, in which the structure to be analysed is embedded in epoxy resin (LY556/HY917/DY070 [382]). The excess of resin is turned (Figure 33). This design enables high productivity while remaining adaptable to the need of specific investigations, e.g. number of struts per pot. Grinding tools manufactured by a filament printer were employed for the investigation of lattice structures of different scales for productivity reasons as well. No resin embedment is required for lattice structures of strut diameters above 300 μm.

Figure 33: Test specimens for optical microscopy.

Samples were grinded with sandpaper of grit ranging from 240 to 1200 depending on the level of details required. Based on the orientation of lattice samples, two main grinding planes were identified. The horizontal plane offers a view-cut of the lattice structures perpendicular to the build direction, whereas the vertical plane provides an insight of their structural integrity in a cross-section parallel to the build direction. The former can be investigated at all scales while the latter can only be investigated at lattice scale.

Recorded pictures were analysed by a self-coded *MATLAB* script developed to realise a systematic and comparable assessment of the quality of the manufactured lattice samples throughout this work. Its first step consists in a pre-processing of the grinding pictures using a pixel-based grey-scale threshold in order to identify the strut's contour (Figure 34, c & f).

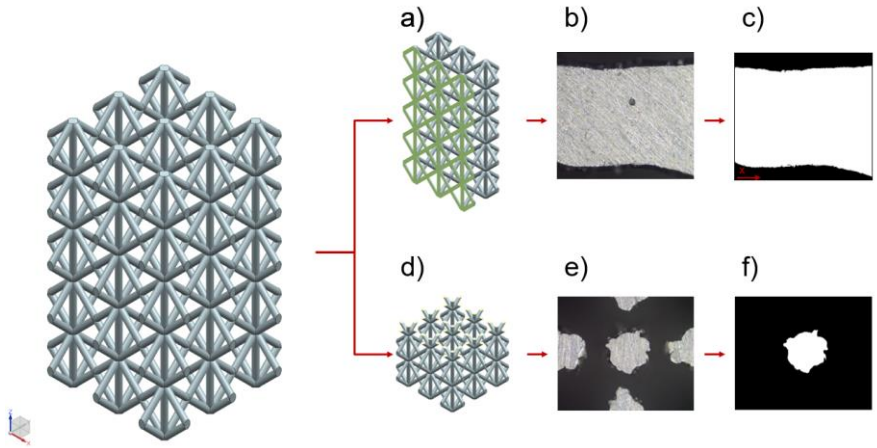

Figure 34: Grinding approach: vertical (a) and horizontal (d) planes, picture examples (b, e) and pre-processing (c, f).

Horizontal grinding pictures (Figure 34, d & e) provide information about strut roundness and diameter. They are both assessed by comparing the area of an equivalent diameter of the obtained cross-sections to an ideal strut. The *circularity measure* C evaluates the roundness of a given cross-section (Eq.13) by comparing its cross-section area A to the perimeter p. The value $C = 1$ stands for an ideal circle while $C = 0$ indicates the absence of a circular pattern. This approach is applicable to diagonal struts as well since the strut diameter corresponds theoretically to the minor axis of the elliptical cross-section. In that case, the four inclined struts are considered and the results are averaged. In the case of f_2cc_z, only the roundness of the vertical struts is assessed since these struts are the load bearing feature of a stretching-dominated unit cell [279, 296].

$$C = \frac{4 * A * \pi}{p^2} \quad C \in [0,1] \tag{13}$$

After pre-processing the vertical grinding pictures (Figure 34, b & c), a contour function is applied to the upper and lower strut borders, $k(x_i)_{up}$ and $k(x_i)_{down}$ respectively. To do so, single struts are isolated independently from their inclination angle and rotated so that they align with the horizontal axis of the picture. Thanks to the contour function, a direct assessment of the *discrete diameter* $t(x_i)$ (Eq.14), the *maximum diameter difference* t_{diff} (Eq.15) and the *diameter variation* along the strut t_{var} (Eq.16) is possible. Moreover, the *strut waviness* W, which stands for the deviation from an ideal straight line, can be evaluated by assessing the standard deviation of the strut average line issued from both contour functions (Eq.17).

$$t(x_i) = k(x_i)_{down} - k(x_i)_{up} \tag{14}$$

$$t_{diff} = max\big(t(x_i)\big) - min\,(t(x_i)) \tag{15}$$

$$t_{var} = std[t(x_i)] \tag{16}$$

$$W = std\left[k(x_i)_{up} + \frac{k(x_i)_{down}}{2}\right] \tag{17}$$

The *surface roughness* R_a from both upper and lower profiles along the strut length L can be extracted from the contour function by means of a high-pass filter that separates the waviness from the roughness (Eq.18). The different profiles enable measuring both up- and downskin roughnesses.

$$R_a = \frac{1}{L} * \sum_{0}^{L} \left|k(x)_{highpassed}\right| \tag{18}$$

4 Design Concepts

This chapter deals with the material independent design concepts developed and their numerical verification. The first two sub-sections propose to solve the load introduction challenge encountered by lattice tensile specimen designs in two distinct ways: designing the transition region by means of either structural grading (section 4.1) or a topology-optimised bulk structure (section 4.2). The last sub-section, section 4.3, handles the problematic of the transition between single lattice unit cells and, in particular, of the nodal area.

In order to perform numerical simulations, arbitrary material properties were used. The material properties of the solid base material are assumed isotropic in all employed models. They are based on the values of the additively printed AlSi10Mg solid material that can be found in the literature. The relevant material properties employed in the framework of linear static calculations are a Young's modulus of AlSi10Mg bulk material in the build direction E_S of 70 GPa [375] and a Poisson's ratio υ of 0.32 [383].

4.1 Load introduction via structural grading

This section develops and proposes a design guideline for tensile test specimens of truss-based cubic lattice structures using a functional grading. This design guideline and corresponding methodology deliver a standardised process for the reliable and reproducible assessment of lattice structure properties without any influence of the specimen design on the considered lattice structures.

While the RUCs employed for the initial development of the sample design methodology are, as mentioned in section 3.1.1, f_2cc_z and bcc, their respective stretching- and bending-dominated counterparts, namely f_2cc and bcc_z, are used to assess on the transferability of the developed approach.

In the framework of this investigation, performing a heuristic stress optimisation was identified as the most effective way to set up a reliable grading. On the one hand, running a numerical optimisation for a high variety of sample configurations in terms of unit cell type and size would involve tremendous hardware capacities and/or time. On the other hand, two main challenges have been identified for the classical analytical optimisation: describing the sample quality within a single function for which its first derivation leads to extremal values and not to zero points, and defining a termination criterion for optimal parameters. This involves that the optimal values may not be reached by heuristic means for the proposed functional grading because the necessary conditions can be reached by an unideal configuration.

Although calculations are performed for an eighth model (see section 3.1.1), all figures of this section are displayed for one half of the sample in order to facilitate reading and assessing the grading quality. In order to facilitate reading and assessing the grading quality, results are visualised in contour plot diagrams with a common colour scale and a commonly used heat plot. Note that intermediate contour line values of result plots may not be fully readable but are not considered as obstacles in the sample quality assessment.

4.1.1 Principle

Figure 35 provides a complete overview of the design principle of the proposed tensile specimen. The design of the transition region consists of a structural grading over the strut diameter of the same RUC as present in the target region. Other approaches would not only restrict design freedom (section 2.3.5) but may also enforce predetermined failure locations. Furthermore, a variation of t involves significantly less supplementary design, modelling and manufacturing efforts than any other measure. Since the main load paths are of interest, the strut thickness is kept constant within each single RUC to facilitate modelling and post-processing as well.

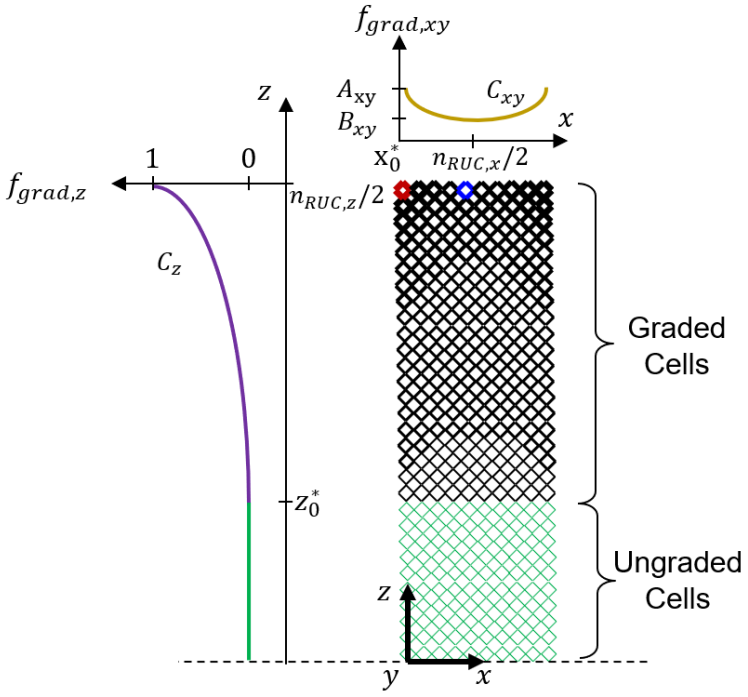

Figure 35: Grading principle shown for the half sample length.

The proposed grading approach is described by a function that factorises the strut thickness of the investigated unit cell t based on the as-designed thickness t_0 (Eq.19) with respect to a local cartesian coordinate system set in the middle of the sample's longitudinal direction.

$$t(x^*, y^*, z^*) = t_0 \cdot f_{grad}^{SCF}(x^*, y^*, z^*) \tag{19}$$

Where x^*, y^* and z^* are the discrete spatial coordinates of the considered unit cell within the transition region in the x, y and z-directions, respectively.

The grading function (Eq.20) consists of a combination of a grading function in the plane perpendicular to the loading direction $f_{grad,xy}(x^*, y^*)$ (Eq.21), a grading function in the loading, here vertical, direction $f_{grad,z}(z^*)$ (Eq.22), and a *stress concentration factor* (SCF) SCF. Similar to Eq.8, power laws are employed for the definition of the grading functions.

$$f_{grad}^{SCF}(x^*, y^*, z^*) = SCF \cdot \left[1 + f_{grad,xy}(x^*, y^*) \cdot f_{grad,z}(z^*)\right] \tag{20}$$

Therein, $f_{grad,xy}(x^*, y^*)$ varies from its start value at the centre of the sample $x^*, y^* = n_{RUC,x,y}/2$ to its end value reached at the borders of the sample with $x^* = x_0$ or $x^* = n_{RUC,x}$ and $y^* = y_0$ or $y^* = n_{RUC,y}$.

The formulation of $f_{grad,xy}(x^*, y^*)$ exploits the symmetry of the quadratic cross section of the proposed sample design (see Figure 28). The function $min\ (x^*, y^*)$ is implemented to enable the transferability of the unidimensional grading function into a two-dimensional space. The quantity A_{xy} describes the maximal strut thickness since leading to the maximum grading factor while B_{xy} for the minimum strut thickness for $z^* = n_{RUC,z}/2$.

The function $f_{grad}(z^*)$ is designed such that it is initiated at the centre of the interface between the ungraded and graded cells ($z^* = z_0$) and grows until its maximum value at the centre of interface between the transition region and the bulk region ($z^* = n_{RUC,z}/2$). Hence, the start and end values corresponding to the grading boundaries in the vertical directions are $A_z = 0$ for $z^* = z_0$ and $B_z = 1$ for $z^* = n_{RUC,z}/2$.

The quantities C_{xy} and C_z describe the variation of the strut thickness in their respective directions, wherein C_{xy} is minimal for $x^*, y^* = n_{RUC,x,y}/2$ and maximal for $x^* = x_0$ or $x^* = n_{RUC,x}$ and $y^* = y_0$ or $y^* = n_{RUC,y}$. The quantity C_z is minimal for $z^* = z_0$ and maximal for $z^* = n_{RUC,z}/2$.

$$f_{grad}(x^*, y^*) = A_{xy} + \left(B_{xy} - A_{xy}\right) \cdot \left(\frac{min\ (x^*, y^*) - x_0^*}{n_{RUC,x}/2 - x_0^*}\right)^{C_{xy}} \tag{21}$$

$$f_{grad}(z^*) = \left(\frac{z^* - z_0^*}{n_{RUC,z}/2 - z_0^*}\right)^{C_z} \tag{22}$$

The presence of a SCF is justified by the fact that edge effect issues are expected to have a restrained influence only on the RUC located at the edge of the sample, i.e. for $x^*, y^* = x_0, y_0$. It is therefore assumed that the edge effect is specific to the sample shape and size, and cannot be solved by the grading formulations described above. Hence, the SCF is assigned a value of 1 for all other RUCS than the ones at the sample's corners (Eq.23 and Eq.24).

$$SCF\big(min(x^*, y^*) = x_0^*, z^* = n_{RUC,z}/2\big) > 1 \tag{23}$$

$$SCF(min(x^*, y^*) \neq x_0^*, z^*) = SCF\big(min(x^*, y^*) = x_0^*, z^* \neq n_{RUC,z}/2\big) = 1 \tag{24}$$

4.1.2 Design methodology

The methodology delivers a standardised process for the reliable and reproducible assessment of lattice structure properties as it enables a systematic identification of the grading parameters z_0, A_{xy}, B_{xy}, C_{xy}, and C_z independently from the considered unit cells. The proposed design methodology relies on observations of both stress and uniaxiality states of the ungraded sample, RUC-specific load paths and assumptions on load equilibrium. As the stress concentration due to the edge effect is not assumed as RUC-specific, the SCF cannot be inferred from the stress state of the ungraded sample and, thus, can only be determined after a first analysis of the graded structure and implemented to locally fulfil the evaluation criteria defined below.

The transition region is assumed constant in the plane perpendicular to the loading direction. The assumed load equilibrium (Eq.25), when combined with the grading definition (Eq.19) and the trivial relationship between stress and forces (Eq.26), leads to a straightforward relationship between the stress state and strut thicknesses (Eq.27), as depicted in Figure 36. This relationship between the stress distribution and strut thickness reflects the correlation between both ungraded and graded sample configurations and, thus, enables the identification of the grading parameters by considering the square root of the normalised stress distribution in the sample.

$$F_0 = F \tag{25}$$

$$\sigma_{VM,0}^* \cdot \frac{{t_0}^2}{4} = \sigma_{VM}^*(x^*, y^*, z^*) \cdot \frac{t^2}{4} \tag{26}$$

$$\sqrt{\frac{\sigma_{VM}^*(x^*, y^*, z^*)}{\sigma_{VM,0}^*}} = \frac{t}{t_0} \tag{27}$$

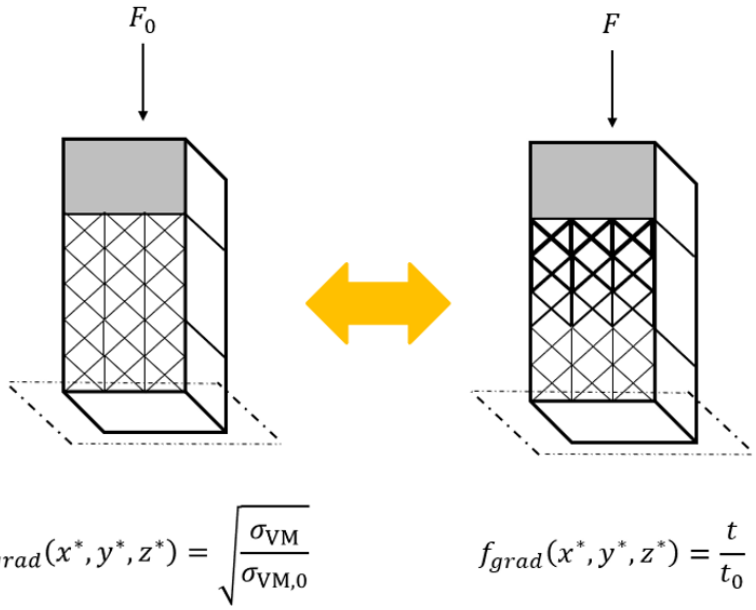

Figure 36: Relationship between grading function, stress and strut thicknesses.

In order to identify load paths in the ungraded sample, the concept of *undisturbed region* is introduced to determine the quality criteria of all samples. The undisturbed region corresponds to a region of the lattice structure in its ungraded state, in which all defined design quality criteria are fulfilled in a plane perpendicular to the loading direction at a given height. Therefore, the undisturbed region can be assimilated to an ideal target region and is employed. In this work and the following examples, an undisturbed region consisting of at least two cell layers in the vertical direction of the ungraded half sample were identified as sufficient for the grading parameters identification.

In order to achieve a universal applicability of the proposed approach, the stress distribution in each sample has to be normalised. To do so, a reference $\sigma^*_{VM,R}$ has to be systematically identified as well. Normalising the stress distribution enables the identification of local maximum and minimum stresses along the RUC-specific relevant stress paths leads, independently from the given AR or sample dimensions. Typical relevant stress path locations in each truss-based lattice sample are assumed to be located along the edge (e.g. $x^*, y^* = x_0, y_0$), the centre ($x^*, y^* = n_{RUC,x,y}/2$) and the centre of any face (e.g. $x^* = x_0, y^* = n_{RUC,x,y}/2$).

While the grading formulation was introduced as starting from the interface between the ungraded and graded cells ($z^* = z_0$), the identification of grading parameters starts from the maximum strut thickness, which is ruled by the parameter A_{xy}, and ends in the transversal plane in which the reference value $\sigma^*_{VM,R}$ is identified. Eq.28 and Eq.29 highlight two remarkable points of the grading principle depicted in Figure 35 that are decisive for the identification of grading parameters, namely A_{xy} and B_{xy}, respectively.

$$f_{grad}\left(x^*, y^* = x_0, y_0, z^* = n_{RUC,z}/2\right) = 1 + A_{xy} \tag{28}$$

$$f_{grad}\left(x^*, y^* = n_{RUC,x,y}/2, y_0, z^* = n_{RUC,z}/2\right) = 1 + B_{xy} \tag{29}$$

Evaluation criteria

In order to determine optimal grading variables, assessing the grading quality is essential. To do so, three measures and corresponding evaluation criteria based on already available justification methods for bulk materials [384, 385] were developed in order to describe the nature of the loading state in the investigated lattice structures and to assess for deviations from an ideal tensile state. Since it is assumed that an ideal state will never be reached by any physical sample, a tolerance range for acceptable deviations of 1% has been determined after a side study that is described in appendix B.

The uniaxiality measure $h^*_{F,uniax}$ (Eq.30) describes the loading path direction within the sample. This measure is employed to determine the number of graded cells in the loading direction. Due to the potentially different strut diameters after grading, this number is based on the relationship between the discrete forces acting onto each upper and lower face of the RUC. The force in the loading direction F_z and the resulting force in the plane perpendicular to the loading direction $\sqrt{F_x^2 + F_y^2}$ are therefore considered. Since an ideal tensile loading state shall lead to $h^*_{F,uniax} = 0$, an uniaxiality criterion (Eq.31) is introduced to ensure a purely tensile loading of the lattice sample at the interface between ungraded and graded cells located at $z^* = z_0^*$.

$$h^*_{F,uniax}(x^*, y^*, z^*) = \frac{\sqrt{F_x(x^*, y^*, z^*)^2 + F_y(x^*, y^*, z^*)^2}}{F_z(x^*, y^*, z^*)} \tag{30}$$

$$h^*_{F,uniax}(x^*, y^*, z^* \leq z_0^*) \leq 0.01 \tag{31}$$

The stress homogeneity measure $h^*_{\sigma,mises}$ (Eq.32) describes the stress distribution within the sample. This measure is employed to identify stress concentrations. This number is based on the deviations between the maximum effective von Mises stress of each discrete RUC and the nominal effective von Mises stress $\sigma^*_{VM,0}$ of the target region. Since an ideal stress state shall ensure a homogeneous and maximal stress state in the target region, a first stress homogeneity criterion leading to $h^*_{\sigma,mises} = 0$ for $z^* = z_0^*$ is introduced (Eq.33). Furthermore, an ideal sample design shall ensure that stresses within the transition region are always smaller than the ones in the target region in order to avoid effects such as yielding or specimen failure in the transition region. A second stress homogeneity criterion is therefore introduced (Eq.34). Given the stress homogeneity measure from Eq.32, when combined with the fact that $t \geq t_0$ (see Eq.19), this criterion shall lead to a negative $h^*_{\sigma,mises}$ in the transition region, i.e. between $z^* = z_0^*$ and $z^* = n_{RUC,z}/2$.

$$h^*_{\sigma,mises} = \frac{\sigma^*_{VM}(x^*, y^*, z^*) - \sigma^*_{VM,0}}{\sigma^*_{VM,0}} \tag{32}$$

$$-0.01 \leq h^*_{\sigma,mises}(x^*, y^*, z^* = z^*_0) \leq 0 \tag{33}$$

$$h^*_{\sigma,mises}(x^*, y^*, z^* > z^*_0) \leq 0 \tag{34}$$

The strain homogeneity measure $h^*_{\epsilon,ana}$ (Eq.35) describes the strain distribution within the sample. This measure enables identifying deformation gradients due to potential transversal contraction as wells as assessing on the predictability of lattice structures. This number is based on the deviations between the local effective strain of each discrete RUC and the nominal effective strain $\epsilon^*_{zz,0}$ of the target region. The latter is based on the load equilibrium and is derived from the constitutive law using the theoretical stiffness E^*_{ana} obtained from the employed analytical model described in section 3.2.1 (Eq.36). Due to the potentially different strut diameters after grading, the effective nominal stress $\sigma^*_{zz,0}$ is derived from the resulting applied force in the (vertical) loading direction $F_{z,0}$ and the nominal cross-section of the lattice structure (Eq.37). Strain criteria are introduced to ensure a homogeneous strain state and that strains within the transition region are always smaller than the ones in the target region. An ideal homogeneous strain state shall avoid specimen failure or plastic deformation in the transition region. Similar to the stress criteria, $h^*_{\epsilon,ana} = 0$ in the target region (Eq.38) and $h^*_{\epsilon,ana}$ shall be negative in the transition region (Eq.39).

$$h^*_{\epsilon,ana} = \frac{\epsilon^*_{zz}(x^*, y^*, z^*) - \epsilon^*_{zz,0}}{\epsilon^*_{zz,0}} \tag{35}$$

$$\epsilon^*_{zz,0} = \frac{\sigma^*_{zz,0}}{E^*_{ana}} \tag{36}$$

$$\sigma^*_{zz,0} = \frac{F_{z,0}}{n_{RUC,x} \cdot n_{RUC,y} \cdot a^2} \tag{37}$$

$$h^*_{\epsilon,ana}(x^*, y^*, z^* > z^*_0) \leq 0 \tag{38}$$

$$-0.01 \leq h^*_{\epsilon,ana}(x^*, y^*, z^* = z^*_0) \leq 0 \tag{39}$$

Grading parameters for the stretching-dominated f_2cc_z and bcc_z structures

A common grading parameter identification method was identified for the two investigated stretching-dominated lattice structures. The used stress paths are depicted in Figure 37 and Figure 38 for the bcc_z structure exemplarily. The first characteristic feature to be identified is the maximum stress within the ungraded sample, edge effect neglected (Figure 37¸1). The load distribution within the graded sample can be predicted by considering the grading formulation, which foresees a diameter increase at the outer corners of the sample at the interface between the bulk region and the transition region, and the stretching-dominated behaviour of the RUCs. In a graded sample, the maximum load will

start at the sample's edge and will reach the target region along the vertical struts since they are aligned with the loading direction. Hence, two statements can be drawn from this consideration: on the one hand, the reference value $\sigma^*_{VM,R}$ (Figure 37, R) is located at the edge of the transversal plane corresponding to the maximum stress in the ungraded state. On the other hand, the stress path for the identification of the maximum thickness grading parameter A_{xy} is located at the edge $(x^*, y^* = x_0, y_0)$ as well. This path starts from a local minimum stress (Figure 38, 2) and ends at a local maximum stress. However, the grading value corresponding to A_{xy} (Figure 37, A) cannot be directly extracted because of the stress concentration due to the edge effect, which is not considered to be representative of the RUC's specific mechanical behaviour. Assuming the local influence of the edge effect, the grading value is extracted using a linear extrapolation of the stresses from the local minimum (Figure 38, 2) until $z^* = \frac{n_{RUC,z}}{2} - 1$ (Figure 37, 3).The extrapolation is performed with a second order polynomial because of the square root relationship between stresses and strut thicknesses (Eq.27). The obtained value $f_{grad}^{extrapolated}$ is used to extract A_{xy} (Eq.40).

$$A_{xy} = f_{grad}^{extrapolated} - 1 \tag{40}$$

From the grading formulation and the previous statements, it can be deduced that the stress path for the identification of B_{xy} is located at the sample's center. Furthermore, since B_{xy} stands indirectly for the minimum strut thickness at the same level of grading parameter A_{xy}, B_{xy} is located at the height equivalent to the maximum non-extrapolated value from the selected load path for the identification of A_{xy} (Figure 37, B). In that case, the value of f_{grad} is used to extract B_{xy} directly (Eq.41).

$$B_{xy} = \sqrt{\frac{\sigma^*_{VM}\left(x^* = n_{RUC,x}/2, y^* = n_{RUC,y}/2, z^* = \frac{n_{RUC,z}}{2} - 1\right)}{\sigma^*_{VM,0}}} - 1 \tag{41}$$

The identification path of the grading parameter C_{xy} can be described by starting from the identification path of B_{xy} (Figure 37, B) and ending at the identification path of A_{xy}. Due to the cubic symmetry of the investigated RUCs, the ending point of this identification path can be picked along one of the directions of the plane transversal to the loading direction (Figure 37, 4). Analogous to the grading formulation, the stress distribution along this path is described by a power law (Eq.42), from which C_{xy} is extracted by considering from the inverse stress distribution (Eq.43).

$$f\left(\sigma^*_{VM}(x^*, y^*, z^*)\right) = a x^{b_{xy}} \tag{42}$$

$$C_{xy} = 1 - b_{Cxy} \tag{43}$$

According to the grading formulation, the identification path of the grading parameter C_z is located along the identification path of B_{xy}, starts from the path's local maximum stress (Figure 38, 1) and ends at the path's local minimum stress (Figure 38, B). Analogous to C_{xy}, C_z is extracted from the power law formulation of the inverse stress distribution (Eq.44).

$$C_z = 1 - b_{Cz} \tag{44}$$

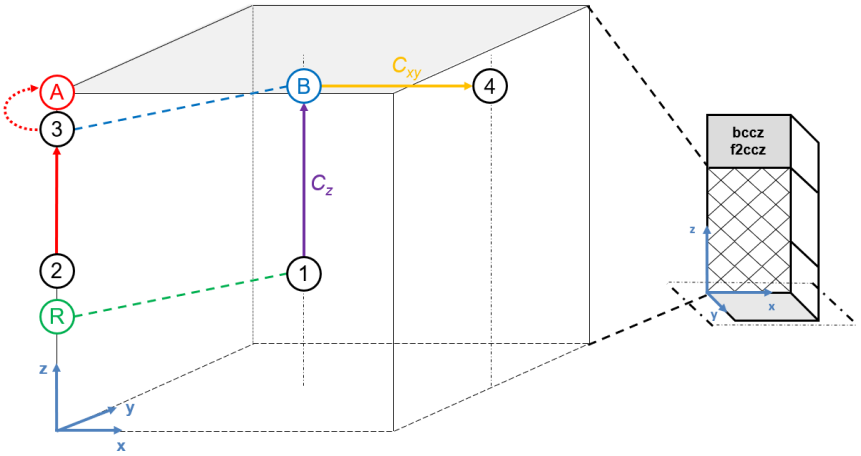

Figure 37: Grading parameters identification: principle for bcc_z / f_2cc_z.

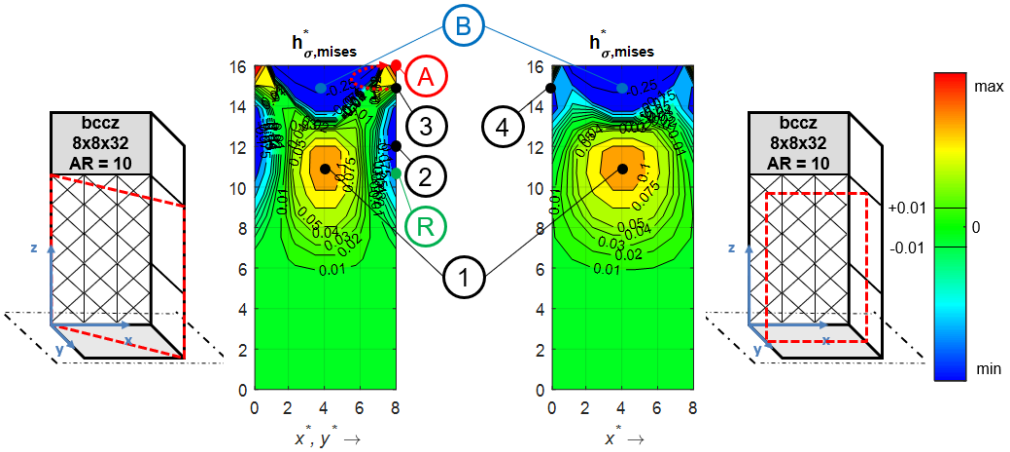

Figure 38: Grading parameters identification: example of bcc_z.

Grading parameters for the body-centred, bending-dominated structure bcc

No common grading parameters identification method was identified for the two investigated bending-dominated lattice structures. The used stress paths for the bcc structure are depicted in Figure 39 and Figure 40. The identified method for bcc is very similar to the

one of the stretching-dominated structures and differs in the following points. In a graded sample, the main load path will start at the sample's edge and will reach the target region along the body-centred diagonal struts and lead, as for the stretching-dominated samples, to a reference value $\sigma^*_{VM,R}$ (Figure 39, R) located at the sample's edge. The reference point is identified by means of a local minimum stress (Figure 40, 1) below the overall maximum stress (Figure 40, 2) along a stress path that is located at the sample's centre. Thus, the grading parameter A_{xy} is identified along this path as well (Figure 39, A), and the identification path of B_{xy} is consequently located at the sample's edge (Figure 39, B). Contrarily to the stretching-dominated structures, local minimum (Figure 40, 1) and maximum (Figure 40, 2) stresses of the A_{xy} path can be identified directly, but an extrapolation until the interface with the bulk region is required to obtain the final grading parameter. The identification of grading parameters B_{xy}, C_{xy} and C_z is based on the same principle as for the stretching-dominated structures with the exception of the starting and ending values of C_z, which are extracted from the local maximum (Figure 39, R) and local minimum (Figure 39, 4) stresses of the identification path of B_{xy}. Eq.40 to Eq.44 are therefore applicable to this configuration.

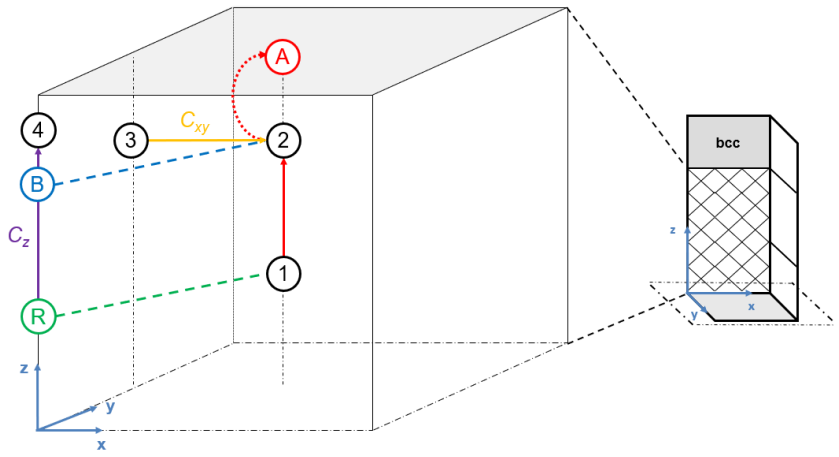

Figure 39: Grading parameters identification: principle for bcc.

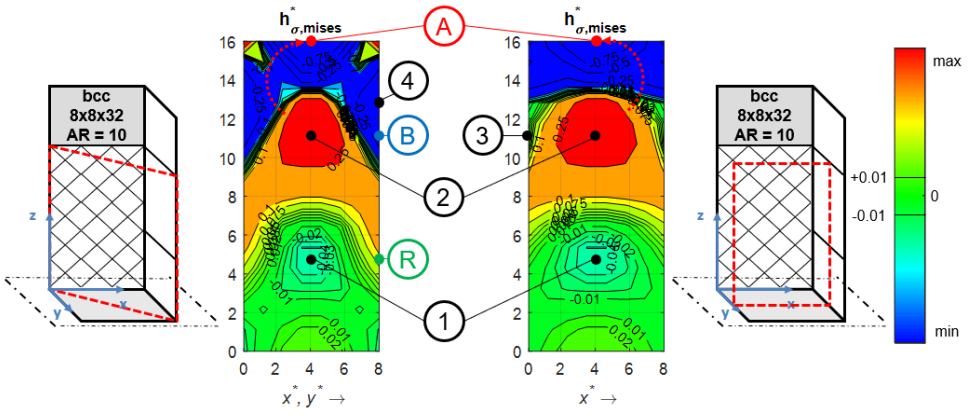

Figure 40: Grading parameters identification: example of bcc.

Grading parameters for the face-centred, bending-dominated structure f2cc

The used stress paths for the f2cc structure are depicted in Figure 41 and Figure 42. The identified method for f2cc can be described as a similar but slightly more complicated case than the bcc one and differs in the following points. In a graded sample, the maximum load will start at the sample's edge and will reach the target region along the face-centred diagonal struts and lead, as for both stretching-dominated and bcc samples, to a reference value $\sigma^*_{VM,R}$ (Figure 41, R) located at the sample's edge. The main difference lies in the identification of grading parameter A_{xy}, which takes place at the centre of one of the sample's external faces. As for the bcc identification method, the stress path starts from a local minimum stress (Figure 42, 2), ends at the local maximum stress (Figure 42, 3) and is then extrapolated to the top of the sample (Figure 42, A). The identification of grading parameters B_{xy}, C_{xy} and C_z is based on the same principle as for the bcc structure. Eq.40 to Eq.44 are therefore applicable to this configuration too.

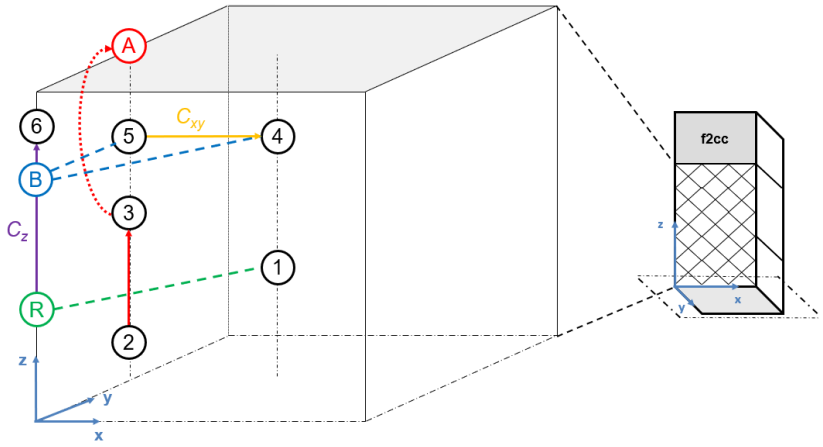

Figure 41: Grading parameters identification: principle of f2cc.

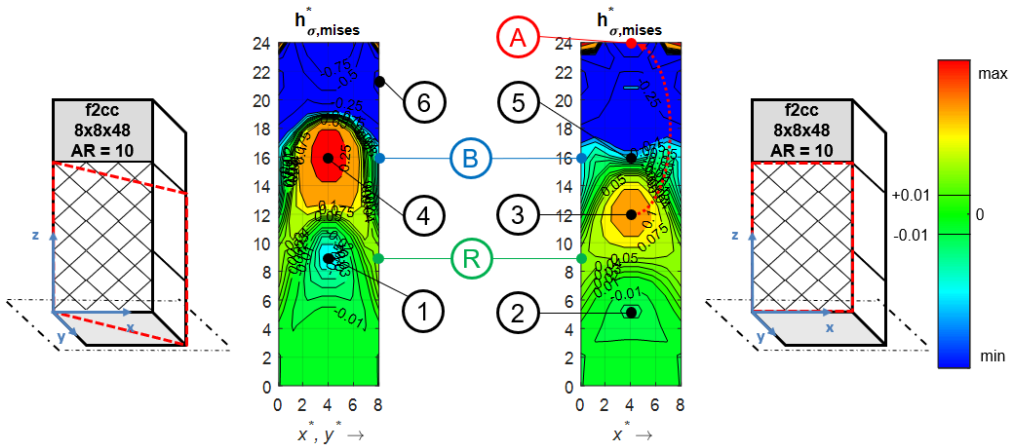

Figure 42: Grading parameters identification: example for f2cc.

Size of grading region

A common identification method was identified for the size of the grading region of the investigated lattice structures. While the grading parameters are inferred from the stress state within the sample, the number of graded cells in the transition region $n_{RUC,z}^{Tr,g}$ can be identified from the uniaxiality criterion of the ungraded state. Since the grading formulation optimises only the stress distribution, it can be assumed that the uniaxiality criterion of a graded sample will necessarily be fulfilled if the corresponding ungraded sample already fulfils the same criterion. The number of graded cells in the transition region is defined by the number of RUCs in the loading directions needed to fulfil the uniaxiality criterion (Eq.31) in the afore-defined relevant stress paths while being located below the maximum stress concentration typical of the considered RUC. Figure 43 and Figure 44 depict application examples for different configurations of bcc_z and bcc structures, respectively.

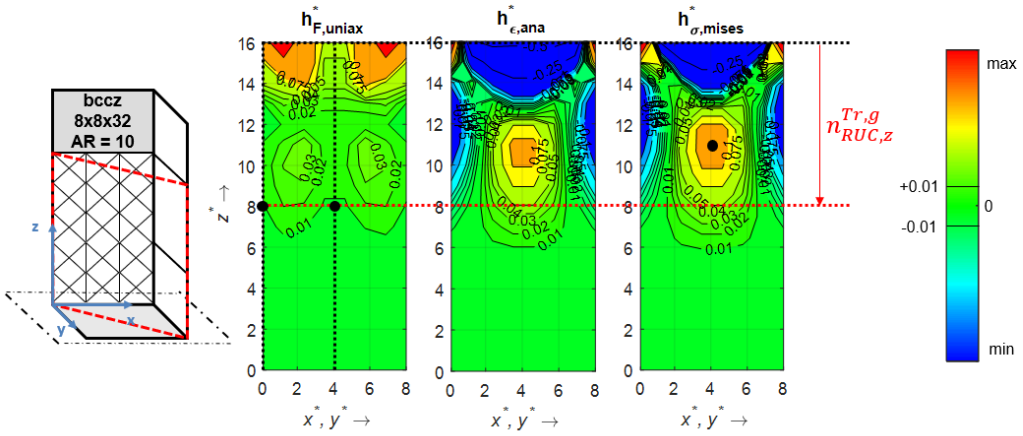

Figure 43: Size of graded region (bcc_z).

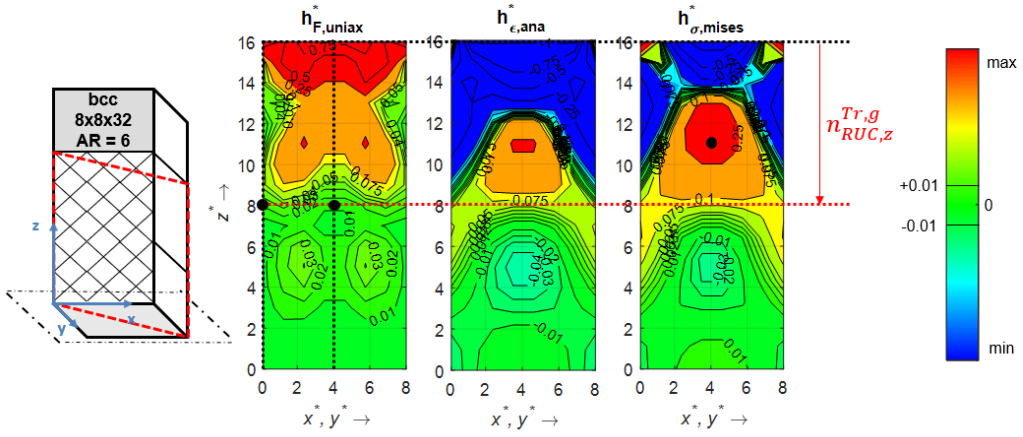

Figure 44: Size of graded region (bcc).

4.1.3 Results

The numerical investigation was performed with the software package *ABAQUS CAE 2017*. As mentioned in section 3.2.2, the sample is idealised as an eighth model thanks to symmetry considerations. The truss lattice structures were modelled with 3-node quadratic Timoshenko beam elements B32 [386]. After a sensitivity analysis, a mesh of 30 elements per strut was selected in order to achieve less than 1 % deviation in stresses compared to a much finer mesh. The boundary conditions applied to the nodes located at the sample interface were defined according to the compatibility conditions. A homogeneous deformation is applied to the nodes of the upper sample surface.

The model generation and calculation were monitored using a *PYTHON* script while a *MATLAB* script dealt with the plot generation. The resulting forces and displacements were directly extracted from the upper and lower nodes of each RUC. The von Mises stresses of each bulk element were directly extracted using the *MISESMAX* field output request in order to account for all integration points within the whole beam cross-section of each strut [386]. The local effective strain $\epsilon_{zz}^{*}(x^{*}, y^{*}, z^{*})$ is obtained from the linear interpolation of nodal displacements in the loading (vertical) direction $w(x^{*}, y^{*}, z^{*})$ with respect of the two neighbouring cells. Since the sample borders $z^{*} = z_{0}^{*}$ and $z^{*} = n_{RUC,z}/2$ only have one neighbouring RUC, the second derivation of the nodal displacement at the border is used [387].

Considering both tolerance range (see section 4.1.2) and aforementioned sensitivity analysis, different final quality ranges are set. A sample design will be considered as appropriate for the mechanical characterisation of tensile properties of lattice structures if, on the one hand, the stress criterion yields remains under 2 % deviations from an ideal state and, on the other hand, deviations observed of both uniaxiality and strain criteria remain below 1 % since forces and displacements extracted from a FE model converge more rapidly than stresses.

Note that for the sake of brevity only sufficient and representative results are reported in diagonally cut views in this section. Please refer to the appendix B for complementary data.

Variation of the aspect ratio of the specimen

Ungraded samples were varied according to their AR_{s} (Eq.10) in order to identify a potential size effect that was assessed for another cellular structure class, the honeycomb cores [388, 389]. Design guidelines extracted from the norm for tensile testing of metallic cellular materials [337] recommend 10 RUCs in each direction as well as an ARS between 1.5 and 2. Based on these recommendations, bcc and f_2cc_z configurations for samples consisting of 10 RUCs in the plane transversal to the loading direction were investigated for ARS varying from 1 to 4. Results are reported from Figure 45 to Figure 47 and from Figure 48 to Figure 50, respectively.

As for honeycomb structures, a size effect can be identified since the defined criteria are fulfilled only after reaching a certain AR_s, being 4 for both investigated RUCs. This means that a pure tensile loading ($h^*_{F,uniax}$), analytical values ($h^*_{\epsilon,ana}$), a homogeneous stress state ($h^*_{\sigma,mises}$) and therefore the comparability with analytical models can only be retrieved for a defined sample size. This analysis justifies the undisturbed region as employed in the grading approach.

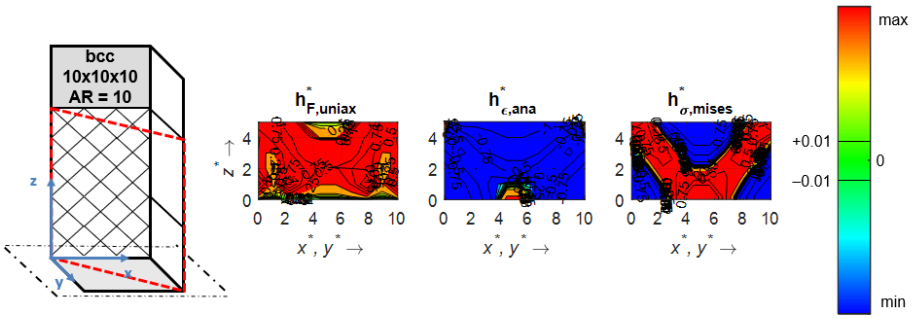

Figure 45: Sample quality results: bcc 10x10x10 AR10 ungraded (diagonal).

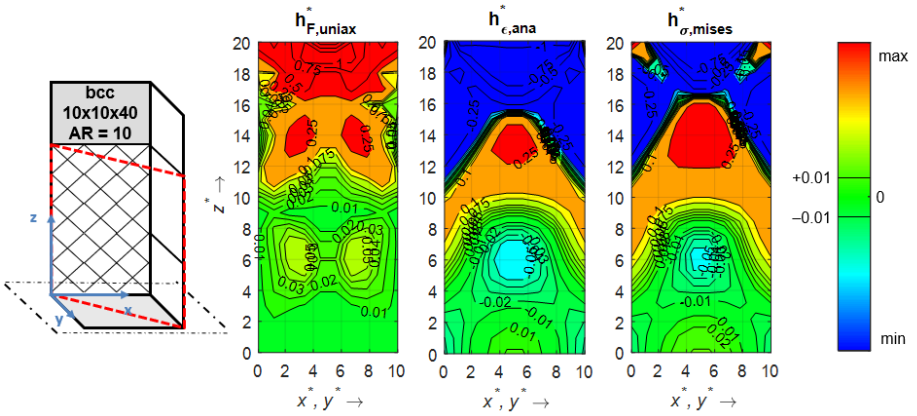

Figure 46: Sample quality results: bcc 10x10x20 AR10 ungraded (diagonal).

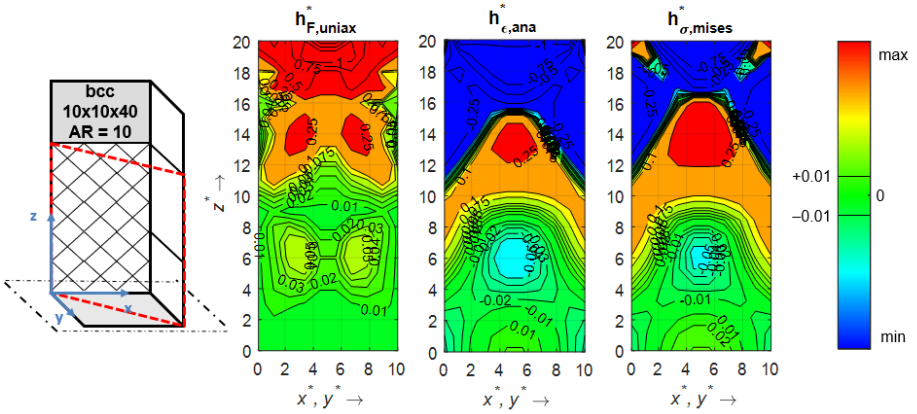

Figure 47: Sample quality results: bcc 10x10x40 AR10 ungraded (diagonal).

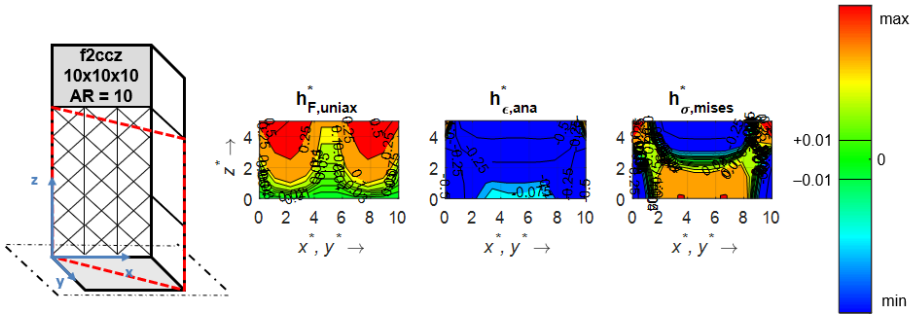

Figure 48: Sample quality results: f_2cc_z 10x10x10 AR10 ungraded (diagonal).

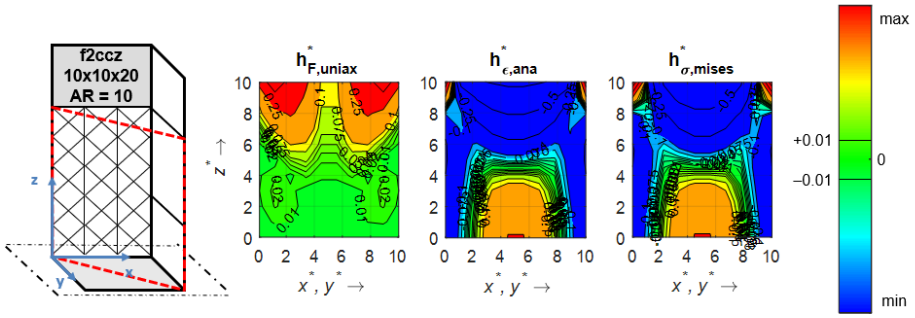

Figure 49: Sample quality results: f_2cc_z 10x10x20 AR10 ungraded (diagonal).

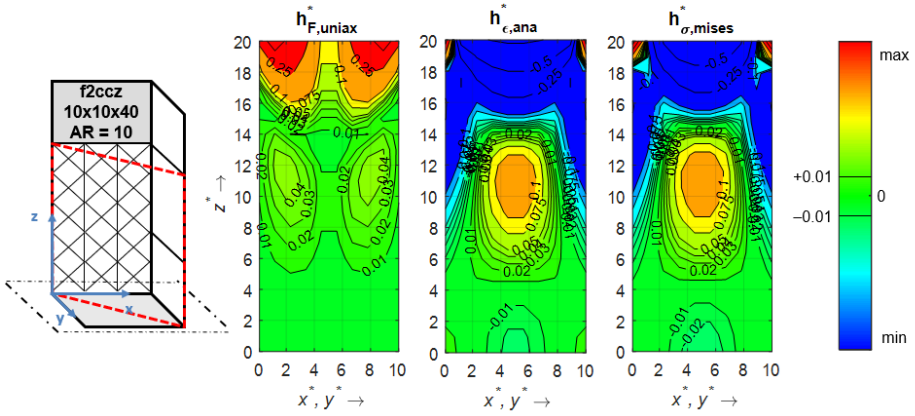

Figure 50: Sample quality results: f_2cc_z 10x10x40 AR10 ungraded (diagonal).

Ungraded vs graded configurations

The results obtained for sample designs with and without structural grading are compared. In order to highlight the general validity of the grading approach, both sample size and AR (Eq.5) were varied while the ARS was kept constant, under the condition that an undisturbed region is guaranteed. The identified AR_s leading to an undisturbed region are,

on the one hand, 4 for the bcc (Figure 51), f_2cc_z (Figure 52) and bcc_z (Figure 53) unit cells and, on the other hand, 6 for the f_2cc (Figure 54) unit cell. The difference in the AR_s values is rooted in the differences in the main load paths used to reach the target region that are specific to each unit cell type, as already depicted in the section dedicated to the identification of grading parameters. The sample size was varied by changing the number of the unit cells used in the plane transversal to the loading direction from 8 to 12 RUCs. While 8 RUCs stand for the least number of cells required by the grading approach, 12 RUCs have been identified as upper bound in order to maintain a reasonable size of the sample. However, f_2cc and bcc_z samples with 12 RUCs in the plane transversal to the loading direction were not investigated in the framework of the verification of the proposed grading approach.

Ungraded samples results plots are reported from Figure 51 to Figure 54. Similarities between the generated plots can be observed (bcc: Figure 47 and Figure 51; f2ccz: Figure 50 and Figure 52). These are due to the normalisation of stress values performed in the grading approach. Therefore, it can be concluded that the load distribution among the sample is unit cell specific and that the plots for one configuration are representative for other ARs and sample size.

It can be further noticed that extending the sample size only does not make the sample eligible for reliable characterisation of tensile properties of lattice structures according to the developed criteria. This is mainly due to the absence of a transition region. Firstly because of the abrupt change in stiffness, or cross section, at the interface between the bulk region and the target region that leads to a stress concentration responsible for an abrupt failure at the end of the load introduction and therefore may not yield the real failure behaviour of an ideal lattice structure, which is in line with early experimental observations [338]. Secondly, a pure tensile loading state is only achieved after a certain number of cell planes below the bulk region. Besides, the presence of another stress peak at the sample's centre and, in some cases, external faces could be a further source of issues for a reliable characterisation. This unit cell specific feature is not necessarily located in an area where tensile loading is guaranteed, for bending-dominated structures at least (Figure 51, Figure 54).

The graded counterparts of the ungraded configurations are reported from Figure 55 to Figure 58, respectively. All graded configurations lead to fully fulfilled criteria in all cases. The variety of specimens shows that the method can reliably lead to grading parameters that can be employed for the design of tensile test specimens, which are expected to fail in the target region under pure tension. This verifies the grading approach although no common SCF in terms of sample size or unit cell type can be identified (see appendix B).

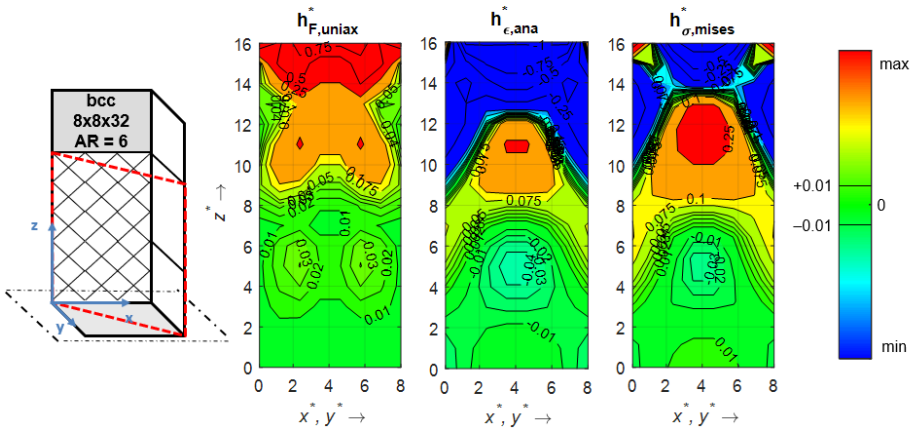

Figure 51: Sample quality results: bcc 8x8x32 AR6 ungraded (diagonal).

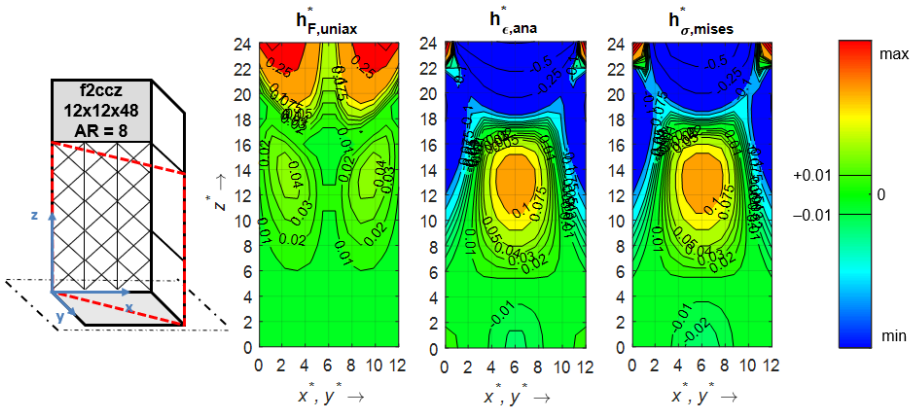

Figure 52: Sample quality results: f_2cc_z 12x12x48 AR8 ungraded (diagonal).

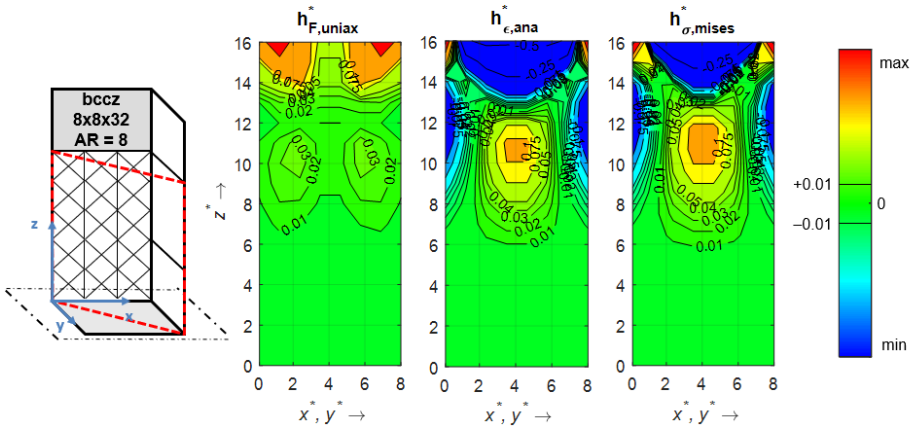

Figure 53: Sample quality results: bcc_z 8x8x32 AR8 ungraded (diagonal).

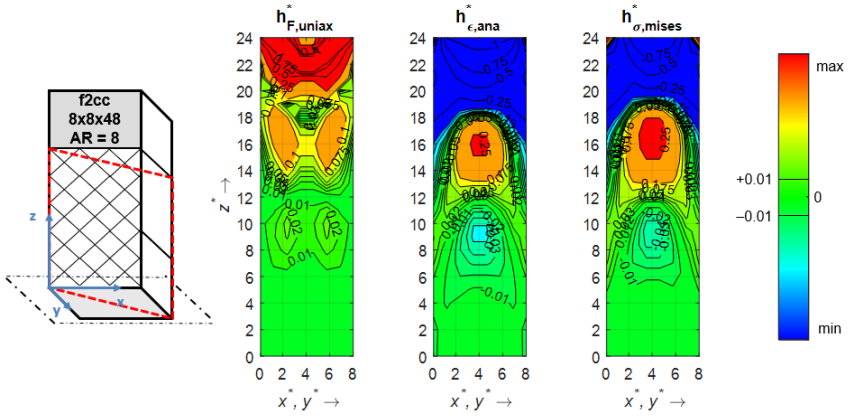

Figure 54: Sample quality results: f_2cc 8x8x48 AR8 ungraded (diagonal).

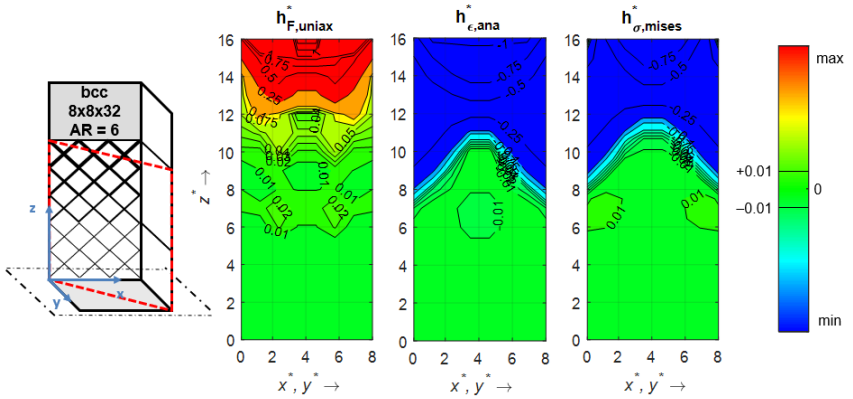

Figure 55: Sample quality results: bcc 8x8x32 AR6 graded (diagonal).

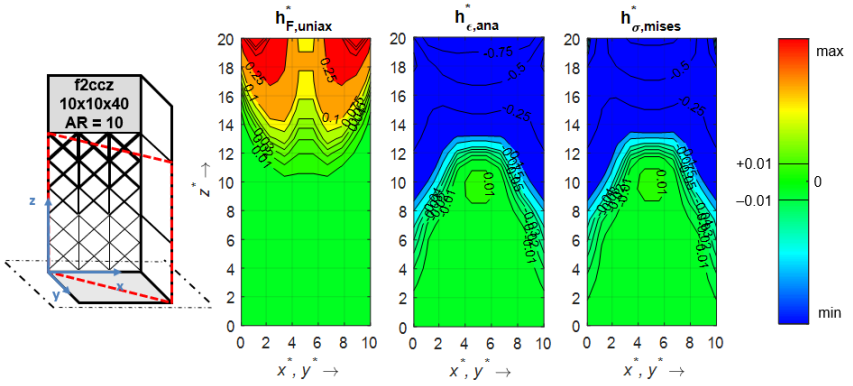

Figure 56: Sample quality results: f_2cc_z 10x10x40 AR10 graded (diagonal).

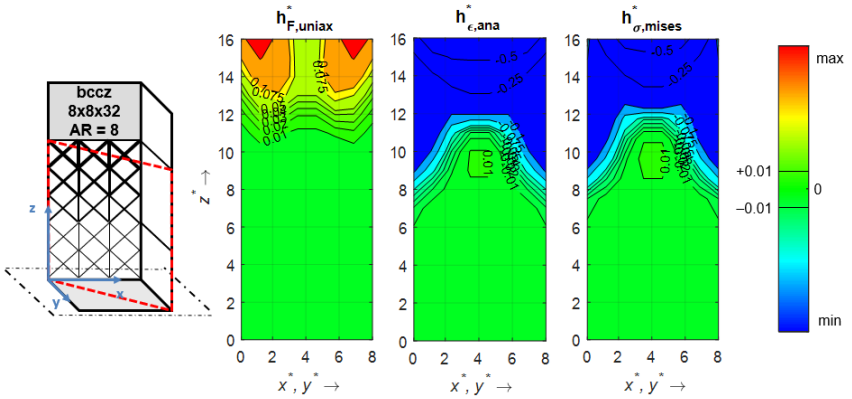

Figure 57: Sample quality results: bcc_z 8x8x32 AR8 graded (diagonal).

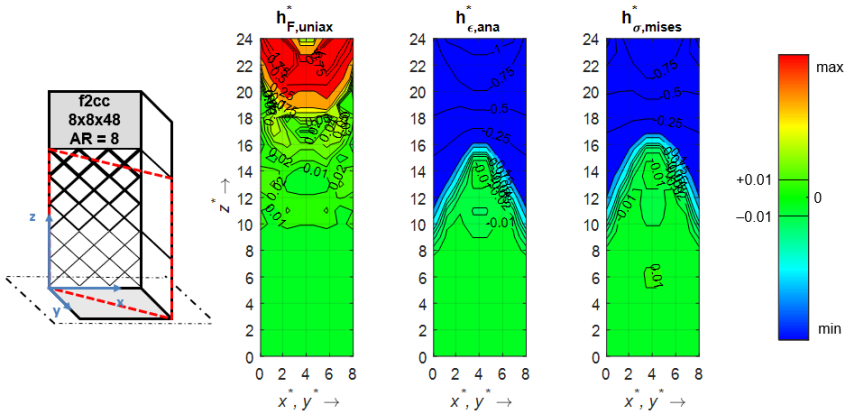

Figure 58: Sample quality results: f_2cc 8x8x48 AR8 graded (diagonal).

Size of the transition region

Similar to the undisturbed area, the size of the transition region defined as the height for which the design quality criteria are fulfilled. Table 3 and Table 4 sum up the number of graded and ungraded cells as well as the total number of cells required for the transition region according to the proposed grading approach.

Although the number of graded cells can be systematically identified by looking at the ungraded sample, the complete size of the transition region cannot be fully predicted. The difference between the number of graded cells and the final size of the transition region can be explained by the still present edge effect, which has not been cleared but rather reduced to a negligible amount. This effect is noticeable from Figure 55 to Figure 58, where the stress criterion converges slower at the sample's corner than at its centre. Therefore, ungraded cells are required in the transition region to act as buffer.

It is further noticeable, that face- and body-centred cells yield different convergence rates of the developed strain and stress criteria at the sample's corners. Moreover, these convergence rates do not seem to be influenced by vertical struts, i.e. reinforcement in the loading direction. It can be deduced that the convergence rates directly depend on the effective

shear moduli of each ungraded URC employed as buffer. When calculated as a function of the aspect ratio, the effective shear moduli prove to be independent from vertical reinforcement ([43], Fig. 16). Besides the effective shear moduli of body-centred unit cells are higher than the ones of the face-centred unit cells ([43], Fig. 16). Therefore, as for the number of graded cells, the convergence of stresses is specific to each structure and depends on the main load path. However, only the inclined struts play a role concerning the required number of ungraded cells. It can be concluded that the nature of the RUC has an influence on the design of the transition region.

Table 3: Size of transition region (bcc & f_2cc_z).

AR	Sample size	bcc			f_2cc_z		
		Graded cells	Ungraded cells	Total size	Graded cells	Ungraded cells	Total size
6	8x8x32	8	1	9	9	3	12
	10x10x40	10	1	11	11	5	16
	12x12x48	12	1	13	13	6	19
8	8x8x32	8	1	9	9	3	12
	10x10x40	10	1	11	12	4	16
	12x12x48	12	1	13	13	6	19
10	8x8x32	8	1	9	9	3	12
	10x10x40	10	1	11	12	4	16
	12x12x48	12	1	13	14	5	19

Table 4: Size of transition region (bcc_z & f_2cc).

AR	Sample size	bcc_z			*f_2cc		
		Graded cells	Ungraded cells	Total size	Graded cells	Ungraded cells	Total size
6	8x8x32 (8x8x48*)	8	1	9	11	3	14
	10x10x40 (10x10x60*)	10	1	11	15	3	18
8	8x8x32 (8x8x48*)	8	1	9	12	3	15
	10x10x40 (10x10x60*)	10	1	11	15	4	19
10	8x8x32 (8x8x48*)	8	1	9	12	3	15
	10x10x40 (10x10x60*)	10	1	11	15	4	19

Size of the target region

Once the size of the transition region is set, all further ungraded cells are considered as part of the target region. Once a uniaxial state is reached, varying the target region and,

thus, the final sample size without impacting its performance is possible with the developed approach. Figure 59 and Figure 60 provide an example based on the graded sample of Figure 57 with respective size increase and reduction.

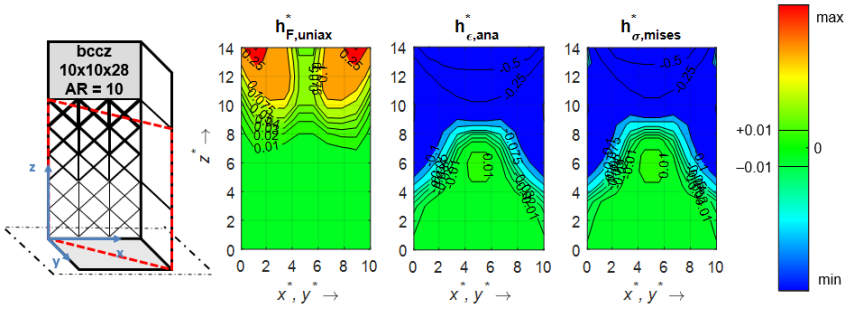

Figure 59: Sample quality results: bcc_z 10x10x28 AR10 graded (diagonal).

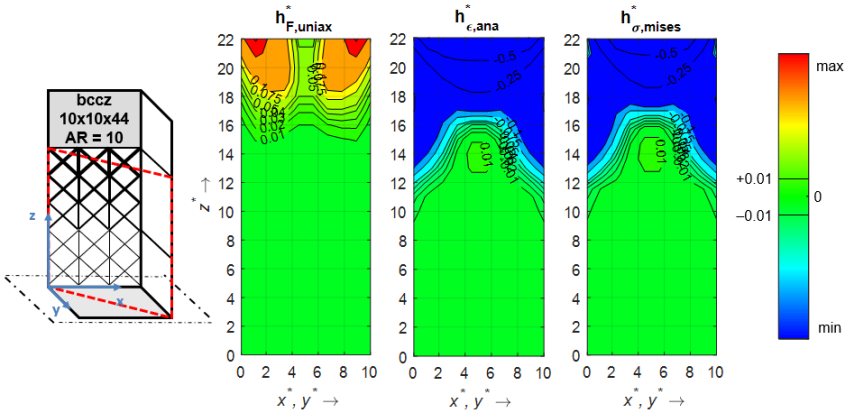

Figure 60: Sample quality results: bccz 10x10x44 AR10 graded (diagonal).

4.1.4 Discussion

The challenges highlighted by this investigation explain why all reported tensile experiments found in the literature reflect the only configuration they investigate on and are not eligible for further comparison. These are mainly due to the absence of a transition region or arbitrary design, which do not necessarily guarantee the absence of edge effect and a pure tensile loading state at the same time. Moreover, local design solutions such as local reinforcement by means of local grading at the sample's edge or first cell layer(s), e.g. by means of pillar [77] or epoxy resin [352], are expected not to solve the load introduction problem but rather shift it to a further cell layer.

In the framework of this investigation, both validity and transferability of the approach was proven for 4 RUCs, verifying the potential of structural grading for load path monitoring. Moreover, this approach covers any combinations of cell size and thickness leading to one of the investigated ARs and, thus, would yield the same grading parameters since

the calculations were performed in the linear elastic domain. Therefore, it is expected that both provided design and methodologies are valid for at least all other truss-based lattice structures of AR higher than 5.

This means that design features aligned to existing norms can be developed (Figure 28). The transition region can be considered a load introduction region made of ungraded and graded cells, for which grading parameters can systematically be identified from the ungraded state. Compared to the bulk material sample, they stand for the parallel length before the gauge and the transition region, respectively. The target region is equivalent to the gauge region of the bulk material sample. However, lattice structures specific rules need to be identified for a detailed sample design. Since the sample size shall be as small as possible, considering 8 RUCs in the plane perpendicular to the loading direction is advised if working with the proposed approach. Nevertheless, to align with existing norms [337], considering 10 RUCs would also be possible with this approach. Although no common SCF in terms of sample size or unit cell type could be identified, harmonising the SCFs for a sample size could be possible. In this case, the influence of the local increase in strut thickness shall remain local and not lead to any stress peak at the transition to neighbouring cells due to load redistribution. Alternatively, a stress concentration factor specific to a given sample size can be considered. Depending on the cell type, both sample slenderness ratio and number of ungraded cells in the transition region can be determined, too. As potential design rule concerning the number of ungraded cells in the transition region, it can be stated that body-centred unit cells, i.e. bcc and bcc_z, need only one cell layer as buffer while face-centred cells, i.e. f_2cc and f_2cc_z, required a number of buffer layers corresponding to at most $n_{RUC,x,y}/2$. No specific size of the target region is proposed at this stage since it will mainly depend on the target of experimental campaigns.

To a further extent, the introduced configuration independent representativity of the normalised plots for one given RUC hints at the possibility of identifying structure specific global rules that could lead towards general design guidelines for lattice structures for different load cases. However, observed unit cell specific features means that a potential design guideline shall at some point differentiate stretching-dominated structures from the bending-dominated ones.

The main drawbacks of this approach are linked to the limits of the beam theory. In the case of structural grading of lattice structure of $AR = 6$, few unit cells see their AR drop below the limit of 5 (see appendix B). The most critical ones are close to be considered as porous bulk material, with relative densities close to 30 % (Figure 22 and Figure 23). However, these values are directly linked to the SCF, which is considered local and, thus, is assumed not to falsify the results. Other deviations in the range of order of 5 are considered as acceptable. Other challenges encountered by this approach are local stress concentrations at the transition between cells involved by thickness changes, the high sample size and their manufacturing as raised in section 2.4.2. These points are addressed further sections of this work (sections 4.3, 4.2 and 5, respectively).

4.2 Load introduction via bulk part modification

The aim of this investigation is to propose an alternative design solution to the structural grading developed in section 4.1 that avoids high samples it may involve. To achieve this, a novel approach combining topology optimisation, numerical design of experiment and correlation analysis is employed. As different design solutions can be expected because of the differences in the mechanical behaviour of bending and stretching dominated RUCs (see section 2.3.4), the main challenge lies in finding a design that is applicable to all RUC types. Innovative design guidelines geared towards simple, efficient and universal sample design are derived and compared to the literature. In addition, recommendations on the most influencing optimisation variables are offered for further investigations.

For the sake of keeping focus on design solutions and their evaluation, chapters dedicated to details on the ranges of the investigated optimisation variables, the analysis methodology and the corresponding results are listed in appendix A.

4.2.1 Design methodology

Firstly, an extensive parameter study is conducted to determine the most influential and thus purposeful optimisation variables and variable ranges using numerical design of experiment (DoE) and correlation analyses. Secondly, topology optimisation calculations are performed based on the identified variables. Resulting design solutions are then evaluated with finite element analyses. Then, recurring features driving the topology-optimised design space are extracted from the load case specific results (see section 2.2.3) and interpreted into structural elements. Finally, a generic sample design is proposed and numerically investigated as well.

Topology optimisation and subsequent finite element analyses are performed using the software package *Altair Hypermesh v14.0* and the *Optistruct* solver. The DoE evaluations are monitored using a *MATLAB* script, while a *PYTHON* script deals with the result post-processing and plot generation.

The employed numerical model is schematically shown Figure 61. As mentioned in section 3.2.2, the sample is idealised as an eighth model with only target and transition regions. The transition region depicted in Figure 28 is defined as design space, which is parametrised so that the lattice sample with and without transition region can be investigated.

Restrictions and objective function are assigned to the identified critical areas of the tensile specimen design. The first critical area is located at the interface between transition and target regions, where load introduction and edge effects take place. Based on preliminary results and the ones from section 4.2.2, this constraint region covers two-thirds of the first lattice layer after the design space. The second critical area is defined at the sample's centre, where failure shall ideally occur. Preliminary investigations have shown that only the

lowest half of the unit cells within the middle layer (nodal area excluded) are relevant to obtain coherent results without regional ambiguity.

In order to obtain a precise mapping of the load distribution and corresponding stress concentration, a three-dimensional continuum model with second-order tetrahedra elements is employed [390]. A fine auto-meshing procedure is preferred over a detailed mapped meshing approach in order to reduce the configuration specific modelling efforts. After a convergence study, the mesh element size is set as 0.2 times the strut diameter. This enables the detection of not only the principal stress maxima but also local sub-maxima throughout the struts of a single unit cell.

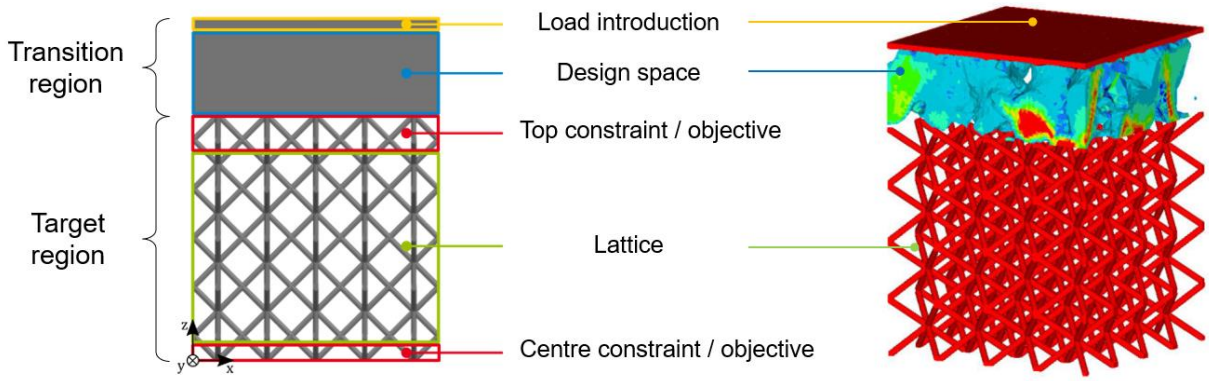

Figure 61: Topology optimisation setup.

Among the parameters and control cards available in Altair Hypermesh, the following variables have been identified influencing topology optimisation results and, thus, relevant for the investigation. They are categorised as follows: geometric variables, modelling variables and optimisation variables. The investigated geometric variables are the aspect ratio AR, the number of RUCs in the xy-plane of the target region $n_{RUC,xy}$, the number of RUCs in the z-direction $n_{RUC,z}$ of the target region and the height of the transition region h_D. The only modelling variable investigated, *load type*, is related the idealisation of the load introduction. The following topology optimisation variables have been selected as relevant for the identification of small-scale features. The volume fraction V_f determines the remaining material infill of the design space and can, therefore, influence the topology towards thinner structure layouts. The minimum and maximum member size variables, respectively m_{minmem} and m_{maxmem}, enable the elimination of either too slender or too large features in order to reach feasible design proposals. They are adapted to the strut diameter as the thinnest structural element. In Optistruct, the parameter *DISCRETE* facilitates the density assignment penalty factor p in the frame of the Solid Isotropic Material with Penalisation (SIMP) optimisation approach [390]. It influences the tendency for elements in a topology optimisation to converge to a material density of 0 or 1, i.e., the tendency to assign material or not for a given element stiffness (see section 2.2.3). Similar to the penalty factor, the *TOPDISC* parameter can aid in the discretisation of the elements to pro-

duce further discrete results, i.e., it increases the probability of proposing filigree structures. In the framework of this investigation, the $Constraint/Objective$ variable is defined as a combination of the applied constraints and targeted optimisation objectives.

4.2.2 Results

In the framework of this investigation, the quality of the load introduction is evaluated by assessing the distribution of von-Mises stresses σ_{VM} within the lattice sample. Coloured scatter plots are used to display the local stress distribution. The element stresses are projected onto representative two-dimensional diagonal view cuts. Given the three-dimensional nature of the elements and the model size, overlapping points exist. In order to keep the maxima visible, the elements are sorted for their respective stress. This ensures the visualisation of the local notch stress increase. An overview of the global stress distribution is provided by underlaid contour plots and two side plots representing the direction axes of the considered view cut. Results are displayed in a quarter of sample, wherein the top right corner corresponds to the sample's edge.

Samples without transition region

Figure 62 and Figure 63 display the stress distribution within the bcc and f_2cc_z lattice samples, respectively. In both cases, the global maxima are observed in the top outer corner. The bcc sample exhibits local maxima at the topmost elements and around the middle distance from the top of the unit cells (Figure 62). The topmost elements in the f_2cc_z sample show the highest stress values as well as two additional local maxima in the vertical strut of the unit cell (Figure 63). In this representation, these two distinct local maxima are located on the topmost layer and below at the inner side half a unit cell from the top are visible. In both structures, the local stress concentrations can be observed in the vicinity of the nodal areas, especially in the sample's centre. However, the order of magnitude of these stress constraints is lower than the ones at the edges. As noted in section 4.1, this means that the structure will be more likely to fail at the corners due to edge effects and, thus, could falsify test results. Moreover, it is visible that these stresses appear at the surface of the struts that endure the highest strain through bending. The localisation of these stress concentrations justifies the area covered for the application of the optimisation constraints and objectives at the sample's top region, as described in section 4.2.1.

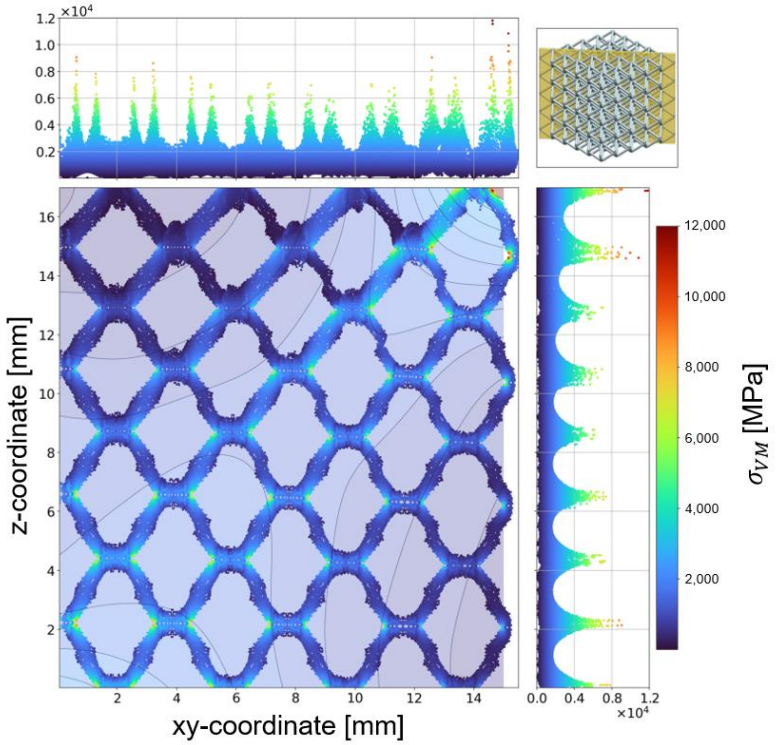

Figure 62: Sample without transition region: Von-Mises stress distribution in a bcc 8x8x8 lattice structure (diagonal).

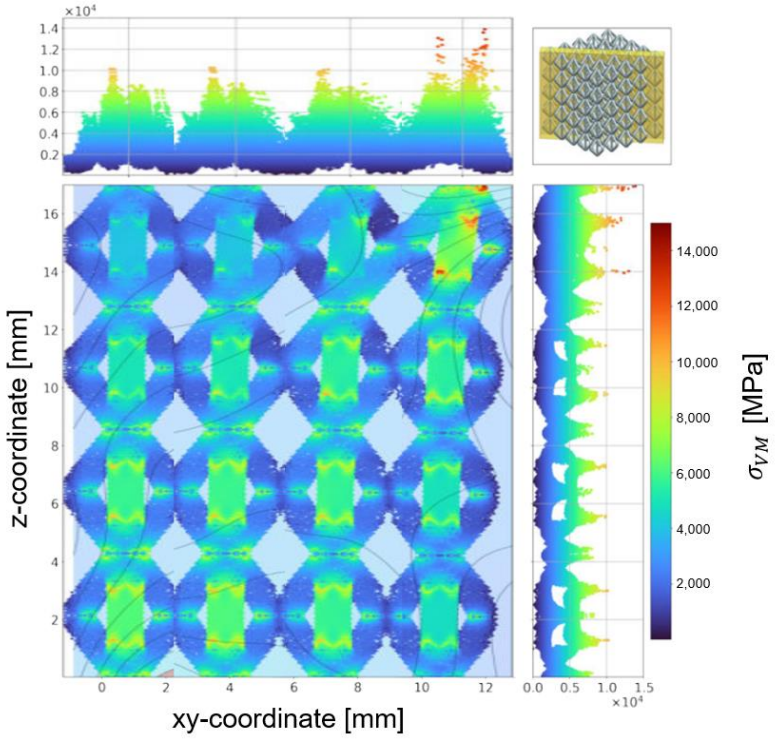

Figure 63: Sample without transition region: Von-Mises stress distribution in a f_2cc_z 8x8x8 lattice structure (diagonal).

Design features

Although the obtained topologies are all different, similarities can be ascertained and common design features applicable to both the bcc and f_2cc_z lattice structures can be identified. To establish the final design draft, the collected results are compiled into key design features. Three main key features were identified in the framework of this study. They are summed up in Figure 64, which shows samples exhibiting all the typical features for the bcc and f_2cc_z, respectively sample 4 (Figure 64, a) and sample 10 (Figure 64, b). Please refer to appendix A for the corresponding sample run configuration.

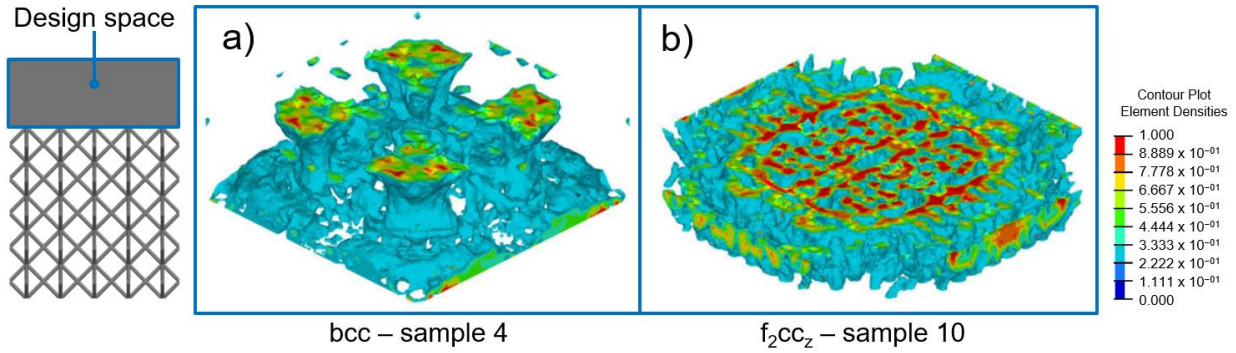

Figure 64: Optimised design space: bcc sample 4 (a) and f_2cc_z sample 10 (b).

The first identified key design feature is the presence of *pillar-like structures*. They were identified at the connection to the unit cells for bcc samples 4, 5, 8, 11 and 15 and for f_2cc_z samples 4, 8, 9, 10 and 12. The strut-based RUCs favour the pillar-like connections to introduce tensile stresses. These pillar-like structures follow the loading direction in the top connection region and ensure a direct load transfer, as described by Mattheck [175]. Then, the pillar shapes depend on the investigated lattice structure because of the differences in the unit-cell-specific load paths (see also section 4.1). As can be expected, a direct pillar connection for the stretching-dominated f_2cc_z lattice structure is generated. The vertical struts are aligned with the loading direction and contribute to the main load path. This design principle for tensile-load-optimised structures can also be found in other contexts for test specimens as it enables a more uniaxial load introduction [391, 392]. For the bcc structure, the pillars are inclined, especially in the regions close to the sample's corner, for the load redistribution and load introduction into the bending-dominated lattice structure. This leads to non-circular cross-sections. A potentially ideal design feature for load introduction in inclined struts should have an elliptical cross-section at the connection with the lattice.

The second identified key design feature is the transition from a quadratic cross-section, which is automatically implied by the unit cells, into an *intermediate concentric cross-section*. This cross-section can be described as circular in the specific frame of this investigation due to the applied symmetry. The best examples were found in bcc samples 3, 4, 8, 10, 11, 12 and 15 and f2ccz samples 3, 9, 10 and 15. It should be noted that, due to the modelling approach (see section 3.2.2), symmetric topology results may be obtained as

well as separating structures. Preliminary studies have shown few qualitative differences between the full and fourth models for significantly different computing times. This means that a potential symmetric outcome is not due to the modelling approach. The pillar-like structure is not clearly pronounced for all the bcc samples. This stems from the absence of vertical struts. In the case of the absence of pillars, the lattice top is connected via a web-like structure. Web-like connections can enable a larger vertical strain through bending and, thus, tend to follow a concentric pattern. In some cases, both pillar and web-like structures are combined. Although this may speak against intuition, since this shape does not comply with the cubic unit cell design, it can easily be understood when considering the results for samples without a transition region (Figure 62 and Figure 63). Circular cross-sections do not exhibit sharp edges and, thus, stress concentrations. A transition from a quadratic cross-section to a circular one can reduce the edge effects and is therefore beneficial for the design. This finding can be compared with the full circular design of some tensile specimen attempts listed by Benedetti et al. [46]. Moreover, independent from the identified structural element, the circular-shaped pattern shows variable diameters, especially in the vicinity of the lattice structures. Thick structures are observed close to the bulk region, while smaller features are observed close to the target region, with the diameters sometimes being smaller than the one of the lattice struts themselves. This means that the stress distribution is not even, and the structurally graded features should be regarded to avoid local stress concentrations. This feature can be considered as the most important design feature for a potential draft, since the concepts of both concentric pattern and structural grading can be retrieved in the grading formulation of section 4.1.

The third and final identified key design feature is linked with the previous point, as is deals with the *absence of a direct connection in the corners* in the vicinity of the connection with the lattice structures. Representative examples are bcc samples 4, 10 and 13 and f2ccz samples 3, 9, 10, 13 and 14. This feature is directly linked with the avoidance of edge effects. The locking of transverse strain results in a necking of the sample and a local stress concentration at the sample's corners (Figure 65, in line with the experimental observations of Gümrük et al. [339]). An elastic deformation at the connection with the lattice structure needs to be enabled to remedy this effect. Interestingly, design solutions proposing this feature yield the best results in terms of stress distribution independently from the design height. Therefore, it can be concluded that a large transition region is not required to achieve optimised specimen characteristics. This provides a real advantage in comparison to a load introduction made of graded lattice structures. This third key design aspect is partially achieved by the pillar connection, as these structures can bend transversely. On the one hand, the outward inclination of the pillars observed in the bcc samples contributes to overcoming the absence of material at the sample's corner and, on the other hand, the longer pillar structures that can be locally identified offer larger deflections in a transverse direction in order to achieve more compliance. At this point, it can be deduced that all three features back each other up and it is, therefore, not meaningful to consider them separately.

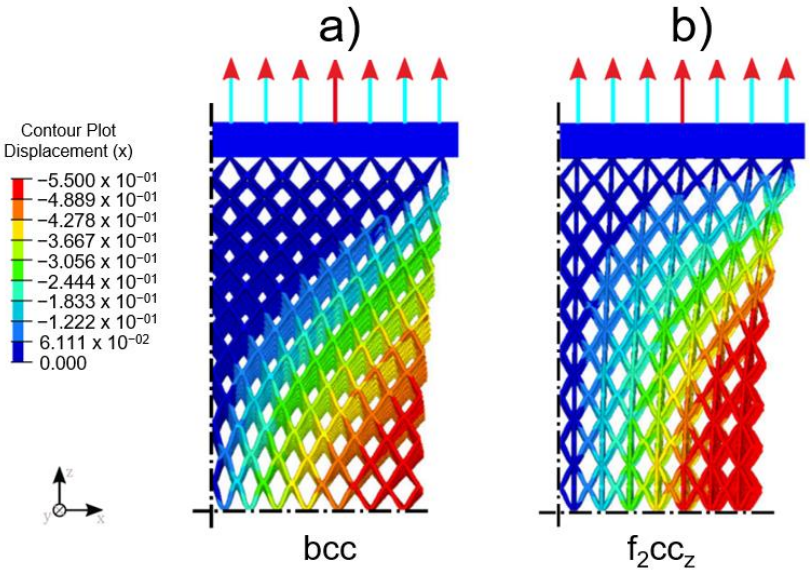

Figure 65: Sample without transition region: displacement in the x-direction of bcc (a) and f_2cc_z (b) lattice structures (front).

Design proposal

Based on the identified features, a design proposal is made. The developed concept shown in Figure 66 is applicable to both f_2cc_z and bcc lattice structures. It takes manufacturing restrictions into account so that no supporting structures are required and no direct adjustments to the lattice need to be made. The DoE analysis (appendix A) hints at wide samples and, based on the observation of the design space height, allows for a narrow transition region. The smallest investigated design space corresponding to a half of the unit cells is therefore used. This avoids unnecessarily high samples and, therefore, reduces the manufacturing time, which does not contradict the parameter trend observed in the DoE. The design of the transition region is notched at its edges above the target region. This results in a more compliant structure that enables larger strains at the corners and, thus, reduces the stress peaks. This design measure can be assimilated into the widely spread relief notch method [393]. The notch is angled so that a new stress maximum inside the transition design is avoided. While this concept can be used for machine connections of either quadratic or circular cross-sections, the upper half of the transition region is directly influenced by the machine connection. In the case of a quadratic cross-section, the intermediate cross-section in the notch root presents a scalene octahedron (Figure 66, a) whereas a straightforward design is possible for a circular cross-section (Figure 66, c). The selected angles comply with the well-known critical inclination angle of 45° for additively manufactured parts. Two solutions for the interface between the target and transition regions are proposed. The first one involves excluding material spaces to create pillar- or alcove-like structures (Figure 66, b) as found in construction, e.g. in the architectural design of churches. A good design alternative lies in the use of cones (Figure 66, c) as structural elements for proper load introduction, which can be seen as graded pillars. This solution further offers the additional advantages of being compliant with DFAM approaches (see section 2.1.4) and providing better manufacturability, although

cones have been used as space fillers rather than load introduction features [247]. The proof of manufacturability is provided in Figure 66, d.

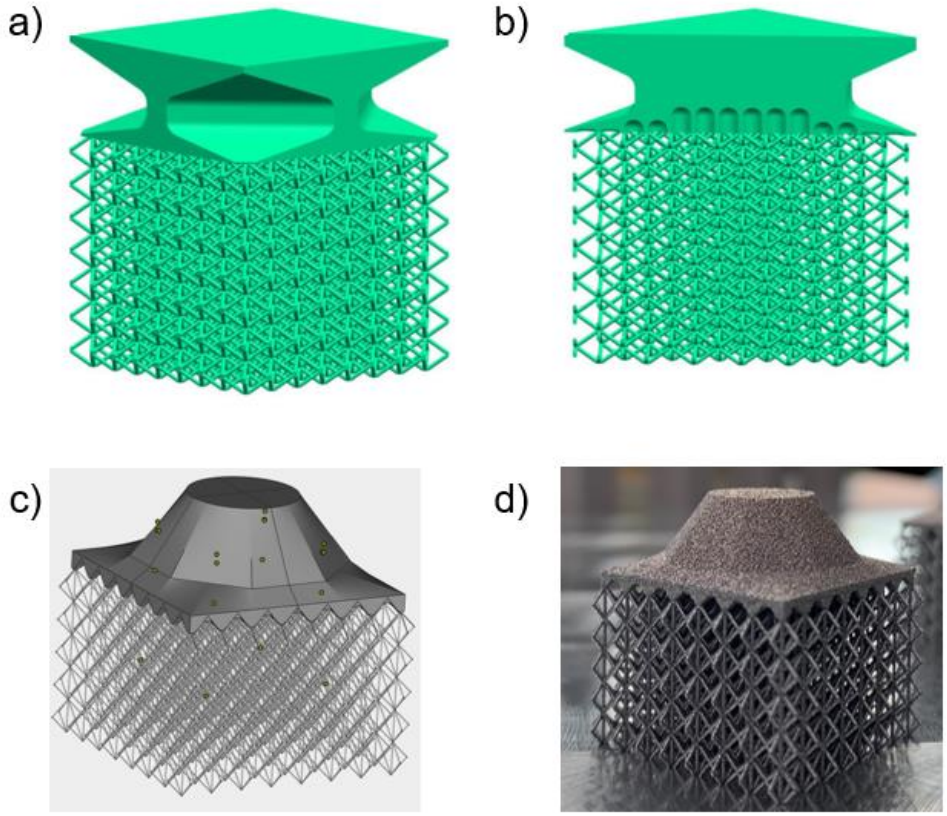

Figure 66: Design proposal: quadratic machine connection (a) with alcoves (b), circular machine connection with cones (c) and proof of manufacturability (d).

In the framework of this investigation, numerical verification analyses of both load introduction alternatives are performed for both the f_2cc_z and bcc lattice structures. As most DFAM compliant and, thus, promising solution, only the results of the design proposal with cones as load introduction feature are reported. Nevertheless, the observations listed below are valid for the design proposal with alcoves too. Figure 67 and Figure 68 show the stress distribution for the bcc and f_2cc_z lattice structures, respectively. The stress distributions clearly show an effective stress reduction on the top corners in both cases. No maxima are present in the sample's upper region, the transition region included. A stress increase towards the sample's centre is achieved for both lattice structures, although it is more pronounced for the f_2cc_z lattice, with a distinct global maximum in the centre section. The bcc maxima are distributed along the z-direction but produce a more even stress distribution in the xy-plane. The deformed shapes hint at the higher compliance of the structure in the corners. These observations prove that the design proposal successfully fulfils its purpose.

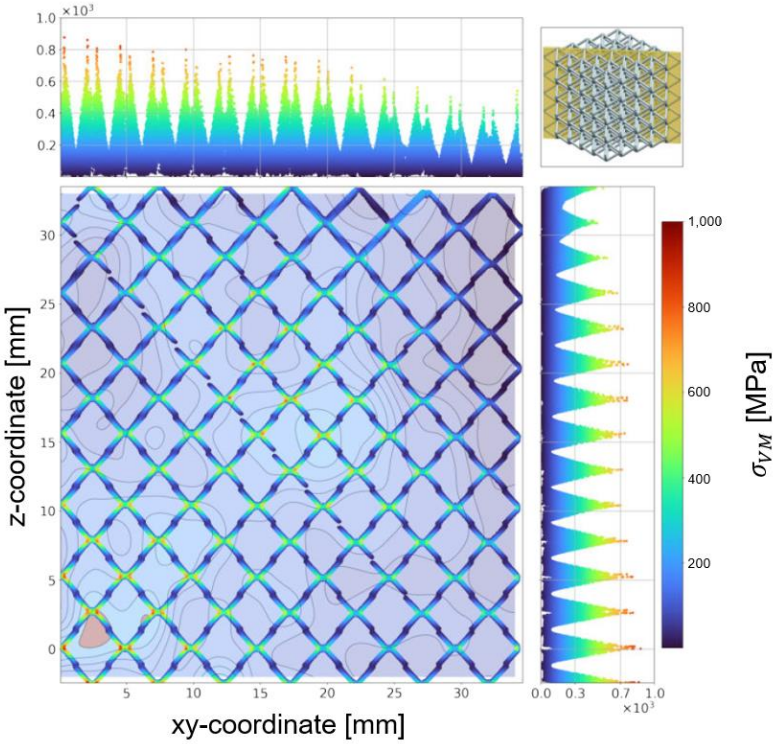

Figure 67: Design proposal (cones): Von-Mises stress distribution in a bcc lattice structure (diagonal).

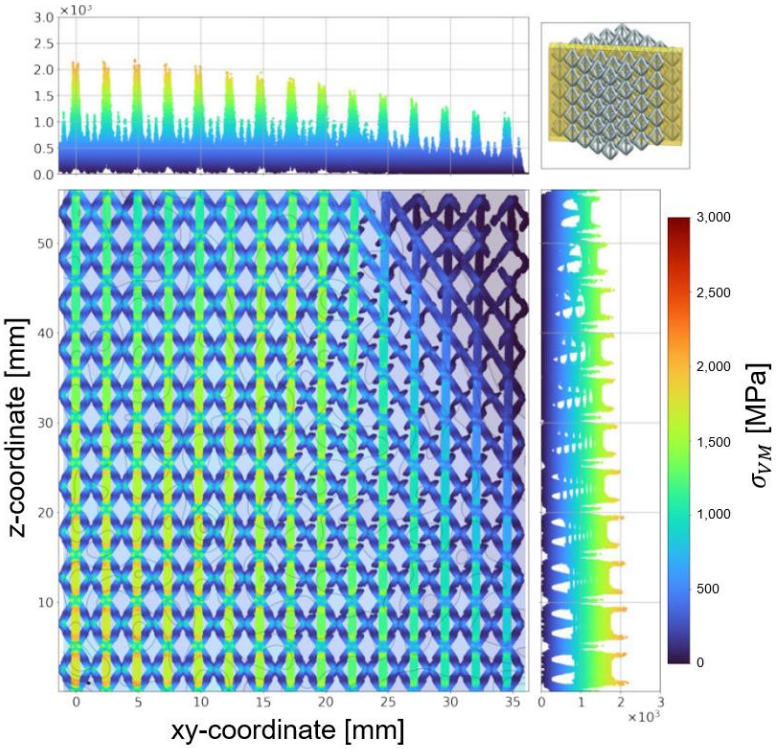

Figure 68: Design proposal (cones): Von-Mises stress distribution in a f_2cc_z lattice structure (diagonal).

4.2.3 Discussion

Despite the number of samples run and the potential inaccuracy of the mesh or convergence problems, the derived topologies of the DoE study present structural aspects that can be rebuilt in CAD models. Although the topologies themselves do not provide a direct design draft for a standardisation, they present characteristics beneficial to tensile load introduction that can support generic design rules. In the investigated cases, a shift in the stress concentration maximum from the corner to the lattice centre is observed and a mitigation of the stresses in the top corner is achieved. Therefore, the targeted goals concerning stress distribution can be successfully addressed with the proposed design measures. However, the current design cannot solve local stress concentrations within the lattice structure, as local peak stresses are still present at the strut junctions. This point is addressed in section 4.3.

As the sample design stems from observations of repetitive features, alternative design proposals can emerge from the observed features (compliant edges, rounded cross-section, pillar or web-like connection). This design proposal exhibits similarities with the different tensile specimen geometries reported in recent literature (see section 2.4.2). This can be explained by the presence of some of the identified key features, including compliant edges, a rounded cross-section and a pillar connection. Among all the reported designs, adding a flat dog bone bulk region at the extremities of the lattice structure seems to be the least suitable design, since it can be interpreted as a sample without a transition region. This automatically implies that the sample design does not offer compliant edges and the edge effect will take place, although uniaxial loading is ensured by the design. Hence, the sample will be more likely to fail at the interface between bulk material and lattice structure, especially in the case of recommended large samples. A sample geometry with threaded ends corresponds to the notched design of the current proposal. In that case, the design has to be DFAM compliant (see section 2.1.1). As demonstrated in section 4.1, a load introduction made of lattice structures requires a load introduction design that depends on the lattice type. This requires investigating the load paths and leads to higher samples than the current design proposal. Furthermore, this RUC dependence raises the question of their representativity and comparability of cylindrical samples. Although they automatically comply with the recommendations concerning rounded cross-sections, their coordinate system differs with the ones of truss-based RUC (see section 2.3.3).

None of the reported samples gather all these driving design features at the same time. Alternative load introduction design with different homogeneous load introduction features, e.g. pillars or cones, have been separately investigated. The results showed that the stress concentration problem is only shifted in the best case. This highlights that the design needs to encompass simultaneously all the presented key features. In this regard, the most promising alternative sample design seems to be the one reported by Dallago et al. [345] since the cylindrical sample design with threaded ends exhibits pillar-like structures as a transition region too. However, the sample design needs to be further parametrised as it has to be ensured that the edges are compliant enough to reliably relocate failure to the

sample's centre. Other design solutions consider a non-uniform shape on the part of the transition region. A combination of a compliant transition region and graded lattice structures could represent another reliable solution in terms of load introduction. However, this would involve more design variables and, therefore, render the design less viable and universal. Furthermore, the results show that a grading of the features in the transition region is not mandatory at this stage of design maturity. Still, this point represents a further optimisation possibility of the current design proposal.

It is highly expected that this promising design concept can be transferred to other lattice structures based on cubic unit cells (strut-based and non-strut-based). Further transferability towards non-cubic lattice unit cells is feasible as far as the samples without transition regions display similar issues in terms of stress concentrations. In the case of deviating challenges, first insights into relevant topology optimisation variable have been provided. A foundation for normative design and corresponding methodology is given.

4.3 Transition between unit cells

This section handles the effect of geometrically induced notches in truss-based lattice structures. As highlighted in section 2.4.2, notches appear at cross-section changes and in the vicinity of sharp edges. In the case of truss-based lattice structures, design notches can be observed at the interface between single strut and nodal area and result in in high local stress concentration (see section 4.2.2). Supplementary notch stresses are present within single struts as well if they are modelled at the RUC's border (Figure 17). These design notches are present in ungraded configurations and emphasised in the case of structural grading (Figure 69). Getting rid of these design notches shall increase the mechanical performance of truss-based lattice structures. In this regard, notch stress reduction methods are investigated to derive simple design rules aiming at recommendations for potential design guidelines.

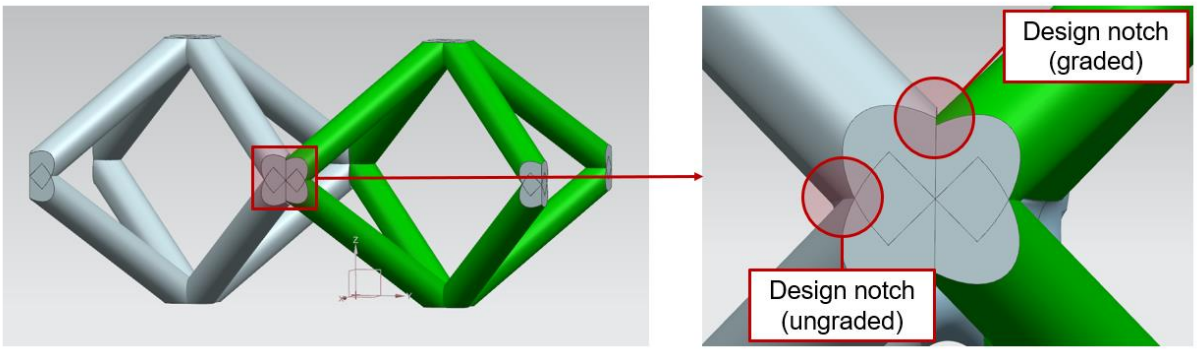

Figure 69: Design notches example in truss-based lattice structures.

While the chosen circular fillet radius solution inarguably offers to exhaust the load-bearing potential of truss-based lattice structures [219, 253, 344, 369], the available literature

for notch optimisation demonstrates that alternative design solutions yield higher efficiency in the reduction of local peak stresses. Some of the most prominent historic stress concentration reduction approaches were developed for the case of flexural hinge shapes. Among them, the Baud shape is a mathematical shape inspired from fluid dynamic [394] while the Thum-Bautz shape, an empirical shape developed for cases where the Baud fillet is not effective [395]. Graphical approaches such as the parabolic Grodzinski shape [396] enable more pragmatic hands-on applications. Zelenika et al. demonstrated that the circular fillet shape is far less compliant than prismatic, wedge or elliptical shapes. For example, it is subjected to 26 % more stresses than the Thum-Bautz shape [397]. Therefore, the static performance of original RUC designs is compared to different notch reduction methods. While the first selected method considers the standard design solution of a circular fillet radius, two alternative notch stress optimisation methods inspired from two-dimensional shape optimisation approaches adapted to lattice structures are proposed. In the framework of the numerical verification of these chosen design approaches, different configurations are investigated under static compression loading.

4.3.1 Design methodology

Selected design methods

The *Fillet Radius Method* (FRM) consists in implementing the well-established fillet radius onto the unit cell tangent to the strut edges in order to avoid notches. A schematic example of the FRM with a constant radius is provided in Figure 70.

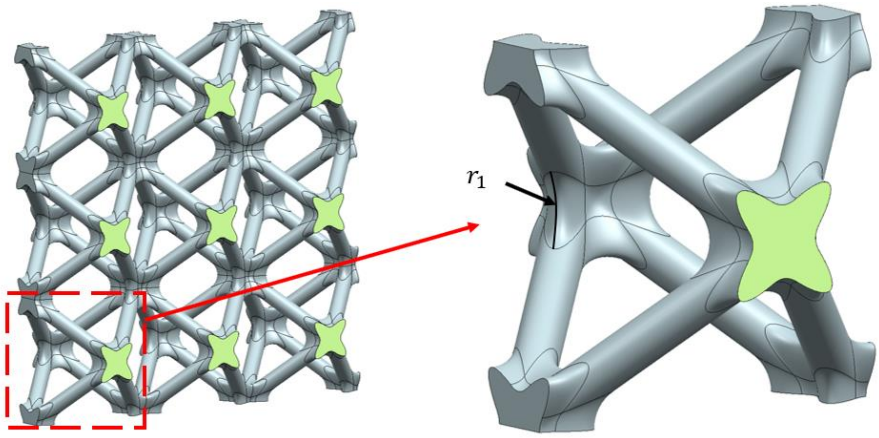

Figure 70: The Fillet Radius Method applied to a bcc lattice structure.

The *Pocket Calculator Method* (PCM) was developed in framework of the notch stress reduction in a stepped bar of diameter D_i subject to tension loading. The principle of this method lies in the compensation of the lateral force F_Q, which induces notch stresses, by the tangential force F_T issued from local nominal stress by optimising the cross-sectional area of the shaft [398]. The principle is depicted in Figure 71, a. The angle α_i describes the angle between the first path of the multi-linearised PCM curve at its starting inflexion

point. Each sharp angle determines an inflexion point. Depending on an empirically determined start angle α_1 and support angle $\alpha_0 = 0°$, the tangential force F_T^i and the lateral force F_Q^i can be calculated. The rate of change of α and the subsequent amount of segments s can thus be assessed to achieve an optimal stress distribution. The two-dimensional shape of the PCM curve is determined using the Eq.45 and Eq.46, issued from [398].

$$D_{i+1} = D_i + 2s \sin\left(\sum_{k=0}^{i} \alpha_k\right) \tag{45}$$

$$\alpha_{i+1} = 2 \arcsin\left(\frac{\frac{D_{i+1}}{D_i}\cos\left(\sum_{k=0}^{i-1}\alpha_k\right)\left(1 + 2\sin\left(\frac{\alpha_i}{2}\right)\right) - \cos\left(\sum_{k=0}^{i}\alpha_k\right)}{2\cos\left(\sum_{k=0}^{i}\alpha_k\right)}\right) \tag{46}$$

The *Tensile Triangle Method* (TTM) is directly inspired from shapes observed in nature such as tree or bones and was developed to reduce the computational time of computer aided shape optimisation and leads to shapes comparable to the PCM [399]. The sharp corner of a part is successively bridged with isosceles triangles (Figure 71, b) until a smooth transition is achieved. The optimal trade-off between mass increase and stress reduction is achieved for three triangles [400].

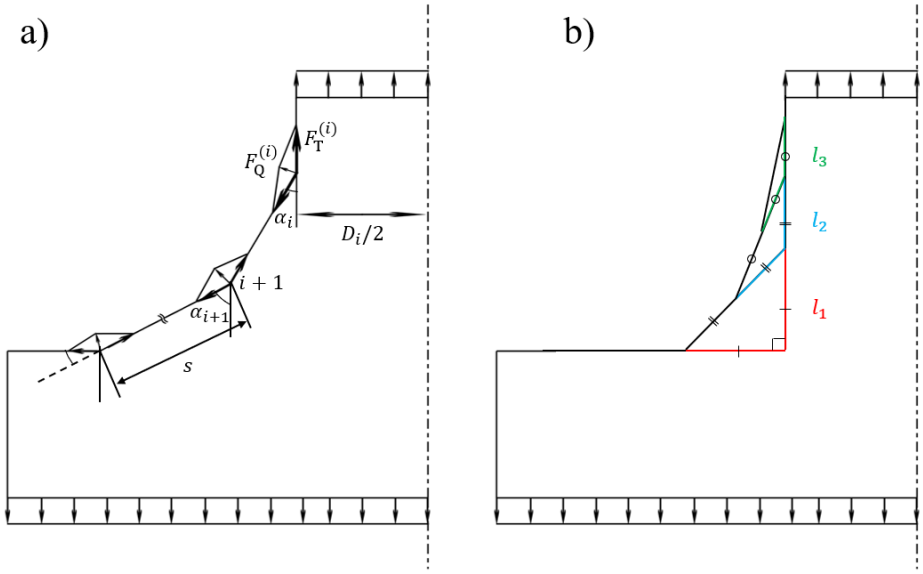

Figure 71: Pocket Calculator Method applied to a stepped bar with rotational symmetry under uniaxial tensile load (a) and Tensile Triangle Method applied to a rectangular notch with 3 tensile triangles (b). Based on and recompiled from [398] and [399].

Application to lattice structures

These methods were extended to the three-dimensional space for the application on the considered truss lattice structures. As mentioned in section 3.1, explicit modelling employing B-splines [252, 253] was used in the framework of the manual parametrisation of the

lattice design (see section 2.3.2). It has to be noted that, although existing functionalities in CAD programs allow the direct implementation of the FRM on lattice structures using a built-in fillet function, a manual construction that bypasses the size limitation of the fillet radius was implemented for consistency and comparison purposes.

For the sake of comparability between the selected notch reduction methods, all the described methods will be further assigned a constant curvature radius. In the case of PCM and TTM, the equivalent curvature radius corresponds to a constant radius at the angle bisector deployed by the FRM (see below). The bcc unit cell is described by one curvature radius r_1, whereas the f_2cc_z configuration is described by two curvature radii r_1 and r_2. In order to facilitate generating any required configuration and to identify potential design rules, the equivalent curvature radii have been parameterised depending on the modelled strut thickness t. To do so, the curvature factors γ and ϑ are introduced. Figure 72 displays exemplarily both bcc and f_2cc_z RUCs in ungraded configurations. Eq.47 and Eq.48 show the corresponding curvature radius parametrisation. In the case of structural grading (Figure 73), the lattice structure is factorised since, similarly to section 4.1, only the same RUCs are considered. A scaling factor f describing the *grading factor* is applied to the initial strut thickness t_{ref} (Eq.49). The curvature factors are scaled by the same factor (Eq.50) as it is assumed that the efficiency of the employed notch reduction approaches is not size-dependent.

$$r_1 = \gamma \cdot t \tag{47}$$

$$r_2 = \theta \cdot t \tag{48}$$

$$t_{graded} = f \cdot t_{ref} \tag{49}$$

$$r_{graded} = \gamma \cdot f \cdot t_{ref} \tag{50}$$

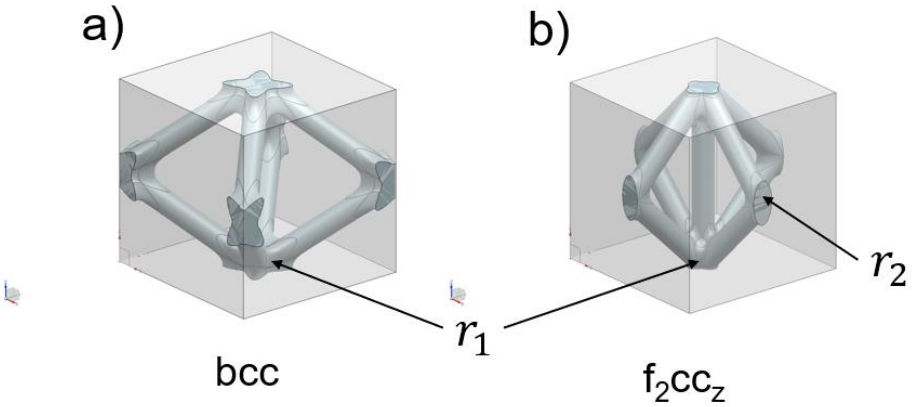

Figure 72: Curvature radius in ungraded configurations: bcc (a) and f_2cc_z (b).

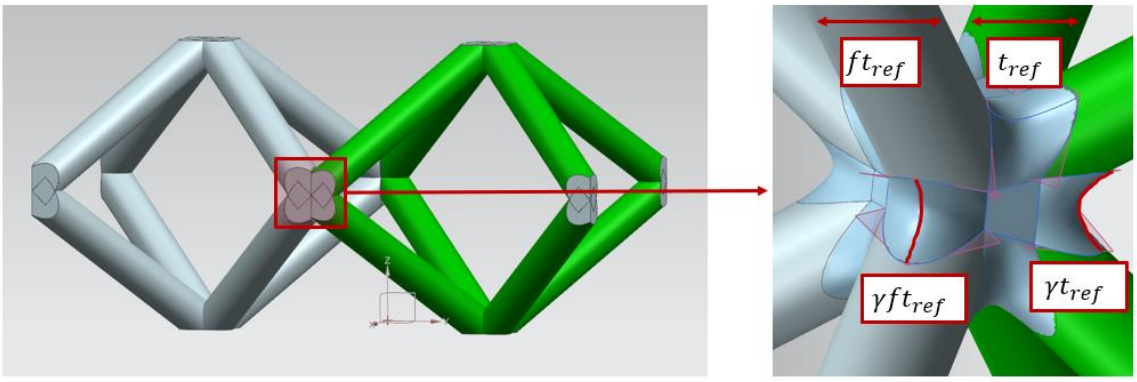

Figure 73: Curvature radius parametrisation in graded configurations.

The 2D curves of each aforementioned notch stress reduction methods are applied onto the nodal area of the unit cell. Depending on the unit cell configuration, the angle φ between each neighbouring strut varies. For the bcc unit cell, curves are constructed for the 109° and 70.53° angles while the f_2cc_z unit cell needs curves for the 45°, 60°, 90° and 120° angles as depicted in Figure 74.

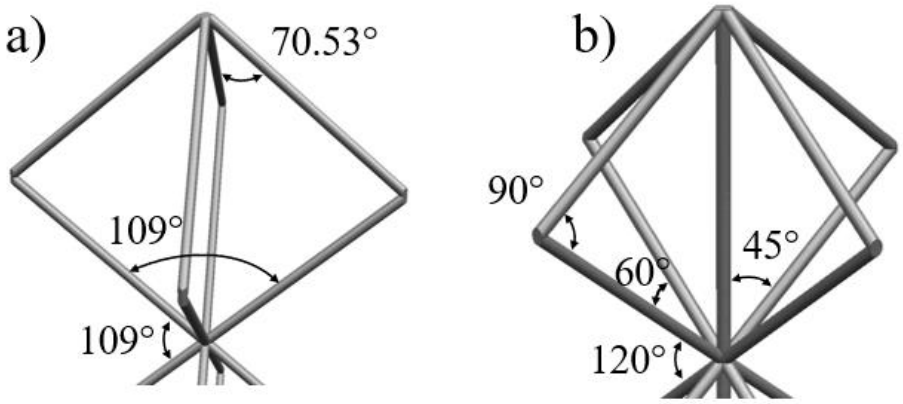

Figure 74: Angle selection for curve generation: bcc (a) & f_2cc_z (b).

In order to be able to apply both PCM and TTM to the investigated unit cells, the bisection method as introduced by Mattheck is employed [399]. This method, initially developed for the TTM, consists in halving the considered φ angle and in applying twice the notch stress reduction method starting from the angle bisector. The bisection method is applied for the PCM curve too by considering a maximum angle $\alpha_{max} = 90° - \varphi/2$, so that no inflection point is present at the intersection point of the PCM curve and the angle bisector. The PCM segment creation of both bcc and f_2cc_z cells is initiated at one of the curve's edges with a starting angle $\alpha_1 = 3°$, an angle identified due to its wide applicability [398]. Both TTM and PCM curves are then smoothed using cubic splines. A construction example for

$\varphi = 70.53°$ is shown in Figure 75 for all considered methods. Construction lines are represented as dashed curves and the points A and B stand for the starting and ending points of the curves generated by PCM and TTM, respectively.

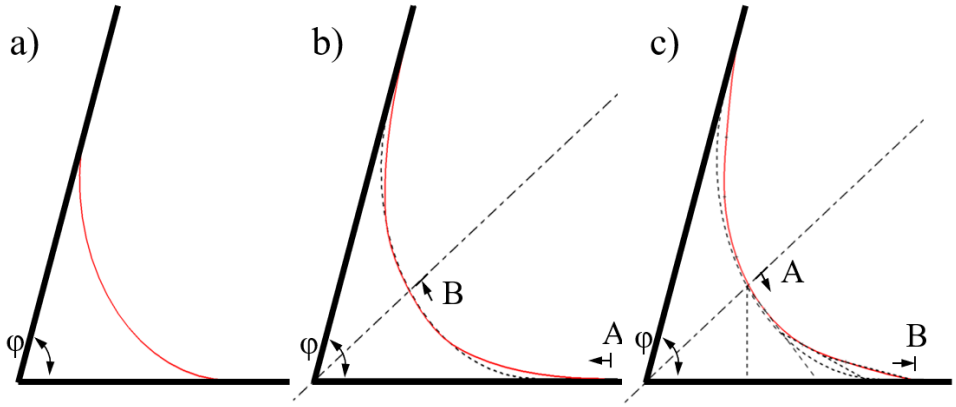

Figure 75: Bisection of φ angle: example of φ = 70.53° in a bcc unit cell for FRM (a), PCM (b) & TTM (c).

The transformation from the generated 2D curves into 3D solid is realised by constructing continuous surfaces using the curves and the unit cells themselves as boundary conditions (Figure 76, a and c). In the case of structural grading, an additional spline is used to account for the offset induced by thickness differences (Figure 69). The surfaces are then sewn together, creating an intermediate body for the nodal area Figure 77. Depending on the location of the interface, various bodies of different degree of complexity, i.e. number of manual splines to be created, are generated. Subsequently, these bodies are merged to surrounding lattice structures to obtain the new local design (Figure 76, b and d).

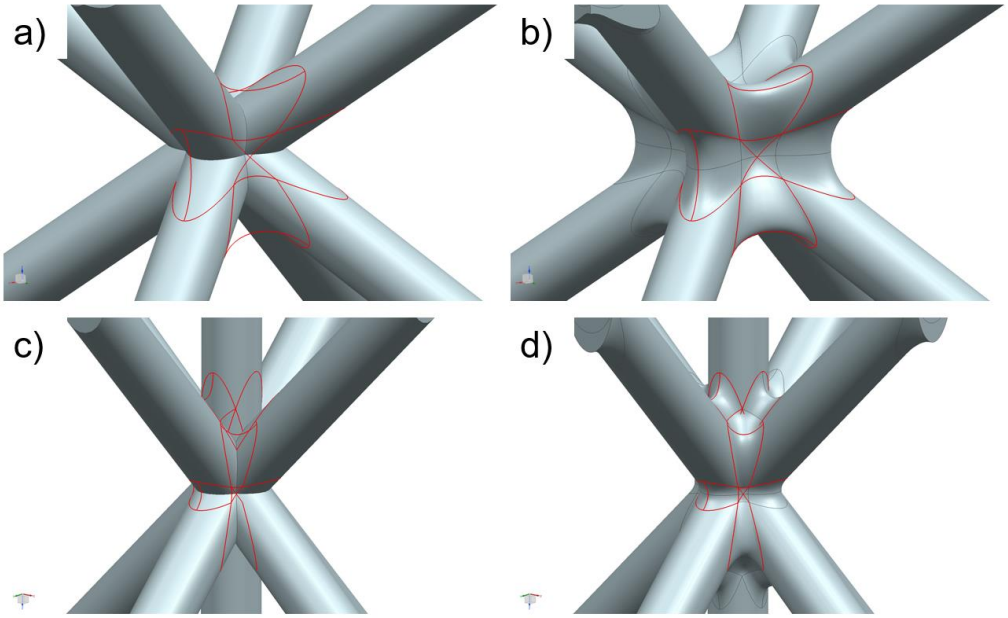

Figure 76: Construction procedure: from splines of (a) bcc & (c) f_2cc_z to RUC volumes (b) of bcc & (d) f_2cc_z.

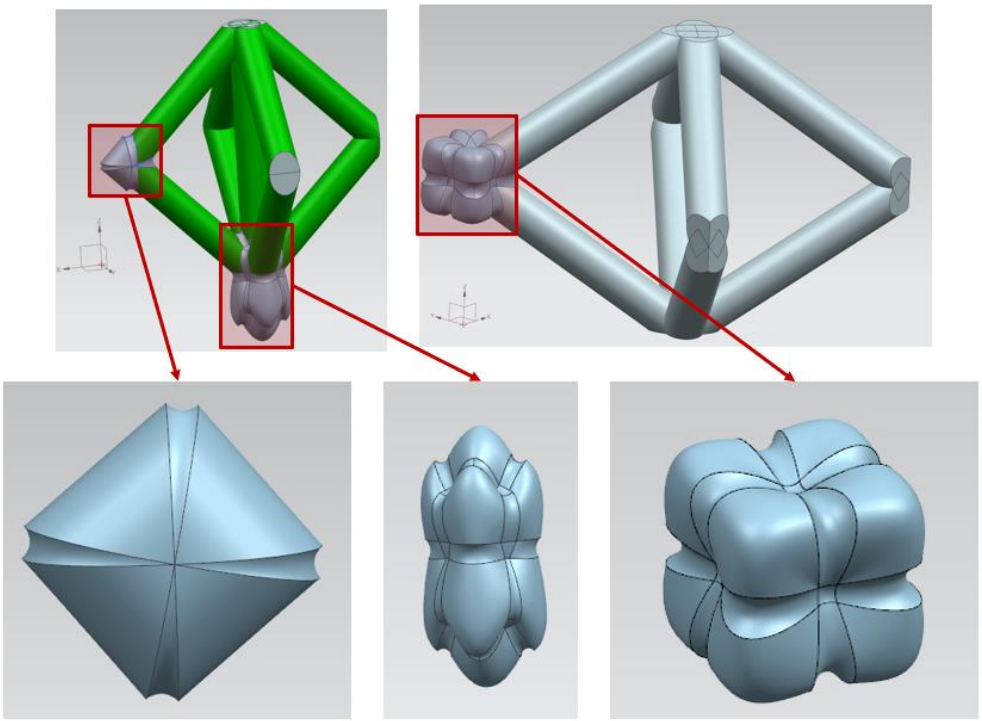

Figure 77: Generated nodal bodies: f_2cc_z (left) and bcc (right).

4.3.2 Results

The numerical investigation was performed with *ABAQUS CAE 2017*. The modelling approach covers the equivalent of a single RUC and depicted in Figure 78, Figure 79 and Figure 80, for ungraded bcc lattice structures, ungraded f_2cc_z lattice structures and structural grading scenarios, respectively. Ungraded configurations were modelled as described by section 3.1.1, Figure 27, for consistency with previous design studies (see sections 4.1 and 4.2). In the case of graded configurations, two halves of different grading factors are represented. Doing so guarantees the analysis of the nodal area without interferences from boundary conditions. Although different types of nodal areas are available for the stretching-dominated f_2cc_z RUC (Figure 77), investigating the nodal area in the vicinity of vertical struts is deemed sufficient to assess on the effectiveness of stress reduction methods in the case of structural grading. As its vertical strut is aligned with the loading direction, it is expected to carry almost exclusively the complete load, leaving inclined struts not involved into the structural load-bearing behaviour in the elastic range [296] (Figure 63 and Figure 68). Independently from the RUC's representation, a homogeneous unitary displacement at its upper cross section is applied while its lower cross section is clamped. The modelled lattice structures were meshed using solid tetrahedron elements with 10-nodes and quadratic interpolation with local and global seed sizes respectively assigned to the nodal area and the lattice struts. The local seed size of both modelled unit cells yields 0.02 mm while the global seed size of the bcc unit cell (0.05 mm) differs from the one of the f_2cc_z unit cell (0.03 mm).

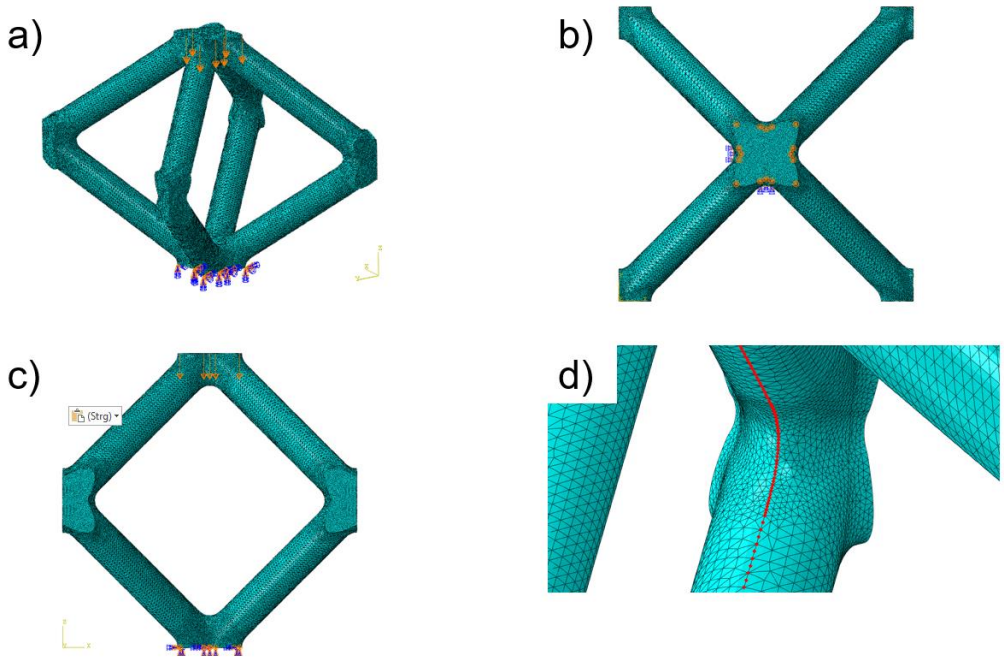

Figure 78: Modelling of bcc cells (ungraded): isometric view (a), top view (b), side view (c), nodal area (d).

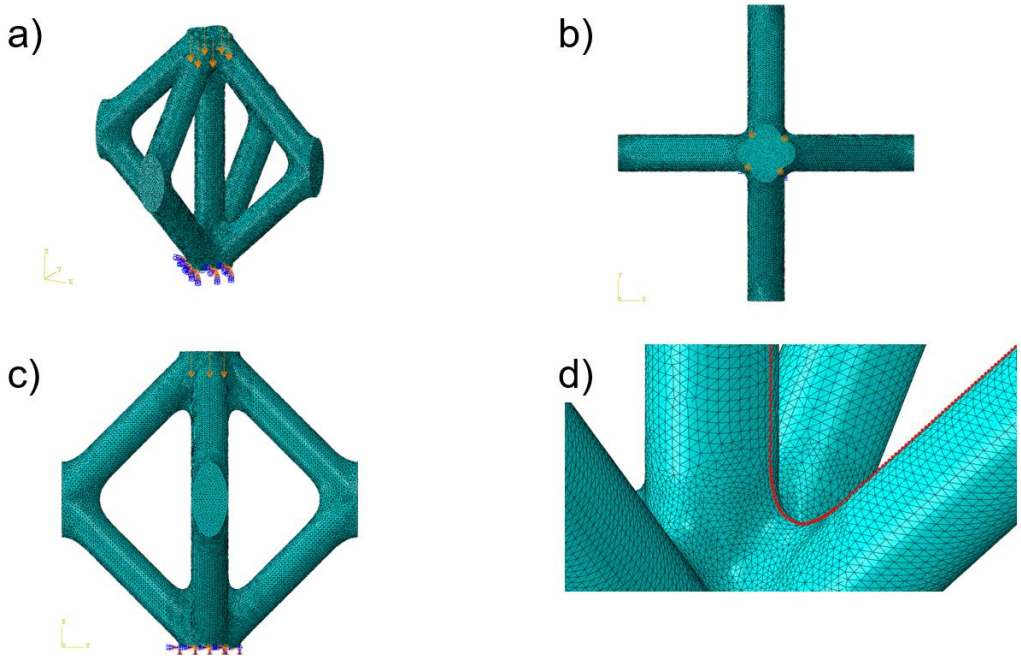

Figure 79: Modelling of f_2cc_z cells (ungraded): isometric view (a), top view (b), side view (c), nodal area (d).

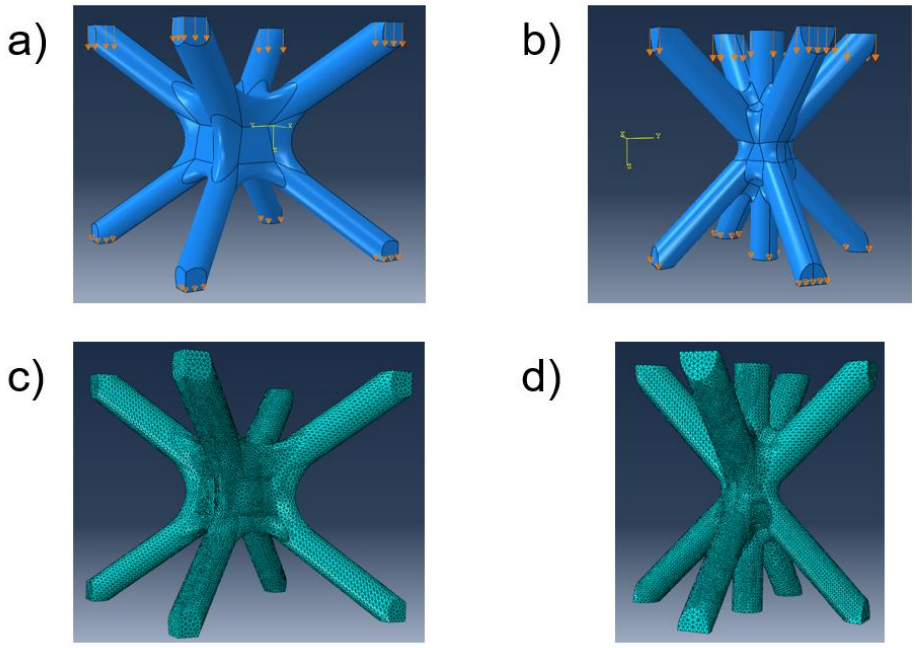

Figure 80: Modelling of graded cells in isometric view: boundary conditions for bcc (a) and f_2cc_z (b), meshing for bcc (c) and f_2cc_z (d).

Notch stresses are identified by means of stress concentration factors K_t. These factors are extracted from the von-Mises stress distribution within the unit cell along a given path. They can be expressed in the form given by Eq.51, where $\sigma_{VM,max}$ is the peak stress and $\sigma_{VM,mean}$ the mean stress of an undisturbed area [401] while $x = 0$ and $x = \lambda$ correspond to both extremity of the stress path. In order to allow a quantitative comparison between the employed notch stress reduction methods at similar equivalent curvature radius, the lightweight grade L (Eq.52) is introduced. It accounts for the supplementary mass involved as it is described by the inverse of the specific stress concentration factor and the relative density $\bar{\rho}$ of the considered unit cell. In order to establish a comparison with the initial, i.e. notched, design, the normalised lightweight grade L^* is introduced (Eq.53). Therefore, the optimal configuration reflects an improvement of the mechanical properties that outgrows the disadvantage brought by the additional mass due to a given curvature.

$$K_t = \frac{\sigma_{VM,max}}{\sigma_{VM,mean}} = \frac{max\big(\sigma(x)\big)}{\sigma_{VM,mean}}, x \,\epsilon [0, \lambda] \tag{51}$$

$$L = (K_t \times \bar{\rho})^{-1} \tag{52}$$

$$L^* = \frac{L(t, \gamma)}{L_{ref}\big(t_{ref}, \gamma = 0\,\big)} \tag{53}$$

Different load paths are considered for the assessment of $\sigma_{VM,mean}$ and $\sigma_{VM,max}$ because of the RUC dependency of the stress state of each investigated configuration. The selected

load path for bending-dominated bcc unit cells starts and ends at two strut halves respectively located at the upper and lower halves of the unit cell (Figure 81, a and c). Due to the homogeneous load distribution in the bcc RUC [296] (Figure 62 and Figure 67), the nominal $\sigma_{VM,mean}$ is assessed at the cross section corresponding to the minimum von-Mises stress within this load path. The load path of the ungraded stretching-dominated f_2cc_z configuration accounts for the aforementioned considerations on the load carrying role of the vertical strut. It therefore starts from the strut half of an inclined strut and ends at the middle point of the vertical strut of the unit cell (Figure 81, b) and $\sigma_{VM,mean}$ is extracted from the minimum mean nominal von-Mises stress of the vertical strut. As different grading scenarios are investigated, the graded f_2cc_z configuration takes several load paths into account. Two load paths similar to the ungraded f_2cc_z configuration are defined in both upper and lower halves of the model as the stress concentration is expected in the vicinity of one of the two vertical struts while the last load path is defined similarly to the ungraded bcc configuration to assess for potential load redistribution (Figure 81, d).

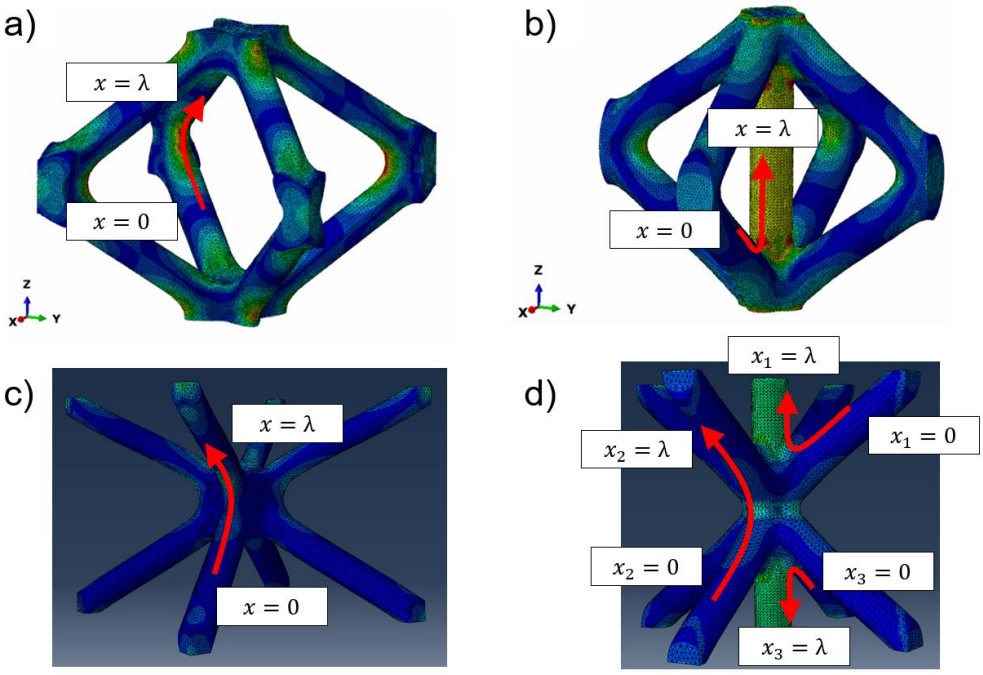

Figure 81: Load path for stress concentration factor assessment: ungraded configurations of bcc (a) and f_2cc_z (b), graded configurations of bcc (c) and f_2cc_z (d).

Ungraded configurations

Figure 82 shows the results obtained for the numerical analysis of bcc cells of 100 μm and 370 μm diameter. The corresponding curvature factors and corresponding lightweight grades are reported in Table 5. It can be noticed that for the 100 μm diameter cells, the optimal lightweight grade was obtained for PCM and outperforms FRM and TTM by 17 % and 12 % respectively, whereas FRM outperforms PCM and TTM by 7 % and 10 %, respectively, at 370 μm.

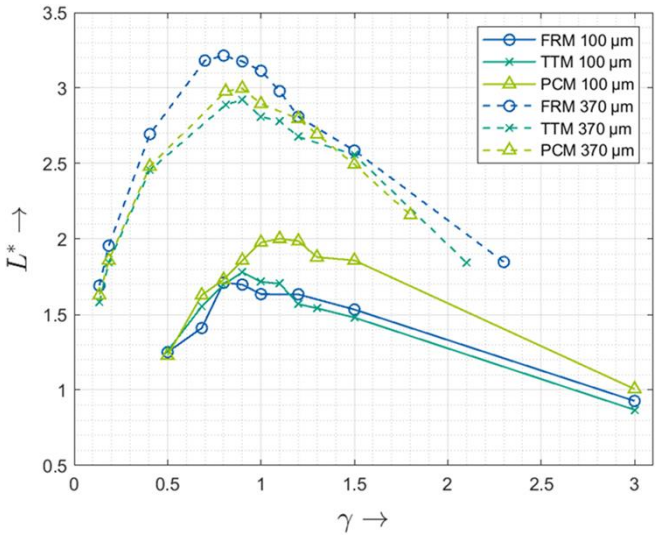

Figure 82: Lightweight grade as function of the curvature radius (bcc).

Table 5: Optimal configuration (R_2) of bcc.

t	FRM		PCM		TTM	
[μm]	γ	L^*	γ	L^*	γ	L^*
100	0.8	1.71	1.1	2.00	0.9	1.78
370	0.8	3.22	0.9	3.00	0.9	2.92

Figure 83 and Figure 84 and display different stress concentration factors and their variation for the selected notch stress reduction approaches exemplarily for $t = 370$ µm, respectively. The initial notched design is compared to, on the one hand, a minimal equivalent curvature radius R_1 ($\gamma = 0.135$) and, on the other hand, the optimal equivalent curvature radius identified in Table 5 above. Figure 83 highlights that the different K_t rapidly decrease from an initial value of $K_t = 17.7$ to reach an asymsptotic value of $K_t = 5$ from $\gamma = 0.7$ on. From Figure 84 it can be noticed that the peak stress occurs for $x/\lambda = 0.5$, which can be expected since the nodal area is located in the middle of the normalised selected path. A decrease of the peak stress is already observed for the small curvature radius R_1, while R_2 offers a more drastic stress reduction with a smooth load redistribution (Figure 85). FRM offers the most homogeneous distribution.

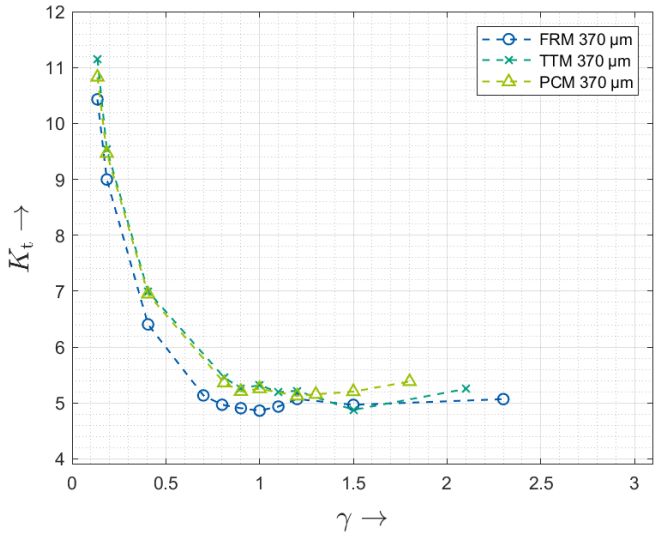

Figure 83: Stress concentration factor as function of the curvature radius (bcc).

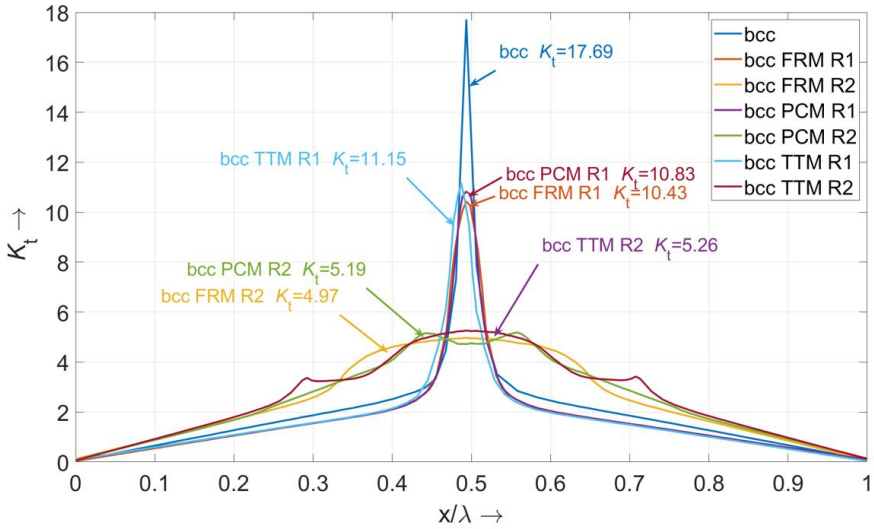

Figure 84: Stress concentration distribution (bcc).

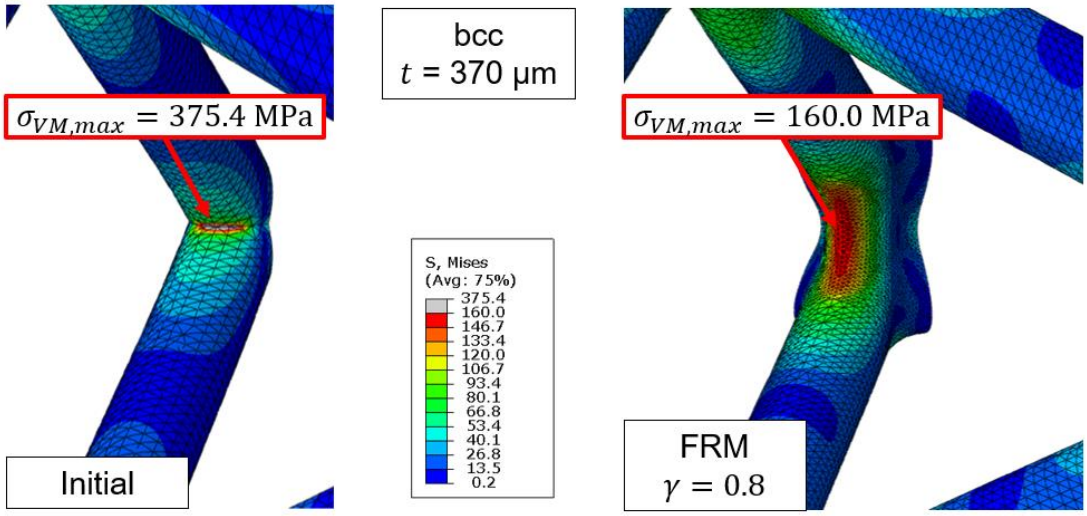

Figure 85 : Stress plots for initial (left) and optimal bcc configuration (right).

In the case of the f_2cc_z unit cell, two radii have to be varied (Figure 72). During the numerical investigation, it has been noticed that the stress concentration is redistributed to diagonal struts for low values of θ. Figure 86 demonstrates that the stress peak at the junction of diagonal struts increases drastically as γ gets larger, leading to a plateau of K_t at $\gamma = 0.3$ or above. Figure 87 illustrates this load redistribution with examples for $\theta = 0.135$ and $\theta = 0.5$. The origin of the plateau lies in the fact that the selected load path does not cover the junction between diagonal struts (Figure 81).

To prevent the effect of stress redistribution, $\theta = 0.5$ is kept constant for further investigations. This value may not lead to an optimal stress concentration at the junction of diagonal struts, but it offers a sufficient load reduction so that the nominal stress is hardly affected by different values of θ. The maximum difference in nominal stress among the different models at $\gamma = 0.5$ is 0.6 %. Thus, it can be ensured that the stress concentration always occurs at junctions involving vertical struts.

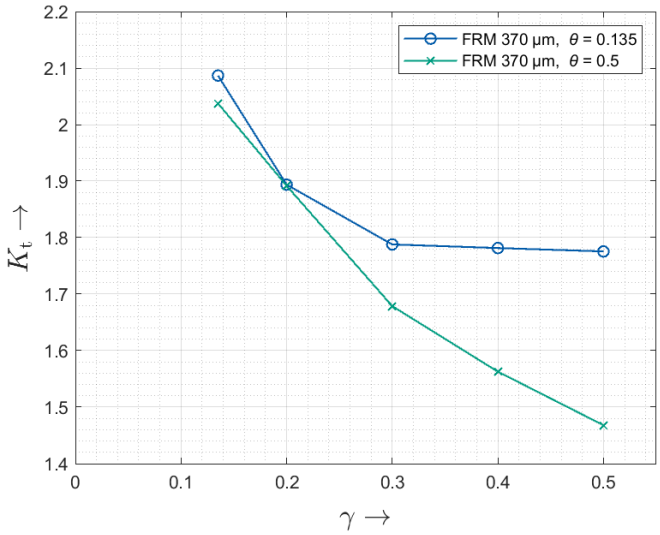

Figure 86: Stress concentration factors variation (f_2cc_z).

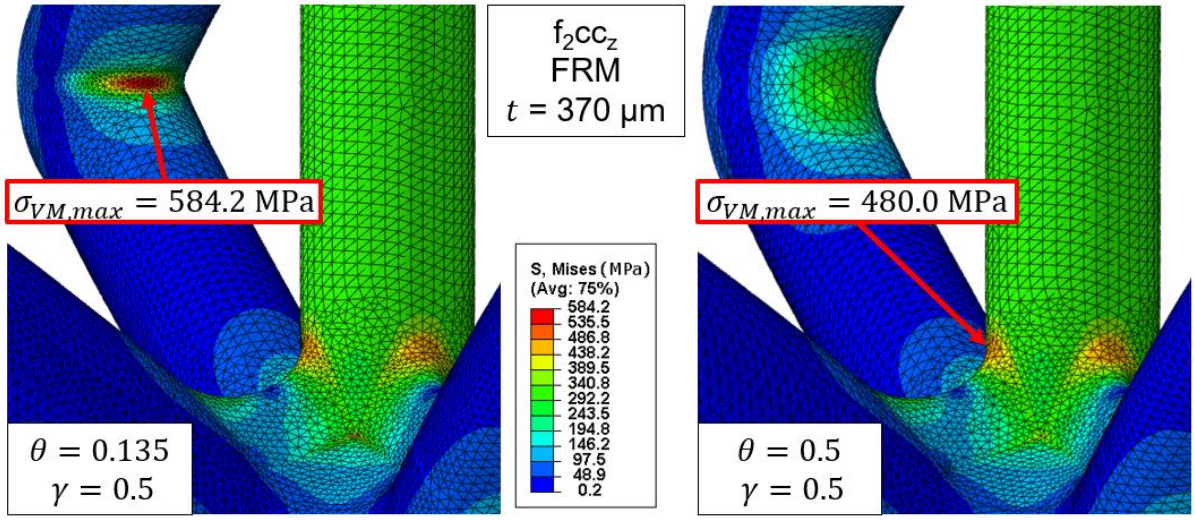

Figure 87: Stress redistribution for θ variation (f_2cc_z).

Figure 88 shows the results obtained for the numerical analysis of bcc cells of 100 μm and 370 μm diameter. The corresponding curvature radii and corresponding lightweight grades are reported in Table 6. It can be noticed that PCM outperforms FRM and TTM for both strut diameters, reducing specific notch stresses by about 16 % for both approaches at 100 μm, and being better by 20 % and 10 %, respectively, at 370 μm.

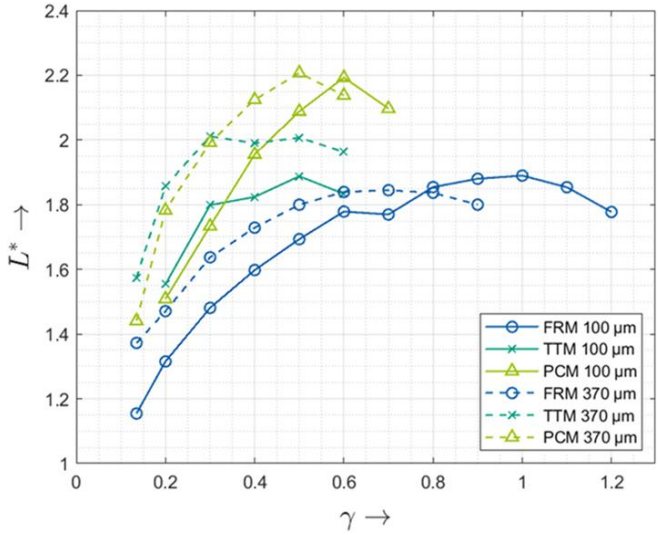

Figure 88: Lightweight grade as function of the curvature radius (f_2cc_z).

Table 6: Optimal configuration (R_2) of f_2cc_z.

t	FRM		PCM		TTM	
[μm]	γ	L^*	γ	L^*	γ	L^*
100	1.0	1.89	0.5	2.19	0.6	1.89
370	0.6	1.84	0.5	2.21	0.3	2.01

Figure 89 and Figure 90 display different stress concentration factors and their variation for the selected notch stress reduction approaches exemplarily for $t = 370$ µm. The maximum stress concentration factor K_t for optimal configuration is shown in Table 6 above. Contrary to the bcc unit cell, only the optimal equivalent curvature radius of each notch stress reduction method is plotted in Figure 90 for better readability. While the decrease of K_t was rapid for bcc (Figure 83), the employed methods yield different efficiency in reducing the initial value of $K_t = 2.25$ (Figure 89). Although TTM tends more rapidly to converge to an asymptote at about $K_t = 1.3$ from $\gamma = 0.3$, it offers less effective stress reduction than PCM (asymptote by $K_t = 1.2$ for $\gamma = 0.5$). FRM tends to converge to a value of $K_t = 1.3$ as well but, according to Figure 88, the gain in mass will surpass the benefit of stress reduction. Figure 90 shows that the initial f_2cc_z peak stress is located at $x/\lambda = \frac{1}{2} \cdot \arccos(45°)$, which is due to the selected load path (Figure 81). It can be noticed that the stress concentration is not only reduced but the peak stress is redistributed into two separate smaller peak stresses (Figure 91).

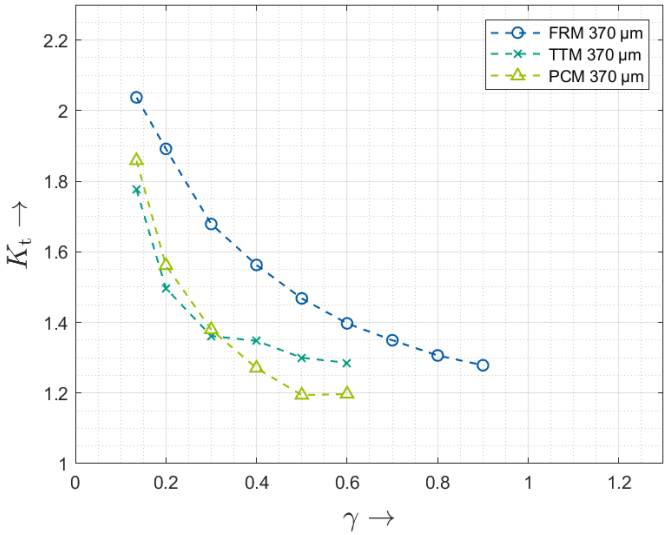

Figure 89: Stress concentration factor as function of the curvature radius (f_2cc_z).

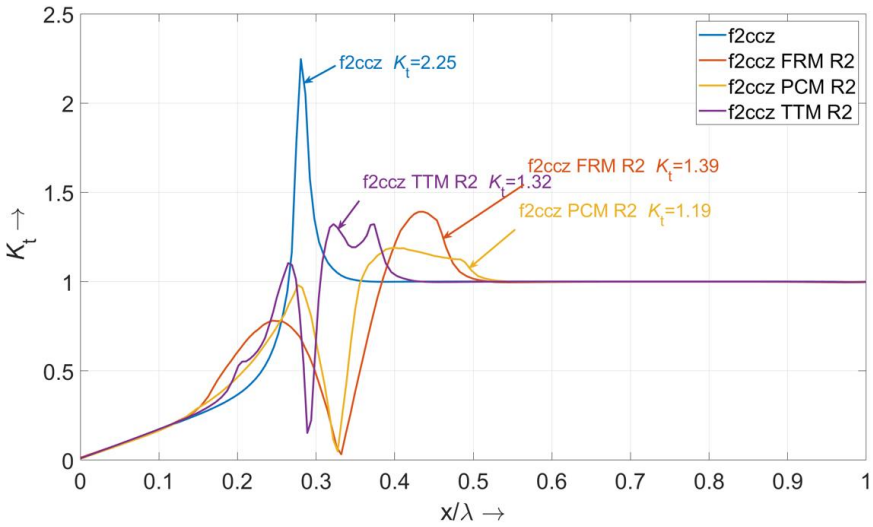

Figure 90: Stress concentration distribution (f_2cc_z).

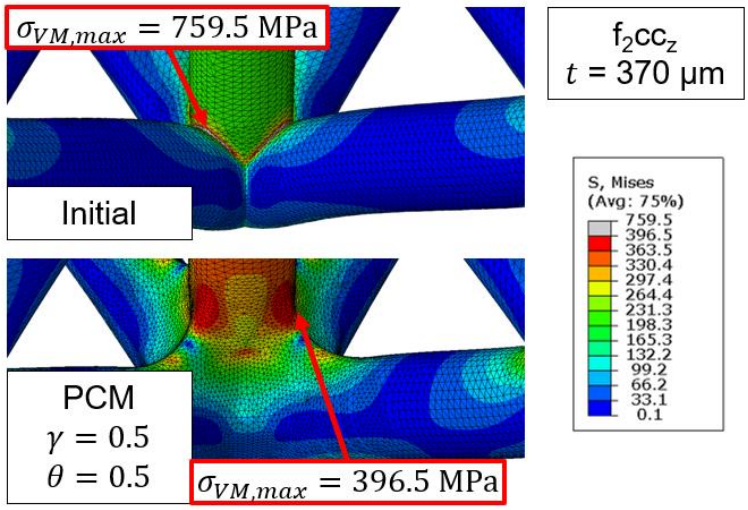

Figure 91: Stress plots for initial (top) and optimal f_2cc_z configuration (bottom).

Graded configurations

Issues have been encountered during the preparation of the numerical investigation of graded lattice structures. Convergence issues occurred while generating the CAD models of the different configurations. These convergence issues stem from nodal shift or incomplete splines (Figure 92, a) and led to connection errors, modifying the sewn surfaces. These inaccuracies in the generated surfaces resulted in defects such as gaps (Figure 92, b) or hollow structures (Figure 92, c). In the best cases, workaround operations such as a modifying slightly the curvature radius, correcting nodes manually, or implementing transition nodes could bypass these issues. In the worst cases, unification operations of nodal bodies (Figure 77) and lattice structures led to defective bodies (Figure 92, d & e). This was the case for both bcc TTM and f_2cc_z PCM configurations, for which systematic errors could not solved. Furthermore, in the case of successful workaround, meshing issues have been encountered too. These issues demonstrate the limits of explicit modelling. They are due to the high number of manual splines in a small area. In comparison to the investigation of ungraded configurations above, a higher number of manual splines are involved for the parametrisation of the CAD model. For the only nodal area shown in Figure 81, 6 manual splines are required by the graded model while only 2 splines are required for the ungraded one for bcc RUCs as symmetry is exploited through patterning or mirroring operations. The f_2cc_z RUCs show a higher degree of complexity with 5 and 8 splines required for both ungraded and graded models, respectively. In addition to that come the corrective splines accounting for the differences in thicknesses (see section 4.3.1).

Despite the aforementioned issues and the resulting restricted number of possible investigations, the results generated are sufficient to identify trends and assess on design rules. The investigated configurations and the related results are listed in appendix A. The initial diameter of 370 μm is varied from 300 μm to 500 μm, which corresponds to grading factors the range of order of the design developed in section 4.1 (see also section 5.1 and 6.3). Only the RUC located in the upper half of the model is varied, as shown in Figure 80. The curvature radius range is based on the optimal ranges of the modellable configurations of each RUC. Therefore, it was varied from 0.25 to 1.50 for bcc, corresponding to the PCM optimal range PCM (Figure 82) and from 0.07 to 0.41 for f_2cc_z, standing for the best TTM results (Figure 88). In order to reduce the modelling efforts, the same curvature radius has been considered for all angles in the vicinity of the considered nodal area (Figure 74). Furthermore, the curvature radius is assigned the same grading factor f as the strut diameter as mentioned in section 4.3.1.

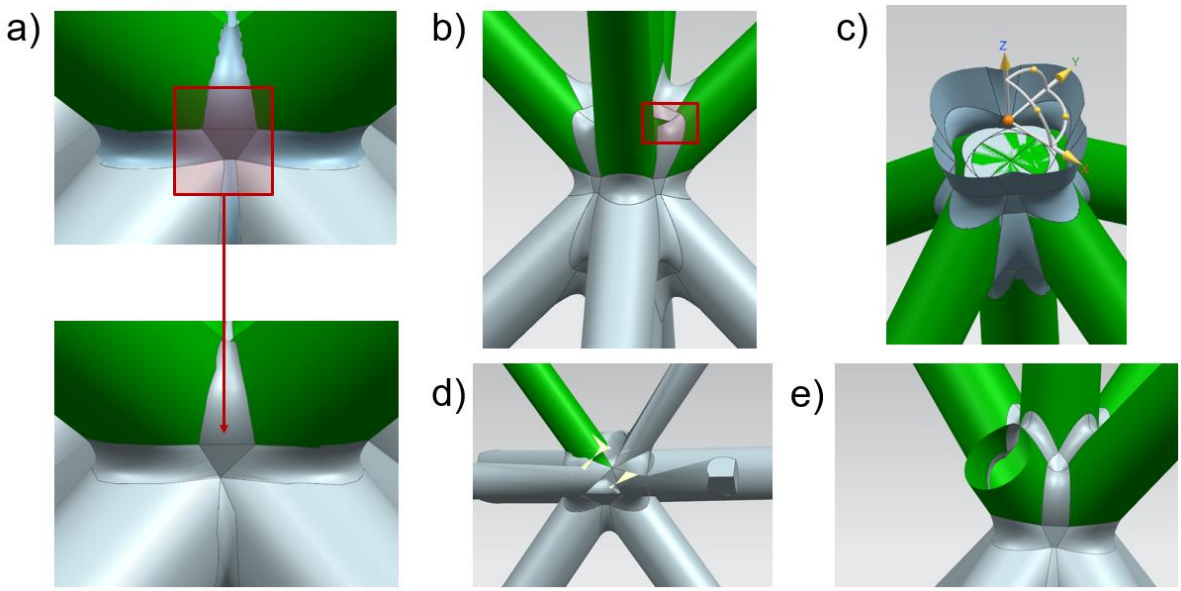

Figure 92: Modelling issues encountered: nodal shift and deterioration of the surface (a), gap (b), hollow body (c), defects (d, e).

The observations made during the investigation of bcc configurations are made first. In bcc lattice structures, the mean stress $\sigma_{VM,mean}$ is proportional to both grading factor f and curvature radius γ. The higher standard deviations in mean stress were obtained for a variation of the curvature radius, which means that it is more impacting than grading as far as the general stress state of the structure is concerned. Bcc lattice structures are more solicited at increased curvature radius as it offers more material aligned to the loading direction, enabling a smoother load distribution. Similar trends are visible for the peak stress $\sigma_{VM,max}$ located at the strut's junction. It is proportional to both f and γ too with exception of the smallest investigated γ of FRM, which tends to be similar to the initial unnotched design. A variation of γ leads to lower deviation in $\sigma_{VM,max}$ than a variation of f. This means that the grading factor influences the notch stress level, whereas the curvature radius can be considered as a correction factor to decrease it. The stress concentration factors K_t show an almost symmetrical result distribution among the investigated configurations. Therefore, the notch reduction methods have similar effectiveness regardless from the grading direction, i.e. thinning or thickening, meaning that only the grading factors can be regarded. This was expected as linear static calculations are employed to investigate on symmetrical structures. The best results were obtained for ungraded configurations ($f = 1.00$) and moderate grading factors ($f = 0.90, 1.10$) while higher grading factors create higher deviations. K_t is inverse proportional to γ. The best results were obtained from $\gamma = 0.7$ on. The normalised lightweight grade L^* shows similar trends with the best results obtained for ungraded configurations and moderately thinner struts. While the former implies that a structural grading is not always the best option, the latter can be explained by the comparable efficiency of the stress reduction method (K_t) for lighter structures. Optimal values of L^* were obtained for values of γ between 0.7 and 1.1 These

results are in line with the ones of the previous investigations and highlight the comparability between graded and ungraded configurations. Furthermore, PCM delivers results than FRM for all investigated bcc configurations, even for ungraded cases. Differences in the representation of the RUC could explain that this result is not completely in line with the previous investigation.

In f_2cc_z lattice structures, load path 1 (on the graded side) and load path 3 (on the ungraded side) are comparable to each other, as can be expected from the modelling philosophy (Figure 81). Both mean stress $\sigma_{VM,mean}$ and peak stress $\sigma_{VM,max}$ correlate the grading factor f. The thinner side will always experience the highest stresses as similar loads are applied for reduced cross-sections. Both load paths yield a proportional correlation with the curvature radius γ. As for bcc configurations, the smallest investigated γ tends to reflect the stress state in the initial notched design and, thus, displays higher $\sigma_{VM,max}$. A variation of γ leads to lower deviation in $\sigma_{VM,mean}$ and $\sigma_{VM,max}$ than a variation of f. This means that the grading factor influences the notch stress level, whereas the curvature radius can be considered as a correction factor to decrease it. It has to be highlighted that a shift of the peak stress towards inclined struts has been observed for configurations of low γ. This hints at a load redistribution similar to the ungraded case (Figure 86, Figure 87). Notch stress reduction methods are not in these areas for comparable load introduction (see Figure 80 and Figure 81) and, thus, the stress peaks in these areas are ignored for this analysis. K_t is inverse proportional to γ. The best results were obtained from $\gamma = 0.20$ on, independently from grading factors. The best results for the normalised lightweight grade L^* were obtained for ungraded configurations ($f = 1.00$) and thinner struts ($f < 1.00$). Similar to bcc, this result is logical. For TTM, the optimal values of L^* were obtained for γ between 0.20 and 0.41 while FRM results imply that the optimal lightweight grade is not reached for the investigated interval. TTM delivers results than FRM for all investigated f_2cc_z configurations. These results are in line with the one of the previous investigations and highlight the comparability between graded and ungraded configurations.

The load path 2 in f_2cc_z configurations deals with the 120° angle of the considered nodal area (Figure 74) and delivers further interesting results. Without surprise, $\sigma_{VM,mean}$ and $\sigma_{VM,max}$ are proportional to f and γ. $\sigma_{VM,mean}$ is always lower than the mean stress in the vertical struts (other load paths) due to the relationships between respective cross-sections. Although $\sigma_{VM,max}$ is relatively uncritical for all graded configurations, it is interesting to notice that ungraded configurations yield peak stresses comparable to other load paths for equivalent curvature radius. Similar to the discussion above, load redistribution scenarios explain this statement. K_t is inverse proportional to γ. The best results were obtained from $\gamma = 0.41$ on. Similar trends are observed for L^*. This means that the optimal lightweight grade is not reached for the investigated interval. FRM yields better results than TTM for all investigated configurations, which hints at different local design solutions. Moreover, the most relevant case, namely the ungraded configuration, leads to sub-optimal values for both criteria. This means that a separate curvature radius shall be assigned, similar to Figure 72. Considering that the load path is located in the vicinity of bending-dominated

struts, into which stress is redirected (see above), and that the angle between struts is in the same range of order as the one of the bcc RUC (Figure 74), it can be concluded that the design solution is similar to the ungraded bcc configurations. This hypothesis is further supported by the trend observed for L^* Table 5, as optimum values are obtained for curvature radius of about $\gamma = 0.8$.

4.3.3 Discussion

The results demonstrate the potential of the selected notch reduction methods. As the stress is more homogenously distributed for increased sizes of fillet curvature, the ability of the specimen to resist deformation is increased too. However, the fillet curvature shall not be indefinitely increased. Firstly, the stress reduction shall be weighed with the additional mass involved by a radius. Secondly, newly formed sharp edges may occur after load redistribution on the fillet perpendicular to the notches increase stress concentration (Figure 91). These new stress concentrations could eventually outgrow the intended notch stress reduction at the fillet and render the new design obsolete.

It was discovered that the load-bearing nature of the struts influences the effectiveness of notch reduction methods and, thus, the optimal shape of nodal areas. Both PCM and TTM are more effective in the vicinity of stretch dominated struts. This can be explained by the fact that these methods were developed for stepped bars [400]. These two notch reduction methods are particularly effective for lattice structures with extremely thin struts since they can be idealised as perfect truss structures with reduced nodal areas. The theoretically better performance of PCM and TTM methods compared to FRM for f2ccz and bcc at small scale can be explained through the approach they follow. TTM being a simplified graphical approach of PCM, it will always result in at most equivalent stress concentration reduction and therefore lead to at best similar mechanical gain in performance. FRM is more effective for nodal areas surrounded by bending-dominated struts. This can be explained by the homogeneous stress distribution they experience [296] as they are not aligned with the load direction and, thus, by more complex loading in the nodal area.

From the observed trends, design rules can be extracted. In order to separate different use cases, the relationship between then loading direction and the bisector angle (Figure 75) is used. Due to its circular shape, FRM is adapted to symmetrical configurations. These configurations are found for nodal areas directly surrounded by bending-dominated struts (bcc, f_2cc_z load path 2) of ungraded lattice structures. In this case, the structure is considered as locally perfectly bending-dominated since the bisector angle is perpendicular to the loading direction. In the case of a structural grading, the bisector angle loses its perpendicularity with respect to the loading direction and FRM is less effective than PCM/TTM. In the practical example of f_2cc_z load path 2, it can be stated that a broader angle between struts as well as a high distance between the load path and the strut's inflexion point help FRM being a good contender to PCM/TTM even in the case of structural grading. In the context of lightweight design, curvature radius ranging between three

quarter to one full strut thickness are advised. In other cases, employing PCM/TTM is advised. These methods are effective for sharp angles in the vicinity of the loading direction, which is a typical design feature of stretching-dominated truss-based lattice structures (see section 2.3.3). The relationship between the loading direction and the bisector angle results from the asymmetrical loading and explains the need for elliptical or prismatic shapes to reduce notch stresses. Recommended values of curvature radius for lightweight design range from one fourth to one half of strut thickness. Independently from the chosen notch reduction approach, the increase in effective mean stress within the lattice structure shall be considered. A structural grading of low grading factor is preferred to keep comparable mean and notch stresses. As demonstrated in section 4.1, sudden drops in stiffness are not beneficial for structurally graded lattice designs. In the framework of this investigation, grading factors of 10 % ensure smooth load stress distribution.

These design rules demonstrate that it is possible to avoid case-specific topology optimisation solutions. As they are strut type and angle dependent and not RUC specific, the transferability potential to other truss-based lattice structures is deemed extremely high. Furthermore, the presented results show that analysing ungraded configurations is sufficient to identify general design principles as they are representative for graded configurations too. This statement regards only the most critical stresses but is worth further investigations because of its potential for rapid dimensioning. This would involve investigating other angles (Figure 74) as other areas could become critical in the case of load redistribution. Influencing the load distribution highlights the potential of such local approaches for load path monitoring as well. According to the design rules discussed above, it is expected that FRM works better for the other angles present in bcc (70.5°) and f_2cc_z (60° and 90°) in the ungraded case since all surrounding struts are bending-dominated.

Further design rules may be identified by means of shape or local topology optimisation. In this case, the methodology developed in section 4.2 can be employed. Extracting structural elements, design features or graphical approaches from optimisation results is in line with the philosophy of the literature reported at the beginning of section 4.3.

Another important topic is to solve modelling issues and to reduce the modelling efforts. In the case of explicit modelling, constantly graded RUCs are the most promising option since they can offer a constant diameter in the vicinity of the nodal area and, thus, reduce the number of specific splines to be created. Mathematical approaches and level set functions are the best alternative. The complex curvature involved by notch reduction methods make truss-based lattice structures locally similar to plate- or surface-based RUCs, for which explicit modelling is not viable anymore. This explains the encountered modelling issues throughout this investigation.

5 Realisation

This chapter deals with the reliable additive manufacturing of design features developed in chapter 4. As highlighted in section 2.4.2, the lack of manufacturing rules is explained by fragmented literature findings that are not directly transferable due to machine and process dependencies. The manufacturability of lattice structures at sub-millimetre range is explored in section 5.1 in order to identify the smallest reliably manufacturable strut diameters with a commercial LB-PBF system and AlSi10Mg powder and, thus, to avoid high samples that may be involved in the special example of structural grading (see section 4.1). Section 5.2 deals with the realisation of the transition between bulk part and lattice structure. Integral and modular design solutions are explored.

5.1 Reliable manufacturing of submillimetre graded lattice structures

The manufacturing approaches described in section 2.1.2 are investigated. Firstly, the basic exposure strategies depicted in Figure 5 are explored, namely the point (section 5.1.1), the contour (section 5.1.2) and the hatch (section 5.1.3) exposure strategies. Secondly, combined exposure strategies are investigated in section 5.1.4 and are compared to the standard exposure combination. Finally, the limitations of each proposed manufacturing approaches are discussed. For the sake of brevity, only the most relevant data highlighting systematic trends are reported. Corresponding data are listed in tables of appendix E.

Each exposure strategy investigation is divided into two main parts. In the first step, the manufacturability of vertical single struts is investigated for as-designed diameters below 1 mm. A strut height h_{strut} of 5 mm representative of the RUC cell size a was chosen. This value aligns with the manufacturability ranges of lattice structures as found in literature (see section 2.3.6) for the investigated aspect ratios (see section 3.1.1). It covers the lowest bound of 500 μm for $AR = 10$ and corresponds to 1 mm strut thickness for $AR = 5$ (see Eq.5). Each exposure strategy and corresponding parameter combination were held constant and three samples were considered. In the second step, lattice structures are manufactured with selected parameters. Equivalent diameter and roundness values of both single struts and lattice structures are estimated by means of horizontal grinding pictures (Figure 34, d & e). In the case of f_2cc_z lattice structures, only the quality of vertical struts is analysed as they are the load-bearing feature of the corresponding RUC (see chapter 4). The results obtained are compared to each other to assess the representativity of struts for lattice structures. Please refer to section 3.3 and to section 3.4.3 for details on the manufacturing and the determination of diameter and roundness, respectively.

While the point exposure has its specific process window [79], other combinations are based on comparable laser power P and laser scanning speed v. In order to ensure good

manufacturability, the process window established by Großmann et al. [76] is taken as basis for the variation of both hatch and contour exposure strategies. The investigated combinations of P and v are shown in Figure 93. Following parameters are held constant: a laser beam diameter d_L of 80 μm, a layer thickness l_s of 30 μm, a build platform temperature T_{bp} of 125°C and an internal differential pressure for inert gas flow of 0.55 mbar.

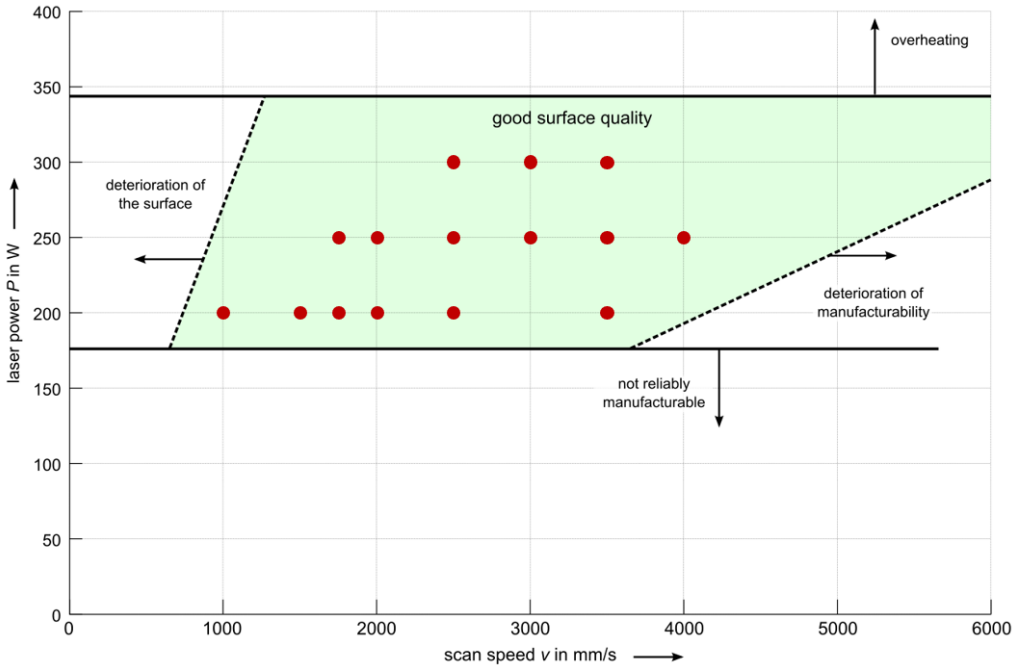

Figure 93: Investigated laser power and scanning speed for hatch and contour exposure variations. Recompiled from [76].

5.1.1 Point exposure strategy

The realisation of single struts by means of the point exposure strategy requires specific pre-processing operations because this exposure strategy is not available as standard exposure strategy in the employed version of the *EOS PRINT* software. In order to be assigned a point exposure, a part has to be defined as support structure. To do so, the part shall not be designed as closed volume but as a slender shell body, i.e. with a high ratio between its width $b_{p,CAD}$ and length $l_{p,CAD}$, along which the scanning path goes as shown in Figure 94. Moreover, the STL file name has to contain the standard file name ending of a support part. In the case of another file name, the standard exposure strategy is automatically assigned and the contour exposure is applied due to the dimensions of the designed shell part. Furthermore, it has been experienced that the contour exposure strategy was automatically assigned to models of shell width of 100 μm too. In this case, it is not possible to assign the support exposure strategy back.

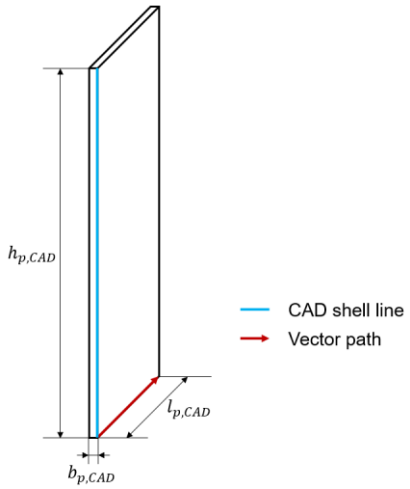

Figure 94: CAD modelling for the point exposure strategy.

In the framework of this investigation $b_{p,CAD}$ was set to 5 μm and $l_{p,CAD}$ ranged from 125 μm to 300 μm. Both laser power and scanning speed values were extracted from the data issued from the investigation on the point exposure performed by Großmann et al. [79]. These values were selected so that the estimated melt pool width is in the same range of order of the shell length to obtain high roundness. Therefore, different line energy densities E_l (Eq.3) were considered for varying $l_{p,CAD}$.

Figure 95 shows exemplarily the quality of single struts obtained by the point exposure strategy for the investigated scanning lengths. While the shape of the thinnest struts hints at the direction of the scanning vector, the influence of particle aggregation is visible. Since the script employed for the analysis of grinding pictures is based on surface equivalent diameters (see section 3.4.3), data issued from the investigation from Großmann et al. [79] are reported in Figure 96 as well. These are issued from manual analyses at light microscope that ignored aggregated particles.

In both analyses, the obtained strut thicknesses follow similar trends, ranging between 170 μm and 300 μm, to match similar values at higher $l_{p,CAD}$. This means that the influence of particle aggregation on the results obtained by the employed script is negligible from thicknesses of about 280 μm on. The high standard deviations in the results of grinding pictures at low $l_{p,CAD}$ (AppendixTable E-1) highlight the particle aggregation phenomenon while the low standard deviations obtained for higher $l_{p,CAD}$ hint at its systematic nature. This statement is further supported by the different circularity values obtained in the corresponding ranges. The average circularity obtained for $l_{p,CAD} = 300$ μm is 0.53, with a maximum value of 0.70 emphasising the excellent roundness obtained when the particle aggregation is negligible, as it can be interpreted from Figure 95. According to EOS data, the AlSi10Mg powder is made of particles of diameter from 25 μm to 70 μm [375]. It can be deduced that the employed script yields accurate results from this range on and that the targeted strut thickness shall be at least 4 times higher than the particle size of the employed powder for good accuracy.

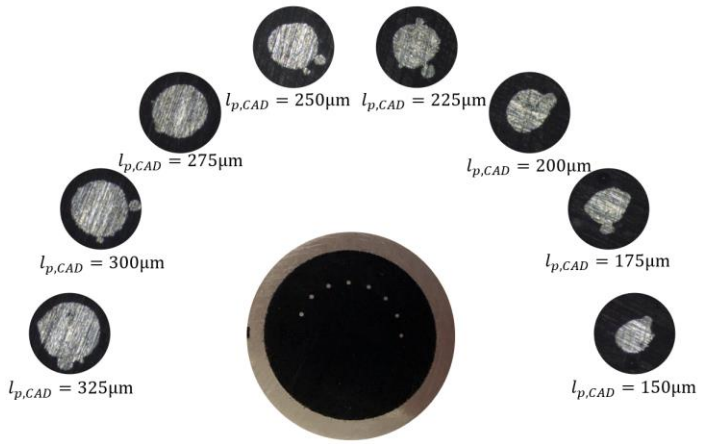

Figure 95: Single struts cross-sections (point exposure, single struts).

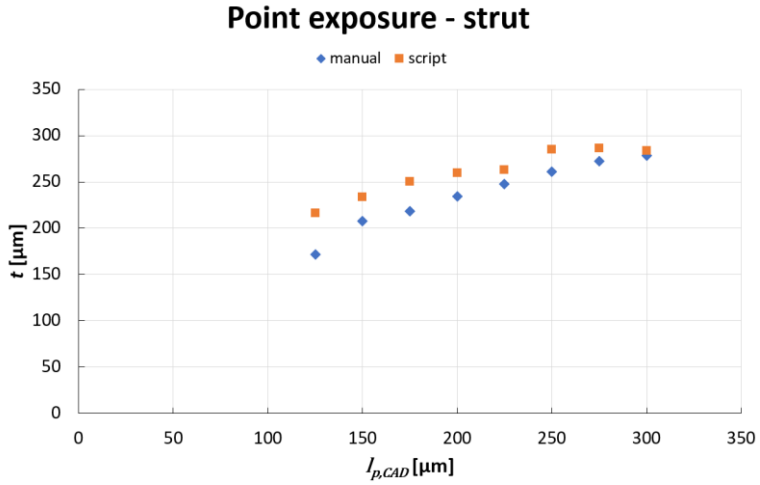

Figure 96: Resulting strut diameters (point exposure, single struts).

Lattice structures made of 3x3x3 RUCs of a cell width of 3 mm were printed as a proof of manufacturability for values of $l_{p,CAD}$ starting from 175 μm. The only lattice structures without defects were obtained for $l_{p,CAD} = 300$ μm. Furthermore, it has to be mentioned that only f_2cc_z lattice structures could be printed as issues were encountered while importing the STL files for the bcc lattice structures into the *EOS PRINT* software, which could not read them. It is here supposed that the support parts are meant to have at least one vertical feature. Therefore, deeper investigations concerning the point exposure strategy were not performed.

5.1.2 Contour exposure strategy

The contour exposure strategy consists in designing a smaller strut diameter than the target one (see Figure 5). For one given manufacturing layer, the required input parameters for the contour strategy lead to a single diameter. The extremities of the diameter formed by the scanning path of the contour exposure can be expressed as an *equivalent hatch*

distance $d_{h,c}$ (Eq.54). As mentioned in section 2.1.2, this value depends on both beam offset bo and as-designed diameter t_{CAD}. The theoretical contour diameter $t_{c,calc}$ can be expressed using Eq.55 if the melt pool width of the single contour exposure b_{SCE} is known. As highlighted by Großmann et al., the melt pool dimensions depend on the shape of the scanning path and, thus, the melt pool width of a single-track exposure cannot be used [79]. In the case of inclined struts, the theoretical strut diameter corresponds to the minor axis of its elliptical cross-section, as mentioned in section 3.4.3. Moreover, the repeatedly exposed areas can be described by the overlap measure OL (Eq.56).

$$d_{h,c} = t_{CAD} - 2 \cdot bo \tag{54}$$

$$t_{c,calc} = t_{CAD} - 2 \cdot bo + b_{SCE} \tag{55}$$

$$OL = 1 - d_{h,c}/b_{SCE} \tag{56}$$

Figure 97 shows the resulting single strut diameters obtained after varying the beam offset, which is defined in the AM software, and the as-designed diameter, which is directly read from the STL file, for equivalent hatch distances $d_{h,c}$ up to 1 mm. In this example, the lowest as-designed diameter was set to 300 μm due to the limit of strut number per grinding pot (see section 3.4). As expected, the results are consistent with each other, which validates Eq.55. Implementing a beam offset can further decrease the hatch distance. Moreover, it was noticed that vectors are not assigned anymore to CAD diameters of 25 μm without beam offset while it was possible to further decrease this limit to an equivalent hatch distance of 5 μm with supplementary beam offset.

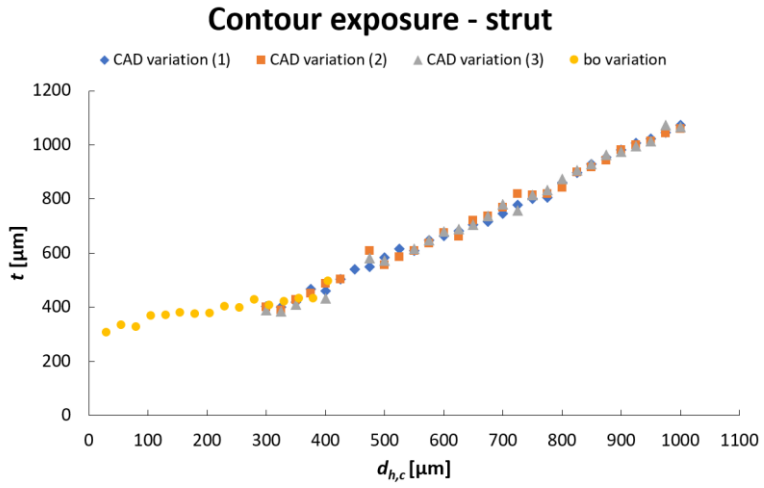

Figure 97: As-built diameters for hatch distance and beam offset variation for $P = 250\text{W}$ and $v = 3500\text{mm/s}$ (contour exposure, single struts).

Among all investigated configurations, the lowest strut diameters reach the range of order of 290 μm with CAD variation and 270 μm with supplementary beam offset. Figure 98

depicts the typical trends of single strut diameter and circularity values with respect to the equivalent hatch distance $d_{h,c}$. These trends have been observed for all manufactured single struts from the aforementioned lower limit on. As hollow struts can be formed, inner and outer diameters are differentiated. Figure 99 is extracted from Figure 98 and provides a more detailed trend of the inner strut diameter. Figure 100 shows examples single struts' cross section for each identified region. Changing the input parameters, i.e. laser power and/or scanning speed, only slightly shifts the curve (see Figure 97 for comparison). Four main regions can be identified. At low equivalent hatch distance, full struts of high circularity (around 0.70) corresponding to the pictures of Figure 7 are manufactured. As for the point exposure strategy, high standard deviations in thickness or circularity mean that particle aggregation occurs since cross-sections of high geometric accuracy can be achieved as shown in Figure 100, 1. However, the equivalent diameters do not linearly correlate with the equivalent hatch distance, which can be explained by high overlap values. Therefore, Eq.55 cannot be employed and the scaling law of Großmann et al. [32] is advised. From equivalent hatch distances corresponding to low or no overlap on, the circularity of the manufactured struts starts decreasing (Figure 98 and Figure 100, 2) while the strut diameters start fluctuating and, in some cases, describe a local plateau (Figure 97). This phenomenon is still observed after the strut becomes hollow (Figure 98 and Figure 100, 3). Although the strut diameter starts increasing linearly, the circularity fluctuates further until the wall thickness of the hollow struts stabilises (Figure 98, Figure 100 and Figure 99, 4) and reaches values between 0.50 and 0.60. From this moment on, the melt pool width can be measured and Eq.55 is able to predict theoretical strut diameters of acceptable range of error (less than 10 %) and, thus, can be employed in the context of a preliminary selection of manufacturing parameters. Although the recorded pictures of stabilised hollow struts (Figure 100, 4) hint at a better inner circularity, this trend is not visible from the data. This is due to an agglomeration of partially melted particles. Moreover, an offset of the centre line of the hollow strut towards the strut's centre was observed by confronting it to the initial scanning path (Figure 101).

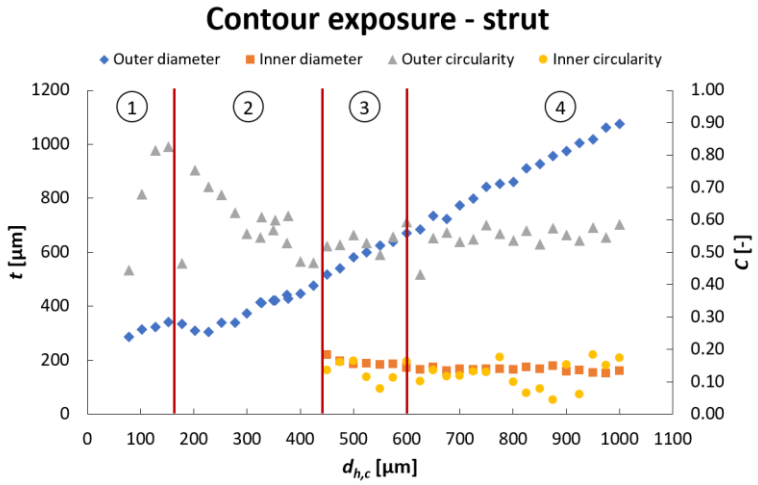

Figure 98: Diameter and circularity for $P = 200\text{W}$ and $v = 2500\text{mm/s}$ (contour exposure, single struts).

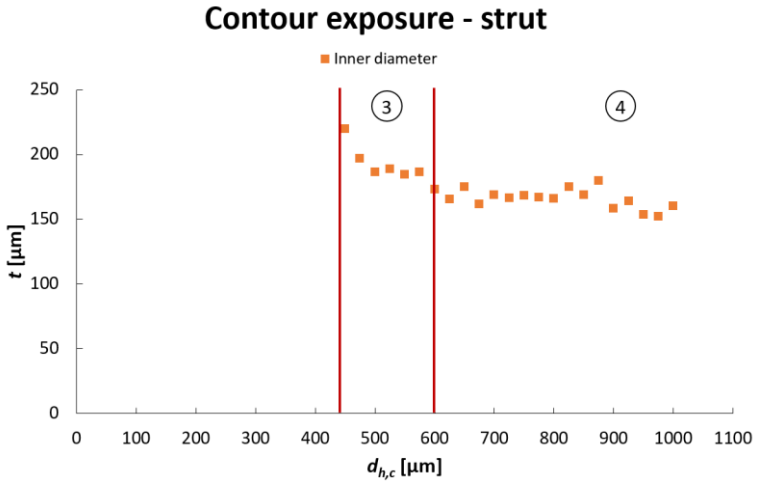

Figure 99: Inner diameter of hollow struts for $P = 200\text{W}$ and $v = 2500\text{mm/s}$ (contour exposure, single struts). Excerpt from Figure 98.

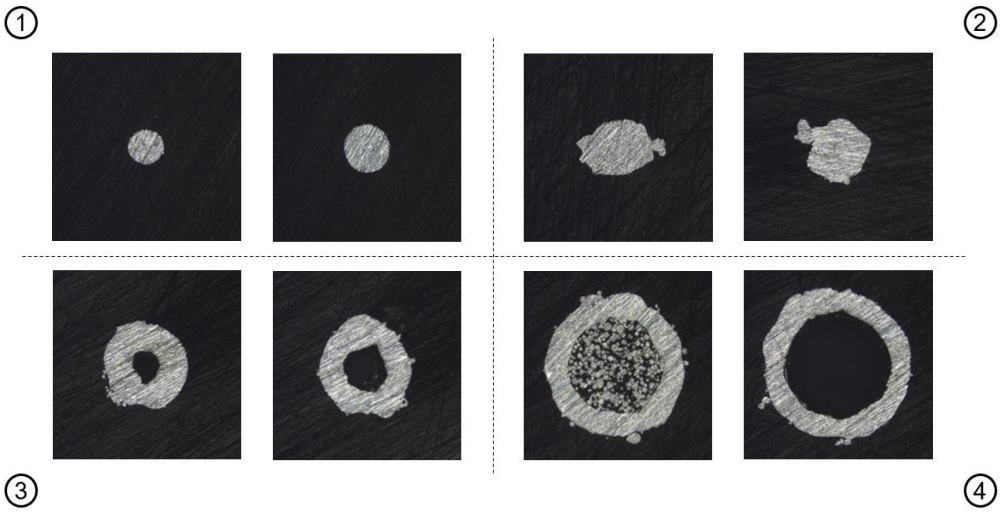

Figure 100: Struts cross-sections for the different regions observed (contour exposure, singe struts).

The instabilities in of both full and hollow strut regions and the offset from the scanning line can be explained by melt pool interactions and the surface tension resulting from local temperature gradients, i.e. the Marangoni effect (see section 2.1.3). In the case of the contour exposure strategy, the surface tension drives the melt flow from the hot laser spot toward the cold centre and leads to a contraction of the melt pool. That is why the transition regime from full strut to hollow is prone to particle aggregation. Although partially molten particle or leftovers of strut defects that were stuck in the hollow strut and came to the surface after resin embedment is not excluded, similar observations were made by Vrána et al. [402].

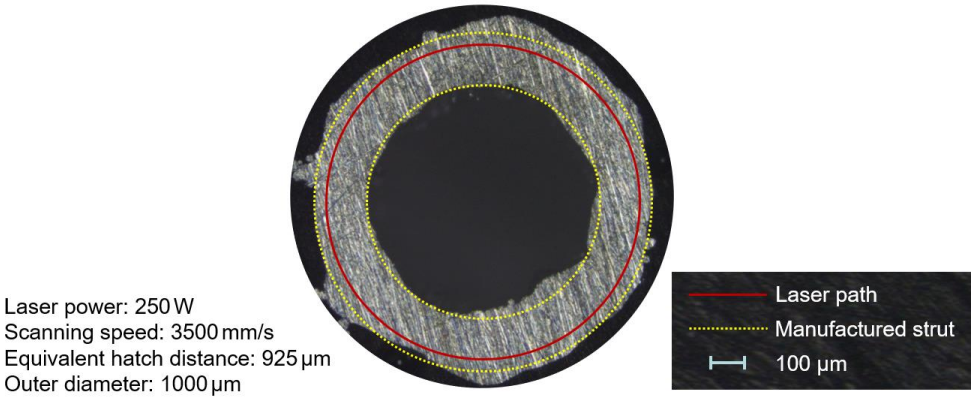

Figure 101: Offset of strut diameter (contour exposure, single struts).

The manufacturability range of lattice structures manufactured with the contour exposure strategy was investigated for equivalent hatch distances below the stable range of hollow struts since full struts are in focus. Lattice structures were reliably manufactured from diameters of 300 μm on. Figure 102 reports the results for f_2cc_z and bcc lattice structures of cell size of 3 mm manufactured by various combinations of laser power and scanning speed with respect to the equivalent hatch distance $d_{h,c}$. Please refer to appendix E for details on the employed parameter sets. It can be noticed that lattice structures could not be printed for equivalent hatch distances corresponding to the region of instable full struts (Figure 98, 2). This corresponds to a thickness range between 450 μm and 550 μm. Lattice structures were reliably manufactured again after this range, which is in line with literature findings (see section 2.3.6). Furthermore, the observed circularity values were slightly lower than the ones of single struts (Figure 98) with values oscillating between 0.35 and 0.50.

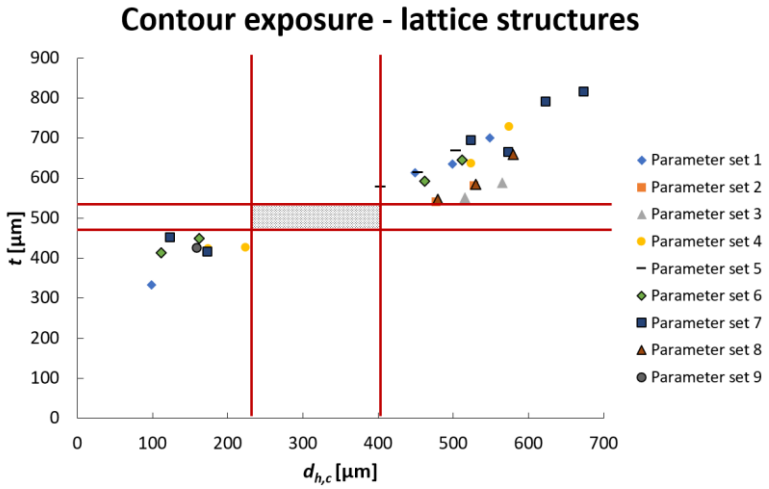

Figure 102: Manufacturability range for different parameter sets (contour exposure, lattice structures).

Figure 103 displays the different strut diameters obtained for single strut, single RUC and lattice structures with respect to the equivalent hatch distance $d_{h,c}$. In the full strut region,

strut diameters of lattice structures are higher than the ones of single struts. The similar values obtained for the only lattice printed in the hollow region suppose that single struts are representative of lattice structures in this case. While manufacturability issues can be identified for lattice structures, single f_2cc_z RUCs could be printed and they follow the same trends as single struts.

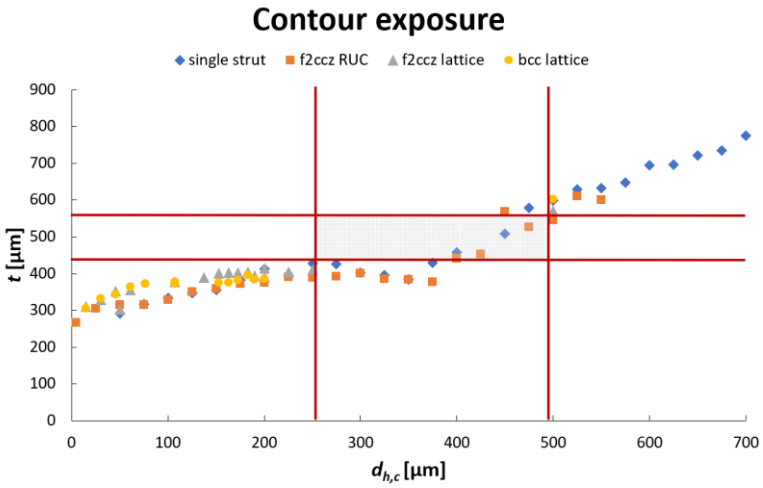

Figure 103: Representativity investigation of single struts for $P = 250\text{W}$ and $v = 2500\text{mm/s}$ (contour exposure).

An explanation to this trend can be found by investigating the nodal area. Figure 104 shows the scanning path as displayed by the AM software for a f_2cc_z RUC in the vicinity of its nodal area for problematic equivalent hatch distances. Several overlaps can be noticed at the strut junctions, which result in locally increased energy density. As a lattice structure is made of a tessellation of RUCs, these overlaps occur more often in a lattice structure than in a single strut or single RUC. Overlapped areas are negligible for smaller hatch distances because they are either narrow or not present at all. No influence of the build platform temperature on the manufacturing quality of lattice structures was observed. Therefore, the issues encountered by lattice structures manufactured with the contour exposure strategy cannot be solved directly. Please refer to appendix E for more details.

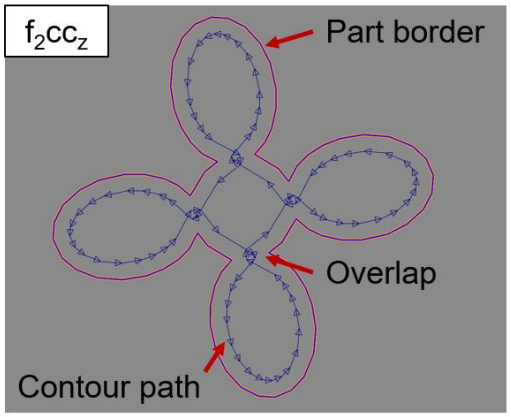

Figure 104: Scanning path in the vicinity of nodal area (contour exposure).

5.1.3 Hatch exposure strategy

Contrary to the contour exposure strategy, the designed lattice struts align with the target diameters (see Figure 5). For one given manufacturing layer, the hatch exposure strategy leads to two distinct diameters. The diameter $t_{h1,calc}$ is directed along the scanning vectors and can be expressed by considering the melt pool width of a single track b_{STE} and the parameters that define the initial cross section to be exposed, namely the beam offset bo and the as-designed diameter t_{CAD} (Eq.57). The second hatch diameter $t_{h2,calc}$ is perpendicular to the scanning vectors and depends on the number of hatch vectors n_H, the hatch distance d_h (Eq.58) and b_{STE}. The repeatedly exposed areas form an ellipse, whose main axes depend on the input parameters of the aforementioned hatch diameters. While the length of the overlap area, which is aligned with $t_{h1,calc}$, is driven by all variables and depends on the vector assignment of the AM software, its maximal width, which is aligned with $t_{h2,calc}$, can be calculated using the overlap measure OL established for the contour exposure strategy (Eq.59). As a matter of fact, the contour exposure strategy can be considered as a special case of the hatch exposure strategy which consists of two hatch vectors placed at both extremities of the radius formed by the scanning path. The contour diameter can be expressed using either Eq.57 or Eq.58 since both hatch diameters become equivalent to each other for $n_H = 2$. Consequently, the overlap area becomes circular and its aspect ratio, i.e. its ratio between length and width, is 1.

$$t_{h1,calc} = t_{CAD} - 2 \cdot bo + b_{STE} \tag{57}$$

$$t_{h2,calc} = (n_H - 1) \cdot d_h + b_{STE} \tag{58}$$

$$OL = 1 - d_h / b_{STE} \tag{59}$$

Figure 105 provides examples of the resulting strut quality of different parameter combinations for a rotation angle between hatch vectors of two successive layers θ_h of 90°. A bad parameter selection leads to lack of fusion pores or inaccurate cross-sections.

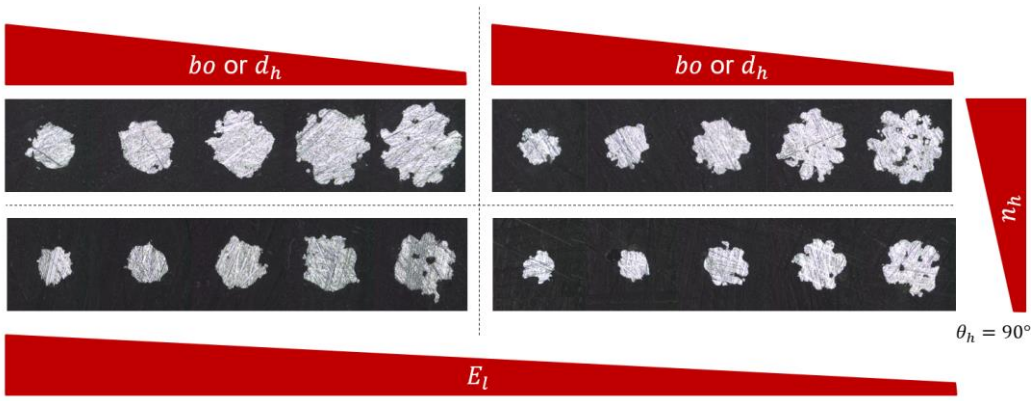

Figure 105: Effect of parameter variation on strut quality (hatch exposure).

To reduce the number of samples in the framework of this investigation, the values of d_h and bo were selected for the representative line energy E_l (Eq.3) so that the connection between melt tracks is ensured. The standard rotation angle between two layers of 67° was kept constant. The hatch exposure strategy was assigned without separation patterns (Figure 6) to ensure the continuity of hatch vectors at small scale. The selected values of d_h are derived from the formulation of the multiple track exposure width d_{MTE} specific to AlSi10Mg as used by Großmann in the early development of his scaling law [57]. This formulation takes the interaction between scanning paths into account. Its validity range was selected to ensure connection between single melt tracks and, at the same time, to avoid keyhole porosity. The values of bo were identified in the framework of preliminary studies on the accuracy of the selected parameter combinations. The selection criterion is the lowest average difference between as-designed and as-built strut diameters to avoid any supplementary corrective beam offsets or any modifications of the CAD model to match the target diameter. Please refer to appendix E for more details.

Figure 106 reports the diameters of single struts achieved for different parameter combinations. Please refer to appendix E for details on the employed parameter sets. As expected, a linear correlation between as-built diameter and as-designed diameters is observed. All struts were reliably manufactured from strut diameters in the range of order of 220 μm.

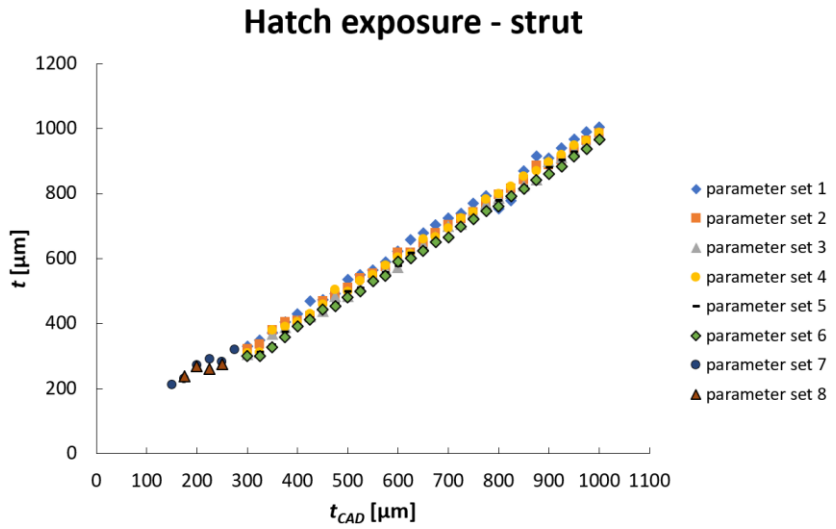

Figure 106: Diameter trends for struts (hatch exposure, single struts).

Figure 107 shows the results for circularity values for one representative example. Two types of results are displayed: discrete values and averaged values for each hatch vector. Although the exact way hatch vectors are assigned in the employed AM software is unknown, it is possible to calculate an arithmetic value of n_H with Eq.58. Figure 107 reports rounded experimental arithmetic values $n_{H,calc}$ obtained from reverse engineering based on the as-built diameters. Similar to the point exposure strategy (see section 5.1.1), issues were encountered for the estimation of circularity for diameters below 280 μm. Therefore,

the corresponding values are not reported. It can be observed that, for an increasing number of hatch vectors, the circularity decreases from values between 0.50 and 0.60 to values around 0.40. The number of hatch vectors for the stabilisation of circularity varies between 5 and 7 depending on the selected parameter combination and is proportional to the overlap value. It can be concluded that, for connected melting tracks, the roundness is more impacted by particle aggregation, which is due to repeated overlapped areas, than by a restricted number of hatch vectors, which deviates from a perfect circle.

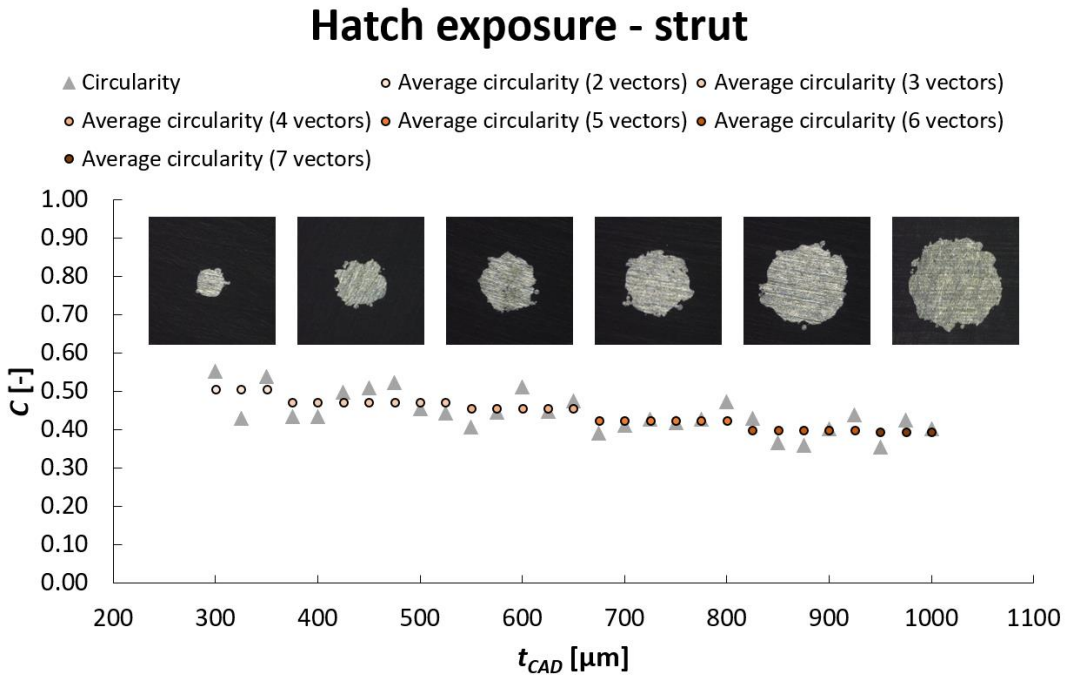

Figure 107 Circularity of struts for $P = 250\text{W}$, $v = 2000\text{mm/s}$, $bo = 29.1\mu\text{m}$ and $d_h = 136.2\mu\text{m}$ (hatch exposure, single struts).

Table 7 reports the manufacturability results of f_2cc_z lattice structures for different parameter combinations. The deviations between strut diameters of lattice structures and single struts are in the range of order of the standard deviations. A slight decrease of circularity is observed for lattice structures. This can be explained by the presence of surrounding struts and, similar to the contour exposure strategy (see section 5.1.2), the influence of the nodal area. Therefore, it can be stated that single struts are representative of struts in lattice structures far from the nodal area under the condition of connection between melt tracks. Moreover, it was noticed that considering 25 % of the melt pool width of a single track b_{STE} for both values of d_h and bo leads to a good compromise between manufacturing precision and predictability of the strut diameter using Eq.57 and Eq.58. Please refer to appendix E for more details.

Table 7: Manufacturability results (hatch exposure, lattice structures).

t_{CAD} [µm]	a [mm]	AR [-]	P [W]	v [mm/s]	E_l [J/m]	bo [μm]	d_h [µm]	t [μm]	$t - t_{CAD}$ [μm]	$t_{Lattice} - t_{Strut}$ [μm]	C [-]
400	4.25	10.1	250	2000	125.0	29.1	104.0	420.6	20.6	-10.3	0.35
400	4.25	10.5	250	2000	125.0	38.9	104.0	403.0	3.0	-5.4	0.24
350	3.00	8.2	250	2000	125.0	29.1	136.2	363.9	13.9	-4.5	0.33
400	4.25	10.9	250	2000	125.0	29.1	136.2	391.0	-9.0	-17.2	0.47
400	4.25	11.0	250	2000	125.0	38.9	136.2	384.8	-15.2	-20.9	0.34
400	4.25	11.2	250	2000	125.0	29.1	156.0	380.7	-19.3	-9.9	0.38
400	4.25	11.1	250	2000	125.0	38.9	156.0	382.0	-18.0	-8.9	0.36

Additional investigations demonstrated that it was possible to simultaneously decrease the limit of the lowest printable strut diameter and to increase the circularity of lattice structures by modifying the rotation angle between two successive hatch vectors. Literature reports melt pool depths of about three times the employed layer thickness of 30 μm [103, 349]. As few hatch vectors are assigned to struts of diameters below 500 μm (Figure 107) and, similar to single layers, a certain overlap between successive layers is required to ensure connection between melt tracks, it was supposed that the standard hatch rotation angle of 67° may not be optimal as it aims at reducing the frequency of overlap of hatch vectors of the same orientation (see section 2.1.4). Table 8 reports the manufacturability of f_2cc_z and bcc lattice structures for a rotation angle of 90°, i.e. an overlap of hatch vectors every two layers. The parameter combination of Table 7 leading to the best accuracy ($t - t_{CAD}$) was selected. All lattice structures were successfully manufactured independently from azimuth angles (Figure 4), which were varied from 0° to 45°. It has to be noted that lattice structures of as-designed diameter of 140 μm could have been printed but they were too frail to be removed from the build platform without damage. Both predictability of diameters and representativity of single struts are given for this parameter set too. The lesser roundness of bcc lattice structures is due to the inclination angle of their struts (see section 2.3.3), which leads to bigger downskin areas and, thus, makes them prone to particle aggregation (see section 2.1.3). Please refer to appendix E for more details.

Table 8: Manufacturability results of f_2cc_z and bcc lattice structures manufactured for $P = 250$W, $v = 2000$mm/s, $bo = 38.9$µm, $d_h = 104$µm and $\theta_h = 90°$ (hatch exposure, lattice structures).

Lattice	t_{CAD} [µm]	a [mm]	t [μm]	AR [-]	$t - t_{CAD}$ [μm]			C [-]
			Min	Max	Mean	Max t	Max StdDev	Mean
f_2cc_z	200-475	3.0	222.4	13.5	17.5±13.0	40.6	24.3	0.51±0.09
		3.5	218.9	16.0	11.2±11.1	18.9	15.9	0.54±0.10
bcc	155-290	3.0	187.2	16.0	38.1±18.9	49.8	26.2	0.35±0.09
		3.5	187.2	18.7	35.0±18.6	45.5	22.2	0.27±0.08

5.1.4 Combination of exposure strategies

The investigated combinations between basic exposure strategies are the contour-hatch, the multiple contour and the multiple contour-hatch combinations. The point exposure strategy is not explored because of its lack of compatibility with other exposures, namely different pre-processing steps and a restricted printability range (see section 5.1.1). As it is not possible to assign different parameter sets specific to each hatch vector without splitting the as-designed part, the core exposure strategy of combinations is the contour exposure strategy. Consequently, the condition for the combination of exposure strategies is the presence of hollow struts. Therefore, each domain specific to single contour exposure strategy (see section 5.1.2) is depicted in the reported diagrams. As the relevant investigation range starts in the unstable hollow strut domain, no results concerning the stable region of full struts (Figure 98, 1) are reported. In the framework of this investigation, the order of combination sequences and the overlap between melt tracks of basic strategies were investigated. For a better comparability of the manufacturing accuracy of each exposure combination, corrective offsets were implemented so that the outer as-built contour diameter matches the as-designed diameter.

Figure 108 and Figure 109 show the results obtained for the contour-hatch exposure combination (CH) regarding strut diameter and strut circularity for overlap values of 0 % (OL 0 %), 25 % (OL 25 %), 50 % (OL 50 %), 100 % (OL 100 %), and -25 % (OL -25 %), respectively. Additionally, the results obtained for a single contour exposure (C) of the same parameter set are depicted as well for comparison. Figure 110 shows examples of single struts' cross section for each identified region of each configuration.

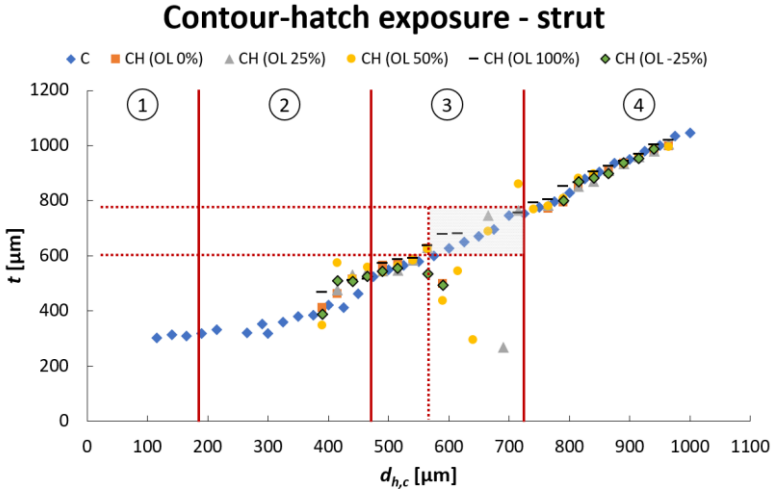

Figure 108: Representative diameter trends for struts with different overlap (contour-hatch combination, single struts).

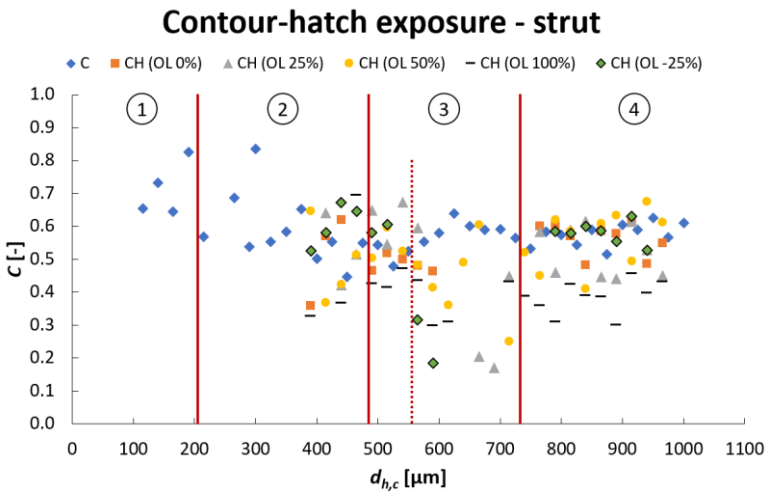

Figure 109: Representative circularity trends for struts with different overlap (contour-hatch combination, single struts).

Changing the energy input, i.e. laser power and scanning speed, influences the quality of manufacturing but the identified trends stay the same. Overall, a good match with the target diameter (differences below 20 μm) is observed and starting with the outer contour increases the roundness. Manufacturability issues occurred in the unstable hollow region of single contour, corresponding to diameters between 600 μm and 800 μm (Figure 108 and Figure 109, 3). The fluctuating values of both diameter and circularity hint at instable interactions between melt tracks and, in the case of successful manufacturing, increased particle aggregation. In other areas, both diameter and circularity trends align with the trends and range of order of the governing single exposure strategies, which can be identified with the achieved circularity values. For an overlap of 100 %, the strut is completely re-melted. The manufacturing accuracy is driven by the hatch exposure strategy because it yields the worst circularity, whereas it has few to no influence for lesser overlap values. The opposite overlap values (-25 % and 0 %) behave similar to a single contour but they exhibit a lack of connection between melt tracks, i.e. lack of fusion porosity. This phenomenon has been observed for some of the big strut diameters manufactured with an overlap of 25 % as well. The best results in terms of manufacturability and accuracy were achieved for an overlap of 50 %. Therefore, it can be concluded that the best manufacturing results are achieved for overlap values between 25 % and 50 %. This is in line with the observation of literature [32, 402]. Lattice structures of cell width of 3 mm were printed as a proof of manufacturability. The obtained strut diameters are in line with the ones of the single struts only considering the hollow strut domain of the single contour exposure strategy. Similar to single contour, a lower roundness compared to single struts was observed for lattice structures.

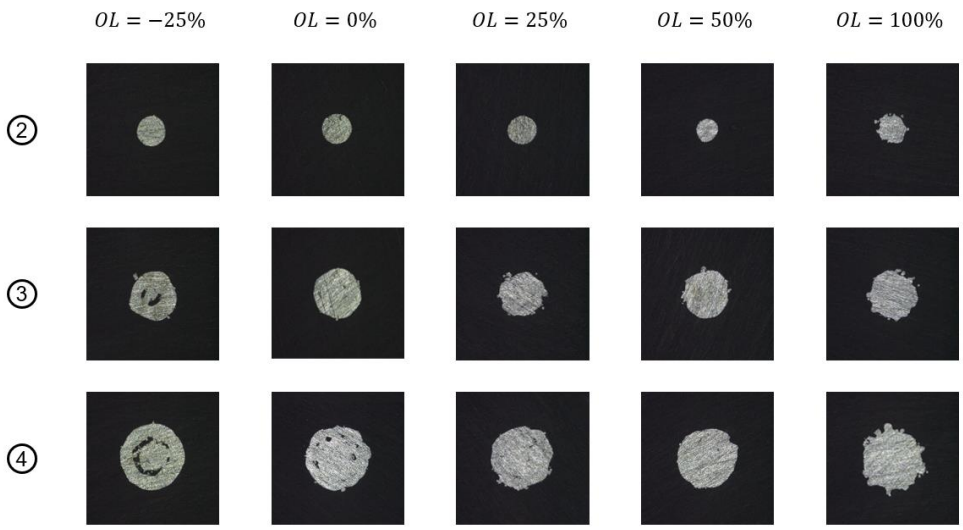

Figure 110: Cross-sections for different overlap values (contour-hatch combination, single struts).

Figure 111 and Figure 112 show the results obtained for the multiple contour exposure combination regarding strut diameter and strut circularity, respectively. Double contour exposures (2C) were investigated for overlap values of 0 % (OL 0 %), 25 % (OL 25 %) and 50 % (OL 50 %) according to the findings of the contour-hatch exposure combination (see above). Both triple contour (3C) and quadruple contour (4C) exposures were investigated as a proof of iterability for one overlap value only. Hollow struts are reported as well (hollow). In order to maintain the efforts involved by the multiple contour exposure combination in a realistic range, both laser power and scanning speed were kept constant for each selected parameter set. Additionally, the results obtained for a single contour exposure (C) of the same parameter set are depicted as well for comparison. Figure 113 shows examples of single struts' cross section for each identified region of each configuration.

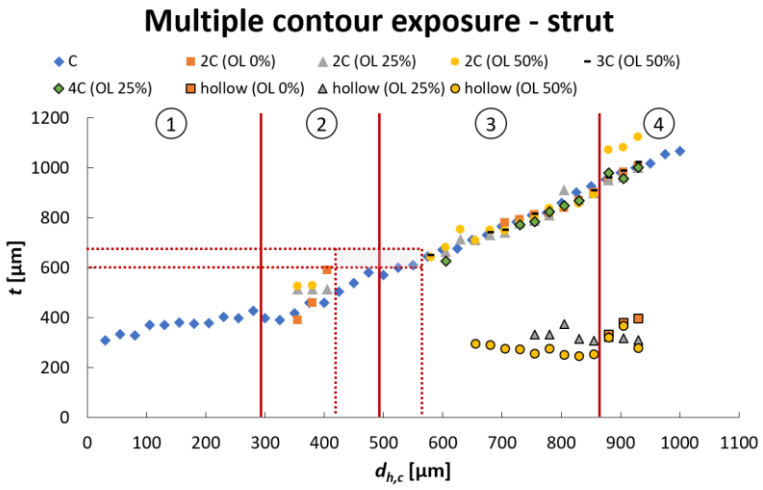

Figure 111: Representative diameter trends for struts with different overlap (multiple contour combination, single struts).

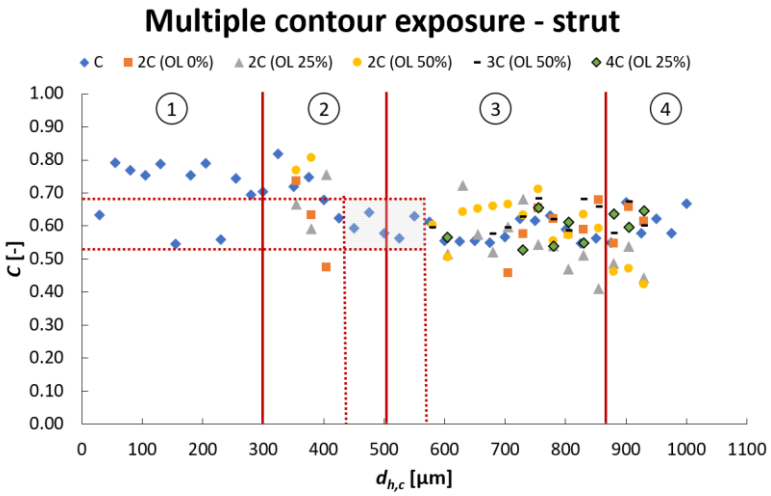

Figure 112: Representative circularity trends for struts with different overlap (multiple contour combination, single struts).

Overall, a good, but lesser than for contour-hatch, match with the target diameter is observed and starting with the outer contour increases the roundness. Manufacturability issues occurred for double contour exposures in the unstable hollow region of single contour (Figure 111 and Figure 112, 2 and 3), corresponding to diameters between 600 μm and 650 μm. The fluctuating values of both diameter and circularity hint at instable interactions between contour melt tracks and, in the case of successful manufacturing, increased particle aggregation. Moreover, a supplementary drop in circularity and deviations from the single contour diameter were observed. Similar to a single contour, they correspond to the formation of hollow struts (Figure 113) and, thus, stand for an unstable hollow region. This secondary hollow region is responsible for further manufacturing issues observed for other multiple contour combinations (Figure 111 and Figure 112, 3 and 4): between 650 μm and 740 μm for the triple contour exposure and between 630 μm and 770 μm for the quadruple contour exposure. These ranges are not consistent with each other since different overlap values have been employed to remain under the upper limit of the investigated target diameter range of 1 mm. This means that the manufacturing ranges depend on energy input parameters and beam offset. In other areas, diameter and circularity trends align with the trends and range of order of the single contour exposure strategy. As for the contour-hatch exposure combination, an overlap value of 0 % leads to a lack of connection between melt tracks. In the unstable range of single contour hollow struts (Figure 111 and Figure 112, 3), no significant difference between the overlap values of 25 % and 50 % were observed. Lattice structures of cell width of 3 mm were printed as a proof of manufacturability. The obtained strut diameters are in line with the ones of the single struts only considering the hollow strut domain of the single contour exposure strategy. Similar to single contour, a lower roundness compared to single struts was observed for lattice structures.

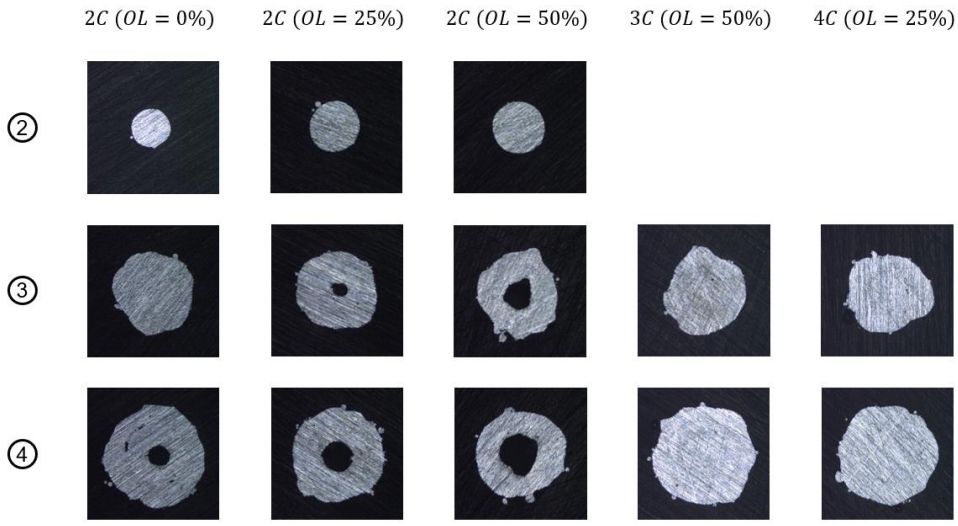

Figure 113: Cross-sections for different overlap values (multiple contour combination, single struts).

Figure 114 shows the results obtained for the double contour-hatch exposure combination (2CH). Additionally, the results obtained for both single contour (C) and double contour (2C) exposures of the same parameter set are depicted as well for comparison Since its realisation follows the same principle of both contour-hatch and double contour exposure combinations, only one parameter combination based on an overlap of 25 % and an initial outer exposure was investigated as a proof of manufacturability. The lowest manufacturable diameters correspond to the manufacturability range of the double contour exposure. The comparability with single contour is given as well. Good manufacturing accuracy was achieved with an average difference of 12.5 μm from the target diameter and a circularity of 0.63.

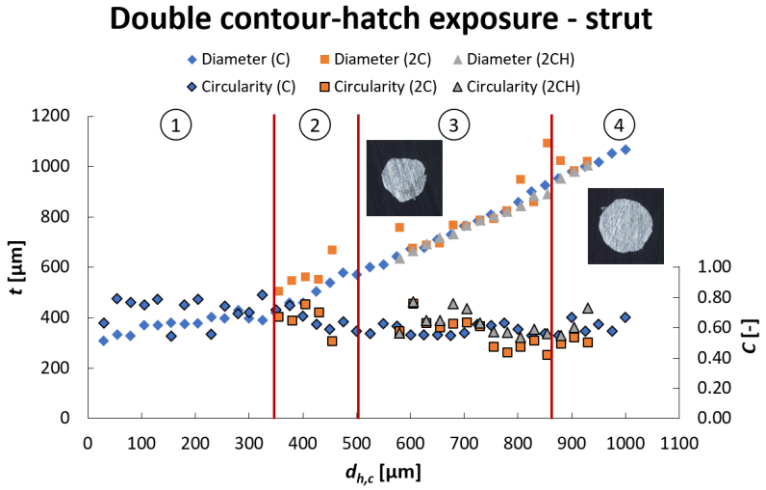

Figure 114: Representative diameter trends for struts with different overlap (multiple contour-hatch combination, single struts).

Figure 115 shows the manufacturing quality of the standard exposure strategy. Please note that the standard parameters are not reported in this work since they are part of non-

disclosed data of a commercial product. The standard strategy consists of a double contour-hatch exposure combination starting with the hatch exposure. Therefore, a direct comparison with the results depicted in Figure 114 is possible. Similar to Figure 114, manufacturing issues were encountered for diameters below 500 μm due to interactions between melt tracks. A single contour can be recognised from the few manufactured struts in this range. Struts could be manufactured reliably from about 600 μm on. However, their quality in the submillimetre range can be qualified as poor compared to the previous results. The high amount of aggregated particles hints at excessive energy input and is responsible for low circularity values (average of 0.24 ± 0.06) and subsequent deviations from the target diameter. It can be concluded that, in line with literature [41, 303], this parameter set is not suited for thin-walled structures.

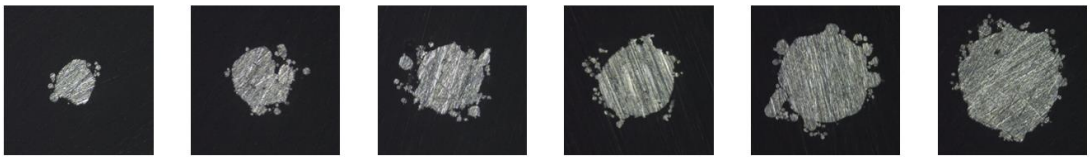

Figure 115: Cross-sections for different as-built diameters (standard parameter set, single struts).

5.1.5 Summary and discussion

Different manufacturing approaches lead to different manufacturability ranges and manufacturing quality. The driving parameters are the energy input, in this example the laser power and the scanning speed (Eq.3), hatch distances and beam offsets. The latter allows adjusting the as-built diameters to match the as-designed ones. Alternatively, compensation approaches can be employed by considering the deviations between as-built and as-designed diameters [132-134].

While the point exposure strategy allows the reliable manufacturing of extremely thin-walled structures (below 300 μm) of good roundness, it has to be considered a special strategy because of its lack of compatibility with other exposure strategies. Adapting the offsets and input parameters of both contour and hatch exposure strategies lead to strut diameters in a similar range of order. The hatch exposure strategy has no upper limit in terms of manufacturable strut diameters. It is not only governed by the aforementioned input parameters but also by the number of hatch vectors and their rotation angle between two consecutive layers. These supplementary variables strongly influence the strut's roundness. The single contour exposure strategy exhibits better roundness than the hatch exposure strategy. However, it is restricted to diameters up to about 500 μm before becoming hollow and, thus, needs to be combined with other exposure strategies for the realisation of full struts. In the case of combinations of exposure strategies, the exposure strategy defining the outer diameter governs the manufacturing quality. Moreover, the

overlap of melt tracks at the transition between exposure strategies governs the manufacturability. Overlap values between 25 % and 50 % consistently lead to melt track connection.

The choice of the exposure strategy and corresponding parameters depends on the range of order of the diameters to be printed. In the framework of AlSi10Mg LB-PBF, lattice structures with strut diameters below 150 μm are prone to damage. Therefore, they need to be either surrounded by protecting structures or avoided. For the specific case of graded lattice structures manufactured by a strategy consisting of at least one contour exposure, manufacturing issues occur for diameters below 600 μm at both strut and lattice structure scales. They are due to the overlap between melt tracks, especially in the vicinity of the nodal area. Since the as-built strut diameter depends on the contour equivalent hatch distance (Eq.55), it can be deduced that the manufacturability of lattice structures further depends on the cell size. This means that, for a given parameter set, varying the aspect ratio may lead to manufacturing issues. One solution to increase the printability of LB-PBF graded lattice structures would be to assign parameters specific to each region, i.e. struts or nodal area. Moreover, different parameters shall be assigned for different inclination angles too [311]. This approach can be considered as a grading of input parameters. However, it involves tremendous pre-processing efforts in the actual state of the employed AM software. For simplicity, a homogeneous parameter set needs to be identified. This explains why only one single parameter set is employed in the reported literature (see sections 2.3.6 and 2.4.2). In this case, compromises regarding the value of some input parameters such as the beam offset need to be made, which unavoidably lead to deviations from as-designed diameters.

The geometrical considerations of both laser path and melt pool width of each exposure strategy (Eq.54 to Eq.59) can be employed for a parameter selection in the context of a pre-sizing phase as they can at least predict the range of order of the as-built diameters. For more accurate diameter predictions, it is advised to employ dimensionless numbers as the interaction between melt pool tracks is specific to each manufacturing approach. Similar to Großmann et al. [32], scaling laws valid for materials other than AlSi10Mg can be derived from these numbers as the encountered issues are not material specific. They could even cover a much wider parameter space with, for example, the ratio between layer thickness and powder particle size to identify parameter combinations simultaneously offering high build rates and good manufacturing accuracy.

It has to be noted that this investigation deals with the manufacturability of lattice structures only while offering a first insight in their quality. Only strut diameter and circularity were considered. These two measures highly depend on the particle aggregation originated by melt pool interactions. The influence of the manufacturing quality on the mechanical properties of lattice structures was not covered. Aggregated particles lead to notch stresses and may even contribute to increase the load-bearing behaviour of the manufactured lattice structures as they offer to increase the strut's cross-sections. Moreover, further

phenomena influencing the mechanical performance of additively manufactured parts such as porosity and local texturing, which are distinguishable on Figure 105, Figure 110, Figure 113 and Figure 115, were not covered either (see sections 2.1.3 and 2.3.6).

5.2 Reliable manufacturing of the lattice-to-bulk transition

The approaches and parameter selection were specifically developed for the realisation of the tensile specimen design developed in section 4.1 and investigated in section 6.3. In order to cover the worst-case scenario of a horizontal overhang, this investigation aims at printing vertical samples, which corresponds to a polar angle Θ of 90° (see section 2.1.2). Although all the successfully printed lattice structure configurations reported section 5.1 can be investigated, ungraded lattice structures of strut diameter of 370 μm and cell width of 3 mm were selected as they corresponded to the initially planned configuration of the target region. For consistency with section 5.1, the initial temperature of the build platform was set to 125°C. As for the design solutions of section 4.1, the strut junctions of the selected RUCs are located in the centre of their upper and lower faces (see section 3.1.1). Section 5.2.1 handles integral design solutions, which consist of monolithic additively manufactured samples, and section 5.2.2 proposes a modular design in order to overcome the encountered manufacturing issues.

5.2.1 Integral design

The aim followed by the proposed integral design solutions is the development of a straightforward manufacturing approach based on a single parameter set and on a design without support structures other than the lattice struts themselves. Figure 116 depicts schematically the specimens employed in the framework of this investigation. A shell layer of initially 300 μm had to be manufactured on lattice structures initially made of 4x4x4 RUCs. In the case of successful manufacturing, the size of the investigated specimen was increased until the dimensions required by the design solutions of section 4.1 were reached. In order to reduce curling at the specimen's edges (see section 2.1.3), the shell layer was designed so that it covers the complete cross-sections of the lattice structures without generating overhanging structures. In order to reduce the investigation efforts, only laser power and scanning speed were varied. The standard layer thickness of 30 μm and the standard hatch distance of 190 μm were kept constant. In order to avoid melt pool instabilities issued from overlapped areas within the shell layer, no hatch separation pattern was used (Figure 6).

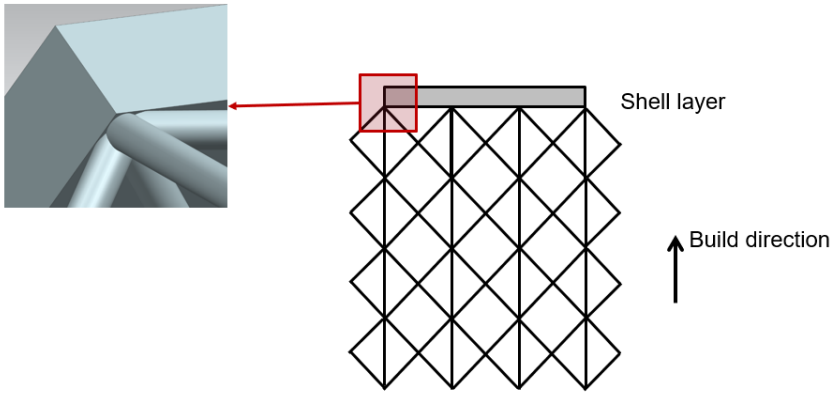

Figure 116: Design principle of the test specimens (example for f_2cc_z).

Figure 117 shows the methodology employed to assess on the manufacturability of the lattice-to-bulk interface. The shell layer of the test specimens can be distributed into several panels P_i, which are supported by and, thus, separated from lattice struts at the interfaces IF_i (Figure 117, a). The analysis methodology consists of two stages. In the first step, an optical evaluation of the manufactured specimens is performed for both up- and downskin shell surfaces of each panel and for each interface. As no perfect structures were expected, the manufactured specimens were evaluated according to the presence of anomalies, i.e. defects such as holes, lack of connection between shell and lattice struts or obviously high geometric deviations (Figure 117, b). Selection criteria for a consistent manufacturability are a homogeneous shell without obvious particle aggregation or porosities and a continuous connection between shell and lattice struts for all interfaces. The specimens exhibiting obvious defects were excluded. In the second step, the dimensional accuracy of the shell layers of the remaining specimens was investigated in order to assess for the influence of powder sinking or particle aggregation. The minimum and maximum shell thicknesses of each panel were measured (Figure 117, c) and confronted to the as-designed shell thickness.

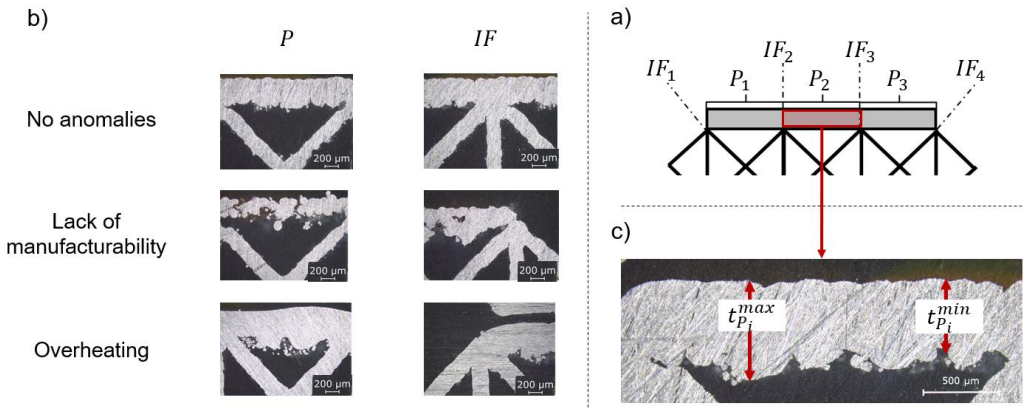

Figure 117: Methodology for assessing the manufacturability of the lattice-to-bulk transition.

Manufacturability of f_2cc_z lattice structures

Figure 118 reports the manufacturability results obtained for the specimens with 4x4x4 f_2cc_z lattice structures. All depicted ranges lead to a reliable lattice-to-bulk interface. The only difference between a good and very good manufacturability is based on the averaged thickness deviations of each as-built shell with respect to the as-designed shell. The deviations from the as-designed shell thickness are in the range of order of 200 μm. Detailed results are not reported though, as manufacturing accuracy was not in the focus of this investigation.

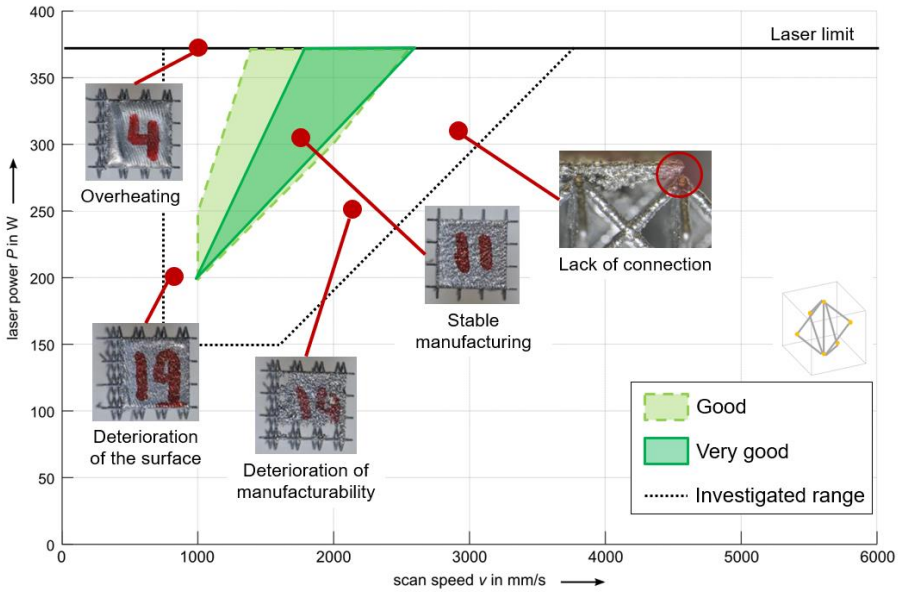

Figure 118: Manufacturability of the lattice-to-bulk transition (f_2cc_z).

Figure 119 reports pictures of each manufactured shell layer recorded by the optical monitoring camera of the employed AM machine. The contrast of these pictures was not modified for comparability between manufactured layers and with the results obtained for the bcc lattice structures (Figure 122). Their low resolution is explained by the fact that the whole build space is recorded by the camera. In spite of this low resolution, different phases can be identified. The first phase is decisive for the manufacturability of the shell layers and is therefore called the critical phase. For all successfully manufactured shells, 10 critical layers were observed. This critical phase is followed by a stabilisation phase, in which the local overheating identified by brighter areas is reduced, and by a stable build phase.

The combination of laser power of 315 W and scanning speed of 1700 mm/s (Figure 118, specimens 11) was selected because it yielded the lowest deviations in shell thickness (about 180 μm) compared to the as-designed shell. The test samples in the foreground of Figure 120 were printed with this parameter and demonstrate its applicability to higher samples, larger surfaces and different lattice parameters. It has to be noted that the temperature of the build platform had to be increased to 190°C in the case of very high samples

to avoid eigenstresses issued from temperature gradients between the upper bulk part of the sample and the surrounding powder.

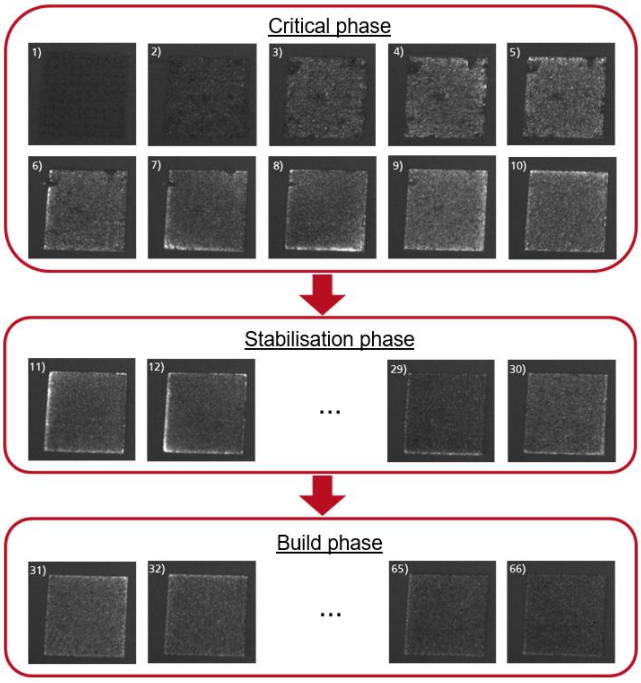

Figure 119: Live monitoring pictures of the manufacturing of the shell layers (f_2cc_z).

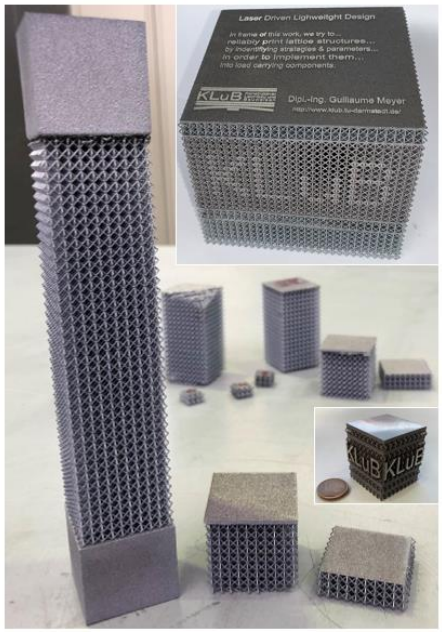

Figure 120: Examples of manufactured samples (f_2cc_z).

Manufacturability of bcc lattice structures

Figure 121 reports the manufacturability results obtained for the bcc lattice structures at different specimen dimensions. For 4x4x4 lattice structures, the manufacturability range is similar to the one of f_2cc_z lattice structures (Figure 118). However, increasing the lattice

dimensions to 8x8x8 leads to a shift of this manufacturability range towards lower energy input densities, i.e. to the right-hand side of the process window. It was impossible to manufacture 8x8x20 specimens without observing a collision with the coater. Neither increasing the temperature of the build platform T_b nor changing the shell inclination relative to the coater, i.e. the azimuth angle Φ (Figure 4), could improve their manufacturability.

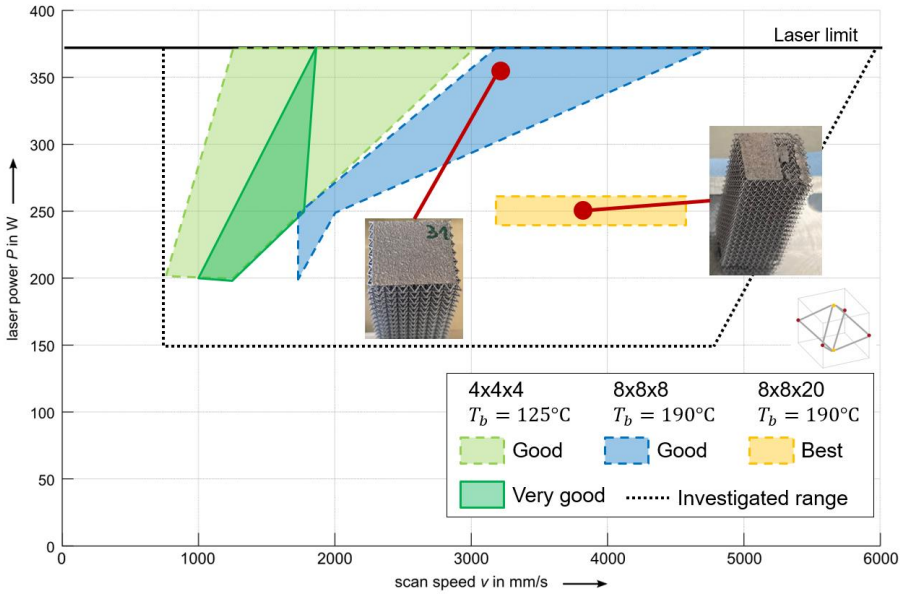

Figure 121: Manufacturability of the lattice-to-bulk transition (bcc).

For all successfully manufactured shells, the number of critical layers varied between 20 and 30, which was only observable after an increase of the as-designed layer thickness. Figure 122 reports pictures of each manufactured shell layer of 4x4x4 bcc lattice structures recorded by the optical monitoring camera of the employed AM machine. For comparison purposes with Figure 119, only the first 10 shell layers are displayed. Compared to the f_2cc_z specimens, the observed higher brightness hints at much higher local temperatures in the shell layers.

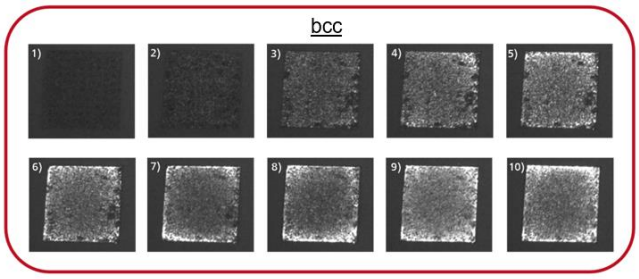

Figure 122: Live monitoring pictures of the manufacturing of the shell layers (bcc). Same parameter and the same format as Figure 119 for comparison purposes.

Figure 123 shows the different specimens manufactured in the framework of this investigation. The most promising result is located on the right-hand side. This sample consists of a locally graded lattice layer at the interface with the shell to redistribute the temperature present in the shell layers. Although a collision with the coater occurred after 18 layers (visible on the top left hand-side of the sample), this solution offers a significant increase of the specimen manufacturability compared to other samples (visible in the background).

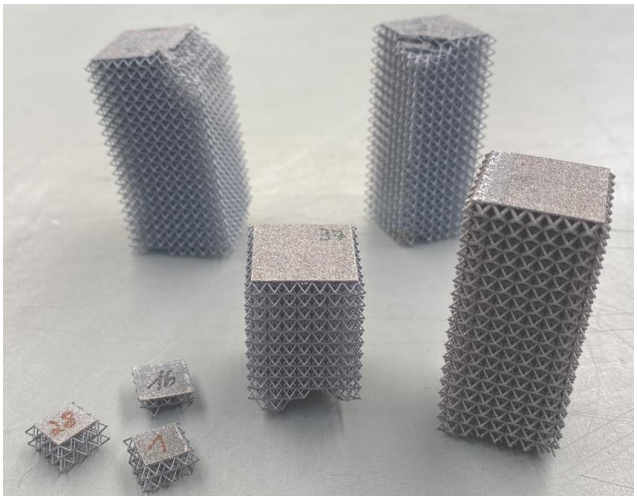

Figure 123: Examples of manufactured samples (bcc).

Based on these observations, further design solutions inspired from the findings of section 4.2 were investigated. The proposed alternative monolithic design solutions for bcc lattice structures involves both structural grading and cones, which can be interpreted as continuously graded vertical struts of high grading factor. In this part of the investigation, the parameter variation depicted in Figure 124 was performed. The cones were modelled based on the cross-section corresponding to the nodal area of the lattice structure. Their height h_{cone} was parametrised according to the cell size a. In order to avoid overlap between the cones of different RUCs, each cone was limited by cutting planes corresponding to the limits of the RUC it is placed on.

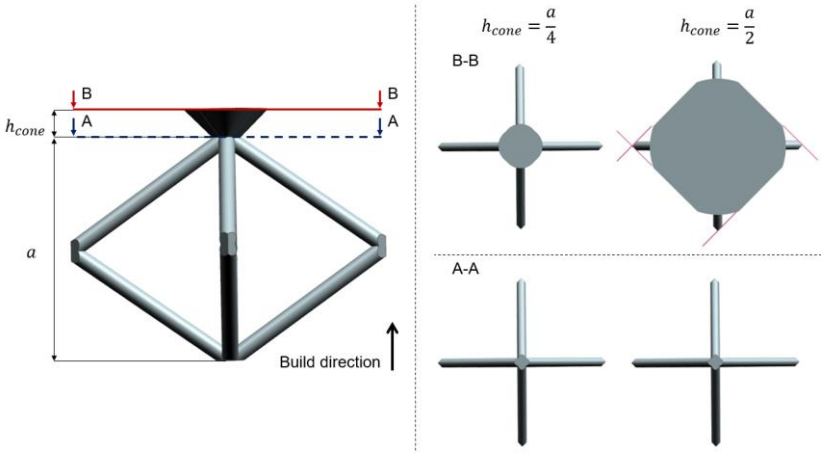

Figure 124: Design principle of the employed cones.

Suitable manufacturing parameters for the realisation of the cones were investigated on 8x8x1 specimens. In order to align with the designs investigated in section 6.3, RUCs of cell width of 3.5 mm were considered. Due to the manufacturing issues encountered, only the graded configuration of samples of aspect ratio of 6 was investigated. This configuration exhibits the highest strut diameters and, thus, is considered as the best-case scenario regarding the thermal conduction from the shell layer to the lattice structure. Different combinations of parameter sets for cones and shells layer were explored: the standard parameter set, the parameter set identified for f_2cc_z specimens (Figure 118, sample 11), one of the parameter sets leading to the best results of 8x8x20 bcc specimens (Figure 121), and one of the parameter sets used for the realisation of lattice structures (see section 5.1). The best results were obtained for the parameter set of the f_2cc_z specimens for both cones and shell layers (Figure 125). After an increase of the specimen height to 4 RUCs in the build direction, reliable manufacturability was observed for a cone height corresponding to one fourth of the cell size only. While local collisions with the coater were observed for smaller cones down to one tenth of the cell size, material swelling occurred for higher cones.

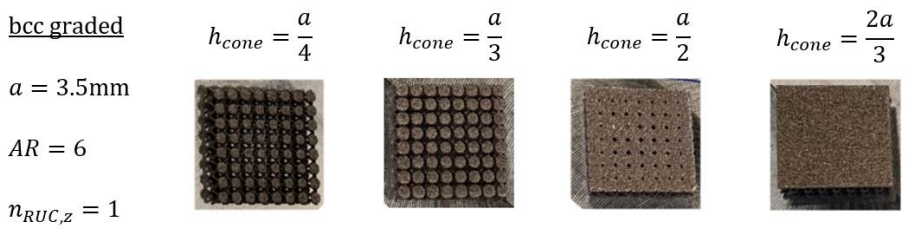

Figure 125: Manufacturability of the shell layers for varied cone height (bcc, cones).

Figure 126 shows the proof of concept of the manufacturability of a bcc tensile specimen with a graded load introduction as designed in section 4.1 and cones of a height corresponding to one fourth of the cell size. The parameter set identified for the f_2cc_z specimens was employed. It can be further noted that f_2cc_z lattice structures were employed as support structure.

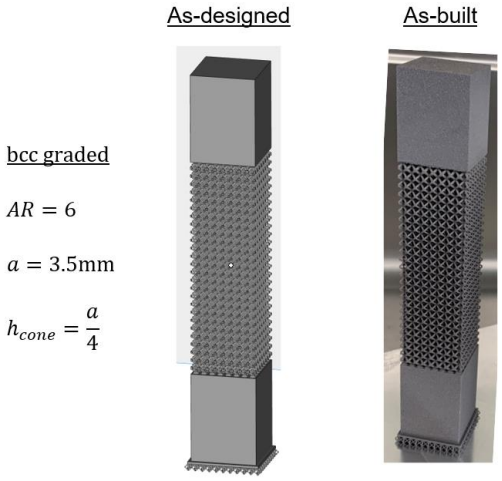

Figure 126: Examples of manufactured samples (bcc, cones).

5.2.2 Modular design

In order to overcome the manufacturing issues encountered by the bcc samples, a modular design was developed. This modular design consists in separating the lattice structure, including both transition and target regions, from the bulk region (Figure 127, b). Although this concept was developed for the special case of the bcc RUCs, it is applicable to any other kind of RUC. In order to assemble the different modules, both bulk regions are pocketed to accommodate in the lattice structure, whose height is increased in accordance with the height of the pocket. The lattice structure is embedded in epoxy resin. A form fit shaft was designed in the case of a lack of adhesion between the resin and the pocket's walls to ensure that the stiffness of the resulting load introduction does not falsify the results of the mechanical investigation. Details on the pocket design are provided in appendix F. The modular samples can be easily differentiated from the monolithic ones (Figure 127, a) with the overhanging surfaces at the sample's sides. In this work, all bcc samples were manufactured using a hybrid approach combining both sample concepts, which enables a reduction of the manufacturing steps. This hybrid approach consists of an AM compliant monolithic module made of one bulk region and the lattice structure on it, and of a separated pocketed bulk region (Figure 127, c). Figure 128 shows the different manufacturing steps involved by the selected manufacturing approach. Both modules are manufactured separately (Figure 128, a). In order to ensure the verticality of each sample, six samples symmetrically distributed over the build platform are manufactured simultaneously. The pockets of the hollow bulk module are filled with resin (Figure 128, b). The exact quantity of required resin can be estimated by geometrical considerations detailed in appendix F. Both build platforms are assembled (Figure 128, c) and, once the resin has cured, the samples are sawn off manually thanks to the lattice structures employed as support.

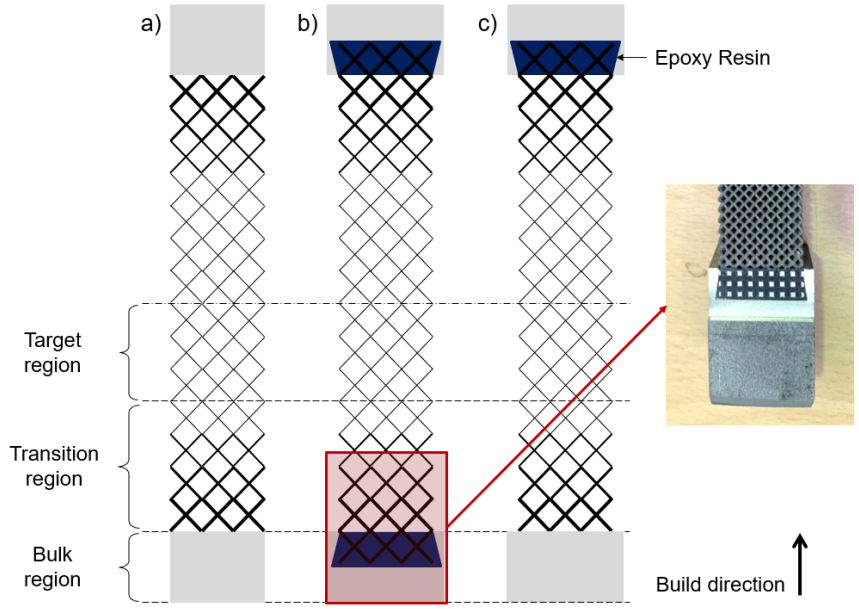

Figure 127: Differences between integral (a), modular (b) and hybrid (c) design approaches.

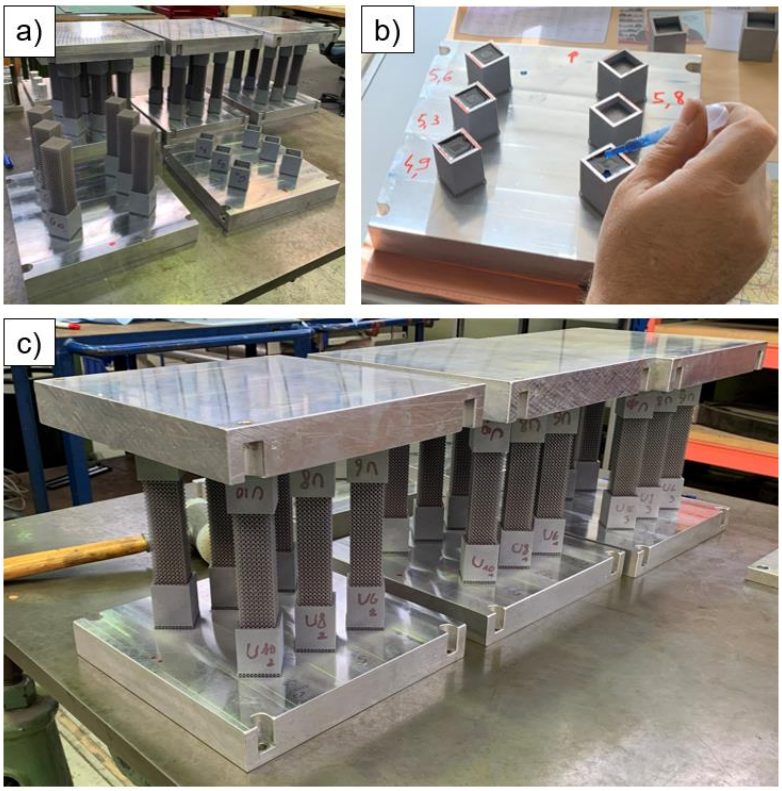

Figure 128: Manufacturing steps: separate manufacturing (a), resin preparation (b) and assembly (c).

5.2.3 Discussion

This investigation demonstrates that it is possible to find a single parameter set for the reliable additive manufacturing of horizontal surfaces with AlSi10Mg powder. This parameter set may not be optimal in terms of porosity and geometrical accuracy but fulfils its purpose. RUCs containing vertical lattice struts were successfully used as punctual support structures of 3.5 mm of distance, enabling an easy part removal and few entrapped powder particles compared to the standard support structures. However, for RUCs deprived from vertical struts like the bcc RUC, heat conduction issues occurred and led to curling or even swelling. Similarities with the stress distributions observed in chapter 4 can be observed as vertical struts offer the heat flow a direct connection to the built platform and the heat accumulation is located at the shell's borders. In the latter case, the heat jam created is similar to the edge effects. Therefore, a structural grading is able to not only homogenise the stress distribution but also the heat flow. It is supposed that a minimum diameter is required for the lattice struts to acts as a heat sink, reducing the universality of this solution. It is assumed that the heat conduction issues encountered for the bcc RUC are valid for all bending-dominated truss-based lattice structures printed vertically and, to a greater extent, to all structures without vertical connections to the build platform.

Among the available alternative solutions, grading the input parameters and optimising the scanning strategy in the first shell layers as reported in the literature [77, 144, 349,

350] are regarded as too extensive and specific to the machine and the powder material employed. In this regard, developing dimensionless numbers dedicated to that phenomenon is highly relevant. It is expected that the heat conductivity capacity depends on the volumetric energy input and on the RUC through the support area it offers as well as through the inclination angles of its struts. The roles of the temperature of the build platform and the surrounding powder need to be quantified as well. However, this is not in focus of the present work. The proposed modular approach offers a simple and universal basis for efficient design and can therefore be regarded as a cost- and time efficient solution that has to be deepened in future investigations.

6 Concept validation

This chapter deals with the experimental validation of the concept developed in chapter 4 as well as assessments on the structural integrity of the manufactured structures. Section 6.1 wants to provide a first insight on the impact of the manufacturing strategy on possible defect generation, i.e. if defects are prone to be triggered by a specific strategy or parameter combination. While both elastic and plastic domains are covered, particular attention will be given to the obtained effective stiffnesses as it was assumed in section 3.4 that defects have few to no influence on the elastic properties. Section 6.2 deals with the experimental validation of the notch reduction methods described in section 4.3. Section 6.3 deals with the experimental validation of the tensile specimen design based on a transition region made of graded lattice structures proposed in section 4.1. The tensile specimen design based on topology optimised bulk material proposed in section 4.2 is only briefly discussed in the framework of a proof-of-concept study as further parameter studies are required to reach design maturity. Details on both manufacturing and experimental setup are given in sections 3.3 and 3.4, respectively.

6.1 Influence of defects

In the framework of this investigation, lattice structures of cell size of 3 mm with the same target diameter (370 μm) are obtained through different exposure strategies and parameter combinations. Qualitative and quantitative assessments on defects such as strut diameter variation or roughness are made while the mechanical performance of lattice structures with different levels of deviation with the target design are compared. Since the same target strut diameter has to be manufactured for comparison purposes, it is assumed that the temperature gradients experienced by the investigated samples are similar to each other [112] (see section 2.3.6). Based on observations made for different contour approaches [265], a local texturing due to miniaturisation is expected to have low to no influence on the quasi-static mechanical behaviour of lattice structures. It is therefore assumed that texture analyses are not required for this study.

In order to contemplate the influence of process-induced defects on the static compression behaviour of the investigated lattice structures, configurations issued from a combination of strategy parameters leading to either high or low deviations are considered in order to offer a fair comparison between the employed manufacturing approaches. In order to compare the influence of manufacturing parameters, nine points per exposure type have been selected (Figure 129) so that they offer three comparable points in terms of either laser power, scanning speed or line energy (Eq.3). The investigated combination of scanning speed and laser power are annotated according to their respective position within the process window. Laser power values are indicated first. High values are located on the top (T) of the process window, average values in its middle (M), and low values on its bottom (B). Scanning speed values follow. High values are located on the right hand-side of the

process window (R), average values in its middle (M), and low values on its left hand-side (L). Parameters which are held constant are the designed diameter (100 μm and 370 μm for contour and hatch, respectively), the layer thickness (30 μm), the laser beam diameter (80 μm), the build platform temperature (125°C) and the rotation angle of hatch vectors between two successive layers (67°).

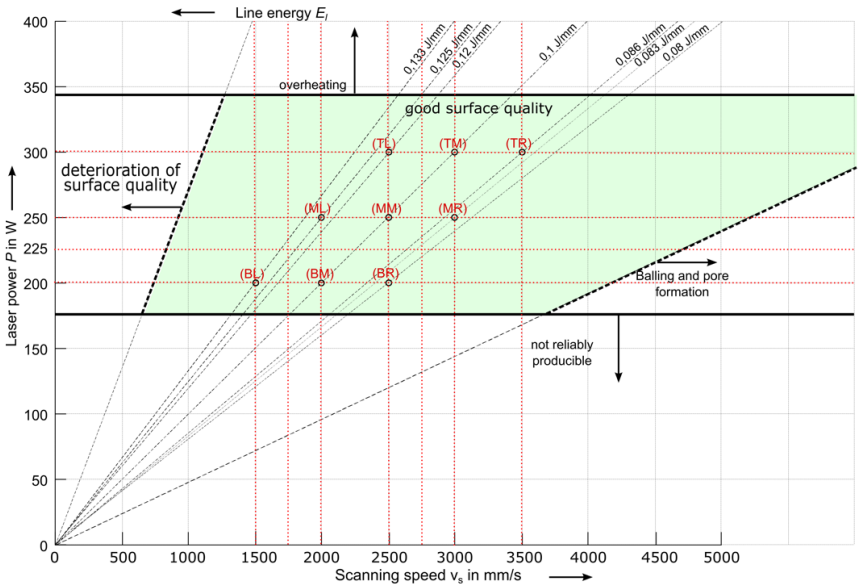

Figure 129: Investigated laser power and scanning speed combinations for both exposure strategies. Recompiled from [76]. Laser power abbreviations: T (top), M (middle), B (bottom). Scanning speed abbreviations: L (left), M (middle), R (right).

This study is divided into two parts. During the first part of the present work, preliminary investigations were performed onto 3x3x3 lattice structures in order to reduce the manufacturing efforts during the identification of parameters leading to the target diameter. For all the eighteen investigated configurations, three printed samples stochastically distributed on the platform were analysed microscopically at three statistical points each. The second part deals with the main investigation, which includes microscopic analysis as well as porosity analysis and mechanical testing. Lattice structures made of 10x10x15 RUCs were employed in the framework of the main investigation. In order to maintain an effective workload in the scope of this investigation, parameter combinations have been selected. On the one hand, the selection criterion for the hatch exposure is the achieved roundness of the lattice struts and, on the other hand, the contour exposure parameter sets were selected according to the roughness of the struts since a higher roundness is expected for this exposure strategy. In the main investigation, seven samples of each configuration stochastically distributed on the platform were manufactured. One sample was used for optical microscopy while the remaining six samples were dedicated to Archimedean density measurement and mechanical testing. For preliminary compression tests, a constant strain rate of 0.45 s^{-1} was used. During the main investigation, a constant strain rate of 0.045 s^{-1} was used. The sample for optical microscopy was grinded at two different horizontal planes: one at low height ($n_{RUC,z} = 3$) to verify the compliance with preliminary

studies, and one at a higher position ($n_{RUC,z} = 9$) in order to investigate on a potential influence of the build height on the lattice structure quality. Vertical grinding pictures were made at three different heights and all possible strut inclination angles were considered. The microscopic analysis was performed for at least nine statistical points for each data entry of each configuration.

6.1.1 Results

For the sake of brevity, only the outcomes of the main investigation are shown in this section. The selected hatch (H) and contour (C) parameter sets from the process window of Figure 129 are shown in Table 9. Among the investigated parameter sets depicted in Figure 129, the contour MM parameter set describes a combination of laser power and scanning speed of medium range, which corresponds to a line energy input of medium range as well. According to the results of the preliminary investigations, it yields the best contour roughness. In turn, the worst contour roughness was obtained for the TR parameter set, which is described by high laser power and high scanning speed, and corresponds to a low line energy input. The selected hatch parameter sets are hatch ML and hatch MR. According to preliminary investigations, they exhibit the best and worst hatch roundness, respectively. While both of them stand for a medium laser power, they correspond to low and high scanning speed, respectively. Besides, hatch MR corresponds to a low line energy input comparable to contour TR. Hatch ML displays the highest line energy input among all four selected parameter sets. In order to facilitate reading the reported tables throughout this section, the results from the parameters leading to the worst results of each selection criterion have been assigned a grey background.

Table 9: Selected parameter sets for the main investigation.

Exposure	Set	Criterion	t_{CAD} [µm]	P [W]	v [mm/s]	E_l [J/m]	bo [µm]	n_h [-]	d_h [µm]	OL [%]	t [μm]
C	MM	Ra_+	100	250	2500	100.0	-19.0	N/A	138.0	3.5	363.4±5.4
C	TR	Ra_-	100	300	3500	85.7	-10.3	N/A	120.6	8.8	369.2±4.3
H	ML	C_+	370	250	2000	125.0	29.1	3	136.2	15.0	379.2±7.6
H	MR	C_-	370	250	3000	83.3	26.5	3	155.6	-19.4	371.3±10.6

The very first observations made are of optical nature. As can be seen in Figure 130 (a), lattice structures printed with the contour exposure can be differentiated from the hatch ones by their brightness: the contour lattice structures appear to be much brighter. Furthermore, manufacturing difficulties have been encountered for the hatch samples. For hatch MR, f_2cc_z lattice structures were not reliably printable while bcc lattice structures display some local defects (Figure 130, b). Therefore, the mechanical investigations of hatch MR f_2cc_z lattice structures could not be carried out. However, the microscopic analysis was performed on sample rests. Concerning hatch ML, only few local defects were detected for f_2cc_z lattice structures and bcc samples did not exhibit defects at all.

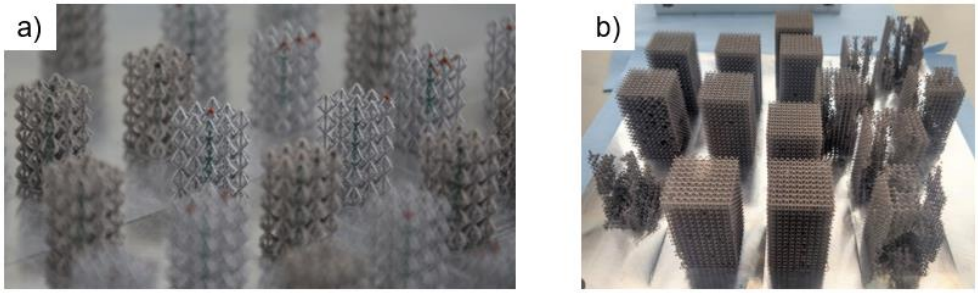

Figure 130: Observations on printed lattice structures: brightness difference (a) and manufacturing issues for the MR hatch parameter set (b).

Table 10 sums up the results obtained from horizontal grinding pictures at two different heights ($n_{RUC,z} = 3$ and $n_{RUC,z} = 9$) for the selected hatch (H) and contour (C) parameter sets. The printed equivalent diameters yield good accuracy when compared to the target diameter of 370 μm with deviations around 10 μm at most, which are in the same range of order of the standard deviations. The hatch exposure has the best accuracy while the contour exposure exhibits a lower standard deviation. Except for contour TR at low height, no noticeable dependency of the diameter accuracy on the inclination angle or on the build height was observed since diameter differences between f_2cc_z and bcc lattice structures remain in the range of order of the assessed standard deviations. Although the presented results for optical microscopy were performed on a single sample, they are compliant with the values obtained in the frame of the preliminary studies (e.g. f_2cc_z diameter of Table 10 vs. Table 9) and, thus, representative of the structure for the given parameter combination. The roundness results are in line with the expectations since contour yields better results than hatch. Only the best roundness obtained for hatch (ML) is in the range of order of the worst contour roundness (TR). A decrease of the roundness for the inclined bcc struts can observed, especially at higher positions in the lattice structure.

Table 10: Microscopic analysis results (horizontal grind).

Exposure	RUC	Set	t [μm]		C [-]	
			$n_{RUC,z} = 3$	$n_{RUC,z} = 9$	$n_{RUC,z} = 3$	$n_{RUC,z} = 9$
C	bcc	MM	363.2±3.6	361.8±3.1	0.66±0.04	0.36±0.06
C	f_2cc_z	MM	359.4±4.7	360.8±6.8	0.70±0.11	0.74±0.05
C	bcc	TR	357.4±5.5	371.9±7.2	0.56±0.08	0.40±0.09
C	f_2cc_z	TR	372.1±8.7	372.2±6.1	0.67±0.11	0.70±0.08
H	bcc	ML	371.1±10.5	381.0±6.5	0.42±0.05	0.28±0.05
H	f_2cc_z	ML	377.1±9.6	383.7±17.4	0.50±0.09	0.51±0.07
H	bcc	MR	364.8±11.9	373.3±11.0	0.34±0.04	0.22±0.02
H	f_2cc_z	MR	364.5±9.7	358.7±14.6	0.42±0.07	0.41±0.09

Table 11 sums up the roughness results obtained by vertical grinding pictures. The contour exposure offers an overall lower roughness than the hatch exposure, in particular for the maximum roughness. The main difference between both contour parameter sets is the

lesser roughness deviation between up- and downskin surfaces, which backs up the parameter selection described in Table 9. While contour exposure exhibits a clear relationship between downskin roughness and inclination angle, a similar trend cannot be identified for hatch exposure. However, different ranges of order are obtained for both hatch ML and hatch MR.

Table 11: Microscopic analysis results (vertical grind, roughness).

Exposure	RUC	Set	Strut angle [°]	R_a [μm]	$R_{a,up}$ [μm]	$R_{a,up}^{max}$ [μm]	$R_{a,down}$ [μm]	$R_{a,down}^{max}$ [μm]
C	bcc	MM	35	0.76±0.09	0.67±0.13	11.22±4.63	0.84±0.14	13.70±5.56
C	f_2cc_z	MM	45	0.71±0.11	0.54±0.10	8.37±3.42	0.87±0.24	15.54±8.26
C	f_2cc_z	MM	90	0.70±0.14	0.66±0.12	12.44±8.15	0.75±0.24	10.28±4.67
C	bcc	TR	35	0.95±0.21	0.75±0.25	14.95±13.03	1.16±0.36	35.20±14.74
C	f_2cc_z	TR	45	0.91±0.25	0.83±0.26	12.05±5.92	1.00±0.38	23.71±14.43
C	f_2cc_z	TR	90	0.74±0.09	0.76±0.16	13.54±6.61	0.72±0.16	13.32±7.91
H	bcc	ML	35	1.17±0.25	1.03±0.27	27.25±18.10	1.31±0.34	28.79±13.82
H	f_2cc_z	ML	45	1.27±0.24	1.09±0.32	24.24±13.21	1.44±0.32	39.21±16.76
H	f_2cc_z	ML	90	1.38±0.18	1.37±0.23	25.70±8.64	1.39±0.26	27.43±8.89
H	bcc	MR	35	1.83±0.47	1.72±0.61	49.36±27.75	1.94±0.45	47.59±17.30
H	f_2cc_z	MR	45	1.79±0.35	1.76±0.41	50.66±17.39	1.83±0.47	45.77±17.88
H	f_2cc_z	MR	90	1.76±0.30	1.83±0.46	51.19±24.33	1.69±0.15	42.47±9.91

Table 12 sums up the remaining results obtained from vertical grinding pictures. Similar to the roughness results, the contour exposure yields better results than the hatch exposure. Moreover, it can be noticed that, apart from the waviness results, the input parameters influence the manufacturing accuracy when comparing the parameter sets of the same exposure strategy (e.g. contour MM vs. contour TR). Both hatch and contour exposure exhibit a dependency towards the strut inclination angle with exception of contour waviness.

Table 12: Microscopic analysis results (vertical grind, other measures).

Exposure	RUC	Set	Strut angle [°]	t_{diff} [μm]	t_{var} [μm]	W [μm]
C	bcc	MM	35	65.33±12.79	13.20±2.02	18.81±4.16
C	f_2cc_z	MM	45	69.17±13.75	13.76±2.05	16.88±3.78
C	f_2cc_z	MM	90	53.36±13.78	10.07±2.63	12.04±3.13
C	bcc	TR	35	98.99±20.69	21.69±4.02	18.64±4.23
C	f_2cc_z	TR	45	90.72±22.27	20.15±5.67	17.85±4.80
C	f_2cc_z	TR	90	56.27±20.56	10.22±3.20	12.98±3.29
H	bcc	ML	35	146.88±33.83	35.71±10.90	21.68±4.66
H	f_2cc_z	ML	45	151.85±28.24	32.78±8.05	26.98±6.30
H	f_2cc_z	ML	90	118.20±27.76	26.22±6.19	20.28±2.75
H	bcc	MR	35	196.68±42.74	42.91±6.02	32.30±5.50
H	f_2cc_z	MR	45	173.04±32.63	39.15±7.25	32.28±6.08
H	f_2cc_z	MR	90	138.35±24.26	29.03±5.38	30.16±5.39

Table 13 sums up the results of the Archimedean density measurement. The overall achieved densities are around 99 % or above. The hatch exposure leads to denser lattice structures than the contour exposure. During this investigation, pores were often to be seen in the vicinity of the strut average line for contour struts (Figure 131). Contrarily to Delroisse et al. [305], Sairaiji et al. [304] or Dong et al. [321], no obvious aggregation of pores has been observed in the downskin part of inclined struts. No dependency of density towards strut inclination angle or strut number can be observed with the present results. For both exposure strategies, the lowest densities were achieved for higher overlap values, namely contour TR and hatch MR (see Table 9), and correspond to the lowest line energies.

Table 13: Density results.

Exposure	RUC	Set	ρ^* [%]
C	bcc	MM	99.23±0.51
C	f_2cc_z	MM	99.23±0.12
C	bcc	TR	99.03±0.18
C	f_2cc_z	TR	98.85±0.14
H	bcc	ML	99.62±0.09
H	f_2cc_z	ML	99.77±0.02
H	bcc	MR	99.53±0.26
H	f_2cc_z	MR	N/A

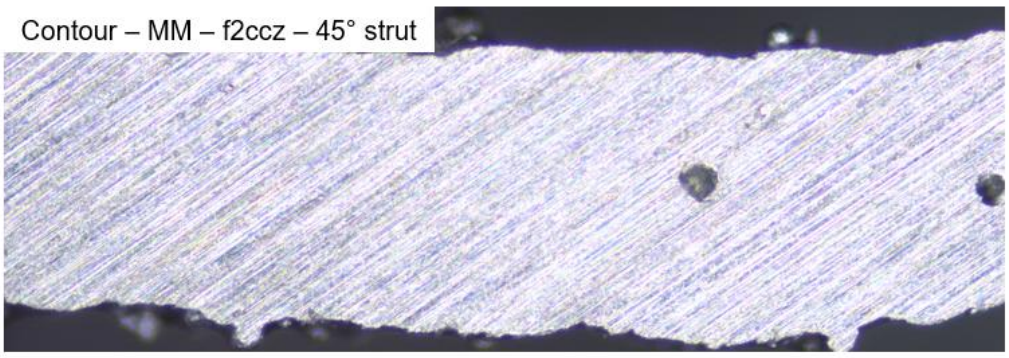

Figure 131: Example of pore close in a contour strut.

The following mechanical properties were assessed during compression tests and reported in Table 14: the effective stiffness, E^* the yield stress R_{eH} and the yield strain A_{eH}. For each investigated unit cell, no differences between manufacturing approaches were observed. Typical shear band failures corresponding to the respective unit cell configuration as reported in literature [39] were observed. The best mechanical properties were obtained for the contour parameter set with the worst results in terms of structural accuracy, namely contour TR. Hatch ML, which exhibits significantly worse structural accuracy, demonstrates a similar mechanical performance despite local defects, yield strain excepted. Hatch MR bcc lattice structures deliver the worst results due to the presence of defects (Figure 130). The assessed lattice stiffnesses were compared to the analytical stiffness $E^*_{ana,t}$ based

on the model of Souza et al. [43] (see section 3.2.1). Tolerance ranges were calculated considering both achieved diameter and standard deviations respective to each investigated configuration reported in Table 10. It can be observed that the stiffnesses of f_2cc_z lattice structures match the tolerance ranges. However, the stiffness of contour TR samples is ranked in the upper range of analytical stiffness, whereas hatch ML and contour MM lean towards its lower boundary. Moreover, apart from hatch MR, the experimental stiffnesses of bcc lattice structures are above the analytical ones.

Table 14: Compression tests results.

Exposure	RUC	Set	R_{eH} [MPa]	A_{eH} [%]	E^* [MPa]	$E^*_{ana,t}$ [MPa]	E^*_{ana} [MPa]
Contour	bcc	MM	1.36±0.07	10.28±0.15	55.2±2.9	38.8	[37.3; 40.3]
Contour	bcc	TR	1.73±0.07	11.29±0.20	72.5±3.9	36.5	[34.3; 38.6]
Hatch	bcc	ML	1.75±0.03	8.66±0.21	69.0±1.4	42.2	[37.7; 47.1]
Hatch	bcc	MR	0.93±0.02	7.80±0.44	35.5±0.6	39.5	[34.7; 44.7]
Contour	f_2cc_z	MM	5.63±0.48	3.02±0.44	853.3±41.6	877.2	[852.5; 902.2]
Contour	f_2cc_z	TR	6.42±0.12	3.38±0.11	979.9±37.6	946.7	[898.7; 996.2]
Hatch	f_2cc_z	ML	6.40±0.35	2.89±0.21	932.8±50.6	974.5	[920.7; 1030]
Hatch	f_2cc_z	MR	N/A	N/A	N/A	N/A	[853.3; 958.2]

6.1.2 Discussion

This investigation demonstrates that it is possible to print lattice structures of a given target design by using different exposure strategies and parameter combinations. However, the manufactured structures are not equivalent to each other, having their own particularities.

First of all, manufacturing issues that did not occur at small scale (3x3x3) have been encountered for the hatch exposure. These issues are due to the vector assignment in the employed commercial software suite. In the ideal case, hatch vectors are assigned symmetrically distributed on the strut cross-section. However, vectors are assigned to the design space defined by the build platform. This leads to a position dependency of the vector assignment (Figure 132, a). The absence of a symmetric pattern implies that the rotation centre of hatch vectors is not located in the strut cross-section. As a consequence, hatch vectors between two l_n and l_{n+1} are not concentric to each other and the cross-section is not consistently exposed (Figure 132, b). This means that the employed commercial software was not initially developed for the additive manufacturing of small-scale features.

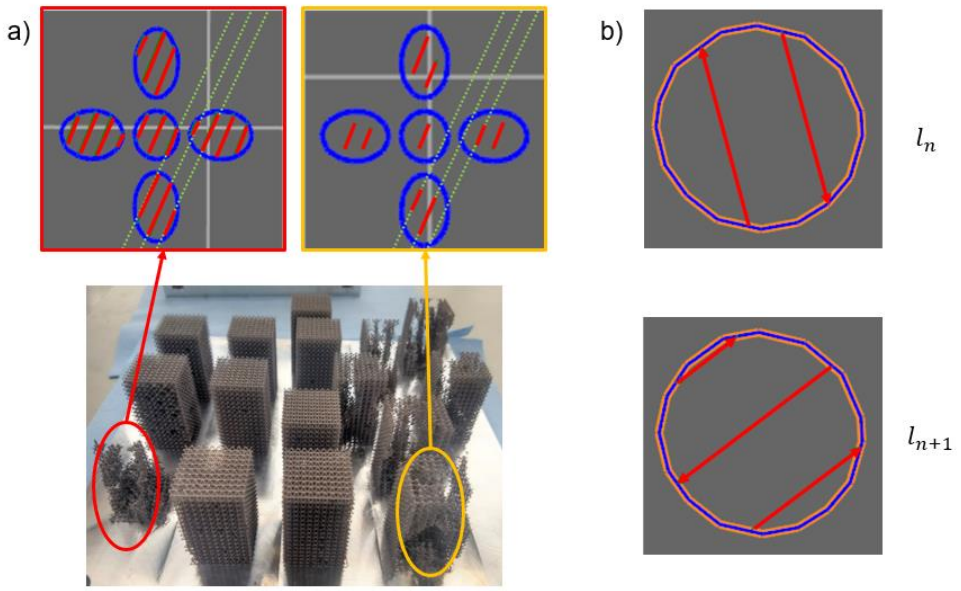

Figure 132: Issues encountered with hatch vectors – location dependency (a) and position shift between two layers (b).

When successfully manufactured, hatch samples exhibit more geometric deviations but are denser than contour ones. As already highlighted in section 5.1, the contour exposure strategy offers better roundness and surface roughness in a more consistent way, with low standard deviations even for inclined struts. However, some observations are against expectations and findings from literature. On the one hand, the worst contour lattice in terms of geometric accuracy yields the best mechanical results and, on the other hand, hatch samples can exhibit mechanical properties such as stiffness or yield strength in a range of order similar to the best contour samples. Sairaiji et al., for example, observed that contour samples could achieve a higher compressive failure strength than the hatch ones [304]. Liu et al. [317] and Li et al. [328] identified the diameter difference as responsible for the differences in yield stresses. The lower yield strain reached by hatch samples follows the trend of the work from Cao et al., who identified a relationship between strut thickness variation and energy absorption [319]. However, this statement cannot be confirmed in the framework of this study because the local defects of hatch lattice structures may have played a non-negligible role.

The differences between the manufactured samples can be explained by the influence of the melt pool and the specificities of each exposure strategy as highlighted in sections 2.3.6 and 5.1. The scanning paths are specific to each exposure strategy and, thus, interact differently with the melt pool. The lesser geometric accuracy of the hatch exposure can be explained through the synergy between melt pool depth, layer thickness and vector rotation angle between two layers. The hatch parameter set of higher line energy (ML) yields a better accuracy than the one with lower line energy (MR). Since the melt pool depth decreases for lower energy input, especially for higher scanning speed [103, 349], it can be stated that a higher melt pool depth seems beneficial for geometric accuracy by hatch. This can be explained by the local re-melting of aggregated particles that takes place if

hatch vectors are aligned to each other after a number of layers corresponding at most to the melt pool depth. In the contrary case, free or even overhanging surfaces are created and can therefore lead to roughness in the range of order of one or more powder particles. It can therefore be deduced that the rotation angle between two hatch layers hampers a local re-melting of aggregated particles if not adjusted to the melt pool depth. This hypothesis is supported by the afore-discussed printability issues of hatch samples, for which the standard vector rotation angle of 67° was maintained. Since hatch vectors located at the vicinity of the strut borders are affected, it can be further deduced that the beam offset plays a non-negligible role on the mechanical behaviour of lattice structures, too. In contrary to hatch exposure, contour exposure offers the same scanning path independently from the layer thickness and, thus, does not require any rotation angle. This enables a more constant and homogeneous re-melting of aggregated particles, which improves roughness and explains the observed differences in brightness with hatch samples. The contour parameter set of lower line energy (MM) yields a better accuracy than the one with higher line energy (TR). This means that a narrow melt pool is beneficial for geometric accuracy by contour, which is in line with the observations from Vrána et al. [301] and Großmann et al. [76]. However, the same sources state that a higher energy input leads to less dense structures [76, 301], which is not verified here. In the present results, a higher line energy does not correlate with the presence of pores for both hatch and contour exposure strategies. Lattice structures with the least pores were obtained for hatch ML, which corresponds to the highest investigated energy input, whereas contour TR is the least dense of all configurations despite lower line energy. This can be explained with one decisive feature: the overlap.

Literature has proven that, for both exposure strategies, the overlap has a non-negligible influence on porosity. Yadroistev et al. [102] and Han et al. [103] stated that reducing the hatch distance, i.e. increasing the overlap for similar line energy, results in increased porosity. This aligns with the results of this investigation. Großmann et al. worked at fixed CAD diameter [76] and, thus, higher energy input automatically resulted in bigger overlapped surfaces. Vrána et al. identified an ideal overlap for AlSi10Mg lattice structures between 25 % and 40 %, with excellent porosity results for 35 % [298, 301]. It has to be further noted that, in the framework of this investigation, obtained pores tend to be due to keyholing rather than lack-of-fusion (see section 2.1.3). An increased number of Keyhole pores is typical of instable melt pool behaviour and takes place for big overlap, e.g. contour TR, while lack-of-fusion pores occur when two melt tracks lie too far from each other, e.g. hatch MR. Furthermore, the overlap also explains the better accuracy of hatch ML when compared with hatch MR since enabling local re-melting. This is in line with the discussion about the melt pool depth and vector assignments above, and highlights the influence of the hatch distance on the geometric accuracy as well.

The results of the mechanical investigation prove that, when there is little or no overlap, the stiffness tends to be governed by the smallest load carrying diameter and, thus, that local particle adhesion does not contribute to the global load carrying behaviour of the

lattice structure. This is the case for hatch ML and contour MM f_2cc_z as well as hatch MR bcc lattice structures, whose assessed effective stiffnesses are comparable to the lower tolerance range of analytical stiffnesses. Once again, the discussion about the melt pool depth and vector assignments suggests that the rotation angle between two hatch layers negatively impacts the load carrying behaviour of the structure. In the case of a non-negligible overlap, an increase of the stiffness is observed. This is the case for contour TR f_2cc_z lattice structures and for all bcc lattice structures except hatch MR. The stiffness of contour TR f_2cc_z lattice structures meets the highest analytical stiffness while the stiffnesses of all bcc lattice structures are way above the analytical ones. It can be consequently stated that the influence of overlap is proportional to the strut inclination. This is due to the proportionally higher overlapped area in an inclined bcc strut because of its elliptical cross-section. Sos et al. [265] showed that overlapped areas of AlSi10Mg contour lattice structures exhibit different texturing and, thus, yields locally higher stiffnesses. Although this observation was made for heat-treated samples, it can be assumed that similar texture is obtained for as-built brittle samples. The role of the overlap in the global load carrying behaviour of additively manufactured lattice structures is therefore demonstrated. It is further deduced that the overlap in struts located in the main load path is the most relevant for the static load case. The only difference in the best mechanical performance between hatch and contour lies in the failure strain. Here, it can be speculated that one constantly exposed bigger area (contour) is more beneficial to the deformed state, e.g. for better energy absorption, than evenly distributed local overlapped areas (hatch). However, once again, the local defects of the hatch lattice structures may have played a non-negligible role. Furthermore, it can be stated that, for the same target diameter, the hypothesis of comparable texturing is not valid. Local texturing is process parameter dependent and it has a non-negligible impact on the global mechanical properties of additively manufactured lattice structures.

6.2 Transition between unit cells

Due to the issues encountered with the design of graded configurations, only ungraded lattice structures are investigated. In the framework of the experimental investigation, 5 samples of each considered configuration were investigated. As for the numerical part, the initial unit cell configurations are compared to, on the one hand, a minimum equivalent curvature radius R_1 ($\gamma = 0.135$) and, on the other hand, the identified optimal equivalent curvature radius R_2 (Table 5, Table 6). The value $\vartheta = 0.5$ is considered for the investigation of the f_2cc_z unit cell as well. The challenges of accurately manufacturing the proposed shapes at a small scale are identified and the relevance of design notches is compared to the influence of manufacturing defects.

All the relevant manufacturing data are listed in Table 15. AlSi10Mg lattice structures consisting of 10x10x10 RUCs were additively manufactured. The cell size of the RUCs is 3 mm and their target diameter 370 μm, leading to an aspect ratio of 8.1. This enables

investigating high aspect ratios for reasonable sample size and, thus, manufacturing time. In order to prevent from a potential influence of the manufacturing parameters on the mechanical properties of the investigated specimens, a constant parameter set based on the contour exposure strategy leading to excellent manufacturing accuracy was selected (see sections 5.1 and 6.1). The employed manufacturing parameter set led to an average as-built strut diameter of $370 \pm 13\ \mu$m for four printed samples of the fourteen investigated configurations (three statistical points minimum). Density measurements were performed for all manufactured samples. One supplementary sample of each specimen was grinded in order to measure the obtained strut diameters and observe the nodal area. Pictures of the cross section at half strut depth were obtained by grinding the lattice directly. In the framework of compressive tests, a constant strain rate of $2 \times 10^{-3}\ s^{-1}$ was used for the preliminary test. During the main compression test, a constant strain rate of $10^{-3}\ s^{-1}$ was used until the first maximum compressive strength and, after the first specimen failure, a constant strain rate of $10^{-2}s^{-1}$ was used until 40 % of the total strain was reached. The stiffness of the machine was considered by correcting the measured displacement of the crosshead. Further details on both manufacturing and experimental setup are given in sections 3.3 and 3.4, respectively.

Table 15: Manufacturing parameters (cell transition investigation).

Process parameter	Value	Unit
Cell size	3	mm
Unit cells per direction	10x10x10	--
Base CAD diameter	100	μm
Scanning strategy	Contour exposure	--
Laser power	250	W
Laser scanning speed	2500	mm/s
Laser beam diameter	80	μm
Layer thickness	30	μm
Build platform temperature	125	°C

6.2.1 Results

The results obtained for the bcc unit cell are shown in Figure 133, Figure 134 and Figure 135. The brittle behaviour of as-built AlSi10Mg can be identified in the stress-strain curves of Figure 133 by the absence of a plateau stress and the consecutive stress peaks standing for sequential load redistribution and consecutive failure (see section 2.3.4). An overall increase in effective Young's moduli estimated by means of hysteresis at R_2 compared to R_1 can be identified, while R_1 do not offer significant improvement compared to the initial configuration (Figure 134). A similar trend is observed from both first maximum compressive strength and energy absorption per unit volume until compressive failure (Figure 135). However, the values for FRM at R_2 are slightly lower than what could be expected. A trend between the relative material density of the specimens and the size of the fillet curvature cannot be established (Figure 134).

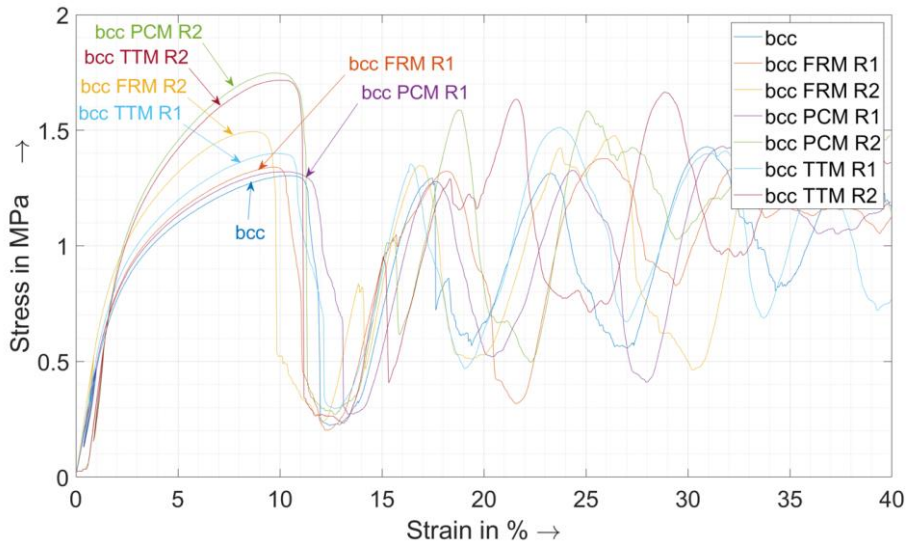

Figure 133: Experimental results (bcc): stress strain curve.

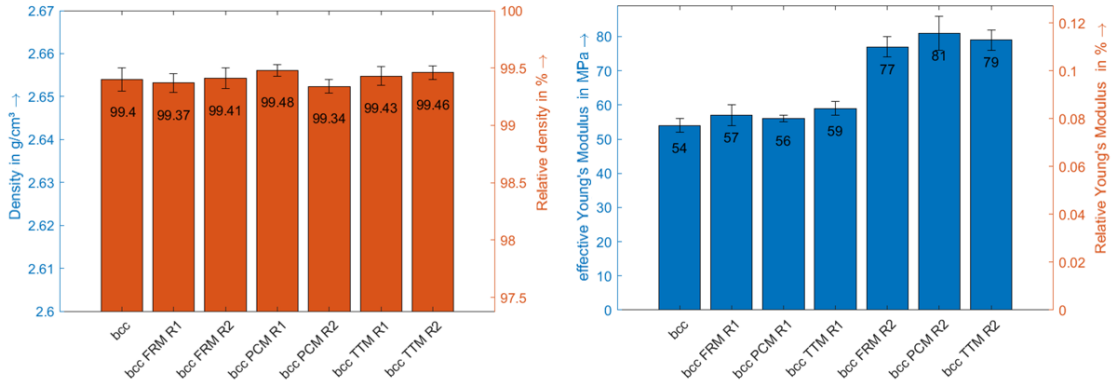

Figure 134: Experimental results (bcc): density (left) & Young modulus (right).

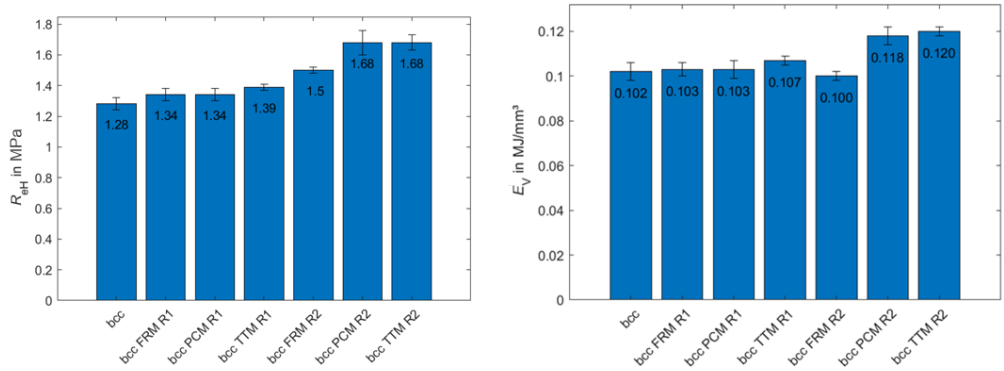

Figure 135: Experimental results (bcc): first maximum compressive strength (left) & energy absorption (right).

The results obtained for the f_2cc_z unit cell are shown in Figure 136, Figure 137 and Figure 138. Similar to the bcc structures, a brittle behaviour can be observed for f_2cc_z cells too (Figure 136). Unlike the numerical results for bcc, no significant trend for increasing

equivalent curvature radius can be identified. Only slight improvements from the original configuration in terms of effective stiffness and energy absorption can be noticed. Compared to bcc specimens, the f_2cc_z samples have a lower relative material density.

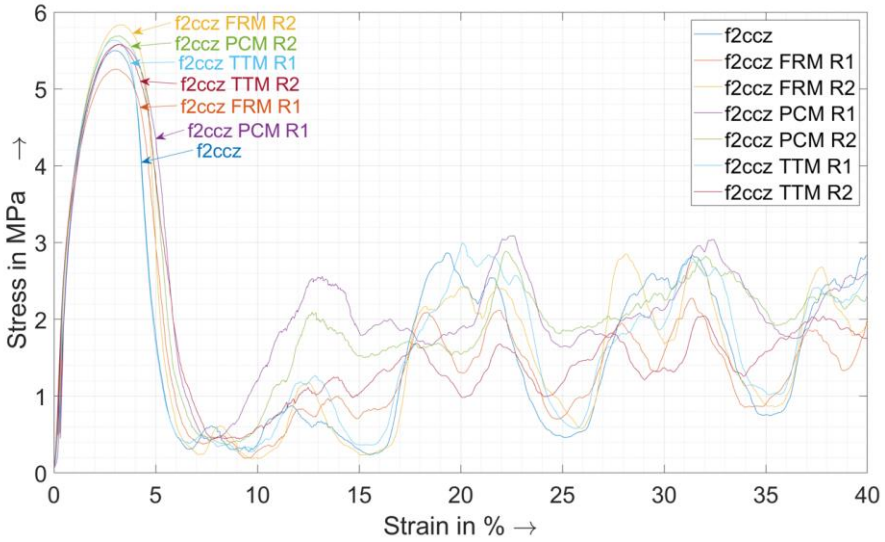

Figure 136: Experimental results (f_2cc_z): stress strain curve.

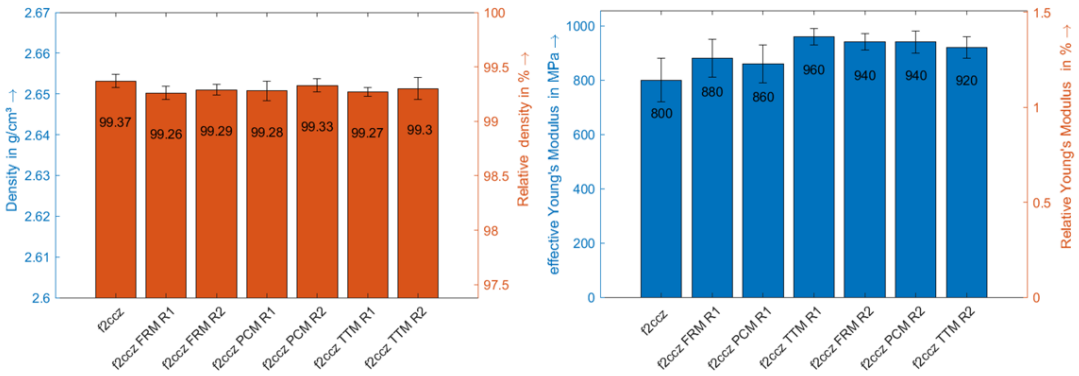

Figure 137: Experimental results (f_2cc_z): density (left) & Young modulus (right).

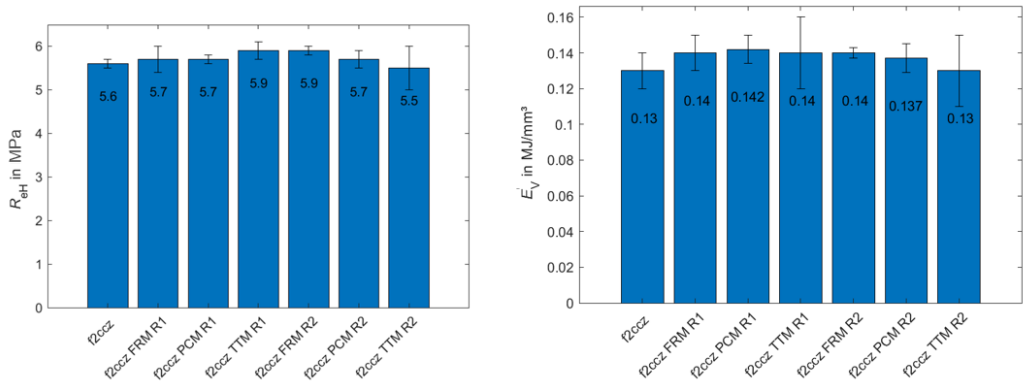

Figure 138: Experimental results (f_2cc_z): first maximum compressive strength (left) & energy absorption (right).

In order to provide more arguments for discussion, Figure 139 and Figure 140 offer an insight into the manufacturing quality of the bcc and f_2cc_z lattice structures, respectively. Overall, it can be observed that lateral fillets were better built than those at both up- and down-skin areas. A significant change in shape is only noticeable for bcc at R_2, with a visible increase in the fillet curvature size (Figure 139, right). Apart from an apparent slightly smoother transition at the up-skin area of R_2, clear differences between f_2cc_z unit cells are not distinguishable. Compared to the bcc samples, a lateral bottlenecking of the nodal area of f_2cc_z cells can be identified.

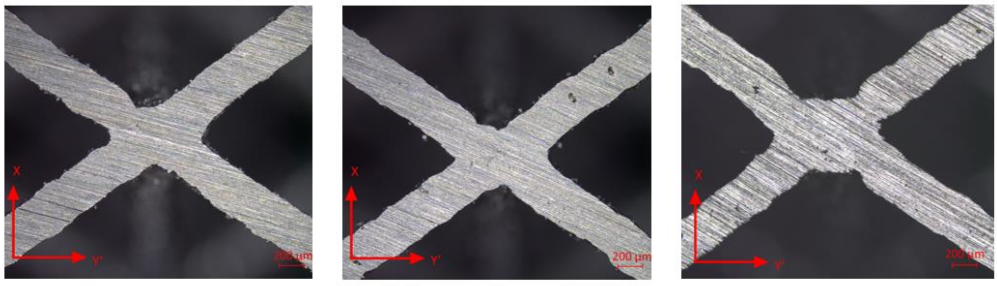

Figure 139: Manufacturing quality (bcc): initial configuration (left), FRM at R_1 (centre) and PCM at R_2 (right).

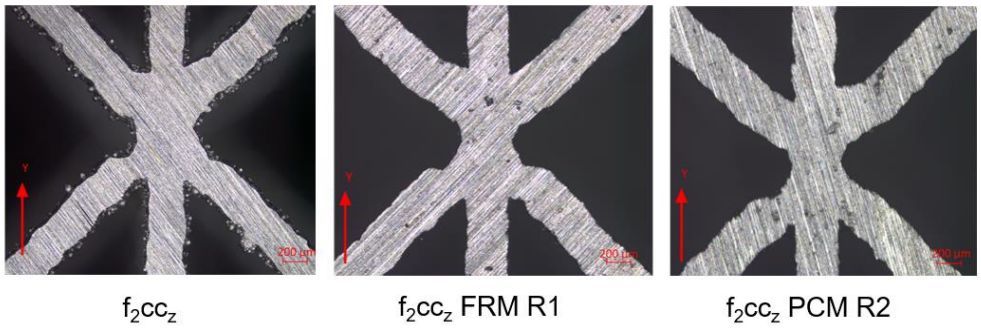

Figure 140: Manufacturing quality (f_2cc_z): initial configuration (left), FRM at R_1 (centre) and PCM at R_2 (right).

6.2.2 Discussion

As far as the bcc specimens are concerned, the experimental results confirm the numerical trends of section 4.3 and from literature [344, 366]. Despite potential manufacturing defects, the notch reduction concepts can be validated. The stress concentration occurs in the inner lateral part of the strut junction (Figure 81 (a), Figure 85), which is the most reliably manufactured nodal feature of the bcc structures.

However, the manufacturing defects seem to have a significantly higher influence on the mechanical properties of the f_2cc_z structures, which is in line with the observations made by Leary et al. [296]. Similar to Dallago et al. [347], applying notch reduction methods to f_2cc_z structures do help, just in a restricted manner. The reason for the limited impact of

notch reduction methods is the lack of visible geometric difference. This is mostly due to the staircase effect (see section 2.1.3) that hinders the differentiation of the already subtly different fillet shapes at the small scale. In the framework of this investigation, the relationship between the design space occupied by the implemented curvature radius is equivalent to some layers of printed material only (Table 15). This results in difficulties for precise and accurate reproduction of the CAD geometries and, thus, hamper the effectivity of the developed approaches.

Another potential contributor to inaccuracies is the instable melt pool behaviour in the nodal area, impacting the design space width *w* as well. This instability is due to, on the one hand, the high of number of struts joining together in this area (e.g. up to 10 for f_2cc_z) and, on the other hand, on the employed manufacturing strategy (see section 2.3.6). This is in good agreement with the fact that bcc specimens have higher relative material density compared to the f_2cc_z ones since they have less struts joining at the nodal area. However, this effect cannot be quantified with current investigation data. No noticeable influence of curvature radius on porosity was identified, which means that it does not have a direct influence on the melt pool for the selected manufacturing parameters.

Conclusively, it can be stated that the size of the fillet curvature plays a more significant role in determining the mechanical properties of the specimen compared to the influence of different notch optimisation methods used at such small scale. The experimental results of bcc FRM at R_1 do not demonstrate the theoretical advantage over PCM or TTM which is explained by the geometric similarities due to manufacturing constraints. At larger scale, where the reliable manufacturability of fillet curvatures shall be ensured, the proposed design rules should follow the presented numerical results and considerably increase the mechanical properties as well [347].

6.3 Tensile specimen design

Section 6.3.1 reports the investigation of the tensile specimen design employing the topology-optimised bulk structure developed in section 4.2 while section 6.3.2 focuses on the structurally graded samples proposed in section 4.1.

6.3.1 Load introduction via bulk part modification

Due to the need for parametric studies to refine the design (section 4.2) and to the manufacturing issues encountered for the reliable manufacturing of the lattice-to-bulk transition for high lattice structures (section 5.2), the validation of this design concept can only take place in the framework of a proof of concept study.

The design proposal with samples suited for a machine connection of circular cross-section depicted in Figure 66, c and d, was investigated. Similar to section 6.2, ungraded lattice

structures were manufactured using a constant parameter set based on the contour exposure strategy leading to excellent manufacturing accuracy was selected (see sections 5.1 and 6.1). The investigated structures were 10×10×10 bcc and 10×10×12 f_2cc_z lattice structures, based on the considerations on the RUC-specific load paths as discussed in section 4.1. The employed laser power, scanning speed and cell size are the same the ones listed in Table 15. The bulk region, including pillars, was assigned the parameter combination developed in the framework of the monolithic additively manufactured samples f_2cc_z lattice structures reported in section 5.2, i.e. the combination of laser power of 315 W and scanning speed of 1700 mm/s without hatch separation pattern while the standard hatch distance of 190 μm, was kept constant. Layer thickness and build plate temperature were held constant at 30 μm and 190°C, respectively. The tensile tests were carried out on a Schenk Trebel RM600 tensile tester at the Center for Structural Materials (MPA-IfW) of the Technical University Darmstadt. The test procedure was carried out according to the standard DIN 50099, which follows the concept of compression testing on cellular metals [337]. For each configuration, five samples were investigated. All of them showed similar behaviour and, thus, the reported samples in Figure 141 are representative for all the tensile test outcomes.

No major imperfections resulting from the design were visible. Both lattice structures showed the typical fracture pattern of stretching- and bending-dominated lattice structures, respectively. Both displayed shear band failures, which developed after a load redistribution into the lattice struts in the vicinity of the initially failed one. It was observed that the failure path of the f_2cc_z specimens failed at the interface to the transition area, while this was not the case for the bcc specimens. Similar to section 4.1, it can be supposed that the typical load and, therefore, failure paths depend on the unit cell considered. Therefore, to prevent a failure of the f_2cc_z lattice structure in the vicinity of the transition area, the aspect ratio of the tensile specimen should be increased.

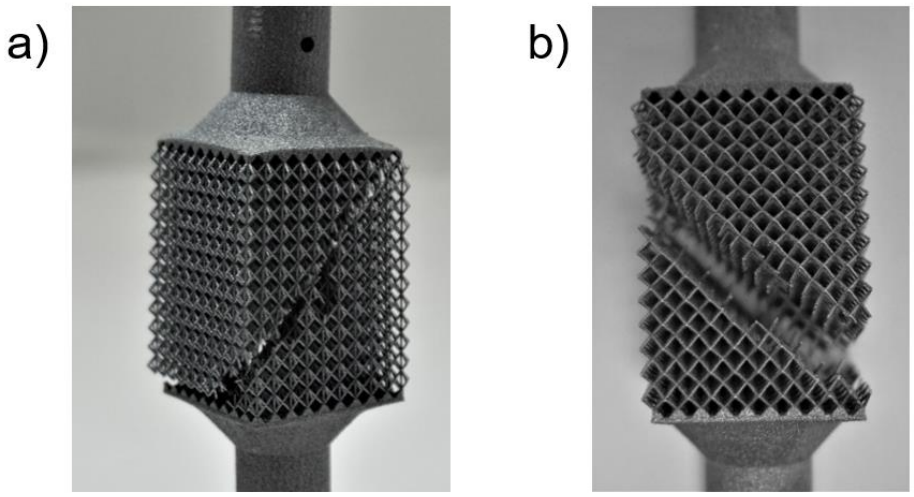

Figure 141: Failed specimens: f_2cc_z (a) and bcc (b).

6.3.2 Load introduction via structural grading

In the framework of this investigation, a comparison between both analytical and experimental stiffnesses of the investigated lattice structures in the as-built state is performed. Therefore, results others than stiffness and pictures of failure modes are not reported. Based on the experimental results, the effectiveness of the proposed sample design with a structurally graded load introduction is confronted to the one of the initial ungraded sample.

In order to reduce the manufacturing efforts, only the RUCs employed for the initial development of the sample design methodology of section 4.1 are investigated, i.e. f_2cc_z and bcc for aspect ratios of 6, 8 and 10. In order to keep the sample size as small as possible, lattice structures of 8 RUCs in the plane perpendicular to the loading direction were investigated as recommended in section 4.1.4. The chosen cell size was selected to offer a compromise between reliable manufacturing and sample size. As local defects were observed for lattice structures of a cell size of 3 mm and an aspect ratio of 10 (involving strut diameters down to 220 μm), the cell size was changed to 3.5 mm. This results in graded lattice structures of strut diameters varying from 260 μm to 1 mm. The number of RUCs in the loading direction was limited to 26 in order to be able to produce the tensile samples in one go, i.e. without refilling the feed region (Figure 2). According to Table 3, this leads to bcc samples made of 9 RUC layers (8 graded and 1 ungraded cell layers) in the transition region and of 8 RUCs in the target region. The f_2cc_z samples consist of 12 RUC layers in the transition region (9 graded and 3 ungraded cell layers) and of 2 in the target area. According to Figure 59 and Figure 60, the smaller target region of the f_2cc_z samples do not impact the performance of the developed grading approach once the uniaxial state is reached. Supplementary data on the tensile specimen design are reported in appendix G.

The investigated lattice structures were manufactured with the hatch parameter set reported in Table 8 of section 5.1.4. In order to account for the platform position dependency of the vector assignment (Figure 132, a) and, thus, improve the manufacturing accuracy, the lattice structures were positioned so that the hatch vectors exhibit a 45° vector with the main axes of the ellipse of the inclined strut's cross-sections (Figure 142, b). Doing so avoids the random assignment of one single vector (Figure 142, a). The bulk regions of both f_2cc_z and bcc were manufactured according to both integral and modular designs reported in section 5.2, respectively. For consistency, the parameters employed for the bulk region correspond to the one of the monolithic f_2cc_z samples. Layer thickness and build plate temperature were held constant at 30 μm and 190°C, respectively. In the framework of tensile tests, a preliminary loading of 100 N was applied and a constant strain rate of 0.3 mm/s was used. At least three samples of each ungraded configuration and five samples of each graded configuration were investigated. Further details on both manufacturing and experimental setup are provided in sections 3.3 and 3.4, respectively.

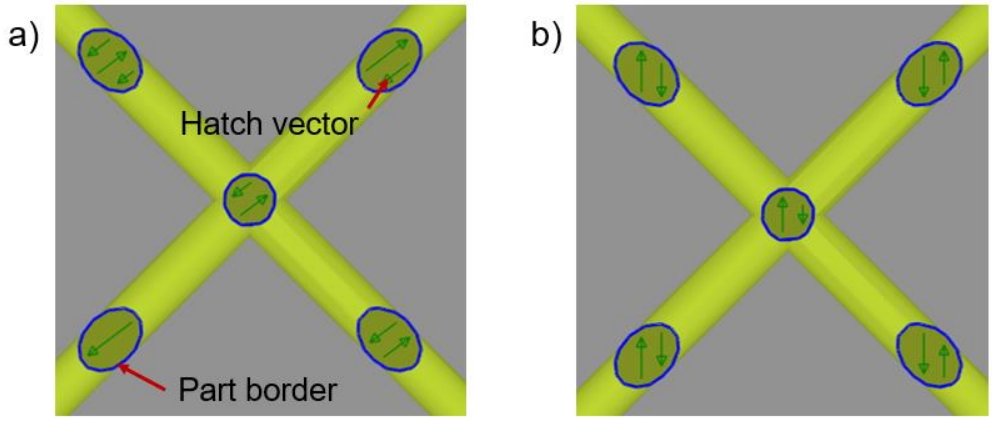

Figure 142: Relative position of lattice structures with respect to hatch vectors: cross sections' axes aligned with hatch vectors (a), 45° angle between cross-sections' axes and hatch vectors (b).

Figure 143, Figure 144 and Figure 145 show the failure modes observed for f_2cc_z ungraded, f_2cc_z graded and bcc samples, respectively. For comparison purposes, both transition and target regions of the graded sample design are depicted as the samples' upper parts are aligned. The regions with graded and ungraded cells are indicated as well. The ungraded f_2cc_z samples of aspect ratio of 6 show systematically, with five out of five samples, an almost flat failure in the vicinity of the bulk region (Figure 143, a and b). Manufacturing issues are excluded as failure occurred at the lower bulk region, which was manufactured with direct supports, and even in the case of overlap between layers of the upper bulk region and of the lower lattice transition region. Samples of other aspect ratios exhibit the typical shear band along the diagonal struts (Figure 143, c to f). In most cases (nine out of twelve), it is visible that failure was initiated at the sample's corner (Figure 143, c and e) while the other cases hint at a failure initiated in the middle of the plane perpendicular to the loading direction (Figure 143, d and f). However, none of the observed failures can be considered as located in the sample's centre as far as the indicated target region is concerned. The f_2cc_z graded samples exhibit a systematic failure in the target region or its vicinity, which correspond to the ungraded cell region. The samples of aspect ratio of 6 hint at a systematic, with five out of five samples, failure initiation in the centre of the target region (Figure 144, a and b). Samples of other aspect ratios exhibit the typical shear band along the diagonal struts, eight out of ten starting from the sample's edge (Figure 144, c and e) and the rest starting from the middle of the plane perpendicular to the loading direction (Figure 144, d and f). All the bcc samples exhibit the typical shear band along their inclined struts. While failure was initiated at the sample's corners or its vicinity for all ungraded configurations, the graded configurations exhibit a systematic failure in the target region or its vicinity, which correspond to the ungraded cell region.

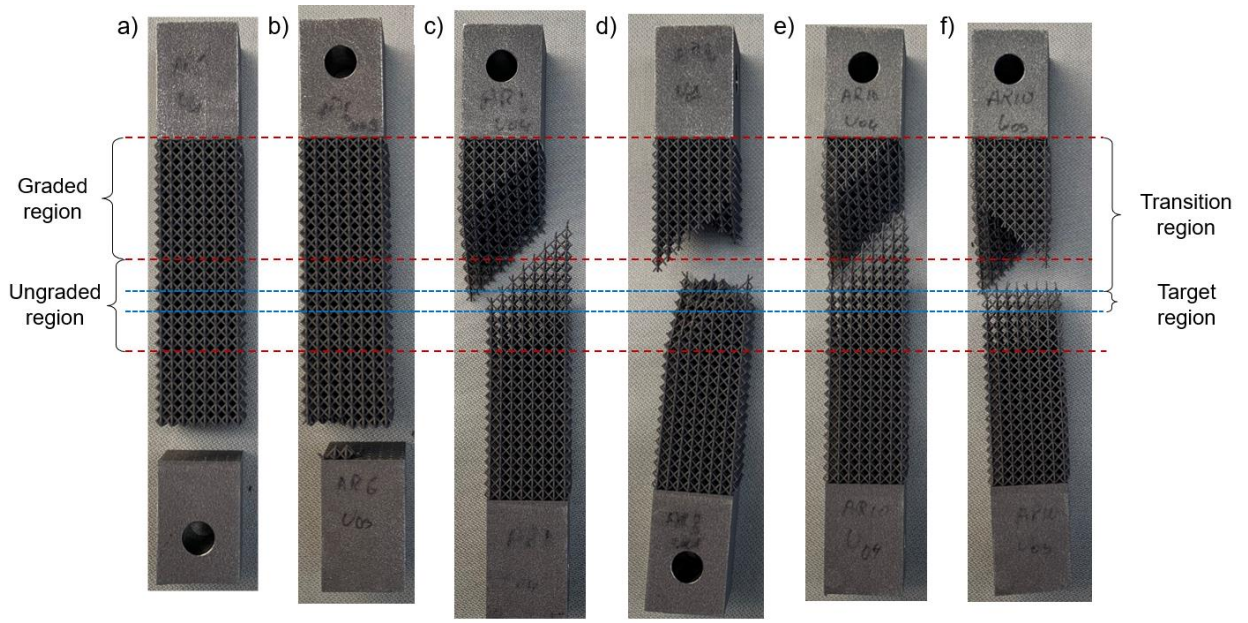

Figure 143: Typical tensile specimen failures (f_2cc_z, ungraded): AR6 (a, b), AR8 (c, d), AR10 (e, f).

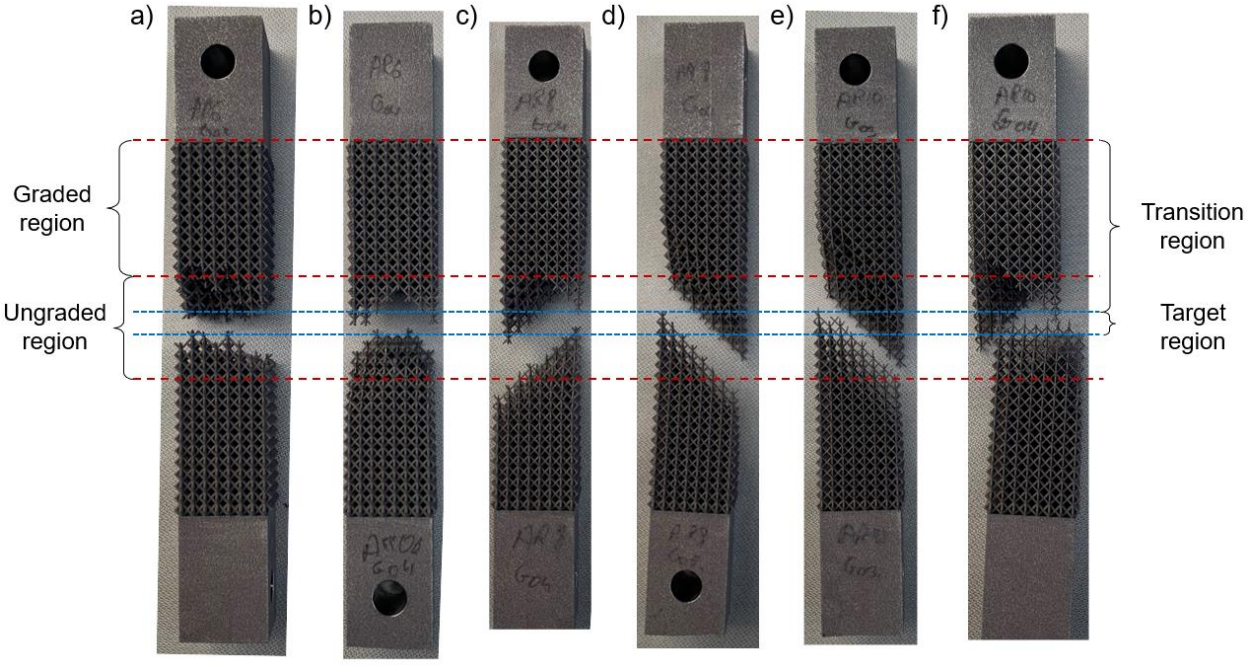

Figure 144: Typical tensile specimen failures (f_2cc_z, graded): AR6 (a, b), AR8 (c, d), AR10 (e, f).

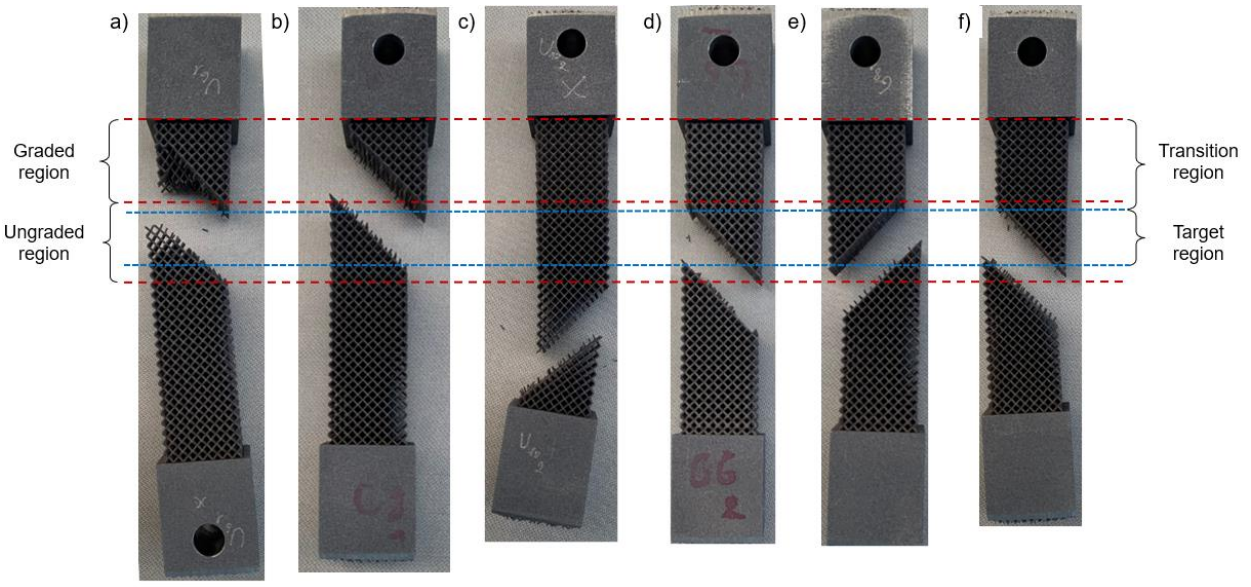

Figure 145: Typical tensile specimen failures (bcc): AR6 ungraded (a), AR8 ungraded (b), AR10 ungraded (c), AR6 graded (d), AR8 graded (e), AR10 graded (f).

Figure 146 depicts typical stress-strain diagrams obtained for all investigated samples. Similar to the observation made by Rehme [247], a settling of the lattice cells can be observed. This settling depends on the investigated RUCs and its aspect ratio: it was observed that the settling range is proportional to the aspect ratio while being narrower for bcc samples. No difference between the bcc bending- and f_2cc_z stretching- dominated were observed because of the brittle state of the as-built sample. Both crack initiation and propagation are hardly distinguishable on the diagram although they were clearly audible while performing the tensile tests. From the tone that lattice struts made during rupture, it was deduced that the thinnest struts failed first.

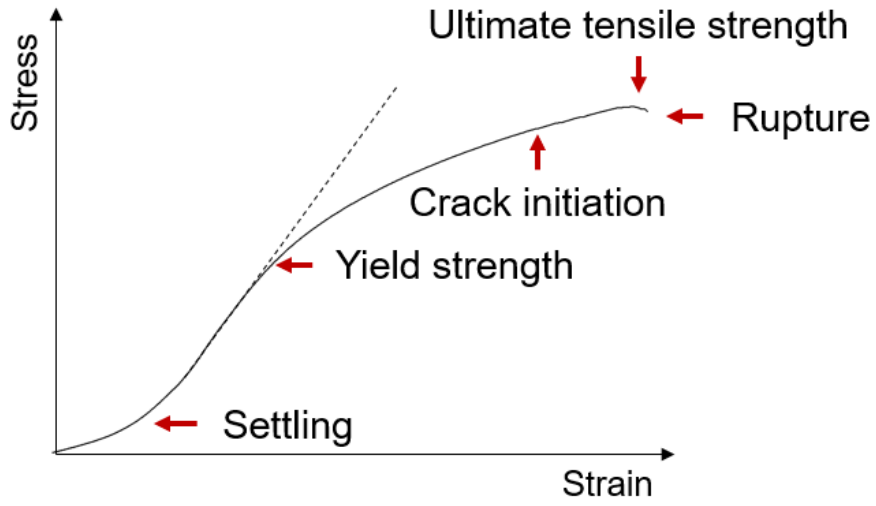

Figure 146: Schematic example of lattice structure behaviours under tensile loading.

The stiffness of each investigated sample is reported in Table 16 and Table 17. The reported values account for the stiffness of the load introduction region as described in section 3.4.1. Please refer to appendix G for more details. The stiffnesses of ungraded and graded configurations, respectively E_u^* and E_g^*, are compared to different analytical values based on the model of Souza et al. [43] (see section 3.2.1). The used bulk material values are in line with the ones employed in chapter 4, i.e. a Young's modulus of AlSi10Mg bulk material in the build direction E_S of 70 GPa [375] and a Poisson's ratio υ of 0.32 [383]. Due to the oversize effect observed for the employed parameter (see Table 8), the stiffness corresponding to the as-designed diameter $E_{ana,CAD}^*$ is considered as the lower limit of the analytical stiffness range. The stiffness corresponding to the as-built diameter $E_{ana,t}^*$ can be considered as the target stiffness. This value is based on both as-designed diameter and mean difference between as-designed and as build diameter $t - t_{CAD}$ reported in Table 8. The upper limit of the analytical stiffness range $E_{ana,max}^*$ considers the standard deviation of the difference between as-designed and as build diameter of the same table. The results obtained for the ungraded f_2cc_z samples yield stiffnesses below the analytical range while exhibiting high standard deviations. The stiffness values of graded samples of aspect ratios of 6 and 8 correspond to the target analytical stiffnesses. For samples of aspect ratio of 10, the experimental stiffnesses are below the analytical range. However, single stiffness values vary from 500 MPa to 581 MPa, meaning that one sample corresponds to the lower limit of the analytical range. The results of the bcc samples of both configurations show similar trends. The experimental stiffnesses of both graded and ungraded bcc samples are above the analytical range with exception of the ungraded sample of aspect ratio of 10. All values exhibit low standard deviations. It has to be noted that the successfully manufactured samples of a cell width of 3 mm were investigated as well in the framework of preparative works. The observed trends and obtained results are in line with the findings of the comparative analysis of samples of 3.5 mm width. This hints at the transferability potential of the developed design.

Table 16: Tensile test results and comparison with theory (f_2cc_z).

AR [-]	E_u^* [MPa]	E_g^* [MPa]	$E_{ana,CAD}^*$ [MPa]	$E_{ana,t}^*$ [MPa]	$E_{ana,max}^*$ [MPa]
6	1747.7±120.8	1969.9±37.4	1833.9	1915.5	1998.7
8	706.4±97.7	947.6±54.5	926.0	1017.9	1074.3
10	423.4±52.8	529.6±33.9	590.0	635.2	677.9

Table 17: Tensile test results and comparison with theory (bcc).

AR [-]	E_u^* [MPa]	E_g^* [MPa]	$E_{ana,CAD}^*$ [MPa]	$E_{ana,t}^*$ [MPa]	$E_{ana,max}^*$ [MPa]
6	227.2±4.1	288.1±0.7	133.4	166.5	186.3
8	78.1±2.3	100.1±0.1	44.0	59.3	68.9
10	30.8±0.9	40±0.5	18.4	26.7	32.1

6.3.3 Discussion

As the tensile specimen design employing the topology-optimised bulk structure shall be considered as preliminary analysis yielding promising results and needs further iterations to reach maturity, the present discussion focuses on the results obtained for the structurally graded specimen design.

The functionality of the developed tensile specimen design employing structural grading is proven by comparing the graded samples to the ungraded ones. Although the observed failure modes follow the load path specific to each RUC as described in section 4.1.2, it is initiated at different positions depending on the location of the stress peak within the lattice structure. Figure 147 and Figure 148 confront the stress distribution of the numerical simulation results reported in section 4.1.3 with the failed samples for both f_2cc_z and bcc configurations, respectively. Failure in ungraded samples can either be triggered at the sample's edge in the vicinity of the transition between bulk and transition regions or in the middle of the plane perpendicular to the loading direction. The latter occurs only for f_2cc_z samples at a height that is not considered as belonging to the target region and where the inclined struts cross. This stress concentration corresponds to a uniaxial loading state (see Figure 52 for qualitative comparison). Although another stress concentration occurs for the bcc samples, no corresponding failure modes were observed. According to simulation results, a corresponding failure mode would not have been driven by pure tensile loading (see Figure 51 for qualitative comparison). Failure in graded samples occur systematically in the sample's middle under pure tensile loading (see Figure 55 and Figure 56), which corresponds to the location of the maximum stress and to the ungraded cells region.

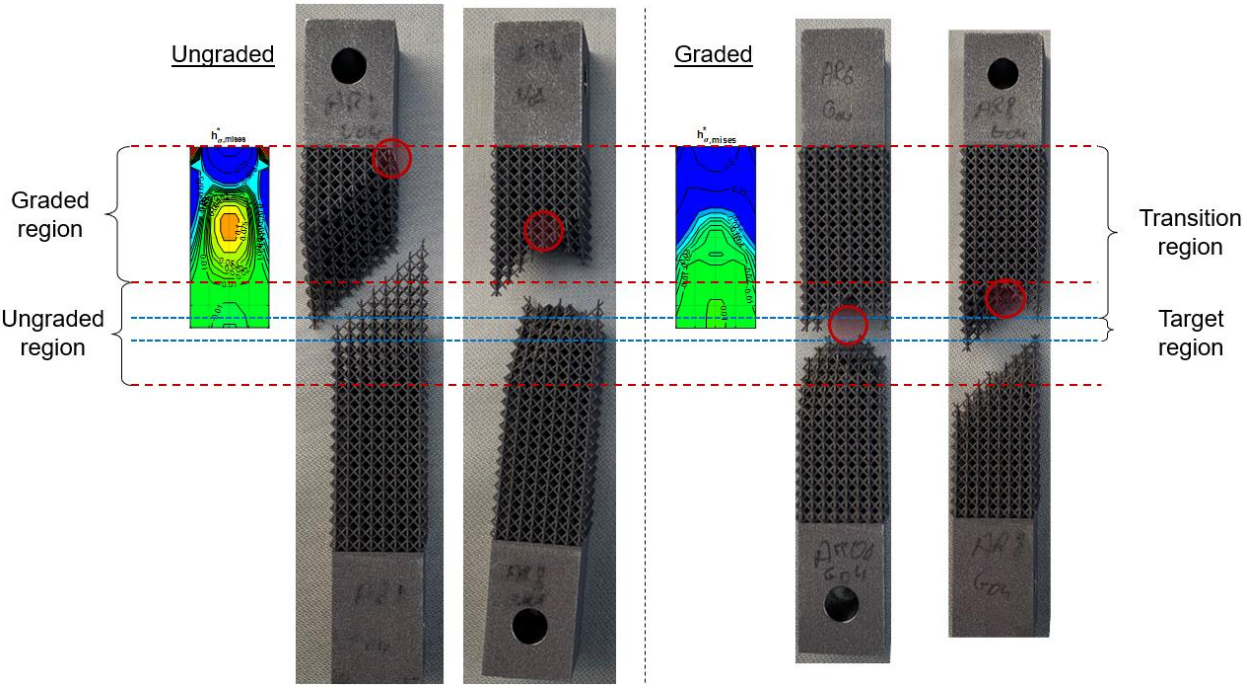

Figure 147: Comparison between stress concentrations identified by FE simulations and failed samples (f_2cc_z).

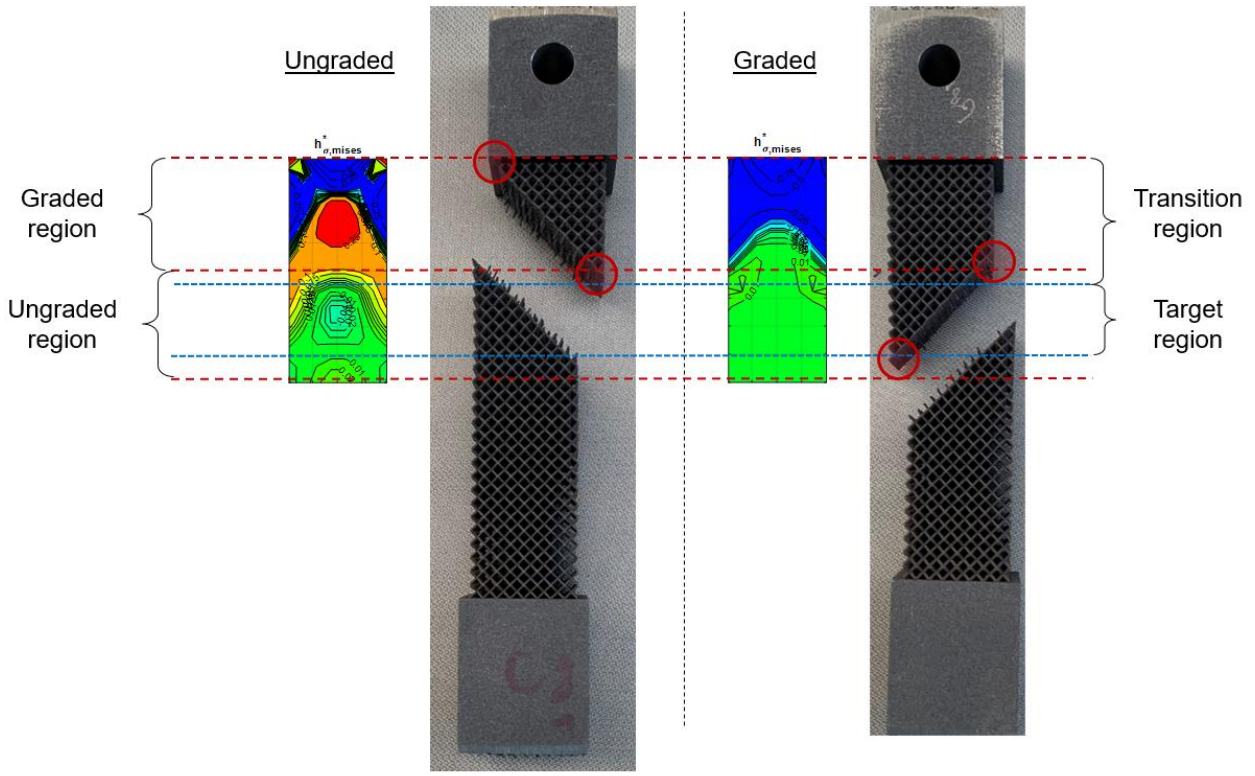

Figure 148: Comparison between stress concentrations identified by FE simulations and failed samples (bcc).

As far as the experimental stiffnesses of f_2cc_z samples are concerned, the ungraded f_2cc_z sample design is not able to retrieve analytical stiffnesses on a reliable basis while the graded f_2cc_z sample design yield excellent results. The deviations obtained for graded samples of aspect ratio of 10 can be explained by the lesser manufacturing quality for smaller diameters because particle aggregation is proportionally more impacting at smaller scale as discussed in section 5.1. This may lessen the efficiency of the grading approach as the diameter variations between two RUCs for AR10 (see appendix G) are in the same range of order as the observed diameter deviations (see Table 8). The results obtained can be further compared to the ML parameter listed in Table 9 of section 6.1.1 since it only differs from the employed parameter to manufacture lattice samples (see Table 8 of section 5.1.3) in the hatch distance. This only difference results in an overlap of hatch vectors of 15 % and 10 %, respectively. Table 14 reports an experimental stiffness of 932.8±50.6 MPa and an analytical stiffness of 974.5 MPa for lattice structures of aspect ratio of about 8.1 under compression loading while tensile specimens of AR8 yield an experimental stiffness of 947.6±54.5 MPa and an analytical stiffness of 1017.9 MPa according to Table 16. These values are in similar ranges of order.

The experimental stiffnesses of both sample designs are above the identified analytical stiffness range. Similar observations were made for the investigation of lattice structures under compression loading (see Table 14 of section 6.1.1) and the influence of the overlap on the stiffness of lattice structures was discussed in section 6.1.2. Since the number of

assigned hatch vectors is proportional to the as-designed diameter (see section 5.1.3), higher aspect ratios involve less hatch vectors and, thus, less overlapped areas. This explains that the underestimation of the experimental stiffness by the analytical stiffness decreases with increasing aspect ratio (Table 17). Similar to f_2cc_z samples, the results obtained can be further compared to the ML parameter listed in Table 9 of section 6.1.1. Although the exact stiffnesses are not comparable since the differences in as-built diameters lead to differences in the elliptical cross sections of the inclined bcc struts and, thus, different surfaces of overlapped areas, the range of order of the deviations in stiffness estimations can be compared. Table 18 gathers the results obtained for lattice structures of aspect ratio of about 8.1 under compression loading (Table 14) and the results of both graded and ungraded tensile specimens of AR8 (Table 17). The ratio between experimental stiffnesses $E^*_{ana,max}$ and the stiffnesses considering the as-built diameter with and without standard deviations, namely $E^*_{ana,max}$ and $E^*_{ana,t}$, respectively, are confronted. It can be observed that the graded bcc tensile samples yield stiffness ratios comparable to compressive test results for similar overlap values.

Table 18: Comparison of stiffness ratio for comparable parameter sets (bcc).

Data	E^* [MPa]	$E^*_{ana,t}$ [MPa]	$E^*_{ana,max}$ [MPa]	$E^*/E^*_{ana,t}$ [-]	$E^*/E^*_{ana,max}$ [-]
Table 17, ungraded	78.1	59.3	68.9	1.32	1.13
Table 17, graded	100.1	59.3	68.9	1.69	1.45
Table 14, ML	69	42.2	47.1	1.64	1.46

It can be concluded that, with regards of the failure location, the comparability of the assessed experimental tensile stiffnesses with analytical values and, for comparable manufacturing parameters, experimental compressive stiffnesses, the tensile specimen design based on a load introduction via structural grading developed in this work is able to systematically assess the mechanical properties of lattice structures in a reliable and reproducible way and is thus recommended for future use in engineering practice.

Furthermore, in the context of standardised tensile test procedure, the estimation of the stiffness needs to account for the RUC and size dependent settling phenomenon. Analogous to traction ropes, the vertical struts of f_2cc_z lattice structures need to be aligned with the load direction to be under pure tensile loading, which requires higher strains than the bcc lattice structures, which exhibit a homogeneous stress distribution and are less stiff (see section 4.2).

7 Concluding remarks

In this chapter, the findings of the present work regarding the implementation of lattice structures into load-bearing components are summarised and suggestions for future research are formulated.

7.1 Summary

In the present work, the state-of-the-art regarding the reliable implementation of truss-based lattice structures into load-bearing components was evaluated and deficiencies were exposed. Stress concentrations located at different interfaces have been identified as crucial for their structural integrity and mechanical performance. Consequently, design solutions were proposed, numerically verified and experimentally validated.

Stress concentrations occur at the interface between bulk part and lattice structures due to high differences in stiffness, as highlighted by the edge effect observed at the example of lattice structures under uniaxial tensile loading. To solve this load introduction issue, two load path monitoring solutions were proposed. The first approach consists in stiffening the lattice structure by means of structural grading. A grading formula and its corresponding design methodology were developed independent from the size of the considered lattice structure and its representative unit cell was proposed. It has to be highlighted that, in the framework of structural grading, working with the aspect ratio is more beneficial than with the relative density since it offers a direct link between strut thickness and stress state, which was exploited in the aforementioned design methodology. The second approach consists in increasing the compliance of the bulk part. Topology optimisation was employed to identify typical features or, to a greater extent, structural elements leading to an efficient design. In the example of tensile specimens, the identified design features are concentric-cross-sections and discrete load distribution elements such as pillar- or web-like structures aiming at avoiding edge effects. This approach led to smaller specimen design rather than employing structural grading.

Other stress concentrations occur at the interface between different representative unit cells and, in particular, at strut junctions, i.e. nodal areas. Stress reduction methods inspired by literature were proposed to solve this issue. It was demonstrated, depending on the behaviour of the representative unit cells, that graphical and simplified approaches alternative to the universal circular fillet radius are beneficial in terms of lightweight. Bending-dominated lattice structures benefit from a fillet radius of circular shape ranging from one fourth to one half of the strut diameter while fillet radii of elliptical shape corresponding to three quarters to one strut diameter yield better results for stretching-dominated lattice structures.

In all investigated cases, the symmetry of the representative unit cells was exploited and a high degree of transferability to other lattice structures was observed, enabling a scalable parametrised design.

However, it was observed that the effectivity of the proposed design solutions highly depends on the manufacturing scale and corresponding approaches. In the framework of the manufacturing of submillimetre parts, the smallest manufacturing range does not necessarily correspond to a reliable and reproducible manufacturing. Combined with other classical input parameters that are laser power and scanning speed, the ratio between particle size and layer thickness and the overlap between scanning paths strongly influence the melt pool and, thus, both manufacturing accuracy and predictability of the mechanical performance of lattice structures. Moreover, designed parts that are not directly linked to the build platform by means of vertical features exhibit heat conduction issues. This needs to be considered in the framework of integral design and monolithic components. Hybrid manufacturing approaches based on modular design and established manufacturing processes have been identified as the most promising solution for the reliable implementation of truss-based lattice structures into load-bearing components.

In spite of manufacturing influences, it was demonstrated in the framework of an extensive validation campaign that the developed structurally graded tensile specimen design leads to reliable and reproducible results that are comparable to analytical stiffnesses and stiffnesses values from compression tests. Moreover, an alignment of the developed design principles and employed test procedure with existing norms is possible. Therefore, in light of this example, the present work can be considered as a first milestone towards the mechanical characterisation of lattice structures for load cases others than pure compression. Furthermore, through the developed design rules and design measures, i.e. stress and strain criterion, this work can also be seen as a first step in the direction of the reliable establishment of lattice structures in a precise niche of technical products.

7.2 Outlook

Based on the literature review of chapter 2, the limits of the achieved work and the encountered challenges, three axes of development for the reliable implementation of lattice structures into load-bearing components and, to a greater extent, for AM in general are discussed.

The first development axis is **design for meso-scale AM**. Design for AM rules need to be established at the meso-scale. In the particular case of lattice structures, it was observed that details of the developed design and corresponding methodology strongly depend on both loading direction and strut orientation of the considered representative unit cell. It is therefore of utmost interest to validate the developed design approaches for other RUCs and lattice structure types such as re-entrant, plate-based or interlocking lattice structures, for different materials or heat-treated samples, for different inclination angles, and for other load cases (one- or multi-dimensional, static and dynamic loading). Consequently, further evaluation criteria, e.g. buckling or yield, need to be developed. Particular attention should be paid to the nodal areas. The applicability of these principles to hollow struts

or sandwich structures with graded lattice cores for an increased lightweight grade and, especially in the framework of modular design, functional integration is recommended too. Grading approaches of higher complexity may be required. If so, a design solution encompassing structural grading, RUC combination and optimised bulk parts is advised. If topology or shape optimisations are unavoidable, it is recommended to try to identify recurring design features as proposed in the present work in order to establish simplified design rules.

The second development axis is **meso-scale AM process dependencies**. Understanding the parameter-structure-performance correlation of meso-scale features is the key for reliable design and robust parts. Since the present work provides a first insight into that topic only, a concrete relationship between exposure strategy, process parameters, quality and performance of lattice structures is still to be unveiled. Standards for recommendations on manufacturing approaches and corresponding parameter sets need to be established to reach high quality parts at all scales. As the manufacturability of lattice structures and surrounding parts depends on the RUC as well, it is expected that these recommendations impact design rules as well (e.g. smallest manufacturable inclination angle or smallest cell size for powder removal). It is recommended to investigate the influence of the melt pool depth, of powder ageing, of the build platform temperature, of the type of coater, of the overlap between scanning paths, and of the ratio between particle size and layer thickness. For a complete understanding of the influence of exposure strategies and process parameters on the mechanical performance of lattice structures, it is advised to employ μCT-scans in order to remedy the local recordings provided by grinding pictures and, thus, obtain a broad screening for the analysis of both pore and thickness distributions. Due to the supposedly strong influence of overlapped areas, texture analyses by means of SEM imaging, EBSD measurement or even nanoindentation are recommended as well.

The third and last identified development axis is **tools adapted to meso-scale AM**. The commercial machine, software and equipment employed in the present work have shown their limits. While producers seek to increase the build space of their AM machines, the following practical needs have been identified: heating of the powder bed in the feed region, high-resolution in-situ monitoring systems, and a fully automatized physical pre-process to reduce handling mistakes. These features may already be available for other machines on the market. As far as software is concerned, the main concern lies in the size of the data generated by CAD or AM tools. The implicit modelling of lattice structures and its compatibility with AM software need to be further explored. Moreover, AM software shall offer parameter assignment approaches adapted to small scale features in a genuine user interface in order to reduce the pre-processing efforts. In the conceptional framework of *laser-driven lightweight design*, AM software is linked to scaling laws or models dedicated to parameter-structure-performance correlations issued from the data and recommendations discussed in the previous paragraph by means of, for example, cloud manufacturing platforms. Feedback on both design and manufacturability (monolithic, modular) of the

loaded part could be implemented too when combining the design rules of the first development axis with artificial intelligence. This shall enable end-users to find an optimum between high build rates, high manufacturing precision according to defined quality restrictions, and reduced efforts.

Similar to the parameter-structure-performance correlation of additively manufactured parts, these three main axes of development are intrinsically linked with each other and, thus, require pluridisciplinary approaches. This list of potential research topics is therefore non-exhaustive. In spite of the concepts of individualisation and complexity for free, nothing in life is free and AM is definitely no exception.

Bibliography

[1] Intergovernmental Panel on Climate Change. *AR6 Synthesis Report: Climate Change 2023*. March 2023. IPCC AR6 SYR. https://www.ipcc.ch/report/ar6/syr/downloads/report/IPCC_AR6_SYR_LongerReport.pdf (last accessed on October 11th 2023)

[2] K. Cromar, N. Lazrak. *Risk communication of ambient air pollution in the WHO European Region: Review of air quality indexes and lessons learned*. March 2023. WHO/EURO:2023-6885-46651-67825. https://www.who.int/publications/i/item/WHO-EURO-2023-6885-46651-67825 (last accessed on October 11th 2023)

[3] M.T. Huang, P.M. Zhai. *Achieving Paris Agreement temperature goals requires carbon neutrality by middle century with far-reaching transitions in the whole society*. Advances in Climate Change Research 12 (2021) 281–286. https://doi.org/10.1016/j.accre.2021.03.004

[4] C. Gao, S. Wolff, S. Wang. *Eco-friendly additive manufacturing of metals: Energy efficiency and life cycle analysis*. Journal of Manufacturing Systems 60 (2021) 459–472. https://doi.org/10.1016/j.jmsy.2021.06.011

[5] M. Armstrong, H. Mehrabi, N. Naveed. *An overview of modern metal additive manufacturing technology*. Journal of Manufacturing Processes 84 (2022) 1001–1029. https://doi.org/10.1016/j.jmapro.2022.10.060

[6] B. Blakey-Milner, P. Gradl, G. Snedden, M. Brooks, J. Pitot, E. Lopez, M. Leary, F. Berto, A. du Plessis. *Metal additive manufacturing in aerospace: A review*. Materials & Design 209 (2021) 110008. https://doi.org/10.1016/j.matdes.2021.110008

[7] Bundesministerium für Wirtschaft und Klimaschutz. *Schlaglichter der Wirtschaftspolitik: Schlüsseltechnologie Leichtbau: Innovationstreiber und Garant für Ressourcen- und Energieeffizienz*. Mai 2019.

[8] H.E. Friedrich. *Leichtbau in der Fahrzeugtechnik*. 1st ed., Springer Vieweg, Wiesbaden, Germany, 2013. ISBN 978-3-8348-2110-2

[9] M. Marino, R. Sabatini. *Advanced Lightweight Aircraft Design Configurations for Green Operations*. Practical Responses to Climate Change conference, Melbourne, Australia, 2014. https://doi.org/10.13140/2.1.4231.8405

[10] T.A. Campbell, O.S. Ivanova. *Additive manufacturing as a disruptive technology: implications of three-dimensional printing*. Technology and Innovation 15 (2013) 67–79. https://doi.org/10.3727/194982413x13608676060655

[11] A. Kanyilmaz, A.G. Demir, M. Chierici, F. Berto, L. Gardner, S.Y. Kandukuri, P. Kassabian, T. Kinoshita, A. Laurenti, I. Paoletti, A. Du Plessis, S.M.J. Razavi. *Role of metal 3D printing to increase quality and resource-efficiency in the construction sector*. Additive Manufacturing 50 (2022) 102541. https://doi.org/10.1016/j.addma.2021.102541

[12] A. Gebhardt. *Additive Fertigungsverfahren: Additive Manufacturing und 3D-Drucken für Prototyping - Tooling - Produktion*. 5th ed, Carl Hanser Verlag, Munich, 2016. ISBN 978-3-446-44401-0

[13] R. Lachmayer, R.B. Lippert, S. Kaierle. *Additive Serienfertigung: Erfolgsfaktoren und Handlungsfelder für die Anwendung*. 1st ed., Springer Vieweg, Berlin, Germany, 2018. ISBN 978-3-662-56463-9

[14] S.M. Yusuf, S. Cutler, N. Gao. *Review: The Impact of Metal Additive Manufacturing on the Aerospace Industry*. Metals 9 (2019) 1286. https://doi.org/10.3390/met9121286

[15] S. Gries, G. Meyer, A. Wonisch, R. Jakobi, C. Mittelstedt. *Towards Enhancing the Potential of Injection Molding Tools through Optimized Close-Contour Cooling and Additive Manufacturing*. Materials 14 (2021) 3434. https://doi.org/10.3390/ma14123434

[16] Roland Berger Strategy Consultants. *Additive Manufacturing: A game changer for the manufacturing industry?* 2013.

[17] M. Schürg, M. Scheibe, C. Mittelstedt. *Anwendungsmöglichkeiten der additiven Fertigung – Entwicklung eines Kabelführungshalters im Seitenleitwerk des Airbus A350*. 3rd NAFEMS DACH conference, Bamberg, Germany, 2016. ISBN 978-1-910643-03-7

[18] M. Bayat, O. Zinovieva, F. Ferrari, C. Ayas, M. Langelaar, J. Spangenberg, R. Salajeghe, K. Poulios, S. Mohanty, O. Sigmund, J. Hattel. *Holistic computational design within additive manufacturing through topology optimization combined with multiphysics multi-scale materials and process modelling*. Progress in Materials Science 138 (2023) 101129. https://doi.org/10.1016/j.pmatsci.2023.101129

[19] C. Emmelmann, P. Sander, J. Kranz, E. Wycisk. *Laser Additive Manufacturing and Bionics: Redefining Lightweight Design*. Physics Procedia 12 (2011) 364–368. https://doi.org/10.1016/j.phpro.2011.03.046

[20] A. Großmann, P. Weis, C. Clemen, C. Mittelstedt. *Optimization and re-design of a metallic riveting tool for additive manufacturing - A case study*. Additive Manufacturing 31 (2020) 100892. https://doi.org/10.1016/j.addma.2019.100892

[21] H.A. Richard, B. Schramm, T. Zipsner. *Additive Fertigung von Bauteilen und Strukturen*. 1st ed., Springer Vieweg, Wiesbaden, Germany, 2017. ISBN 978-3-658-17780-5

[22] D. Buchbinder. *Selective Laser Melting von Aluminiumgusslegierungen*. Ph.D. thesis. Shaker Verlag, Aachen, Germany, 2013. ISBN 9783844024395

[23] Wohlers Associates. *Wohlers Report 2022: 3D Printing and Additive Manufacturing - Global State of the Industry*. Fort Collins, USA, 2022. ISBN 978-0-9913332-9-5

[24] A.E. Oros Daraban, C.S. Negrea, F.G.P. Artimon, D. Angelescu, G. Popan, S.I. Gheorghe, M. Gheorghe. *A Deep Look at Metal Additive Manufacturing Recycling and Use Tools for Sustainability Performance*. Sustainability 11 (2019) 5494. https://doi.org/10.3390/su11195494

[25] O. Diegel, S. Singamneni, S. Reay, A. Withell. *Tools for Sustainable Product Design: Additive Manufacturing*. Journal of Sustainable Development 3 (2010) 3. https://doi.org/10.5539/jsd.v3n3p68

[26] H.Y. Chia, J. Wu, X. Wang, W. Yan. *Process parameter optimization of metal additive manufacturing: a review and outlook*. Journal of Materials Informatics 2 (2022) 16. https://doi.org/10.20517/jmi.2022.18

[27] Verein Deutscher Ingenieure. *VDI 3405 Part 3. Additive manufacturing processes, rapid manufacturing - Design rules for part production using laser sintering and laser beam melting*. Verein Deutscher Ingenieure e.V., Düsseldorf, Germany, 2015.

[28] S. Kumar. *Additive manufacturing processes*. Springer Nature, Cham, Switzerland, 2020. ISBN 978-3-030-45089-2

[29] C. Brecher. *Advances in Production Technology*. 1st ed., Springer International Publishing (Cham), Heidelberg, Germany, 2015. ISBN 978-3-319-12304-2

[30] J. Metelkova, Y. Kinds, K. Kempen, C. de Formanoir, A. Witvrouw, B. Van Hooreweder. *On the influence of laser defocusing in Selective Laser Melting of 316L*. Additive Manufacturing 23 (2018) 161–169. https://doi.org/10.1016/j.addma.2018.08.006

[31] M.C. Sow, T. De Terris, O. Castelnau, Z. Hamouche, F. Coste, R. Fabbro, P. Peyre. *Influence of beam diameter on Laser Powder Bed Fusion (L-PBF) process*. Additive Manufacturing 36 (2020) 101532. https://doi.org/10.1016/j.addma.2020.101532

[32] A. Großmann, J. Mölleney, T. Frölich, H. Merschroth, J. Felger, M. Weigold, A. Sielaff, C. Mittelstedt. *Dimensionless process development for lattice structure design in laser powder bed fusion*. Materials and Design 194 (2020) 108952. https://doi.org/10.1016/j.matdes.2020.108952

[33] Y. Yang, A. Großmann, P. Kühn, J. Mölleney, L. Kropholler, C. Mittelstedt, B.-X. Xu. *Validated dimensionless scaling law for melt pool width in laser powder bed fusion*. Journal of Materials Processing Tech. 299 (2022) 117316. https://doi.org/10.1016/j.jmatprotec.2021.117316

[34] M.F. Ashby, R.F. Mehl Medalist. *The mechanical properties of cellular solids*. Metallurgical Transactions A 14 (1983) 1755–1769. https://doi.org/10.1007/BF02645546

[35] A. du Plessis, C. Broeckhoven, I. Yadroitsava, I. Yadroitsev, C. H. Hands, R. Kunju, D. Bhate. *Beautiful and Functional: A Review of Biomimetic Design in Additive Manufacturing*. Additive Manufacturing 27 (2019) 408–427. https://doi.org/10.1016/j.addma.2019.03.033

[36] D. Bhate, C.A. Penick, L.A. Ferry, C. Lee. *Classification and Selection of Cellular Materials in Mechanical Design: Engineering and Biomimetic Approaches*. Designs 3 (2019) 19. https://doi.org/10.3390/designs3010019

[37] F. Liska. *Vergleich der mechanischen Eigenschaften von spongiösem Knochen verschiedener Spezies und künstlichem Knochen*. Ph.D. thesis. TU München, Munich, Germany, 2010.

[38] M. Helou, S. Kara. *Design, analysis and manufacturing of lattice structures: an overview*. International Journal of Computer Integrated Manufacturing 31 (2018) 243–61. https://doi.org/10.1080/0951192X.2017.1407456

[39] L.Y. Chen, S.X. Liang, Y. Liu, L.C. Zhang. A*dditive manufacturing of metallic lattice structures: Unconstrained design, accurate fabrication, fascinated performances, and challenges*. Materials Science & Engineering R 146 (2021) 100648. https://doi.org/10.1016/j.mser.2021.100648

[40] J.R. Greer, V.S. Desphande. *Three-dimensional architected materials and structures: Design, fabrication, and mechanical behavior*. MRS Bulletin 44 (2019) 750–757. https://doi.org/10.1557/mrs.2019.232

[41] E. Abele, H.A. Stoffregen, K. Klimkeit, H. Hoche, M. Oechsner. *Optimisation of process parameters for lattice structures*. Rapid Prototyping Journal 21 (2015) 117–127. https://doi.org/10.1108/RPJ-10-2012-0096

[42] L.J. Gibson, M.F. Ashby. *Cellular Solids*. 2nd ed., Cambridge University Press, Cambridge, United Kingdom, 2001. ISBN 978-0-5214-9911-8

[43] J. Souza, A. Großmann, C. Mittelstedt. *Micromechanical analysis of the effective properties of lattice structures in additive manufacturing*. Additive Manufacturing 23 (2018) 53–69. https://doi.org/10.1016/j.addma.2018.07.007

[44] N.A. Fleck, V.S. Desphande, M.F. Ashby. *Micro-architectured materials: past, present and future*. Proceedings of the Royal Society A 466 (2010) 2495-2516. https://doi.org/10.1098/rspa.2010.0215

[45] D. Carluccio, A.G. Demir, M.J. Bermingham, M.S: Dargusch. *Challenges and Opportunities in the Selective Laser Melting of Biodegradable Metals for Load-Bearing Bone Scaffold Applications*. Metallurgical and Materials Transactions A 7 (2020) 3311–3344. https://doi.org/10.1007/s11661-020-05796-z

[46] M. Benedetti, A. du Plessis, R.O. Ritchie, M. Dallago, S. Razavi, F. Berto. *Architected cellular materials: A review on their mechanical properties towards fatigue-tolerant design and fabrication*. Materials Science & Engineering R 144 (2021) 100606. https://doi.org/10.1016/j.mser.2021.100606

[47] N.S. Ha, G. Lu. *A review of recent research on bio-inspired structures and materials for energy absorption applications*. Composites Part B: Engineering 181 (2020) 107496. https://doi.org/10.1016/j.compositesb.2019.107496

[48] C.W. Isaac, F. Duddeck. *Current trends in additively manufactured (3D printed) energy absorbing structures for crashworthiness application – a review*. Virtual and Physical Prototyping 17 (2022) 1058–1101. https://doi.org/10.1080/17452759.2022.2074698

[49] A.E. Medvedev, T. Maconachie, M. Leary, M. Qian, M. Brandt. *Perspectives on additive manufacturing for dynamic impact applications*. Materials & Design 221 (2022) 110963. https://doi.org/10.1016/j.matdes.2022.110963

[50] A. du Plessis, S.M.J. Razavi, M. Benedetti, S. Murchio, M. Leary, M. Watson, D. Bhate, F. Berto. *Properties and applications of additively manufactured metallic cellular materials: A review*. Progress in Materials Science 125 (2022) 100918. https://doi.org/10.1016/j.pmatsci.2021.100918

[51] J. Plocher, A. Panesar. *Review on design and structural optimisation in additive manufacturing: Towards next-generation lightweight structures*. Materials and Design 183 (2019) 108164. https://doi.org/10.1016/j.matdes.2019.108164

[52] A. Seharing, A.H. Azman, S. Abdullah. *A review on integration of lightweight gradient lattice structures in additive manufacturing parts*. Advances in Mechanical Engineering 12 (2020) 1–21. https://doi.org/10.1177/1687814020916951

[53] T. Maconachie, M. Leary, B. Lozanovski, X. Zhang, M. Qian, O. Faruque, M. Brandt. *SLM lattice structures: Properties, performance, applications and challenges*. Materials and Design 183 (2019) 108137. https://doi.org/10.1016/j.matdes.2019.108137

[54] A. Du Plessis, I. Yadroitsava, I. Yadroitsev. *Effects of defects on mechanical properties in metal additive manufacturing: A review focusing on X-ray tomography insights*. Materials and Design 187 (2020) 108385. https://doi.org/10.1016/j.matdes.2019.108385

[55] L. Riva, S. Ginestra, E. Ceretti. *Mechanical characterization and properties of laser-based powder bed–fused lattice structures: a review*. The International Journal of Advanced Manufacturing Technology 113 (2021) 649–671. https://doi.org/10.1007/s00170-021-06631-4

[56] M. Seifi, M. Gorelik, J. Waller, N. Hrabe, N. Shamsael, S. Daniewicz, J.J. Lewandowski. *Progress Towards Metal Additive Manufacturing Standardization to Support Qualification and Certification*. JOM 69 (2017) 3. https://doi.org/10.1007/s11837-017-2265-2

[57] A. Großmann. *Fertigungsgetriebene Gestaltung zellulärer Strukturen beim pulverbasierten Laserstrahlschmelzen*. Ph.D. thesis. TU Darmstadt, Darmstadt, Germany 2020.

[58] Deutsches Institut für Normung. *DIN EN ISO/ASTM 52900. Additive manufacturing – General principles – Terminology*. Deutsches Institut für Normung e. V., Berlin, Germany, 2018.

[59] Deutsches Institut für Normung. *DIN 8580. Manufacturing processes – Terms and definitions, division*. Deutsches Institut für Normung e. V., Berlin, Germany, 2020.

[60] A. Gebhardt. J. Kessler, L. Thurn. *3D Printing: Understanding Additive Manufacturing*. 2nd ed. Carl Hanser Verlag, Munich, Germany, 2019. ISBN 978-1-56990-703-0

[61] D. Bourell, J.P. Kruth, M. Leu, G. Levy, D. Rosen, A.M. Beese, A. Clare. *Materials for additive manufacturing*. CIRP Annals - Manufacturing Technology 66 (2017) 659–681. https://doi.org/10.1016/j.cirp.2017.05.009

[62] Verein Deutscher Ingenieure. *VDI 3405. Additive manufacturing processes, rapid manufacturing: Basics, definitions, processes*. Verein Deutscher Ingenieure e.V., Düsseldorf, Germany, 2014.

[63] E. Toyserkani, D. Sarker, O. Obehi Ibhadode, F. Liravi, P. Russo, K. Taherkhani. *Metal Additive Manufacturing*. 1st ed., John Wiley & Sons Ltd, Hoboken, USA, 2022. ISBN 978-1-1192-1084-9

[64] J. Breuninger, R. Becker, A. Wolf, S. Rommel, A. Verl. *Generative Fertigung mit Kunststoffen: Konzeption und Konstruktion für Selektives Lasersintern*. 1st ed., Springer Vieweg, Berlin, Germany, 2013. ISBN 978-3-642-24325-7

[65] I. Gibson, D. Rosen, B. Stucker. *Additive Manufacturing Technologies: 3D Printing, Rapid Prototyping, and Direct Digital Manufacturing*. 2nd ed., Springer Science+Business Media, New York, USA, 2015. ISBN 978-1-4939-2113-3

[66] Helmut Zeyn. *Industrie 4.0 - Industrialisierung der Additiven Fertigung: Digitalisierte Prozesskette: von der Entwicklung bis zum einsetzbaren Artikel*. 1st ed., Beuth Verlag GmbH, Berlin, Germany, 2017. ISBN 978-3-410-26919-9

[67] D. Thomas. *The Development of Design Rules for Selective Laser Melting*. Ph.D. thesis. University of Wales Institute, Cardiff, Wales, 2009.

[68] H. Biedermann, A. Kinz. *Lean Smart Maintenance: Agiles, lern- und wertschöpfungsorientiertes Instandhaltungsmanagement*. 1st ed., Springer Gabler, Wiesbaden, Germany, 2021. ISBN 978-3-658-35473-2

[69] T. Schmidt. *Potentialbewertung generativer Fertigungsverfahren für Leichtbauteile*. Ph.D. thesis. Springer Vieweg, Berlin Heidelberg, Germany, 2016. ISBN 978-3-662-52996-6

[70] W.J. Sames, F.A. List, S. Pannala, R.R. Dehoff, S.S. Babu. *The metallurgy and processing science of metal additive manufacturing*. International Materials Reviews 61 (2016) 315–360. https://doi.org/10.1080/09506608.2015.1116649

[71] N. Li, S. Huang, G. Zhang, R. Qin, W. Liu, H. Xiong, G. Shi, J. Blackburn. *Progress in Additive Manufacturing on New Materials*. Journal of Materials Science and Technology 35 (2018) 242–269. https://doi.org/10.1016/j.jmst.2018.09.002

[72] R. Lachmayer, R.B. Lippert, T. Fahlbusch. *3D-Druck beleuchtet: Additive Manufacturing auf dem Weg in die Anwendung*. 1st ed., Springer Vieweg, Berlin Heidelberg, Germany, 2016. ISBN 978-3-662-49056-3

[73] F. Klocke. *Fertigungsverfahren 5: Gießen, Pulvermetallurgie, Additive Manufacturing*. 4th ed., Springer Vieweg, Berlin Heidelberg, Germany, 2015. ISBN 978-3-540-69512-7

[74] Verein Deutscher Ingenieure. *VDI 3405 Part 2. Additive manufacturing processes, rapid manufacturing - Beam melting of metallic parts: Qualification, quality assurance and post processing*. Verein Deutscher Ingenieure e.V., Düsseldorf, Germany, 2013.

[75] A. Gebhardt, J. Kessler, A. Schwarz. *Produktgestaltung für die Additive Fertigung*. 1st ed., Carl Hanser Verlag, Munich, Germany, 2019. ISBN 978-3-446-46133-8

[76] A. Großmann, J. Gosmann, C. Mittelstedt. *Lightweight lattice structures in selective laser melting: Design, fabrication and mechanical properties*. Materials Science & Engineering A 766 (2019) 138356. https://doi.org/10.1016/j.msea.2019.138356

[77] S.J. Merkt. *Qualifizierung von generativ gefertigten Gitterstrukturen für maßgeschneiderte Bauteilfunktionen*. Ph.D. thesis. RWTH Aachen, Aachen, Germany, 2015.

[78] F. Guaglione, L. Caprio, B. Previtali, A.G. Demir. *Single point exposure LPBF for the production of biodegradable Zn-alloy lattice structures*. Additive Manufacturing 48 (2021) 102426. https://doi.org/10.1016/j.addma.2021.102426

[79] A. Großmann, M. Klyk, L. Kohn, G. Meyer, M. Greiner, Y. Yang, C. Mittelstedt. *Bio-inspired airwings: Design and additive manufacturing of a geometrically graded microscale maple seed*. SSRN Preprint. http://dx.doi.org/10.2139/ssrn.4420965

[80] W. Meiners. *Direktes selektives Laser Sintern einkomponentiger metallischer Werkstoffe*. Ph.D. thesis. Shaker Verlag, Aachen, Germany, 1999. ISBN 3-8265-6571-1

[81] T.M. Wischeropp. *Advancement of Selective Laser Melting by Laser Beam Shaping*. Ph.D. thesis. Springer Vieweg, Berlin, Germany, 2021.

[82] I. Yadroitsev, I. Yadroitsava, A. Du Plessis, E. MacDonald. *Fundamentals of laser powder bed fusion of metals*. 1st ed., Elsevier, Amsterdam, Netherlands, 2021.

[83] M.E. Eisen. *Optimierte Parameterfindung und prozessorientiertes Qualitaätsmanagement fuür das Selective-Laser-Melting-Verfahren*. Ph.D. thesis. Shaker Verlag, Duisburg, Germany, 2010. ISBN 978-3-8322-8827-3

[84] J.P. Kruth, L. Froyen, J. Van Vaerenbergh, P. Mercelis, M. Rombouts, B. Lauwers. *Selective laser melting of iron-based powder*. Journal of Materials Processing Technology 149 (2004) 616–622. https://doi.org/10.1016/j.jmatprotec.2003.11.051

[85] K. Kempen, L. Thijs, J. Van Humbeeck, J.-P. Kruth. *Processing AlSi10Mg by selective laser melting: parameter optimisation and material characterization*. Materials Science and Technology 31 (2014) 917–923. https://doi.org/10.1179/1743284714Y.0000000702

[86] T. Kurzynowski, K. Gruber, W. Stopyra, B. Kuźnicka, E. Chlebus. *Correlation between process parameters, microstructure and properties of 316 L stainless steel processed by selective laser melting*. Materials Science & Engineering A 718 (2018) 64–73. https://doi.org/10.1016/j.msea.2018.01.103

[87] M. Balbaa, S. Mekhiel, M. Elbestawi, J. *On selective laser melting of Inconel 718: Densification, surface roughness, and residual stresses*. Materials and Design 193 (2020) 108818. https://doi.org/10.1016/j.matdes.2020.108818

[88] R. Gotoh, B.I. Furst, S.N. Roberts, S. Cappucci, T. Daimaru, E.T. Sunada. *Experimental and analytical investigations of AlSi10Mg, stainless steel, Inconel 625 and Ti-6Al-4V porous materials printed via powder bed fusion*. Progress in Additive Manufacturing 7 (2022) 943–55. https://doi.org/10.1007/s40964-022-00269-8

[89] A.H. Maamoun, Y.F. Xue, M.A. Elbestawi, S.C. Veldhuis. *Effect of Selective Laser Melting Process Parameters on the Quality of Al Alloy Parts: Powder Characterization, Density, Surface Roughness, and Dimensional Accuracy*. Materials 11 (2018) 2343. https://doi.org/10.3390/ma11122343

[90] R. Li, J. Liu, Y. Shi, L. Wang, W. Jiang. *Balling behavior of stainless steel and nickel powder during selective laser melting process*. International Journal Advanced Manufacturing Technology 59 (2012) 1025–1035. https://doi.org/10.1007/s00170-011-3566-1

[91] S.A. Khairallah, A.T. Anderson, A. Rubenchik, W.E. King. *Laser powder-bed fusion additive manufacturing: Physics of complex melt flow and formation mechanisms of pores, spatter, and denudation zones*. Acta Materialia 108 (2016) 36–45. https://doi.org/10.1016/j.actamat.2016.02.014

[92] A.V. Gusarov, I. Yadroitsev, P. Bertrand, I. Smurov. *Heat transfer modelling and stability analysis of selective laser melting*. Applied Surface Science 254 (2007) 975–979. https://doi.org/10.1016/j.apsusc.2007.08.074

[93] T. Mukherjee, H.L. Wei, A. De, T. DebRoy. *Heat and fluid flow in additive manufacturing – Part II: Powder bed fusion of stainless steel, and titanium, nickel and aluminum base alloys*. Computational Materials Science 150 (2018) 369–380. https://doi.org/10.1016/j.commatsci.2018.04.027

[94] W.E. King, H.D. Barth, V.M. Castillo, G.F. Gallegos, J.W. Gibbs, D.E. Hahn, C. Kamath, A.M. Rubenchik. *Observation of keyhole mode laser melting in laser powder-bed fusion additive manufacturing*. Journal of Materials Processing Technology 214 (2014) 2915–2925. https://doi.org/10.1016/j.jmatprotec.2014.06.005

[95] T. Qi, H. Zhu, H. Zhang, J. Yin, L. Ke, X. Zeng. *Selective laser melting of Al7050 powder: Melting mode transition and comparison of the characteristics between the keyhole and conduction mode*. Materials and Design 135 (2017) 257–266. https://doi.org/10.1016/j.matdes.2017.09.014

[96] P. Wei, Z. Wei, Z. Chen, Y. He, J. Du. *Thermal behavior in single track during selective laser melting of AlSi10Mg powder*. Applied Physics A 123 (2017) 604. https://doi.org/10.1007/s00339-017-1194-9

[97] M.J. Matthews, G. Guss, S.A. Khairallah, A.M. Rubenchik, P.J. Depond, W.E. King. *Denudation of metal powder layers in laser powder bed fusion processes*. Acta Materialia 114 (2016) 33–42. https://doi.org/10.1016/j.actamat.2016.05.017

[98] T. Kimura, T. Nakamoto. *Microstructures and mechanical properties of A356 (AlSi7Mg0.3) aluminum alloy fabricated by selective laser melting*. Materials and Design 89 (2016) 1294–1301. https://doi.org/10.1016/j.matdes.2015.10.065

[99] C. Weingarten, D. Buchbinder, N. Pirch, W. Meiners, K. Wissenbach, R. Poprawe. *Formation and reduction of hydrogen porosity during selective laser melting of AlSi10Mg*. Journal of Materials Processing Technology 221 (2015) 112–120. https://doi.org/10.1016/j.jmatprotec.2015.02.013

[100] A.K. Mishra, R.K. Upadhyay, A. Kumar. *Surface Wear Anisotropy in AlSi10Mg Alloy Sample Fabricated by Selective Laser Melting: Effect of Hatch Style, Scan Rotation and Use of Fresh and Recycled Powder*. Journal of Tribology 143 (2021) 021701. https://doi.org/10.1115/1.4047788

[101] G.R. Nazami, S. Sahoo. *Influence of hatch spacing and laser spot overlapping on heat transfer during laser powder bed fusion of aluminum alloy*. Journal of Laser Application 32 (2020) 042007. https://doi.org/10.2351/7.0000157

[102] I. Yadroitsev, L. Thivillon, P. Bertrand, I. Smurov. Strategy of manufacturing components with designed internal structure by selective laser melting of metallic powder. Applied Surface Science 254 (2007) 980–983. https://doi.org/10.1016/j.apsusc.2007.08.046

[103] X. Han, H. Zhu, X. Nie, G. Wang, X. Zeng. *Investigation on Selective Laser Melting AlSi10Mg Cellular Lattice Strut: Molten Pool Morphology, Surface Roughness and Dimensional Accuracy*. Materials 11 (2018) 392. https://doi.org/doi:10.3390/ma11030392

[104] M.J. Heiden, S.C. Jensen, J.R. Koepke, D.J. Saiz, S.M. Dickens, B.H. Jared. *Process and feedstock driven microstructure for laser powder bed fusion of 316L stainless steel*. Materialia 21 (2022) 101356. https://doi.org/10.1016/j.mtla.2022.101356

[105] L. Thijs, K. Kempen, J.P. Kruth, J. Van Humbeeck. *Fine-structured aluminium products with controllable texture by selective laser melting of pre-alloyed AlSi10Mg powder*. Acta Materialia 61 (2013) 1809–1819. https://doi.org/10.1016/j.actamat.2012.11.052

[106] L. Thijs, F. Verhaeghe, T. Craeghs, J. Van Humbeeck, J.P. Kruth. *A study of the microstructural evolution during selective laser melting of Ti-6Al-4V*. Acta Materialia 58 (2010) 3303–3312. https://doi.org/10.1016/j.actamat.2010.02.004

[107] F. Brenne, T. Niendorf. *Damage tolerant design by microstructural gradation - Influence of processing parameters and build orientation on crack growth within additively processed 316L*. Materials Science and Engineering A 764 (2019) 138186. https://doi.org/10.1016/j.msea.2019.138186

[108] S. Ghorbanpour, K. Deshmukh, S. Sahu, T. Riemslag, E. Reinton, E. Borisov, A. Popovich, V. Bertolo, Q. Jiang, M. Terol Sanchez, M. Knezevic, V. Popovich. *Additive manufacturing of functionally graded inconel 718: Effect of heat treatment and building orientation on microstructure and fatigue behaviour*. Journal of Materials Processing Tech. 306 (2022) 117573. https://doi.org/10.1016/j.jmatprotec.2022.117573

[109] Z. Dong, X. Zhang, W. Shi, H. Zhou, H. Lei, J. Liang. *Study of Size Effect on Microstructure and Mechanical Properties of AlSi10Mg Samples Made by Selective Laser Melting*. Materials 11 (2018) 2463. https://doi.org/10.3390/ma11122463

[110] N. Takata, H. Kodaira, A. Suzuki, M. Kobashi. *Size dependence of microstructure of AlSi10Mg alloy fabricated by selective laser melting*. Materials Characterization 143 (2018) 18–26. https://doi.org/10.1016/j.matchar.2017.11.052

[111] T. Niendorf, F. Brenne, M. Schaper. *Lattice structures manufactured by SLM–On the e ect of geometrical dimensions on microstructure evolution during processing*. Metallurgical and Materials Transactions B 45 (2014) 1181–1185. https://doi.org/10.1007/s11663-014-0086-z

[112] G. Meyer, F. Brenne, T. Niendorf, C. Mittelstedt. *Influence of the Miniaturisation Effect on the Effective Stiffness of Lattice Structures in Additive Manufacturing*. Metals 10 (2020) 1442. https://doi.org/10.3390/met10111442

[113] T. Ishimoto, K. Hagihara, K. Hisamoto, S.H. Sun, T. Nakano. *Crystallographic texture control of beta-type Ti–15Mo–5Zr–3Al alloy by selective laser melting for the development of novel implants with a biocompatible low Young's modulus*. Scripta Materialia 132 (2017) 34–38. https://doi.org/10.1016/j.scriptamat.2016.12.038

[114] T. Niendorf, F. Brenne, M. Schaper, A. Riemer, S. Leuders, W. Reimche, D. Schwarze, H.J. Maier. *Labelling additively manufactured parts by microstructural gradation–advanced copy-proof design*. Rapid Prototyping Journal 22 (2016) 630–635. https://doi.org/10.1108/RPJ-12-2014-0183

[115] L. Parry, I.A. Ashcroft, R.D. Wildman. *Understanding the effect of laser scan strategy on residual stress in selective laser melting through thermo-mechanical simulation*. Additive Manufacturing 12 (2016) 1–15. https://doi.org/10.1016/j.addma.2016.05.014

[116] J. Robinson, I. Ashton, P. Fox, E. Jones, C. Sutcliffe. *Determination of the effect of scan strategy on residual stress in laser powder bed fusion additive manufacturing*. Additive Manufacturing 23 (2018) 13–24. https://doi.org/10.1016/j.addma.2018.07.001

[117] A.E. Patterson, S.L. Messimer, P.A. Farrington. *Overhanging Features and the SLM/DMLS Residual Stresses Problem: Review and Future Research Need*. Technologies 5 (2017) 15. https://doi.org/10.3390/technologies5020015

[118] L.A. Parry, I.A. Ashcroft, R.D. Wildman. Geometrical effects on residual stress in selective laser melting. Additive Manufacturing 25 (2019) 166–175. https://doi.org/10.1016/j.addma.2018.09.026

[119] V. Viale, J. Stavridis, A. Salmi, F. Bondioli, A. Saboori. *Optimisation of downskin parameters to produce metallic parts via laser powder bed fusion process: an overview*. The International Journal of Advanced Manufacturing Technology 123 (2022) 2159–2182. https://doi.org/10.1007/s00170-022-10314-z

[120] A. Charles, M. Bayat, A. Elkaseer, L. Thijs, J.H. Hattel, S. Scholz. *Elucidation of dross formation in laser powder bed fusion at down-facing surfaces: Phenomenon-oriented multiphysics simulation and experimental validation*. Additive Manufacturing 50 (2022) 102551. https://doi.org/10.1016/j.addma.2021.102551

[121] J. Kranz. *Methodik und Richtlinien für die Konstruktion von laseradditiv gefertigten Leichtbaustrukturen*. Ph.D. thesis. Springer Vieweg, Berlin, Germany, 2017. ISBN 978-3-662-55339-8

[122] P. Edwards, M. Ramulu. *Fatigue performance evaluation of selective laser melted Ti–6Al–4V*. Materials Science and Engineering A 598 (2014) 327–337. https://doi.org/10.1016/j.msea.2014.01.041

[123] G. Piscopo, A. Salmi, E. Atzeni. *On the quality of unsupported overhangs*. International Journal of Manufacturing Research 14 (2019) 198–216. https://doi.org/10.1504/IJMR.2019.100012

[124] Deutsches Institut für Normung. *ISO/ASTM 52911 Part 1. Additive manufacturing – Design – Laser-based powder bed fusion of metals*. Deutsches Institut für Normung e. V., Berlin, Germany, 2020.

[125] J. Jiang, X. Xu, J. Stringer. *Support Structures for Additive Manufacturing: A Review*. Journal of Manufacturing and Material Processing 2 (2018) 64. https://doi.org/10.3390/jmmp2040064

[126] M. Leary, T. Maconachie, A. Sarkera, O. Faruque, M. Brandt. *Mechanical and thermal characterisation of AlSi10Mg SLM block support structures*. Materials and Design 183 (2019) 108138. https://doi.org/10.1016/j.matdes.2019.108138

[127] A. Khobzi, F. Farhang Mehr, S. Cockcroft, D. Maijer, S.L. Sing, W.Y. Yeong. *The role of block-type support structure design on the thermal field and deformation in components fabricated by Laser Powder Bed Fusion*. Additive Manufacturing 51 (2022) 102644. https://doi.org/10.1016/j.addma.2022.102644

[128] Wohlers Associates. *Post-Processing of AM and 3D-Printed Parts*. 1st ed., Wohlers Associates Inc., Fort Collins, USA, 2021. ISBN 978-0-9913332-8-8

[129] N.T. Aboulkhair, I. Maskery, C. Tuck, I. Ashcroft, N.M. Everitt. The microstructure and mechanical properties of selectively laser melted AlSi10Mg: The effect of a conventional T6-like heat treatment. Materials Science & Engineering A 667 (2016) 139–146. https://doi.org/10.1016/j.msea.2016.04.092

[130] F. Alghamdi, X. Song, A. Hadadzadeh, B. Shalchi-Amirkhiz, M. Mohammadi, M. Haghshenas. *Post heat treatment of additive manufactured AlSi10Mg: On silicon morphology, texture and small-scale properties*. Materials Science & Engineering A 783 (2020) 139296. https://doi.org/10.1016/j.msea.2020.139296

[131] X. Peng, L. Kong, J. Y. H. Fuh, and H. Wang. *A review of post-processing technologies in additive manufacturing*. Journal of Manufacturing and Materials Processing 5 (2021) 38. https://doi.org/10.3390/jmmp5020038

[132] S. Afazov, E. Semerdzhieva, D. Scrimieri, A. Serjouei, B. Kairoshev, F. Derguti. *An improved distortion compensation approach for additive manufacturing using optically scanned data*. Virtual and Physical Prototyping 16 (2021) 1–13. https://doi.org/10.1080/17452759.2021.1881702

[133] C. Hartmann, P. Lechner, B. Himmel, Y. Krieger, T.C. Lueth, W. Volk. *Compensation for Geometrical Deviations in Additive Manufacturing*. Technologies 7 (2019) 83. https://doi.org/10.3390/technologies7040083

[134] C. Wang, S. Li, D. Zeng, X. Zhu. Quantification and compensation of thermal distortion in additive manufacturing: A computational statistics approach. Comput. Methods Appl. Mech. Engrg. 375 (2021) 113611. https://doi.org/10.1016/j.cma.2020.113611

[135] Z. Li, D. Zhengwen Zhang, P. Dong, I. Kucukkoc. *A lightweight and support-free design method for selective laser melting.* International Journal of Advanced Manufacturing Technology 90 (2017) 2943–2953. https://doi.org/10.1007/s00170-016-9509-0

[136] F. Calignano. Design optimization of supports for overhanging structures in aluminum and titanium alloys by selective laser melting. Materials and Design 64 (2014) 203–213. https://doi.org/10.1016/j.matdes.2014.07.043

[137] M.X. Gan, C.H. Wong. *Practical support structures for selective laser melting*. Journal of Materials Processing Technology 238 (2016) 474–484. https://doi.org/10.1016/j.jmatprotec.2016.08.006

[138] G. Strano, L. Hao, R.M. Everson, K.E. Evans. *A new approach to the design and optimisation of support structures in additive manufacturing*. International Journal of Advanced Manufacturing Technology 66 (2013) 1247–1254. https://doi.org/10.1007/s00170-012-4403-x

[139] A. Hussein, L. Hao, C. Yan, R. Everson, P. Young. *Advanced lattice support structures for metal additive manufacturing*. Journal of Materials Processing Technology 213 (2013) 1019– 1026. https://doi.org/10.1016/j.jmatprotec.2013.01.020

[140] K. Cooper, P. Steele, B. Cheng, K. Chou. *Contact-Free Support Structures for Part Overhangs in Powder-Bed Metal Additive Manufacturing*. Inventions 3 (2018) 2. https://doi.org/10.3390/inventions3010002

[141] O. Gülcan, K. Günaydın, A. Çelik, E. Yasa. *The effect of contactless support parameters on the mechanical properties of laser powder bed fusion produced overhang parts*. The International Journal of Advanced Manufacturing Technology 122 (2022) 3235–3253. https://doi.org/10.1007/s00170-022-10135-0

[142] U. Paggi, L. Thijs, B. Van Hooreweder. *Implementation of contactless supports for industrially relevant additively manufactured parts in metal*. Additive Manufacturing Letters 3 (2022) 100095. https://doi.org/10.1016/j.addlet.2022.100095

[143] B. Vandenbroucke, J.P. Kruth. *Selective laser melting of biocompatible metals for rapid manufacturing of medical parts*. Rapid Prototyping Journal 13 (2007) 4. https://doi.org/10.1108/13552540710776142

[144] M. Cloots, A.B. Spierings, K. Wegener. *Assessing new support minimizing strategies for the additive manufacturing technology SLM*. 2013 International Solid Freeform Fabrication Symposium, Austin, USA 2013. http://dx.doi.org/10.26153/tsw/15588

[145] M. Cloots, L. Zumofen, A.B. Spierings, A. Kirchheim, K. Wegener. *Approaches to minimize overhang angles of SLM parts*. Rapid Prototyping Journal 13 (2017) 196–203. https://doi.org/10.1108/RPJ-05-2015-0061

[146] D. Wang, Y. Yang, Z. Yi, X. Su. *Research on the fabricating quality optimization of the overhanging surface in SLM process*. International Journal of Advanced Manufacturing Technology 65 (2013) 1471–1484. https://doi.org/10.1007/s00170-012-4271-4

[147] D. Wang, S. Mai, D. Xiao, Y. Yang. *Surface quality of the curved overhanging structure manufactured from 316-L stainless steel by SLM*. International Journal of Advanced Manufacturing Technology 86 (2016) 781–792. https://doi.org/10.1007/s00170-015-8216-6

[148] J. Čapek, E. Polatidis, N. Casati, R. Pederson, C. Lyphout, M. Strobl. *Influence of laser powder bed fusion scanning pattern on residual stress and microstructure of alloy 718*. Materials & Design 221 (2022) 110983. https://doi.org/10.1016/j.matdes.2022.110983

[149] T. Kurzynowski, W. Stopyra, K. Gruber, G. Ziółkowski, B. Kuźnicka, E: Chlebus. *Effect of Scanning and Support Strategies on Relative Density of SLM-ed H13 Steel in Relation to Specimen Size*. Materials 12 (2019) 239. https://doi.org/10.3390/ma12020239

[150] T. Mukherjee, T. DebRoy. *Migation of lack of fusion defects in powder bed fusion additive manufacturing*. Journal of Manufacturing Processes 36 (2018) 442–449. https://doi.org/10.1016/j.jmapro.2018.10.028

[151] J. Karimi, C. Suryanarayana, I. Okulov, K.G. Prashanth. *Selective laser melting of Ti6Al4V: Effect of laser re-melting*. Materials Science & Engineering A 805 (2021) 140558. https://doi.org/10.1016/j.msea.2020.140558

[152] D.R. Gunasegaram, A.B. Murphy, M.J. Matthews, T. DebRoy. *The case for digital twins in metal additive manufacturing*. Journal of Physics: Materials 4 (2021) 040401. https://doi.org/10.1088/2515-7639/ac09fb

[153] P. Nath, S. Mahadevan. *Probabilistic Digital Twin for Additive Manufacturing Process Design and Control*. Journal of Mechanical Desing 144 (2022) 091704. https://doi.org/10.1115/1.4054521

[154] A. Almalki, D. Downing, B. Lozanovski, R. Tino, A. Du Plessis, M. Qian, M. Brandt, M. Leary. *A Digital-Twin Methodology for the Non-destructive Certification of Lattice Structures*. JOM 74 (2022) 1784-1797. https://doi.org/10.1007/s11837-021-05144-5

[155] K. Taherkhani, O. Ero, F. Liravi, S. Toorandaz, E. Toyserkani. *On the application of in-situ monitoring systems and machine learning algorithms for developing quality assurance platforms in laser powder bed fusion: A review*. Journal of Manufacturing Processes 99 (2023) 848–897. https://doi.org/10.1016/j.jmapro.2023.05.048

[156] R. McCann, M.A. Obeidi, C. Hughes, E. McCarthy, D.S. Egan, R.K. Vijayaraghavan, A.M. Joshi, V. Acinas Garzon, D.P. Dowling, P.J. McNally, D. Brabazon. *In-situ sensing, process monitoring and machine control in Laser Powder Bed Fusion: A review*. Additive Manufacturing 45 (2021) 102058. https://doi.org/10.1016/j.addma.2021.102058

[157] G. Tapia, A. Elwany. *A Review on Process Monitoring and Control in Metal-Based Additive Manufacturing*. Journal of Manufacturing Science and Engineering 136 (2014) 060801. https://doi.org/10.1115/1.4028540

[158] D.R. Gunasegaram, A.B. Murphy, A. Barnard, T. DebRoy, M.J. Matthews, L. Ladani, D. Gu. *Towards developing multiscale-multiphysics models and their surrogates for digital twins of metal additive manufacturing*. Additive Manufacturing 46 (2021) 102089. https://doi.org/10.1016/j.addma.2021.102089

[159] M. Mozaffar, S. Liao, X. Xie, S. Saha, C. Park, J. Cao, W.K. Liu, Z. Gan. *Mechanistic artificial intelligence (mechanistic-AI) for modeling, design, and control of advanced manufacturing processes: Current state and perspectives*. Journal of Materials Processing Technology 302 (2022) 117485. https://doi.org/10.1016/j.jmatprotec.2021.117485

[160] B. Mondal, T. Mukherjee, T. DebRoy. *Crack free metal printing using physics informed machine learning*. Acta Materialia 226 (2022) 117612. https://doi.org/10.1016/j.actamat.2021.117612

[161] Z. Zhan, H. Li. *Machine learning based fatigue life prediction with effects of additive manufacturing process parameters for printed SS 316L*. International Journal of Fatigue 142 (2021) 105941. https://doi.org/10.1016/j.ijfatigue.2020.105941

[162] H. Pahlavani, M. Amani, M. Cruz Saldívar, J. Zhou, M.J. Mirzaali, A.A. Zadpoor. *Deep learning for the rare-event rational design of 3D printed multi-material mechanical metamaterials*. Communications Materials 3 (2022) 46. https://doi.org/10.1038/s43246-022-00270-2

[163] M.P. Bendsøe, N. Kikuchi. *Generating optimal topologies in structural design using a homogenization method*. Computer Methods in Applied Mechanics and Engineering 71 (1988) 197–224. https://doi.org/10.1016/0045-7825(88)90086-2

[164] T. Mukherjee, V. Manvatkar, A. De, T. DebRoy. *Dimensionless numbers in additive manufacturing*. Journal of Applied Physics 121 (2017) 064904. https://doi.org/10.1063/1.4976006
[165] L.R. Goossens, B. van Hooreweder. *A virtual sensing approach for monitoring melt-pool dimensions using high speed coaxial imaging during laser powder bed fusion of metals*. Additive Manufacturing 40 (2021) 101923. https://doi.org/10.1016/j.addma.2021.101923
[166] T. Mukherjee, V. Manvatkar, A. De, T. DebRoy. *Mitigation of thermal distortion during additive manufacturing*. Scripta Materialia 127 (2017) 79–83. https://doi.org/10.1016/j.scriptamat.2016.09.001
[167] A. Großmann, M. Rexer, M. Greiner, G. Meyer, J. Mölleney, L. Kohn, V. Abbatiello, P.F. Pelz, C. Mittelstedt. *Material and process invariant scaling laws to predict porosity of dense and lattice structures in laser powder bed fusion*. SSRN Preprint. http://dx.doi.org/10.2139/ssrn.4189610
[168] B. Rankouhi, A.K. Agrawal, F.E. Pfefferkorn, D.J. Thoma. *A dimensionless number for predicting universal processing parameter boundaries in metal powder bed additive manufacturing*. Manufacturing Letters 27 (2021) 13–17. https://doi.org/10.1016/j.mfglet.2020.12.002
[169] F.J. Ayala. *Darwin's greatest discovery: design without designer*. The Proceedings of the National Academy of Sciences 104 (2007) 8567–8573. https://doi.org/10.1073/pnas.0701072104
[170] W. Wawers. *Bionik: Bionisches Konstruieren verstehen und anwenden*. 1st ed., Springer Vieweg, Wiesbaden, Germany, 2020. ISBN 978-3-658-31873-4
[171] R. Müller, N. Abaid, J.B. Boreyko, C. Fowlkes, A.K. Goel, C. Grimm, S. Jung, B. Kennedy, C. Murphy, N.D. Cushing, J.-P. Han. *Biodiversifying bioinspiration*. Bioinspiration & Biomimetics 13 (2018) 053001. https://doi.org/10.1088/1748-3190/aac96a
[172] C. Dick, J. Georgii, R. Burgkart, R. Westermann. *Stress tensor field visualization for implant planning in orthopaedics*. IEEE Transactions on Visualization and Computer Graphics 15 (2009) 1399–1406. https://doi.org/10.1109/TVCG.2009.184
[173] J. Wu, N. Aage, R. Westermann, O. Sigmund. *Infill optimization for additive manufacturing-approaching bone-like porous structures*. IEEE transactions on visualization and computer graphics 24 (2018) 1127–1140. https://doi.org/10.1109/TVCG.2017.2655523
[174] D. Taylor. *Fatigue-resistant components: What can we learn from nature?* Proceedings of the Institution of Mechanical Engineers, Part C: Journal of Mechanical Engineering Science 229 (2015) 1186–1193. https://doi.org/10.1177/0954406214530881
[175] C. Mattheck. *Design and growth rules for biological structures and their application to engineering*. Fatigue & Fracture of Engineering Materials and Structures 13 (1990) 535–550. https://doi.org/10.1111/j.1460-2695.1990.tb00623.x
[176] M. Gralow, F. Weigand, D. Herzog, T. Wischeropp, C. Emmelmann. *Biomimetic design and laser additive manufacturing— A perfect symbiosis?* Journal of Laser Applications 32 (2020) 021201. https://doi.org/10.2351/1.5131642

[177] Verein Deutscher Ingenieure. *VDI 2221. Systematic approach to the development and design of technical systems and products*. Verein Deutscher Ingenieure e.V., Düsseldorf, Germany, 1993.
[178] Verein Deutscher Ingenieure. *VDI 2221 Part 1. Design of technical products and systems model of product design*. Verein Deutscher Ingenieure e.V., Düsseldorf, Germany, 2019.
[179] Deutsches Institut für Normung. *DIN EN ISO/ASTM 52910. Additive manufacturing – Design – Requirements, guidelines and recommendations*. Deutsches Institut für Normung e. V., Berlin, Germany, 2020.
[180] M. Baumers. *Economic aspects of additive manufacturing: benefits, costs and energy consumption*. Ph.D. thesis. Loughborough University, Loughborough, United Kingdom, 2012. https://dspace.lboro.ac.uk/2134/10768 (last accessed on October 12th 2023)
[181] E. Atzeni, L. Iuliano, P. Minetola, A. Salmi. *Redesign and cost estimation of rapid manufactured plastic parts*. Rapid Prototyping Journal 16 (2010) 308–317. https://doi.org/10.1108/13552541011065704
[182] Verein Deutscher Ingenieure. *VDI 6224. Biomimetics - Integrated product development process for biomimetic optimisation*. Verein Deutscher Ingenieure e.V., Düsseldorf, Germany, 2017.
[183] Verein Deutscher Ingenieure. *VDI 2222. Design engineering methodics - Setting up and use of design catalogues*. Verein Deutscher Ingenieure e.V., Düsseldorf, Germany, 1982.
[184] S.C. Fu, X.L. Zhong, Y. Zhang, T.W. Lai, K.C. Chan, K.Y. Lee, Christopher Y.H. Chao. *Bio-inspired cooling technologies and the applications in buildings*. Energy & Buildings 225 (2020) 110313. https://doi.org/10.1016/j.enbuild.2020.110313
[185] EOS GmbH. *Kundenreferenz Luft- und Raumfahrt - Additive Fertigung für den neuen A350 XWB*. https://www.eos.info/01_parts-and-applica-tions/case_studies_applications_parts/_case_studies_pdf/de_cases/cs_m_aerospace_sogeti_de.pdf (last accessed on October 12th 2023)
[186] G. Meyer, P. Weis, A. Großmann, C. Clemen, C. Mittelstedt. *C-Frame design optimization for selective laser melting*. Deutscher Luft- und Raumfahrtkongress, Darmstadt, Germany, 2019. https://www.dglr.de/publikationen/2019/490053.pdf (last accessed on October 11th 2023)
[187] A. Schumacher. *Optimierung mechanischer Strukturen*. 1st ed., Springer Vieweg, Berlin Heidelberg, Germany, 2013. ISBN 978-3-642-34700-9
[188] M.P. Bendsøe, O. Sigmund. *Topology optimization: theory, methods and applications*. 2nd ed., Springer Vieweg, Berlin Heidelberg, Germany, 2004. ISBN 978-3-540-42992-0
[189] D. Yago, J. Cante, O. Lloberas-Valls, J. Oliver. *Topology optimizationmethods for 3d structural problems: A comparative study*. Archives of Computational Methods in Engineering 29 (2021) 1525–1567. https://doi.org/10.1007/s11831-021-09626-2

[190] G.I.N. Rozvany, M. Zhou, T. Birker. *Generalized shape optimization without homogenization*. Structural Optimization 4 (1992) 250–252. https://doi.org/10.1007/BF01742754

[191] N.P. van Dijk, K. Maute, M. Langelaar, F. van Keulen. *Level-set methods for structural topology optimization: a review*. Structural and Multidisciplinary Optimization 48 (2013) 437–472. https://doi.org/10.1007/s00158-013-0912-y

[192] M.P. Bendsøe, O. Sigmund. *Material interpolation schemes in topology optimization.* Archive of Applied Mechanics 69 (1999) 635–654. https://doi.org/10.1007/s004190050248

[193] M. Zhou, G.I.N. Rozvany. *The COC algorithm, part II: topological, geometry and generalized shape optimization*. Computer Methods in Applied Mechanics and Engineering 89 (1991) 309–336. https://doi.org/10.1016/0045-7825(91)90046-9

[194] F.M. Ballo, M. Gobbi, G. Mastinu, G. Previati. *Optimal Lightweight Construction Principles*. 1st ed., Springer Nature, Cham, Switzerland, 2021. ISBN 978-3-030-60835-4

[195] J. Freund, A. Karakoç, J. Sjölund. *Computational homogenization of regular cellular material according to classical elasticity*. Mechanics of Materials 78 (2014) 56–65. https://doi.org/10.1016/j.mechmat.2014.07.018

[196] S. Xu, J. Shen, S. Zhou, X. Huang, Y.M. Xie. *Design of lattice structures with controlled anisotropy*. Materials and Design 93 (2016) 443–447. https://doi.org/10.1016/j.matdes.2016.01.007

[197] M.P. Bendsøe. *Optimal shape design as a material distribution problem*. Structural Optimization 1 (1989) 193–202. https://doi.org/10.1007/BF01650949

[198] Y.M. Xie, G.P. Steven. *Evolutionary structural optimization*. 1st ed., Springer, London, United Kingdom, 1997. ISBN 978-1-4471-0985-3

[199] X. Huang, Y.M. Xie. *Evolutionary topology optimization of continuum structures.* 1st ed., John Wiley & Sons Ltd, London, United Kingdom, 2010. ISBN 978-0-4706-8948-6

[200] G. Allaire, F. Jouve, A.M. Toader. *Structural optimization using sensitivity analysis and a level-set method*. Journal of Computational Physics 194 (2004) 363–393. https://doi.org/10.1016/j.jcp.2003.09.032

[201] M.Y. Wang, X.M. Wang, D.M. Guo. *A level set method for structural topology optimization*. Computer Methods in Applied Mechanics and Engineering 192 (2003) 227–246. https://doi.org/10.1016/S0045-7825(02)00559-5

[202] J.A. Sethian, A. Wiegmann. *Structural boundary design via level set and immersed interface methods*. Journal of Computational Physics 163 (2000) 489– 528. https://doi.org/10.1006/jcph.2000.6581

[203] J. Zhu, H. Zhou, C. Wang, L. Zhou, S. Yuan, W. Zhang. *A review of topology optimization for additive manufacturing: Status and challenges*. Chinese Journal of Aeronautics 34 (2021) 91–110. https://doi.org/10.1016/j.cja.2020.09.020

[204] Y. Saadlaoui, J.L. Milan, J.M. Rossi, P. Chabrand. *Topology optimization and additive manufacturing: Comparison of conception methods using industrial codes*. Journal of Manufacturing Systems 43 (2017) 178–186. https://doi.org/10.1016/j.jmsy.2017.03.006

[205] O. Sigmund. *Manufacturing tolerant topology optimization*. Acta Mechanica Sinica 25 (2009) 227–239. https://doi.org/10.1007/s10409-009-0240-z

[206] A.T. Gaynor, J.K. Guest. *Topology optimization considering overhang constraints: Eliminating sacrificial support material in additive manufacturing through design*. Structural and Multidisciplinary Optimization 54 (2016) 1157–1172. https://doi.org/10.1007/s00158-016-1551-x

[207] M. Hoffarth, N. Gerzen, C. Pedersen. *Alm overhang constraint in topology optimization for industrial applications*. 12th World Congress on Structural and Multidisciplinary Optimisation, Braunschweig, Germany, 2017.

[208] M. Langelaar. *Combined optimization of part topology, support structure layout and build orientation for additive manufacturing*. Structural and Multidisciplinary Structural and Multidisciplinary Optimization 57 (2018) 1985–2004. https://doi.org/10.1007/s00158-017-1877-z

[209] L. Cheng, X. Liang, J. Bai, Q. Chen, J. Lemon, A. To. *On utilizing topology optimization to design support structure to prevent residual stress induced build failure in laser powder bed metal additive manufacturing*. Additive Manufacturing 27 (2019) 290–304. https://doi.org/10.1016/j.addma.2019.03.001

[210] M. Langelaar. *Topology Optimization of 3D Self-Supporting Structures for Additive Manufacturing*. Additive Manufacturing 12 (2016) 60–70. https://doi.org/10.1016/j.addma.2016.06.010

[211] Q. Li, W. Chen, S. Liu, L. Tong. *Structural topology optimization considering connectivity constraint*. Structural and Multidisciplinary Optimization 54 (2016) 971–984. https://doi.org/10.1007/s00158-016-1459-5

[212] J. Liu, H. Yu. *Concurrent deposition path planning and structural topology optimization for additive manufacturing*. Rapid Prototyping Journal 23 (2017) 930–942. https://doi.org/10.1108/RPJ-05-2016-0087

[213] J. Liu, A.T. Gaynor, S. Chen, Z. Kang, K. Suresh, A. Takezawa, L. Li, J. Kato, J. Tang, C.C.L. Wang, L. Cheng, X. Liang, A.C. To. *Current and future trends in topology optimization for additive manufacturing*. Structural and Multidisciplinary Optimization 57 (2018) 2457–2483. https://doi.org/10.1007/s00158-018-1994-3

[214] A. Panesar, M. Abdi, D. Hickman, I. Ashcroft. *Strategies for functionally graded lattice structures derived using topology optimisation for additive manufacturing*. Additive Manufacturing 19 (2018) 81–94. https://doi.org/10.1016/j.addma.2017.11.008

[215] M. Alzahrani, S.K. Choi, D.W. Rosen. *Design of truss-like cellular structures using relative density mapping method*. Materials and Design 85 (2015) 349–360. https://doi.org/10.1016/j.matdes.2015.06.180

[216] G. De Pasquale, M. Montemurro, A. Catapano, G. Bertolino, L. Revelli. *Cellular structures from additive processes: Design, homogenization and experimental validation*. Procedia Structural Integrity 8 (2018) 75–82. https://doi.org/10.1016/j.prostr.2017.12.009

[217] H. Rodrigues, J.M. Guedes, M.P. Bendsøe. *Hierarchical optimization of material and structure*. Structural and Multidisciplinary Optimization 24 (2002) 1–10. https://doi.org/10.1007/s00158-002-0209-z

[218] J. Alexandersen, B.S. Lazarov. *Topology optimisation of manufacturablemicrostructural details without length scale separation using a spectral coarse basis preconditioner*. Computer Methods in Applied Mechanics and Engineering 290 (2015) 156–182. https://doi.org/10.1016/j.cma.2015.02.028

[219] X. Wang, L. Zhu, L. Sun, N. Li. *Optimization of graded filleted lattice structures subject to yield and buckling constraints.* Materials & Design 206 (2021) 109746. https://doi.org/10.1016/j.matdes.2021.109746

[220] S. Arabnejad, D. Pasini. *Mechanical properties of lattice materials via asymptotic homogenization and comparison with alternative homogenization methods.* International Journal of Mechanical Sciences 77 (2013) 249–262. https://doi.org/10.1016/j.ijmecsci.2013.10.003

[221] L. Cheng, J. Bai, A.C. To. *Functionally graded lattice structure topology optimization for the design of additive manufactured components with stress constraints*. Computer Methods in Applied Mechanics and Engineering 344 (2019) 334–359. https://doi.org/10.1016/j.cma.2018.10.010

[222] P. Geoffroy-Donders, G. Allaire, O. Pantz. *3-D topology optimization of modulated and oriented periodic microstructures by the homogenization method*. Journal of Computational Physics 401 (2020) 108994. https://doi.org/10.1016/j.jcp.2019.108994

[223] T. Primo, M. Calabrese, A. Del Prete, A. Anglani. *Additive manufacturing integration with topology optimization methodology for innovative product design*. The International Journal of Advanced Manufacturing Technology 93 (2017) 467–479. https://doi.org/10.1007/s00170-017-0112-9

[224] M. Montemurro, G. Bertolino, T. Roiné. *A general multi-scale topology optimisation method for lightweight lattice structures obtained through additive manufacturing technology*. Composite Structures 258 (2021) 113360. https://doi.org/10.1016/j.compstruct.2020.113360

[225] G. Bertolino, M. Montemurro, G. De Pasquale. *Multi-scale shape optimisation of lattice structures: an evolutionary-based approach*. International Journal on Interactive Design and Manufacturing 13 (2019) 1565–1578. https://doi.org/10.1007/s12008-019-00580-9

[226] V.S. Deshpande, N.A. Fleck, M.F. Ashby. *Effective properties of the octet-truss lattice material*. Journal of the Mechanics and Physics of Solids 49 (2001) 1747–1769. https://doi.org/10.1016/S0022-5096(01)00010-2

[227] L. Makatura, B. Wang, Y.L. Chen, B. Deng, C. Wojtan, B. Bickel, W. Matusik. *Procedural Metamaterials: A Unified Procedural Graph for Metamaterial Design*. ACM Transactions on Graphics 42 (2023) 168. https://doi.org/10.1145/3605389

[228] M.F. Ashby, A.G. Evans, N.A. Fleck, L.J. Gibson, J.W. Hutchinson, H.N.G. Wadley. *Metal Foams: A Design Guide*. 1st ed., Butterworth-Heinemann, Oxford, United Kingdom, 2000. ISBN 978-0-7506-7219-1.

[229] T. Tancogne-Dejean, M. Diamantopoulou, M.B. Gorji, C. Bonatti, D. Mohr. *3D Plate-Lattices: An Emerging Class of Low-Density Metamaterial Exhibiting Optimal Isotropic Stiffness*. Advanced Materials 30 (2018) 1803334. https://doi.org/10.1002/adma.201803334

[230] M.G. Rashed, Mahmud Ashraf, R.A.W. Mines, P.J. Hazell. *Metallic microlattice materials: A current state of the art on manufacturing, mechanical properties and applications*. Materials and Design 95 (2016) 518–533. https://doi.org/10.1016/j.matdes.2016.01.146

[231] S.K. Moon, Y.E. Tan, J. Hwang, Y.J. Yoon. *Application of 3D Printing Technology forDesigning Light-weight Unmanned Aerial Vehicle Wing Structures*. International Journal of Precision Engineering and Manufacturing-Green Technology 1 (2014) 223–228. https://doi.org/10.1007/s40684-014-0028-x

[232] E.A.A. Alkebsi, H. Ameddah, T. Outtas, A. Almutawakel. *Design of graded lattice structures in turbine blades using topology optimization*. International Journal of Computer Integrated Manufacturing: 34 (2021) 370–384. https://doi.org/10.1080/0951192X.2021.1872106

[233] S. Yin, H. Chen, Y. Wu, Y. Li, J. Xu. *Introducing composite lattice core sandwich structure as an alternative proposal for engine hood*. Composite Structures 201 (2018) 131–140. https://doi.org/10.1016/j.compstruct.2018.06.038

[234] G. De Pasquale, A. Tagliaferri. *Modeling and characterization of mechanical and energetic elastoplastic behavior of lattice structures for aircrafts anti-icing systems*, Proceedings of the Institution of Mechanical Engineers, Part C: Journal of Mechanical Engineering Science 235 (2021) 1828–1839. https://doi.org/10.1177/0954406219853857

[235] M. Davidson, S. Roberts, G. Castro, R.P. Dillon, A. Kunz, H. Kozachkov, M.D. Demetriou, W.L. Johnson, S. Nutt, D.C. Hofmann. *Investigating amorphous metal composite architectures as spacecraft shielding*., Advanced Engineering Materials 15 (2013) 27–33. https://doi.org/10.1002/adem.201200313

[236] Y. Kim, I. Kim, J. Park. *An approximate formulation for the progressive failure analysis of a composite lattice cylindrical panel in aerospace applications*. Aerospace Science and Technology 106 (2020) 106212. https://doi.org/10.1016/j.ast.2020.106212

[237] B.J.R. Smeets, E.M. Fagan, K. Matthews, R. Telford, B.R. Murray, L. Pavlov, B. Weafer, P. Meier, J. Goggins. *Structural testing of a shear web attachment point on a composite lattice cylinder for aerospace applications*. Composites Part B 212 (2021) 108691. https://doi.org/10.1016/j.compositesb.2021.108691

[238] X. Wang, Z. Zhong, T. Zeng, G. Xu, Y. Cui, K. Zhang. *Heat transfer property of C/SiC composite pyramidal lattice core sandwich structures*. Composite Structures 301 (2022) 116215. https://doi.org/10.1016/j.compstruct.2022.116215

[239] X. Shi, Z. Yang, W. Chen, M.K. Chyu. *Investigation of the effect of lattice structure on the fluid flow and heat transfer of supercritical CO2 in tubes*. Applied Thermal Engineering 207 (2022) 118132. https://doi.org/10.1016/j.applthermaleng.2022.118132

[240] K.J. Maloney, K.D. Fink, T.A. Schaedler, J.A. Kolodziejska., A.J. Jacobsen, C.S. Roper. *Multifunctional heat exchangers derived from three-dimensional micro-lattice structures*. International Journal of Heat and Mass Transfer 55 (2012) 2486–2493. https://doi.org/10.1016/j.ijheatmasstransfer.2012.01.011

[241] J. Feng, B. Liu, Z. Lin, J. Fu. *Isotropic octet-truss lattice structure design and anisotropy control strategies for implant application*. Materials & Design 203 (2021) 109595. https://doi.org/10.1016/j.matdes.2021.109595

[242] E. Liverani, G. Rogati, S. Pagani, S. Brogini, A. Fortunato, P. Caravaggi. *Mechanical interaction between additive-manufactured metal lattice structures and bone in compression: implications for stress shielding of orthopaedic implants*. Journal of the Mechanical Behavior of Biomedical Materials 121 (2021) 104608. https://doi.org/10.1016/j.jmbbm.2021.104608

[243] E. Alabort, D. Barba, R.C. Reed. *Design of metallic bone by additive manufacturing*. Scripta Materialia 164 (2019) 110–114. https://doi.org/10.1016/j.scriptamat.2019.01.022

[244] J. Mun, B.G. Yun, J. Ju, B.M. Chang. *Indirect additive manufacturing based casting of a periodic 3D cellular metal – Flow simulation of molten aluminum alloy*. Journal of Manufacturing Processes 17 (2015) 28–40. https://doi.org/10.1016/j.jmapro.2014.11.001

[245] G.W. Kooistra, H.N.G. Wadley. *Lattice truss structures from expanded metal sheet*. Materials & Design 28 (2007) 507–514. https://doi.org/10.1016/j.matdes.2005.08.013

[246] D.T. Queheillalt, H.N.G. Wadley. *Cellular metal lattices with hollow trusses*. Acta Materialia 53 (2005) 303–313. https://doi.org/10.1016/j.actamat.2004.09.024

[247] O. Rehme. *Cellular Design for Laser Freeform Fabrication*. Ph.D. thesis. Cuvillier Verlag, Göttingen, 2010. ISBN 9783869552736

[248] C. Beyer, D. Figueroa. *Design and Analysis of Lattice Structures for Additive Manufacturing*. Journal of Manufacturing Science and Engineering 138 (2016) 1–15. https://doi.org/10.1115/1.4033957

[249] O. Al-Ketan, R.K. Abu Al-Rub. *Multifunctional Mechanical Metamaterials Based on Triply Periodic Minimal Surface Lattices*. Advanced Engineering Materials 21 (2019) 1900524. https://doi.org/10.1002/adem.201900524

[250] O. Weeger. *Isogeometric sizing and shape optimization of 3d beams and lattice structures at large deformations*. Structural and Multidisciplinary Optimization 65 (2022) 43. https://doi.org/10.1007/s00158-021-03131-7

[251] W. Xiong, R. Pan, C. Yan, M. He, Q. Chen, S. Li, X. Chen, L. Hao, Y. Li. *Subdivisional modelling method for matched metal additive manufacturing and its implementation on novel negative Poisson's ratio lattice structures*. Additive Manufacturing 68 (2023) 103525. https://doi.org/10.1016/j.addma.2023.103525

[252] D.F. Rogers, J.A. Adams. *Mathematical Elements for Computer graphics*. 2nd ed., McGraw Hill, New York, USA, 1990. ISBN 9780070535305

[253] A. Goel, S. Anand. *Design of Functionally Graded Lattice Structures using Bsplines for Additive Manufacturing*. Procedia Manufacturing 34 (2019) 655–665. https://doi.org/10.1016/j.promfg.2019.06.193

[254] P.J.F. Gandy, S. Bardhan, A.L. Mackay, J. Klinowski. *Nodal surface approximations to the P,G,D and I-WP triply periodic minimal surfaces*. Chemical Physics Letters 336 (2001) 187–95. https://doi.org/10.1016/S0009-2614(00)01418-4

[255] Q. Zhang, L. Ma, X. Ji, Y. He, Y. Cui, X. Liu, C. Xuan, Z. Wang, W. Yang, M. Chai, X. Shi. *High-Strength Hydroxyapatite Scaffolds with Minimal Surface Macrostructures for Load-Bearing Bone Regeneration*. Advanced Functional Materials 32 (2022) 2204182. https://doi.org/10.1002/adfm.202204182

[256] Q. Li, Q. Hong, Q. Qi, X. Ma, X. Han, J. Tian. *Towards additive manufacturing oriented geometric modeling using implicit functions*. Visual Computing for Industry, Biomedicine, and Art 1 (2018) 9. https://doi.org/10.1186/s42492-018-0009-y

[257] O. Al-Ketan, D.W. Lee, R. Rowshan, R.K. Abu Al-Rub. *Functionally graded and multi-morphology sheet TPMS lattices: Design, manufacturing, and mechanical properties*, Journal of the Mechanical Behavior of Biomedical Materials 102 (2020) 103520. https://doi.org/10.1016/j.jmbbm.2019.103520

[258] X. Ma, D.Z. Zhang, M. Zhao, J. Jiang, F. Luo, H. Zhou. *Mechanical and energy absorption properties of functionally graded lattice structures based on minimal curved surfaces*. The International Journal of Advanced Manufacturing Technology 118 (2022) 995–1008. https://doi.org/10.1007/s00170-021-07768-y

[259] M. McMillan, M. Jurg, M. Leary, M. Brandt. *Programmatic lattice generation for additive manufacture*. Procedia Technology 20 (2015) 178–184. https://doi.org/10.1016/j.protcy.2015.07.029

[260] M. McMillan, M. Jurg, M. Leary, M. Brandt. *Programmatic generation of computationally efficient lattice structures for additive manufacture*. Rapid Prototyping Journal 23 (2017) 486–494. https://doi.org/10.1108/RPJ-01-2016-0014

[261] D. Downing, M. McMillan, M. Brandt, M. Leary. *Programmatic lattice generation tools for additive manufacture*. Software Impacts 12 (2022) 100262. https://doi.org/10.1016/j.simpa.2022.100262

[262] F. Hoffmann. *Faszination Kristalle und Symmetrie: Einführung in die Kristallographie*. 1st ed., Springer Fachmedien, Wiesbaden, Germany, 2016. ISBN 978-3-658-09581-9

[263] M. Mazur, M. Leary, S. Sun, M. Vcelka, D. Shidid, M. Brandt. *Deformation and failure behaviour of Ti-6Al-4V lattice structures manufactured by selective laser melting (SLM)*. The International Journal of Advanced Manufacturing Technology 84 (2016) 1391–1411. https://doi.org/10.1007/s00170-015-7655-4

[264] S. Liseni, A. Coluccia, G. Meyer, C. Mittelstedt, G. De Pasquale. *Numerical method for energy absorption maximimzation in lattice structures and experimental validation*. 17th ECSSMET, Toulouse, France, 2023.

[265] M. Sos, G. Meyer, K. Durst, C. Mittelstedt, E. Bruder. *Microstructure and mechanical properties of additively manufactured AlSi10Mg lattice structures from single contour exposure*. Materials & Design 227 (2023) 111796. https://doi.org/10.1016/j.matdes.2023.111796

[266] A. Suzuki, K. Sekizawa, M. Liu, N. Takata, M. Kobashi. *Effects of Heat Treatments on Compressive Deformation Behaviors of Lattice-Structured AlSi10Mg Alloy Fabricated*

by Selective Laser Melting. Advanced Engineering Materials 21 (2019) 1900571. https://doi.org/10.1002/adem.201900571

[267] D. Li, R. Qin, J. Xu, B. Chen, X. Niu. *Effect of heat treatment on AlSi10Mg lattice structure manufactured by selective laser melting: Microstructure evolution and compression properties*. Materials Characterization 187 (2022) 111882. https://doi.org/10.1016/j.matchar.2022.111882

[268] M.F. Ashby. *The properties of foams and lattices*. Philosophical Transactions of the Royal Society A: Mathematical, Physical and Engineering Sciences 364 (2006) 15–30. https://doi.org/10.1098/rsta.2005.1678

[269] H. Zhong, T. Song, C. Li, R. Das, J. Gu, Ma Qian. *The Gibson-Ashby model for additively manufactured metal lattice materials: Its theoretical basis, limitations and new insights from remedies*. Current Opinion in Solid State and Materials Science 27 (2023) 101081. https://doi.org/10.1016/j.cossms.2023.101081

[270] M. Naebe, K. Shirvanimoghaddam. *Functionally graded materials: A review of fabrication and properties*. Applied Materials Today 5 (2016) 223–245. https://doi.org/10.1016/j.apmt.2016.10.001

[271] B. Saleh, J. Jiang, R. Fathi, T. Al-hababi, Q. Xu, L. Wang, D. Song, A. Ma. *30 Years of functionally graded materials: An overview of manufacturing methods, Applications and Future Challenges*. Composites Part B 201 (2020) 108376. https://doi.org/10.1016/j.compositesb.2020.108376

[272] H. Lippert. *Lehrbuch Anatomie*. 8th ed., Urban&Fischer, Munich Jena, Germany, 2011. ISBN 978-3-437-42365-9

[273] R. Weiske, G.M. Lingg, C.C. Glüer. *Osteoporose: Atlas der radiologischen Diagnostik und Differentialdiagnose*. 1st ed., Stuttgart, Gustav Fischer, Stuttgart Jena Lübeck Ulm, Germany, 1998. ISBN 978-3-437-21380-9

[274] Y. Li, H. Jahr, P. Pavanram, F.S.L. Bobbert, U. Puggi, X.Y. Zhang, B. Pouran, M.A. Leeflang, H. Weinans, J. Zhou, A.A. Zadpoor. *Additively manufactured functionally graded biodegradable porous iron*. Acta Biomaterialia 96 (2019) 646–661. https://doi.org/10.1016/j.actbio.2019.07.013

[275] W.J.M. Rankine. *XVII. Principle of the equilibrium of polyhedral frames*. The London, Edinburgh, and Dublin Philosophical Magazine and Journal of Science 27 (1864) 92. https://doi.org/10.1080/14786446408643629

[276] J.C. Maxwell. *L. On the calculation of the equilibrium and stiffness of frames*. The London, Edinburgh, and Dublin Philosophical Magazine and Journal of Science 27 (1864) 294–299. https://doi.org/10.1080/14786446408643668

[277] J.C. Maxwell. *I.—On Reciprocal Figures, Frames, and Diagrams of Forces*. Earth and Environmental Science Transactions of The Royal Society of Edinburgh 26 (1870) 1–40. https://doi.org/10.1017/S0080456800026351

[278] A. Michell. *LVIII. The limits of economy of material in frame-structures*. The London, Edinburgh, and Dublin Philosophical Magazine and Journal of Science 8 (1904) 589–597. https://doi.org/10.1080/14786440409463229

[279] I. Maskery, N.T. Aboulkhair, A.O. Aremu, C.J. Tuck, I.A. Ashcroft, R.D. Wildman, R.J.M. Hague. *A mechanical property evaluation of graded density Al-Si10-Mg lattice*

structures manufactured by selective laser melting. Materials Science & Engineering A 670 (2016) 264–274. https://doi.org/10.1016/j.msea.2016.06.013

[280] D.S.J. Al-Saedi, S.H. Masood, M. Faizan-Ur-Rab, A. Alomarah, P. Ponnusamy. *Mechanical properties and energy absorption capability of functionally graded F2BCC lattice fabricated by SLM*. Materials & Design 144 (2018) 32–44. https://doi.org/10.1016/j.matdes.2018.01.059

[281] L. Yang, R. Mertens, M. Ferrucci, C. Yan, Y. Shi, S. Yang. *Continuous graded Gyroid cellular structures fabricated by selective laser melting: Design, manufacturing and mechanical properties*. Materials and Design 162 (2019) 394–404. https://doi.org/10.1016/j.matdes.2018.12.007

[282] J. Plocher, A. Panesar. *Effect of density and unit cell size grading on the stiffness and energy absorption of fibre-reinforced functionally graded lattice structures*. Additive Manufacturing 33 (2020) 101171. https://doi.org/10.1016/j.addma.2020.101171

[283] I. Maskery, A. Hussey, A. Panesar, A: Aremu, C.J. Tuck, I. Ashcroft, R. Hague. *An investigation into reinforced and functionally graded lattice structures*. Journal of Cellular Plastics 53 (2017) 151–165. https://doi.org/10.1177/0021955X16639035

[284] L. Yang, S. Wu, C. Yan, P. Chen, L. Zhang, C. Han, C. Cai, S. Wen, Y. Zhou, Y. Shi. *Fatigue properties of Ti-6Al-4V Gyroid graded lattice structures fabricated by laser powder bed fusion with lateral loading*. Additive Manufacturing 46 (2021) 102214. https://doi.org/10.1016/j.addma.2021.102214

[285] M.C. Saldívar, E. Tay, E.L. Doubrovski, M.J. Mirzaali, A. A. Zadpoor. *Bioinspired rational design of multi-material 3D printed soft-hard interfaces*. arXiv (2022). https://doi.org/10.48550/arXiv.2206.13615

[286] K. Lietaert, A. Cutolo, D. Boey, B. Van Hooreweder. *Fatigue life of additively manufactured Ti6Al4V scaffolds under tension-tension, tension-compression and compression-compression fatigue load*. Scientific Reports 8 (2018) 4957. https://doi.org/10.1038/s41598-018-23414-2

[287] L. Cheng, P. Zhang, E. Biyikli, J. Bai, J. Robbins, A. To. *Efficient design optimization of variable-density cellular structures for additive manufacturing: Theory and experimental validation*. Rapid Prototyping Journal 23 (2017) 660–677. https://doi.org/10.1108/RPJ-04-2016-0069

[288] A. Radman, X. Huang, Y.M. Xie. *Topology optimization of functionally graded cellular materials*. Journal of Materials Science 48 (2013) 1503–1510. https://doi.org/10.1007/s10853-012-6905-1

[289] F. Liu, Z. Mao, P. Zhang, D.Z. Zhang, J. Jiang, Z. Ma. *Functionally graded porous scaffolds in multiple patterns: New design method, physical and mechanical properties*. Materials & Design 160 (2018) 849–860. https://doi.org/10.1016/j.matdes.2018.09.053

[290] I. Maskery, A.O. Aremu, L. Parry, 7R.D. Wildman, C.J. Tuck, I.A. Ashcroft. *Effective design and simulation of surface-based lattice structures featuring volume fraction and cell type grading*. Materials and Design 155 (2018) 220–232. https://doi.org/10.1016/j.matdes.2018.05.058

[291] N. Yang, Z. Quan, D. Zhang, Y. Tian. *Multi-morphology transition hybridization CAD design of minimal surface porous structures for use in tissue engineering*. Computer-Aided Design 56 (2014) 11–21. https://doi.org/10.1016/j.cad.2014.06.006

[292] L. Bai, C. Gong, X. Chen, Y. Sun, L. Xin, H. Pu, Y. Peng, J. Luo. *Mechanical properties and energy absorption capabilities of functionally graded lattice structures: Experiments and simulations*. International Journal of Mechanical Sciences 182 (2020) 105735. https://doi.org/10.1016/j.ijmecsci.2020.105735

[293] Q.Y. Jin, J.H. Yu, K.S. Ha, W.J. Lee, S.H. Park. *Multi-dimensional lattices design for ultrahigh specific strength metallic structure in additive manufacturing*. Materials and Design 201 (2021) 109479. https://doi.org/10.1016/j.matdes.2021.109479

[294] A. Coluccia, G. Jiang, G. Meyer, G. De Pasquale, C. Mittelstedt. *Nonlinear static and dynamic modeling of energy absorption lattice structures behavior*. Mechanics of Advanced Materials and Structures 30 (2023) 2838–2849. https://doi.org/10.1080/15376494.2022.2064016

[295] M. Nightingale, R. Hewson, M. Santer. *Multiscale optimisation of resonant frequencies for lattice-based additivemanufactured structures*. Structural and Multidisciplinary Optimization 63 (2021) 1187-1201. https://doi.org/10.1007/s00158-020-02752-8

[296] M. Leary, M. Mazur, J. Elambasseril, M. McMillan, T. Chirent, Y. Sun, M. Qian, M. Easton, M. Brandt. *Selective laser melting (SLM) of AlSi12Mg lattice structures*. Materials and Design 98 (2016) 344–357. https://doi.org/10.1016/j.matdes.2016.02.127

[297] C. López-García, E. García-López, H.R. Siller, J.A. Sandoval-Robles, C.A. Rodriguez. *A dimensional assessment of small features and lattice structures manufactured by laser powder bed fusion*. Progress in Additive Manufacturing 7 (2022) 751–763. https://doi.org/10.1007/s40964-022-00263-0

[298] R. Vrána, T. Koutecký, O. Červinek, T. Zikmund, L. Pantělejev, J. Kaiser, D. Koutný. *Deviations of the SLM Produced Lattice Structures and Their Influence on Mechanical Properties*. Materials 15 (2022) 3144. https://doi.org/10.3390/ma15093144

[299] M. Leary, M. Mazur, H. Williams, E. Yang, A. Alghamdi, B. Lozanovski, X. Zhang, D. Shidid, L. Farahbod-Sternahl, G. Witt, I. Kelbassa, P. Choong, M. Qian, M. Brandt. *Inconel 625 lattice structures manufactured by selective laser melting (SLM): Mechanical properties, deformation and failure modes*. Materials & Design 157 (2018) 179–199. https://doi.org/10.1016/j.matdes.2018.06.010

[300] H. Soul, P. Terriault, V. Brailovski. *The Static and Fatigue Behavior of AlSiMg Alloy Plain, Notched, and Diamond Lattice Specimens Fabricated by Laser Powder Bed Fusion*. Journal of Manufacturing and Materials Processing 2 (2018) 25. https://doi.org/10.3390/jmmp2020025

[301] R. Vrána, D. Koutný, D. Paloušek, L. Pantělejev, J. Jaroš, T. Zikmund, J. Kaiser. *Selective Laser Melting Strategy for Fabrication of Thin Struts Usable in Lattice Structures*. Materials 11 (2018) 1763. https://doi.org/10.3390/ma11091763

[302] C. Li, H. Lei, Z. Zhang, X. Zhang, H. Zhou, P. Wang, D. Fang. *Architecture design of periodic truss-lattice cells for additive manufacturing*. Additive Manufacturing 34 (2020) 101172. https://doi.org/10.1016/j.addma.2020.101172

[303] J. Noronha, M. Qian, M. Leary, E. Kyriakou, A. Almalki, S. Brudler, M. Brandt. *Additive manufacturing of Ti-6Al-4V horizontal hollow struts with submillimetre wall thickness by laser powder bed fusion*. Thin-Walled Structures 179 (2022) 109620. https://doi.org/10.1016/j.tws.2022.109620

[304] M. Sairaiji, H. Yoshizaki, H. Iwaoka, S. Hirosawa, S. Maruo. *Effect of Scan Strategy on Mechanical Properties of AlSi12 Lattice Fabricated by Selective Laser Melting*. Journal of Laser Micro/Nanoengineering 15 (2020). https://doi.org/10.2961/jlmn.2020.01.2002

[305] P. Delroisse, P.J. Jacques, E. Maire, O. Rigo, A. Simar. *Effect of strut orientation on the microstructure heterogeneities in AlSi10Mg lattices processed by selective laser melting*. Scripta Materialia 141 (2017) 32–35. https://doi.org/10.1016/j.scriptamat.2017.07.020

[306] Z. Dong, Y. Liu, W. Li, J. Liang. *Orientation dependency for microstructure, geometric accuracy and mechanical properties of selective laser melting AlSi10Mg lattices*. Journal of Alloys and Compounds 791 (2019) 490–500. https://doi.org/10.1016/j.jallcom.2019.03.344

[307] A.D. Dressler, E.W. Jost, J.C. Miers, D.G. Moore, C.C. Seepersad, B.L. Boyce. *Heterogeneities dominate mechanical performance of additively manufactured metal lattice struts*. Additive Manufacturing 28 (2019) 692–703. https://doi.org/10.1016/j.addma.2019.06.011

[308] C. Qiu, S. Yue, N.J. Adkins, M. Ward, H. Hassanin, P.D. Lee, P.J. Withers, M.M. Attallah. *Influence of processing conditions on strut structure and compressive properties of cellular lattice structures fabricated by selective laser melting*. Materials Science & Engineering A 628 (2015) 188–197. https://doi.org/10.1016/j.msea.2015.01.031

[309] S.A. Naghavi, H. Wang, S.N. Varma, M. Tamaddon, A. Marghoub, R. Galbraith, J. Galbraith, M. Moazen, J. Hua, W. Xu, C. Liu. *On the Morphological Deviation in Additive Manufacturing of Porous Ti6Al4V Scaffold: A Design Consideration*. Materials 15 (2022) 4729. https://doi.org/10.3390/ma15144729

[310] X.Z. Zhang, H.P. Tang, J. Wang, L. Jia, Y.X: Fan, M. Leary, M. Qian. *Additive manufacturing of intricate lattice materials: Ensuring robust strut additive continuity to realize the design potential*. Additive Manufacturing 58 (2022) 103022. https://doi.org/10.1016/j.addma.2022.103022

[311] G. Meyer, J. Musekamp, F. Göbel, F. Gardian, C. Mittelstedt. *Manufacturability investigation of inclined AlSi10Mg lattice struts by means of selective laser melting*. Manufacturing Letters 31 (2022) 101–105. https://doi.org/10.1016/j.mfglet.2021.08.002

[312] S.L. Sing, F.E. Wiria, W.Y. Yeong. *Selective laser melting of lattice structures: A statistical approach to manufacturability and mechanical behavior*. Robotics and Computer–Integrated Manufacturing 49 (2018) 170–180. https://doi.org/10.1016/j.rcim.2017.06.006

[313] S. Tsopanos, R. Mines, S. McKown, Y. Shen, W.J. Cantwell, W. Brooks, C.J. Sutcliffe. *The Influence of Processing Parameters on the Mechanical Properties of Selectively Laser Melted Stainless Steel Microlattice Structures*. Journal of Manufacturing Science and Engineering 132 (2010) 041011. https://doi.org/10.1115/1.4001743

[314] X. Wang, J.A. Muñiz-Lerma, O. Sánchez-Mata, M. Attarian Shandiz, M. Brochu. *Microstructure and mechanical properties of stainless steel 316L vertical struts manufactured by laser powder bed fusion process*. Materials Science and Engineering: A 736 (2018) 27–40. https://doi.org/10.1016/j.msea.2018.08.069

[315] S.I. Shahabad, U. Ali, Z. Zhang, A Keshavarzkermani, R. Esmaeilizadeh, A. Bonakdar, E. Toyserkani. *On the effect of thin-wall thickness on melt pool dimensions in laser powder-bed fusion of Hastelloy X: Numerical modeling and experimental validation*. Journal of Manufacturing Processes 75 (2022) 435–449. https://doi.org/10.1016/j.jmapro.2022.01.029

[316] O. Poncelet, M. Marteleur, C. van der Rest, O. Rigo, J. Adrien, S. Dancette, P.J. Jacques, A. Simar. *Critical assessment of the impact of process parameters on vertical roughness and hardness of thin walls of AlSi10Mg processed by laser powder bed fusion*. Additive Manufacturing 38 (2021) 101801. https://doi.org/10.1016/j.addma.2020.101801

[317] L. Liu, P. Kamm, F. García-Moreno, J. Banhart, D. Pasini. *Elastic and failure response of imperfect three-dimensional metallic lattices: the role of geometric defects induced by Selective Laser Melting*. Journal of the Mechanics and Physics of Solids 107 (2017) 160–184. https://doi.org/10.1016/j.jmps.2017.07.003

[318] M. Dallago, F. Zanini, S. Carmignato, D. Pasini, M. Benedetti. *Effect of the geometrical defectiveness on the mechanical properties of SLM biomedical Ti6Al4V lattices*. Procedia Structural Integrity 13 (2018) 161–167. https://doi.org/10.1016/j.prostr.2018.12.027

[319] X. Cao, Y. Jiang, T. Zhao, P. Wang, Y. Wang, Z. Chen, Y. Li, D. Xiao, D. Fang. *Compression experiment and numerical evaluation on mechanical responses of the lattice structures with stochastic geometric defects originated from additive-manufacturing*. Composites Part B: Engineering 194 (2020) 108030. https://doi.org/10.1016/j.compositesb.2020.108030

[320] P. Sugg, P. Sperling, G. Meyer, M. Ellenberger, C. Mittelstedt, D. Pasini, F. Coppens. *CT based geometrical analysis of process induced defects in thin lattice struts*. ASTM International Conference on Additive Manufacturing, Orlando, USA, 2022.

[321] Z. Dong, Y. Liu, Q. Zhang, J. Ge, S. Ji, W. Li, J. Liang. *Microstructural heterogeneity of AlSi10Mg alloy lattice structures fabricated by selective laser melting: Phenomena and mechanism*. Journal of Alloys and Compounds 833 (2020) 155071. https://doi.org/10.1016/j.jallcom.2020.155071

[322] T. Tancogne-Dejean, A.B. Spierings, D. Mohr. *Additively-manufactured metallic micro-lattice materials for high specific energy absorption under static and dynamic loading*. Acta Materialia 116 (2016) 14–28. https://doi.org/10.1016/j.actamat.2016.05.054

[323] R. Wauthle, B. Vrancken, B. Beynaerts, K. Jorissen, J. Schrooten, J.P. Kruth, J. Van Humbeeck. *Effects of build orientation and heat treatment on the microstructure and mechanical properties of selective laser melted Ti6Al4V lattice structures*. Additive Manufacturing 5 (2015) 77–84. https://doi.org/10.1016/j.addma.2014.12.008

[324] L. Huynh, J. Rotella, M.D. Sangid. *Fatigue behavior of IN718 microtrusses produced by additive manufacturing*. Materials and Design 105 (2016) 278–289. https://doi.org/10.1016/j.matdes.2016.05.032

[325] A. Moussa, D. Melancon, A. El Elmi, D. Pasini. *Topology optimization of imperfect lattice materials built with process-induced defects via Powder Bed Fusion*. Additive Manufacturing 37 (2021) 101608. https://doi.org/10.1016/j.addma.2020.101608

[326] C. Bonatti, D. Mohr. *Large deformation response of additively-manufactured FCC metamaterials: From octet truss lattices towards continuous shell mesostructures*. International Journal of Plasticity 92 (2017) 122–147. https://doi.org/10.1016/j.ijplas.2017.02.003

[327] M.C. Messner. *Optimal lattice-structured materials*. Journal of the Mechanics and Physics of Solids 96 (2016) 162–183. https://doi.org/10.1016/j.jmps.2016.07.010

[328] Z. Li, Y. Nie, B. Liu, Z. Kuai, M. Zhao, F. Liu. *Mechanical properties of AlSi10Mg lattice structures fabricated by selective laser melting*. Materials & Design 192 (2020) 108709. https://doi.org/10.1016/j.matdes.2020.108709

[329] S. Drücker, J. Kajo Lüdeker, M. Blecken, A. Kurt, K. Betz, B. Kriegesmann, B. Fiedler. *Probabilistic analysis of additively manufactured polymer lattice structures*. Materials & Design 213 (2022) 110300. https://doi.org/10.1016/j.matdes.2021.110300

[330] R.M. Gorguluarslan, S. Park, D.W. Rosen, S. Choi. *A Multilevel Upscaling Method for Material Characterization of Additively Manufactured Part Under Uncertainties*. Journal of Mechanical Design 137 (2015) 111408. https://doi.org/10.1115/1.4031012

[331] B. Bahrami Babamiri, J.R. Mayeur, K. Hazeli. *Synchronous involvement of topology and microstructure to design additively manufactured lattice structures*. Additive Manufacturing 52 (2022) 102618. https://doi.org/10.1016/j.addma.2022.102618

[332] B. Lozanovski, D. Downinga, P. Tran, D. Shidid, M. Qian, P. Choong, M. Brandt, M. Leary. *A Monte Carlo simulation-based approach to realistic modelling of additively manufactured lattice structures*. Additive Manufacturing 32 (2020) 101092. https://doi.org/10.1016/j.addma.2020.101092

[333] H.D. Carlton, N.A. Volkoff-Shoemaker, M.C. Messner, N.R. Barton, M. Kumar. *Incorporating defects into model predictions of metal lattice-structured materials*. Materials Science & Engineering A 832 (2022) 142427. https://doi.org/10.1016/j.msea.2021.142427

[334] S. Van Bael, G. Kerckhofs, M. Moesen, G. Pyka, J. Schrooten, J.P. Kruth. *Micro-CT-based improvement of geometrical and mechanical controllability of selective laser melted Ti6Al4V porous structures*. Materials Science and Engineering A 528 (2011) 7423–7431. https://doi.org/10.1016/j.msea.2011.06.045

[335] J.U. Surjadi, Y. Lu. *Design criteria for tough metamaterials*. Nature Materials 21 (2022) 272–274. https://doi.org/10.1038/s41563-022-01193-6

[336] A.J.D. Shaikeea, H. Cui, M. O'Masta, X.R. Zheng, V.S. Deshpande. *The toughness of mechanical metamaterials*. Nature Materials 21 (2022) 297–304. https://doi.org/10.1038/s41563-021-01182-1

[337] Deutsches Institut für Normung. *DIN 50099. Tensile testing of metallic cellular materials*. Deutsches Institut für Normung e. V., Berlin, Germany, 2018.

[338] H. Alsalla, L. Hao, C. Smith. *Fracture toughness and tensile strength of 316L stainless steel cellular lattice structures manufactured using the selective laser melting technique*. Material Science & Engineering: A 669 (2016) 1–6. https://doi.org/10.1016/j.msea.2016.05.075

[339] R. Gümrük, R.A.W. Mines, S. Karadeniy. *Static mechanical behaviours of stainless-steel micro-lattice structures under different loading conditions*. Materials Science & Engineering A 586 (2013) 392–406. https://doi.org/10.1016/j.msea.2013.07.070

[340] A. Barbas, A.S. Bonnet, P. Lipinski, R. Pesci, G. Dubois. *Development and mechanical characterization of porous titanium bone substitutes*. Journal of the mechanical behavior of biomedical material 9 (2012) 34–44. https://doi.org/10.1016/j.jmbbm.2012.01.008

[341] F: Brenne, T. Niendorf, J.H. Maier. *Additively manufactured cellular structures: Impact of microstructure and local strains on the monotonic and cyclic behavior under uniaxial and bending load*. Journal of Materials Processing Technology 13 (2013) 1558–1564. https://doi.org/10.1016/j.jmatprotec.2013.03.013

[342] P. Köhnen, C. Haase, J. Bültmann, S. Ziegler, J.H. Schleifenbaum, W. Bleck. *Mechanical properties and deformation behavior of additively manufactured lattice structures of stainless steel*. Materials and Design 145 (2018) 205–217. https://doi.org/10.1016/j.matdes.2018.02.062

[343] Q. Burr, T. Persenot, P.T. Doutre, J.Y. Buffiere, P. Lhuissier, G. Martin, R. Dendievel. *A numerical framework to predict the fatigue life of lattice structures built by additive manufacturing*. International Journal of Fatigue 139 (2020) 105769. https://doi.org/10.1016/j.ijfatigue.2020.105769

[344] K. Refai, C: Brugger, M. Montemurro, N. Saintier. *An experimental and numerical study of the high cycle multiaxial fatigue strength of titanium lattice structures produced by Selective Laser Melting (SLM)*. International Journal of Fatigue 138 (2020) 105623. https://doi.org/10.1016/j.ijfatigue.2020.105623

[345] M. Dallago, V. Fontanari, E. Torresani, M. Leoni, C. Pederzolli, C. Potrich, M. Benedetti. *Fatigue and biological properties of Ti-6Al-4V cellular structures with variously arranged cubic cells made by selective laser melting*. Journal of the Mechanical Behavior of Biomedical Materials 78 (2018) 381–394. https://doi.org/10.1016/j.jmbbm.2017.11.044

[346] S. Raghavendra, A. Molinari, V. Fontanari, M. Dallago, V. Luchin, G. Zappini, M. Benedetti. *Effect of strut cross section and strut defect on tensile properties of cubic cellular structure*. Material Design & Processing Communications 2 (2020) 118. https://doi.org/10.1002/mdp2.118

[347] M. Dallago, S. Raghavendrea, V. Luchin, G. Zappini, D. Pasini, M. Benedetti. *The role of node fillet, unit-cell size and strut orientation on the fatigue strength of Ti-6Al-4V lattice materials additively manufactured via laser powder bed fusion*. International Journal of Fatigue 142 (2021) 105946. https://doi.org/10.1016/j.ijfatigue.2020.105946

[348] N. Soro, N. Saintier, J. Merzeau, M. Veidt, M.S. Dargusch. *Quasi-static and fatigue properties of graded Ti-6Al-4V lattices produced by Laser Powder Bed Fusion (LPBF)*. Additive Manufacturing 37 (2021) 101653. https://doi.org/10.1016/j.addma.2020.101653

[349] H. Chen, D. Gu, J. Xiong, M. Xia. Improving additive manufacturing processability of hard-to-process overhanging structure by selective laser melting. Journal of Materials Processing Tech. 250 (2017) 99–108. https://doi.org/10.1016/j.jmatprotec.2017.06.044

[350] S. Weber, J. Montero, M. Bleckmann, K. Paetzold. *Support-Free Metal Additive Manufacturing: A Structured Review on the State of the Art in Academia and Industry*. Proceedings of the International Conference on Engineering Design, Gothenburg, Sweden, 2021. https://doi.org/10.1017/pds.2021.542

[351] ASTM International. *ASTM C297/C297M-16. Standard Test Method for Flatwise Tensile Strength of Sandwich Constructions*. ASTM International, West Conshohocken, United States, 2017.

[352] X. Geng, Y. Lu, C. Liu, W. Li, Z. Yue. *Fracture characteristic analysis of cellular lattice structures under tensile load*. International Journal of Solids and Structures 163 (2019) 170–177. https://doi.org/10.1016/j.ijsolstr.2019.01.006

[353] H. Lei, C. Li, J. Meng, H. Zhou, Y. Liu, X. Zhang, P. Wang, D. Fang. *Evaluation of compressive properties of SLM-fabricated multi-layer lattice structures by experimental test and μ-CT-based finite element analysis*. Materials and Design 169 (2019) 107685. https://doi.org/10.1016/j.matdes.2019.107685

[354] M. Shinde, I.E. Ramirez-Chavez, D. Anderson, J. Fait, M. Jarrett, D. Bhate. *Towards an Ideal Energy Absorber: Relating Failure Mechanisms and Energy Absorption Metrics in Additively Manufactured AlSi10Mg Cellular Structures under Quasistatic Compression.* Journal of Manufacturing and Materials Processing 6 (2022) 140. https://doi.org/10.3390/jmmp6060140

[355] J. Niu, H.L. Choo, W. Sun, S.H. Mok. *Numerical study on load-bearing capabilities of beam-like lattice structures with three different unit cells*. International Journal of Mechanics and Materials in Design 14 (2018) 443–460. https://doi.org/10.1007/s10999-017-9384-3

[356] D. Noviello. *Understanding the Mechanical Properties of AM Lattice Structures with Testing and Simulation*. Autodesk University, Las Vegas, USA, 2016. https://www.autodesk.com/autodesk-university/class/Understanding-Mechanical-Properties-Additively-Manufactured-Lattice-Structures-Testing-and (last accessed on October 13th 2023)

[357] A. Taube, W. Reschetnik, L. Pauli, K.P. Hoyer, G. Kullmer, M. Schaper. *Numerische und mechanische Untersuchung additiv gefertigter TiAl6V4 Gitterstrukturen*. In: H. Richard, B. Schramm, T. Zipsner (Eds.). *Additive Fertigung von Bauteilen und Strukturen*. 1st ed., Springer Vieweg, Wiesbaden, Germany, 2017, 201–214. https://doi.org/10.1007/978-3-658-17780-5_13

[358] J.K. Chen, M.W. Wu, T.L. Cheng, P.H. Chiang. *Continuous compression behaviors of selective laser melting Ti-6Al-4V alloy with cuboctahedron cellular structures.* Materials Science & Engineering C 100 (2019) 781–788. https://doi.org/10.1016/j.msec.2019.03.054

[359] S. Daynes, S. Feih, W.F. Lu, J. Wei. *Optimisation of functionally graded lattice structures using isostatic lines*. Materials & Design 127 (2017) 215–223. https://doi.org/10.1016/j.matdes.2017.04.082

[360] S. Teufelhart. *Belastungsoptimiertes Design von Gitterstrukturen für die additive Fertigung nach dem bionischen Prinzip der kraftflussgerechten Gestaltung*. Ph.D. thesis. TU München, Munich, Germany, 2016.

[361] C. Liu, Z. Du, W. Zhang, Y. Zhu, X. Guo. *Additive Manufacturing-Oriented Design of Graded Lattice Structures Through Explicit Topology Optimization*. Journal of Applied Mechanics 84 (2017) 081008. https://doi.org/10.1115/1.4036941

[362] V. Sufiiarov, V. Sokolova, E. Borisov, A. Orlov, A. Popovich. *Investigation of accuracy, microstructure and properties of additive manufactured lattice structures*. Materials Today: Proceedings 30 (2020) 572–577. https://doi.org/10.1016/j.matpr.2020.01.137

[363] C: Wang, X. Gu, J. Zhu, H. Zhou, S. Li, W. Zhang. *Concurrent design of hierarchical structures with three-dimensional parameterized lattice microstructures for additive manufacturing*. Structural and Multidisciplinary Optimization 61 (2020) 869–894. https://doi.org/10.1007/s00158-019-02408-2

[364] L. Paul, J. Favre, B. Piotrowski, S. Kenzari, P. Laheurte. *Stress Concentration and Mechanical Strength of Cubic Lattice Architectures*. Materials 11 (2018) 1146. https://doi.org/10.3390/ma11071146

[365] M. Smith, Z. Guan, W.J. Cantwell. *Finite element modelling of the compressive response of lattice structures manufactured using the selective laser melting technique*. International Journal of Mechanical Sciences 67 (2013) 28–41. https://doi.org/10.1016/j.ijmecsci.2012.12.004

[366] L. Bai, C. Yi, X. Chen, Y. Sun, J. Zhang. *Effective Design of the Graded Strut of BCC Lattice Structure for Improving Mechanical Properties*. Materials 12 (2019) 2192. https://doi.org/10.3390/ma12132192

[367] Z. Xiao, Y. Yang, R. Xiao, Y. Bai, C. Song, D. Wang. *Evaluation of topology-optimized lattice structures manufactured via selective laser melting*. Materials & Design 143 (2018) 27–37. https://doi.org/10.1016/j.matdes.2018.01.023

[368] E. Träff, O. Sigmund, J.P. Groen. *Simple single-scale microstructures based on optimal rank-3 laminates*. Structural and Multidisciplinary Optimization 59 (2019) 1021–1031. https://doi.org/10.1007/s00158-018-2180-3

[369] G. Savio, A. Curtarello, S. Rosso, R. Meneghello, G. Concheri. *Homogenization driven design of lightweight structures for additive manufacturing*. International Journal on Interactive Design and Manufacturing 13 (2019) 263–276. https://doi.org/10.1007/s12008-019-00543-0

[370] L. Bai, Y. Xu, X. Chen, L. Xin, J. Zhang, K. Li, Y. Sun. *Improved mechanical properties and energy absorption of Ti6Al4V laser powder bed fusion lattice structures using curving lattice struts*. Materials & Design 211 (2021) 110140. https://doi.org/10.1016/j.matdes.2021.110140

[371] A. Bertocco, G. Iannitti, A. Caraviello, L. Esposito. *Lattice structures in stainless steel 17-4PH manufactured via selective laser melting (SLM) process: dimensional accuracy, satellites formation, compressive response and printing parameters optimization*. The International Journal of Advanced Manufacturing Technology 120 (2022) 4935–4949. https://doi.org/10.1007/s00170-022-08946-2

[372] Deutsches Institut für Normung. *DIN EN ISO 527 Part 3. Plastics - Determination of tensile properties - Test conditions for films and sheets.* Deutsches Institut für Normung e. V., Berlin, Germany, 2019.

[373] Deutsches Institut für Normung. *DIN EN ISO 6892 Part 1. Metallic materials - Tensile testing - Method of test at room temperature.* Deutsches Institut für Normung e. V., Berlin, Germany, 2017

[374] S.P. Timoshenko, J.M. Gere, W. Prager. *Theory of Elastic Stability, Second Edition*. Journal of Applied Mechanics 29 (1962) 220–221. https://doi.org/10.1115/1.3636481

[375] EOS GmbH. *EOS Aluminium AlSi10Mg - Material data sheet*. January 2022. https://www.eos.info/03_system-related-assets/material-related-contents/metal-materials-and-examples/metal-material-datasheet/aluminium/material_datasheet_eos_aluminium-alsi10mg_en_web.pdf (last accessed on October 13th 2023)

[376] B. Lozanovski, M. Leary, P. Tran, D. Shidid, M. Qian, P. Choong, M. Brandt. *Computational modelling of strut defects in SLM manufactured lattice structures*. Materials and Design 171 (2019) 107671. https://doi.org/10.1016/j.matdes.2019.107671

[377] Deutsches Institut für Normung. *DIN 50134. Testing of metallic materials - Compression test of metallic cellular materials.* Deutsches Institut für Normung e. V., Berlin, Germany, 2008.

[378] J. Weidmann, A. Großmann, C. Mittelstedt. *Laser powder bed fusion manufacturing of aluminum honeycomb structures: Theory and testing*. International Journal of Mechanical Sciences 180 (2020) 105639. https://doi.org/10.1016/j.ijmecsci.2020.105639

[379] Deutsches Institut für Normung. *DIN EN ISO 3369. Impermeable sintered metal materials and hardmetals - Determination of density.* Deutsches Institut für Normung e. V., Berlin, Germany, 2010.

[380] W.M. Haynes. *CRC Handbook of Chemistry and Physics*. 95th ed., CRC Press, Hoboken, United States, 2014. ISBN 978-1-4822-0868-9

[381] Verein Deutscher Ingenieure. *VDI 3405 Part 2. Additive manufacturing processes – Design rules – Test artefacts and test features for limiting geometric elements*. Verein Deutscher Ingenieure e.V., Düsseldorf, Germany, 2019.

[382] Huntsman Advanced Materials (Deutschland) GmbH & Co. KG. *Araldite® LY556 / Aradur® 917-1 / Accelerator DY070*. March 2017.

[383] E. Sert, E. Schuch, A. Öchsner, L. Hitzler, E. Werner, M. Merkel. *Tensile strength performance with determination of the Poisson's ratio of additively manufactured AlSi10Mg samples*. Material science & Egineerin Technology 50 (2019) 539–545. https://doi.org/10.1002/mawe.201800233

[384] F. Becker. *Entwicklung einer Beschreibungsmethodik für das mechanische Verhalten unverstärkter Thermoplaste bei hohen Deformationsgeschwindigkeiten*. Ph.D. thesis. Martin-Luther-Universität Halle-Wittenberg, Halle (Saale), Germany, 2009.

[385] M. Wächter, C. Müller, A. Esderts. *Angewandter Festigkeitsnachweis nach FKM-Richtlinie*. 1st ed., Springer Vieweg. Wiesbaden, Germany, 2017. ISBN 978-3-658-17459-0

[386] Abaqus. *Abaqus 6.14 Online Documentation*. Dassault Systems, Providence, United States, 2014. http://130.149.89.49:2080/v6.14/ (last accessed on October 13th 2023)

[387] M. Schäfer. *Numerik im Maschinenbau*. 1st ed., Springer Berlin Heidelberg, Berlin Heidelberg, Germany, 1999. ISBN 978-3-540-65391-2

[388] P.R. Onck, E.W. Andrews, L.J. Gibson. *Size effects in ductile cellular solids. Part I: modeling*. International Journal of Mechanical Sciences 43 (2001) 681–699. https://doi.org/10.1016/S0020-7403(00)00042-4

[389] E.W. Andrews, G. Gioux, P. Onck, L.J. Gibson. *Size effects in ductile cellular solids. Part II: experimental results*. International Journal of Mechanical Sciences 43 (2001) 701–713. https://doi.org/10.1016/S0020-7403(00)00043-6

[390] Altair Engineering Inc. *HyperWorks 14.0: OptiStruct User's Guide*. Altair Engineering Inc., Troy, United States, 2015.

[391] P. Tiernan, A. Hannon. *Design optimisation of biaxial tensile test specimen using finite element analysis*. International Journal of Material Forming 7 (2014) 117–123. https://doi.org/10.1007/s12289-012-1105-8

[392] Y. Wang, M.Y. Wang, F. Chen. *Structure-material integrated design by level sets.* Structural and Multidisciplinary Optimization 54 (2016) 1145–1156. https://doi.org/10.1007/s00158-016-1430-5

[393] M. Bijak-Zochowski, A.M. Waas, W.J. Anderson, C.E. Miniatt. *Reduction of contact stress by use of relief notches*. Experimental Mechanics 31 (1991) 271–275. https://doi.org/10.1007/BF02326071

[394] R.V. Baud. *Beiträge zur Kenntnis der Spannungsverteilung in prismatischen und keilförmigen Konstruktionselementen mit Querschnittsübergangen*. PhD thesis. ETH Zürich, Zürich, Switzerland, 1934.

[395] A. Thum, W. Bautz. *Der Entlastungsübergang: Günstigste Ausbildung des Überganges an abgesetzten Wellen u. dgl*. Forschung auf dem Gebiet des Ingenieurwesens A 6 (1935) 269–73. https://doi.org/10.1007/bf02592563

[396] P. Grodzinski. *Investigations on shaft fillets*. Engineering. London 152 (1941) 321–324.
[397] S. Zelenika, S. Henein, L. Myklebust. *Investigation of Optimised Notch Shapes for Flexural Hinges*. 3rd International Workshop on Mechanical Engineering Design of Synchrotron Radiation Equipment and Instrumentation (MEDSI 2004), Grenoble, France, 2004.
[398] M. Scherrer. *Kerbspannung und Kerbformoptimierung*. PhD thesis. Forschungszentrum Karlsruhe, Karlsruhe, Germany, 2004.
[399] C. Mattheck C. *Teacher tree: The evolution of notch shape optimization from complex to simple*. Engineering Fracture Mechanics 73 (2006) 1732–1742. https://doi.org/10.1016/j.engfracmech.2006.02.007
[400] J. Sörensen. *Untersuchungen zur Vereinfachung der Kerbformoptimierung*. PhD thesis. Forschungszentrum Karlsruhe, Karlsruhe, Germany, 2008.
[401] W.D. Pilkey. *Peterson's stress concentration factors*. 2nd ed. John Wiley & Sons inc., New York, United States, 1997. ISBN 978-0-471-53849-3
[402] R. Vrána, J. Jaroš, D. Koutný, J. Nosek, T. Zikmund, J. Kaiser, D. Paloušek. *Contour laser strategy and its benefits for lattice structure manufacturing by selective laser melting technology*. Journal of Manufacturing Processes 74 (2022) 640–57. https://doi.org/10.1016/j.jmapro.2021.12.006
[403] K. Siebertz, D. van Bebber, T. Hochkirchen. *Statistische Versuchsplanung: Design of Experiments (DoE)*. 1st ed., Springer Vieweg, Berlin Heidelberg, Germany, 2010. ISBN 978-3-642-05493-8
[404] F.A.C. Viana. *A Tutorial on Latin Hypercube Design of Experiments*. Quality and Reliability Engineergin International 32 (2016) 1975–1985. https://doi.org/10.1002/qre.1924
[405] F. Cady. *The Data Science Handbook*. 1st ed., Wiley, Hoboken, United States, 2017. 978-1119092940
[406] D.N. Reshef, Y.A. Reshef, H.K. Finucane, S.R. Grossman, G. McVean, P.J. Turnbaugh, E.S. Lander, M. Mitzenmacher, P.C: Sabeti. *Detecting novel associations in large data sets*. Science 334 (2011) 1518–1524. https://doi.org/10.1126/science.1205438
[407] P. Duysinx, M. Bendsøe. *Topology optimization of continuum structures with local stress constraints*. International Journal for Numerical Methods in Engineering 43 (1998) 1453–1478. https://doi.org/10.1002/(SICI)1097-0207(19981230)43:8<1453::AID-NME480>3.3.CO;2-U
[408] E. Holmberg, B. Torstenfelt, A. Klarbring. *Stress constrained topology optimization*. Structural and Multidisciplinary Optimization 48 (2013) 33–47. https://doi.org/10.1007/s00158-012-0880-7
[409] M. Zhou, O. Sigmund. *On fully stressed design and p-norm measures in structural optimization*. Structural and Multidisciplinary Optimization 56 (2017) 731–736. https://doi.org/10.1007/s00158-017-1731-3

[410] K. Lee, K. Ahn, J. Yoo. *A novel P-norm correction method for lightweight topology optimization under maximum stress constraints.* Computers & Structures 171 (2016) 18–30. https://doi.org/10.1016/j.compstruc.2016.04.005

[411] C. Le, J. Norato, T. Bruns, C. Ha, D. Tortorelli. *Stress-based topology optimization for continua*. Structural and Multidisciplinary Optimization 41 (2010) 605–620. https://doi.org/10.1007/s00158-009-0440-y

List of Figures

List of Tables

A Publications and supervised theses

This section gathers all journal publications, conference contributions and supervised student theses in the frame of my stay at the Technical University of Darmstadt. Some of the contents of this work have already been published in international journals or presented at conferences before writing it.

Peer reviewed publications, project reports and submitted manuscripts

- F. Birk, G. Meyer, M. Weigold, C. Mittelstedt. *Schlussbericht zu IGF-Vorhaben Nr. 19172 N*. Technical Universtiy of Darmstadt, Darmstadt, Germany, 2021. https://doi.org/10.26083/tuprints-00013311

- G. Meyer, F. Brenne, T. Niendorf, C. Mittelstedt. *Influence of the Miniaturisation Effect on the Effective Stiffness of Lattice Structures in Additive Manufacturing*. Metals 10 (2020) 1442. https://doi.org/10.3390/met10111442

- S. Gries, G. Meyer, A. Wonisch, R. Jakobi, C. Mittelstedt. *Towards Enhancing the Potential of Injection Molding Tools through Optimized Close-Contour Cooling and Additive Manufacturing*. Materials 14 (2021) 3434. https://doi.org/10.3390/ma14123434

- G. Meyer, J. Musekamp, F. Göbel, F. Gardian, C. Mittelstedt. *Manufacturability investigation of inclined AlSi10Mg lattice struts by means of selective laser melting*. Manufacturing Letters 31 (2022) 101–105. https://doi.org/10.1016/j.mfglet.2021.08.002

- A. Coluccia, G. Jiang, G. Meyer, G. De Pasquale, C. Mittelstedt. *Nonlinear static and dynamic modeling of energy absorption lattice structures behavior*. Mechanics of Advanced Materials and Structures 30 (2023) 2838–2849. https://doi.org/10.1080/15376494.2022.2064016

- G. Meyer, K. Schelleis, O. Weeger, C. Mittelstedt. *Tensile specimen design proposal for truss-based lattice structures*. Mechanics of Advanced Materials and Structures 30 (2022) 4473–4500. https://doi.org/10.1080/15376494.2022.2097352

- G. Meyer, H. Wang, C. Mittelstedt. *Influence of geometrical notches and form optimization on the mechanical properties of additively manufactured lattice structures*. Materials & Design 222 (2022) 111082. https://doi.org/10.1016/j.matdes.2022.111082

- H. Georges, G. Meyer, C. Mittelstedt, W. Becker. *2D Elasticity solution for sandwich panels with functionally graded lattice cores*. Composite Structures 300 (2022) 116045. https://doi.org/10.1016/j.compstruct.2022.116045

- J. Jung, G. Meyer, M. Greiner, C. Mittelstedt. *Load Introduction Specimen Design for the Mechanical Characterisation of Lattice Structures under Tensile Loading*. Journal of Manufacturing and Materials Processing 7 (2023) 37. https://doi.org/10.3390/jmmp7010037

- M. Sos, G. Meyer, K. Durst, C. Mittelstedt, E. Bruder. *Microstructure and mechanical properties of additively manufactured AlSi10Mg lattice structures from single contour exposure*. Materials & Design 227 (2023) 111796. https://doi.org/10.1016/j.matdes.2023.111796

- A. Großmann, M. Klyk, L. Kohn, G. Meyer, M. Greiner, Y. Yang, C. Mittelstedt. *Bio-inspired airwings: Design and additive manufacturing of a geometrically graded microscale maple seed*. SSRN Preprint. http://dx.doi.org/10.2139/ssrn.4420965

- A. Großmann, M. Rexer, M. Greiner, G. Meyer, J. Mölleney, L. Kohn, V. Abbatiello, P.F. Pelz, C. Mittelstedt. *Material and process invariant scaling laws to predict porosity of dense and lattice structures in laser powder bed fusion*. SSRN Preprint. http://dx.doi.org/10.2139/ssrn.4189610

Confence contributions

- G. Meyer, A. Landmann, C. Mittelstedt. *Cost-efficient lightweight design and performance increase of tooling machines through the implementation of fibre reinforced composite components.* ICCS21, Bologna, Italy, 2018.

- G. Meyer, F. Brenne, A. Großmann, T. Niendorf, C. Mittelstedt. *Influence of the miniaturization effect on the effective stiffness of lattice structures in additive manufacturing*. Sim-AM 2019, Pavia, Italy, 2019.

- G. Meyer, P. Weis, A. Großmann, C. Clemen, C. Mittelstedt. *C-Frame design optimization for selective laser melting*. Deutscher Luft- und Raumfahrtkongress, Darmstadt, Germany, 2019. https://www.dglr.de/publikationen/2019/490053.pdf (last accessed on October 11th 2023)

- G. Meyer, E. Bruder, K. Durst, C. Mittelstedt. *Influence of the miniaturization effect on lattice structures by means of PBF with AlSi10Mg*. MSE 2020, online, 2020.

- A. Großmann, H. Merschroth, J. Felger, G. Meyer, M. Weigold, P. Pelz, C. Mittelstedt. *Towards Component Series Production in Laser Powder Bed Fusion by Melt Pool Control*. MSE 2020, online, 2020.

- G. Meyer, H. Wang, S. Mokdad, C. Mittelstedt. *Influence of a constructive form optimization on the mechanical properties of additively manufactured lattice structures*. ICMAE, online, 2021.

- A. Coluccia, G. De Pasquale, G. Meyer, C. Mittelstedt. *Modeling of lattice structures energy absorption under impact loads*. ICMAE, online, 2021.

- G. Meyer, H. Georges, M. Greiner, A. Großmann, C. Mittelstedt. *Beitrag zur zuverlässigen Implementierung von additiv gefertigten zellulären Strukturen in Leichtbaustrukturen*. DLRK 2021, online, 2021.

- G. Meyer, C. Mittelstedt. *Towards the reliable implementation of additively manufactured lattice structures into lightweight components*. ESA ICAM22, online, 2022.

- G. Meyer, K. Schelleis, O. Weeger, C. Mittelstedt. *Systematic Sample Design Methodology for Reliable Determination of Tensile Effective Lattice Structure Properties by Means of Functional Grading*. M2D2022, Funchal, Portugal, 2022.

- H. Wang, G. Meyer, C. Mittelstedt. *Influence of a constructive form optimization on the mechanical properties of additively manufactured lattice structures*. M2D2022, Funchal, Portugal, 2022.

- A. Coluccia, G. Meyer, C. Mittelstedt, G. De Pasquale. *Compact modeling of energy absorption by lattice structures under impact loads*. M2D2022, Funchal, Portugal, 2022.

- M. Sos, G. Meyer, E. Bruder, C. Mittelstedt. K. Durst. *Influence of heat treatment on microstructural and mechanical properties of AlSi10Mg lattice structures*. MSE 2022, Darmstadt, Germany, 2022.

- P. Sugg, P. Sperling, G. Meyer, M. Ellenberger, C. Mittelstedt, D. Pasini, F. Coppens. *CT based geometrical analysis of process induced defects in thin lattice struts*. ASTM International Conference on Additive Manufacturing, Orlando, USA, 2022.

- S. Liseni, A. Coluccia, G. Meyer, C. Mittelstedt, G. De Pasquale. *Numerical method for energy absorption maximimzation in lattice structures and experimental validation*. 17th ECSSMET, Toulouse, France, 2023.

- M. Greiner, J. Jung, G. Meyer, C. Mittelstedt. *Specimen design for tensile load introduction into lattice structures*. 17th ECSSMET, Toulouse, France, 2023.

- G. Meyer, R. Pfeffer, Z. Eckert, C. Mittelstedt. *Tensile specimen for truss-based lattice structures: manufacturing and experimental validation*. 17th ECSSMET, Toulouse, France, 2023.

Directly supervised Design Projects, Bachelor and Master theses

- F. Diz. *Untersuchung des Verhaltens von Stahl-Hubbalkenarmen und Entwicklung von Konstruktionsregeln für eine Umsetzung in einer CFK-Bauweise*. Master thesis. TU Darmstadt, Darmstadt, Germany, 2017.

- L. Buchmann. *Untersuchung des Verhaltens eines Stahl-Spindelstocks für die zukünftige Umsetzung in einer CFK-Bauweise*. Bachelor thesis. TU Darmstadt, Darmstadt, Germany, 2018.

- L. Ladewig, P. Jakobi, J. Niewiadomski, R. Dziedzitz, M. Masarczyk. *Erstellung von Konstruktionsvarianten eines CFK-Spindelstocks und Bewertung der Konzepte für einen zukünftigen Aufbau*. Advanced Research Project. TU Darmstadt, Darmstadt, Germany, 2018.

- T. Buschulte. *Laminatauslegung eines CFK-Spindelstocks und Gegenüberstellung mit seinem Stahlpendant*. Bachelor thesis. TU Darmstadt, Darmstadt, Germany, 2018.

- S. Gries. *Parameteroptimierung von Kühlkanal-Designs in Spritzgießwerkzeugen basierend auf dem lokalen Kühlbedarf*. Master thesis. TU Darmstadt, Darmstadt, Germany, 2019.

- H. Weigert. *Konzipierung und Validierung zuverlässiger additiv gefertigter Zugproben zur Ermittlung von Gitterstruktureigenschaften aus AlSi10Mg*. Master thesis. TU Darmstadt, Darmstadt, Germany, 2019.

- F. Göbel. *Untersuchungen zum stützstrukturfreien Drucken beim selektiven Laserschmelzen von AlSi10Mg*. Bachelor thesis. TU Darmstadt, Darmstadt, Germany, 2020.

- K. Schelleis. *Zur Optimierung der Gradierung von Gitterstrukturen beim selektiven Laserschmelzen von AlSi10Mg*. Master thesis. TU Darmstadt, Darmstadt, Germany, 2020.

- H. Wang. *Einfluss einer konstruktiven Formoptimierung auf die mechanischen Eigenschaften von Gitterstrukturen beim selektiven Laserschmelzen von AlSi10Mg*. Bachelor thesis. TU Darmstadt, Darmstadt, Germany, 2020.

- A. Coluccia. *Modeling and simulation of lightweight lattice structures for impact energy absorption*. Master thesis. Politecnico di Torino / TU Darmstadt, Torino / Darmstadt, Italy / Germany, 2021.

- B. Traenckner. *Untersuchung der mehrfachen Konturbelichtung als Herstellungsstrategie von Gitterstrukturen beim selektiven Laserschmelzen von AlSi10Mg*. Bachelor thesis. TU Darmstadt, Darmstadt, Germany, 2021.

- M. Ellenberger. *Einfluss der Belichtungsstrategie auf die mechanischen Eigenschaften von Gitterstrukturen beim selektiven Laserschmelzen von AlSi10Mg*. Bachelor thesis. TU Darmstadt, Darmstadt, Germany, 2021.

- M. Sos. *Microstructural and Mechanical Properties of Additively Manufactured AlSi10Mg Lattices*. Master thesis. TU Darmstadt, Darmstadt, Germany, 2021.

- K. Raetz. *Zur Optimierung der Wirtschlaftlichkeit des PBF-Verfahrens: Analyse und Potentialabschätzung der Auswirkungen einzelner Elemente der Prozesskette.* Bachelor thesis. TU Darmstadt, Darmstadt, Germany, 2021.

- M. Acedo Mestre, M.G. Frank, P.C. Webler, L. Zerhusen, Z. Zhang. *Zur Gestaltung der Krafteinleitung bei additiv gefertigten Zugproben beim selektiven Laserschmelzen von AlSi10Mg*. Advanced Design Project. TU Darmstadt, Darmstadt, Germany, 2021.

- M. Bode. *Zur Herstellung eines Gitter-Hülle Übergangs bei additiv gefertigten Zugproben beim selektiven Laserschmelzen von AlSi10Mg.* Master thesis. TU Darmstadt, Darmstadt, Germany, 2021.

- G. Jiang. *Modelling and simulation of lattice structures with different aspect ratios*. Master thesis. Politecnico di Torino / TU Darmstadt, Torino / Darmstadt, Italy / Germany, 2021.

- J. Jung. *Zur Gestaltung der Krafteinleitung bei Proben für die mechanische Charakterisierung von Gitterstruktureigenschaften unter Zugbelastung*. Master thesis. TU Darmstadt, Darmstadt, Germany, 2022.

- Z. Eckert. *Zur zuverlässigen Herstellung gradierter Gitterstrukturen bei additiv gefertigten Zugproben beim selektiven Laserschmelzen von AlSi10Mg*. Bachelor thesis. TU Darmstadt, Darmstadt, Germany, 2022.

- P.S. Becks. *Implementierung von Kerbwirkungsverringerungsansätze zur Gestaltung eines homogenen Einheitszellenübergang bei additiv gefertigten AlSi10Mg gradierten Gitterstrukturen*. Master thesis. TU Darmstadt, Darmstadt, Germany, 2022.

- L. Fischer. *Zur Herstellung eines Gitter-Hülle Übergangs bei additiv gefertigten Zugproben beim selektiven Laserschmelzen von AlSi10Mg*. Bachelor thesis. TU Darmstadt, Darmstadt, Germany, 2022.

- R.S. Pfeffer. *Zur experimentellen Validierung eines Krafteinleitungskonzeptes bei Versuchsproben für die mechanische Charakterisierung von Gitterstruktureigenschaften unter Zugbelastung*. Master thesis. TU Darmstadt, Darmstadt, Germany, 2022.

- S. Liseni. *Modeling and validation of lightweight lattice structures for high specific energy absorption*. Master thesis. Politecnico di Torino / TU Darmstadt, Torino / Darmstadt, Italy / Germany, 2022.

- M. Wicker. *Mechanische Charakterisierung additiv gefertigter Gitter aus AlSi10Mg nach Wärmebehandlung*. Bachelor thesis. TU Darmstadt, Darmstadt, Germany, 2022.

- H. Wang. *Parametric Design and Validation of Additively Manufactured Catalytic Converter based on Triply Periodic Minimal Surface (TPMS)*. Master thesis. TU Darmstadt, Darmstadt, Germany, 2023.

B Design: structural grading

This section offers complementary data to the investigation of the structural grading reported in section 4.1.

Theoretical effective properties

AppendixTable B-1 lists the used theoretical properties resulting from the analytical model of Souza et al. (see section 3.2.1) with the material properties of the solid base material described in chapter 4. The used effective properties are the aspect ratio AR, the relative density $\bar{\rho}$ and the effective Young's modulus E^*_{ana}.

AppendixTable B-1: Theoretical effective properties.

bcc			$f_2$ccz			bcc$_z$			$f_2$cc		
AR	$\bar{\rho}$	E^*_{ana} [MPa]	**AR**	$\bar{\rho}$	E^*_{ana} [MPa]	**AR**	$\bar{\rho}$	E^*_{ana} [MPa]	**AR**	$\bar{\rho}$	E^*_{ana} [MPa]
6	0.128	133	6	0.120	1834	6	0.144	1661	6	0.105	307
8	0.075	44	8	0.071	963	8	0.085	903	8	0.062	104
10	0.049	18	10	0.047	594	10	0.056	568	10	0.040	44
6	0.128	133	6	0.120	1834	6	0.144	1661	6	0.105	307

Determination of tolerance range

The tolerance range is assessed based on the investigation of sample designs extracted from existing testing norms for conventional bulk materials. The selected designs are the sample type 1B from the testing norm for the determination of plastics tensile properties DIN EN ISO 527-3 [372] and the sample form 2 from the B1 table of the norm for tensile testing of metallic materials DIN EN ISO 6892-1 [373]. Both samples are compared to the tensile sample proposed by the norm for tensile testing of metallic cellular materials DIN 50099 [337]. In order to enable a fair comparison at the gauge region between the different sample designs, sample dimensions are scaled according to the normalised path $L(x)$, which is defined by the ratio between the *gauge length* L_0 and the whole *parallel length* L_1. Analogous to the lattice tensile specimen, the investigated samples are analysed according to sample quality criteria that are assessed at both the centre and the edge of the sample. The quality criterion h_{uniax}, see Eq.30, describes the uniaxiality degree and is derived from the comparison between von Mises and principal stresses in the loading direction. The quality criterion h_σ, see Eq.32, describes the loading state of the sample and is derived from the comparison between local and half gauge length stresses. AppendixFigure B-1 provides a schematic explanation of all relevant dimensions, while AppendixTable B-2 gathers the relevant dimensions of the investigated samples. The analysis is performed using a 2D plate model of the samples using the software package *ABAQUS CAE 2017*.

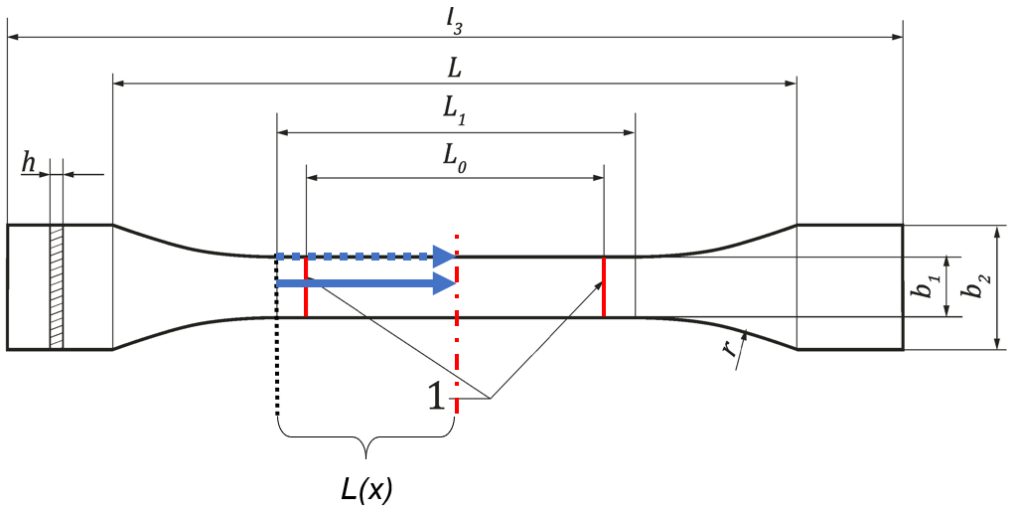

AppendixFigure B-1: Sample dimensions. Recompiled from sample 1B [372].

AppendixTable B-2: Investigated sample dimensions.

Dimensions [mm]	DIN 50099	DIN 6892-1	DIN EN ISO 527
b_1	50	20	10
b_2	60	24	20
r	5	20	60
L_0	83	100	50
L_1	100	120	60
L	110	137	108
l_3	140	177	138
L_0 / L_1	0.83	0.83	0.83
L_0 / b_1	1.66	5	5

The results depicted in AppendixFigure B-2 and AppendixFigure B-3 highlight a more rapid convergence of both quality criteria after reaching the gauge region (1) for samples extracted from the norms for tensile testing of conventional materials. On the one hand, this can be explained by the differences in radius requirements that have a major impact on the loading state. The smallest recommended radius by the DIN 50099 corresponds to 10 % of the sample diameter, which is proportionally much smaller than the recommendations of other norms. On the other hand, the smaller slenderness ratio L_0/b_1 of DIN 50099 with, in this example, 1.66 or 2 according to the norm recommendation, offers slower convergence along the normalised path and hints at potential issues in the definition of a gauge. Thus, DIN 50099 cannot be taken as basis and only norms for conventional materials are regarded. The arbitrary tolerance range for deviating from defined sample quality criteria is set to 1 % at the interface between the transition region and the target region.

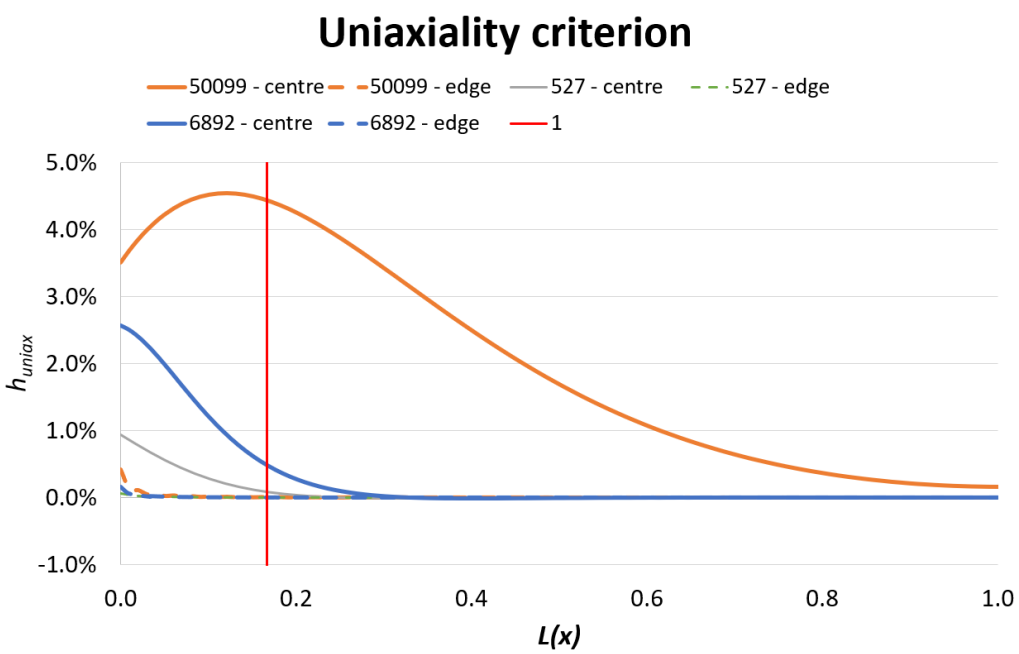

AppendixFigure B-2: Uniaxiality criterion results.

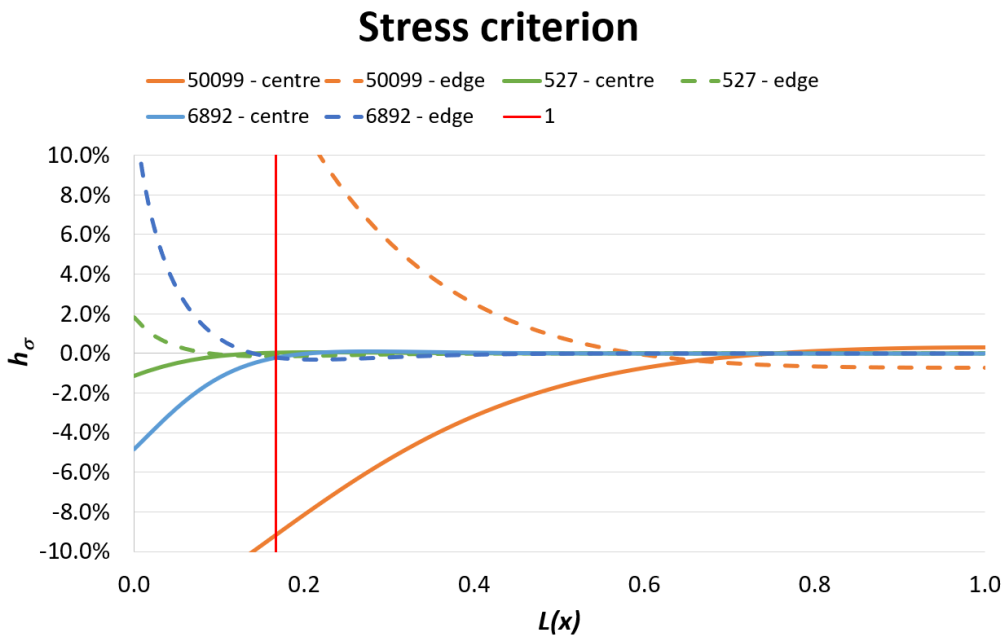

AppendixFigure B-3: Stress criterion results.

Grading parameters

AppendixTable B-3 to AppendixTable B-6 provide the list of the systematically identified grading parameters for all the investigated configurations.

AppendixTable B-3: Grading parameters (bcc).

AR	Size	A_{xy}	B_{xy}	C_{xy}	C_z	SCF
6	8x8x32	0.343	-0.198	0.893	1.123	1.20
	10x10x40	0.395	-0.220	0.897	1.120	1.25
	12x12x48	0.423	-0.231	0.902	1.117	1.30
8	8x8x32	0.379	-0.236	0.875	1.146	1.20
	10x10x40	0.414	-0.254	0.887	1.141	1.25
	12x12x48	0.453	-0.262	0.894	1.138	1.30
10	8x8x32	0.395	-0.260	0.863	1.161	1.20
	10x10x40	0.426	-0.273	0.881	1.140	1.25
	12x12x48	0.460	-0.278	0.891	1.140	1.30

AppendixTable B-4: Grading parameters (f_2cc_z).

AR	Size	A_{xy}	B_{xy}	C_{xy}	C_z	SCF
6	8x8x32	0.379	-0.228	0.859	1.155	1.25
	10x10x40	0.400	-0.260	0.832	1.178	1.40
	12x12x48	0.466	-0.291	0.816	1.177	1.43
8	8x8x32	0.373	-0.248	0.844	1.170	1.25
	10x10x40	0.392	-0.283	0.820	1.195	1.40
	12x12x48	0.460	-0.315	0.806	1.194	1.43
10	8x8x32	0.358	-0.259	0.839	1.179	1.25
	10x10x40	0.378	-0.295	0.816	1.187	1.40
	12x12x48	0.445	-0.328	0.804	1.203	1.43

AppendixTable B-5: Grading parameters (bcc_z).

AR	Size	A_{xy}	B_{xy}	C_{xy}	C_z	SCF
6	8x8x32	0.212	-0.100	0.905	1.117	1.25
	10x10x40	0.250	-0.125	0.891	1.130	1.30
8	8x8x32	0.218	-0.104	0.902	1.124	1.25
	10x10x40	0.257	-0.130	0.887	1.137	1.30
10	8x8x32	0.243	-0.089	0.901	1.155	1.25
	10x10x40	0.258	-0.133	0.886	1.141	1.30

AppendixTable B-6: Grading parameters (f_2cc).

AR	Size	A_{xy}	B_{xy}	C_{xy}	C_z	SCF
6	8x8x48	0.266	-0.059	1.085	1.011	1.30
	10x10x60	0.255	-0.065	1.055	1.112	1.50
8	8x8x48	0.351	-0.062	1.122	1.135	1.30
	10x10x60	0.337	-0.067	1.083	1.135	1.50
10	8x8x48	0.395	-0.060	1.155	1.151	1.30
	10x10x60	0.380	-0.063	1.110	1.151	1.50

Critical aspect ratio after grading

AppendixTable B-7 and AppendixTable B-8 sum up the most critical ARs with SCF and the next critical AR without SCF for all the investigated configurations. The AR values below 5 are marked with red font.

AppendixTable B-7: ARs obtained after grading (bcc & f_2cc_z).

AR (target)	Sample size	bcc		f_2cc_z	
		Crit. AR (SCF)	Next crit. AR	Crit. AR (SCF)	Next crit. AR
6	8x8x32	3.72	4.63	3.48	4.53
	10x10x40	3.44	4.30	3.06	4.29
	12x12x48	3.24	4.22	2.86	4.09
8	8x8x32	4.83	5.80	4.66	5.83
	10x10x40	4.53	5.66	4.11	5.75
	12x12x48	4.23	5.51	3.83	5.48
10	8x8x32	5.97	7.17	5.89	7.36
	10x10x40	5.61	11.16	5.19	7.50
	12x12x48	5.27	6.85	4.84	6.92

AppendixTable B-8: ARs obtained after grading (bcc_z & f_2cc).

AR (target)	Sample size	bcc_z		$*f_2cc$	
		Crit. AR (SCF)	Next crit. AR	Crit. AR (SCF)	Next crit. AR
6	8x8x32 (8x8x48*)	3.96	5.08	3.64	4.82
	10x10x40 (10x10x60*)	3.69	4.80	3.19	5.58
8	8x8x32 (8x8x48*)	5.25	5.42	4.55	5.92
	10x10x40 (10x10x60*)	4.90	6.99	3.99	7.88
10	8x8x32 (8x8x48*)	6.44	7.20	5.52	8.02
	10x10x40 (10x10x60*)	6.12	7.26	4.83	8.26

Upper corner stress values

As a complement to the chosen graphical display of the results, AppendixTable B-9 and AppendixTable B-10 sum up the values obtained from the stress criterion at the sample's upper corner $h^*_{\sigma,mises,corner}$, i.e. at the interface between bulk and transition regions.

AppendixTable B-9: Stress criterion at the sample's corner (bcc & f_2cc_z).

$h^*_{\sigma,mises,corner}$		bcc		f2ccz	
AR	**Sample size**	**Ungraded**	**Graded**	**Ungraded**	**Graded**
6	8x8x32	0.69	0.01	0.89	-0.01
	10x10x40	0.87	0.00	1.10	-0.05
	12x12x48	1.04	0.01	1.31	-0.05
8	8x8x32	0.58	-0.02	0.78	0.00
	10x10x40	0.75	0.01	0.99	-0.03
	12x12x48	0.90	0.00	1.18	-0.02
10	8x8x32	0.50	-0.03	0.70	0.00
	10x10x40	0.65	0.00	0.90	-0.02
	12x12x48	0.73	0.00	1.09	0.00

AppendixTable B-10: Stress criterion at the sample's corner (bcc_z & f_2cc).

$h^*_{\sigma,mises,corner}$		bcc		f2ccz	
AR	**Sample size**	**Ungraded**	**Graded**	**Ungraded**	**Graded**
6	8x8x32 (8x8x48*)	0.63	-0.04	0.61	-0.01
	10x10x40 (10x10x60*)	0.77	-0.04	0.85	-0.02
8	8x8x32 (8x8x48*)	0.57	-0.06	0.50	-0.09
	10x10x40 (10x10x60*)	0.70	-0.06	0.73	-0.05
10	8x8x32 (8x8x48*)	0.53	-0.11	0.40	-0.12
	10x10x40 (10x10x60*)	0.65	-0.08	0.62	-0.05

Representativity of diagonal view cut

AppendixFigure B-4 to AppendixFigure B-9 show one example of all cut views for the bcc RUCs in both ungraded and graded configurations. The following representative view cuts are selected for displaying results: front ($x^* = x_0$), middle ($x^* = n_{RUC,x,y}/2$) and diagonal (from $x^*, y^* = x_0, y_0$ to $x^*, y^* = n_{RUC,x,y}/2$). This set of pictures proves the representativity of the diagonal view cut and, together with AppendixTable B-9 and AppendixTable B-10, ensures that no singularities are present.

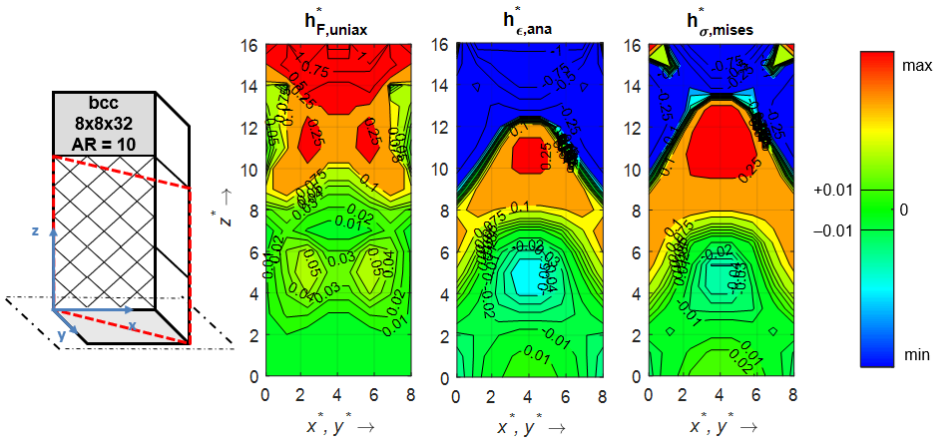

AppendixFigure B-4: Sample quality results: bcc 8x8x32 AR10 ungraded (diagonal).

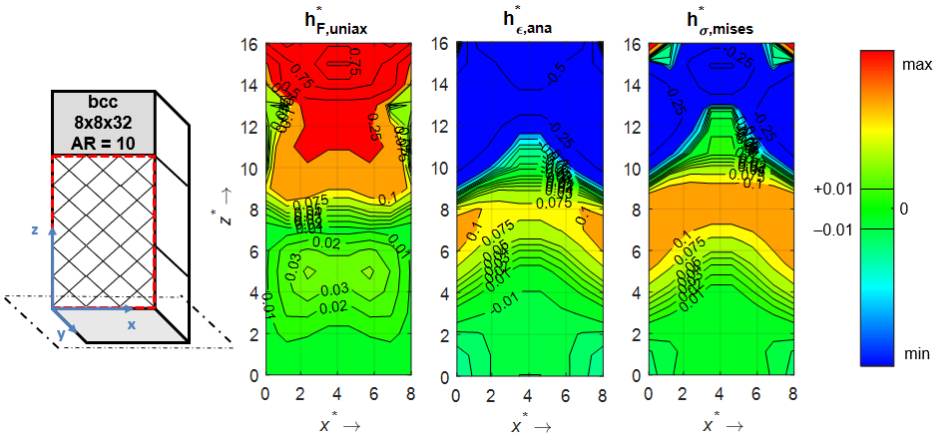

AppendixFigure B-5: Sample quality results: bcc 8x8x32 AR10 ungraded (front).

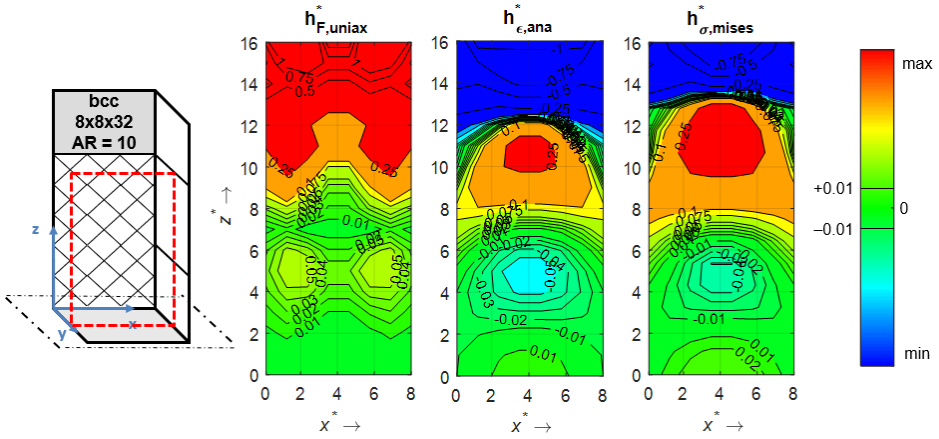

AppendixFigure B-6: Sample quality results: bcc 8x8x32 AR10 ungraded (middle).

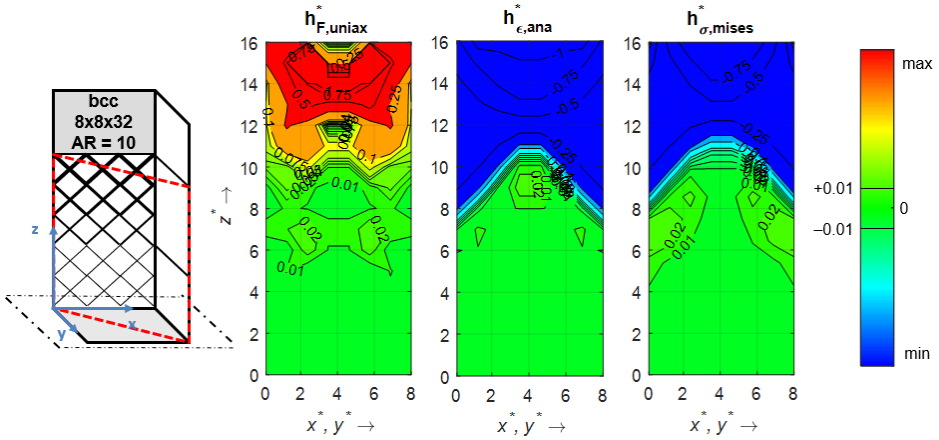

AppendixFigure B-7: Sample quality results: bcc 8x8x32 AR10 graded (diagonal).

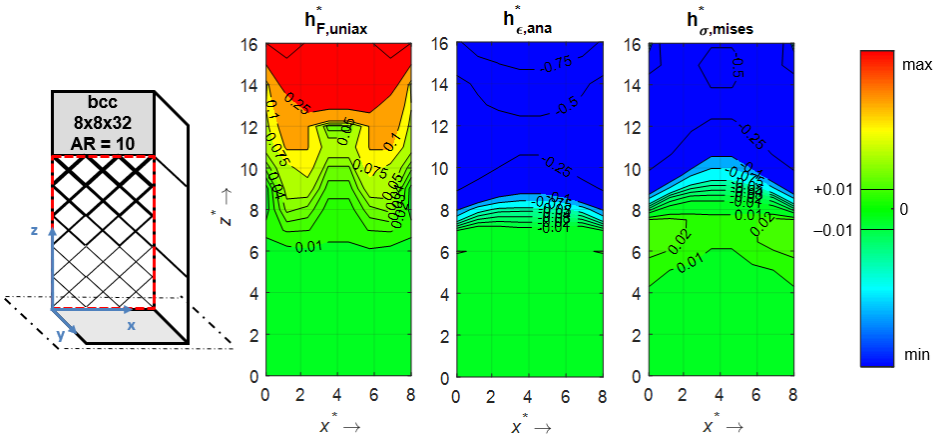

AppendixFigure B-8: Sample quality results: bcc 8x8x32 AR10 graded (front).

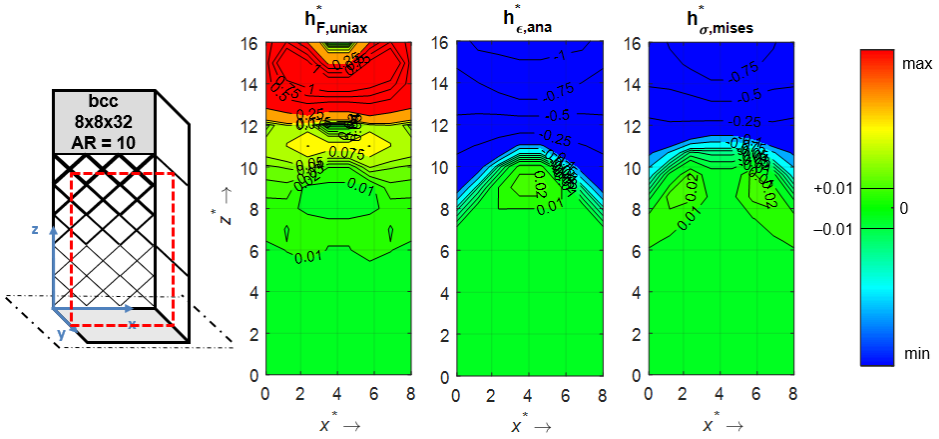

AppendixFigure B-9: Sample quality results: bcc 8x8x32 AR10 graded (middle).

C Design: structural optimisation

This section offers complementary data to the investigation of the topology optimised load introduction reported in section 4.2.

Optimisation variable ranges

The lower limit of the investigated aspect ratio AR considers both assumed limit between the lattice structure and porous material (see section 2.3.4) and critical aspect ratios without SCF of AppendixTable B-7 and AppendixTable B-8 while its upper limit accounts for realistic and relevant lightweight use-cases as mentioned in section 3.1.1.

$$4 \leq AR \leq 10 \tag{C1}$$

Both number of RUCs in the xy-plane of the target region $n_{RUC,xy}$ and number of RUCs in the z-direction $n_{RUC,z}$ of the target region are based on the sample dimensions listed in the literature in order to cover different sample sizes (see section 2.4.2).

$$6 \leq n_{RUC,xy} \leq 16 \tag{C2}$$

$$8 \leq n_{RUC,z} \leq 24 \tag{C3}$$

The upper limit of the height of the transition region h_D has been set to reduce the sample height in comparison to a load introduction approach using graded lattice structures (see section 4.1). Its lower limit is deemed to propose a realistic converging design showing the first differences when compared with a configuration without a transition region.

$$0.5 \cdot a \leq h_D \leq 6 \cdot a \tag{C4}$$

The first load introduction type *load type* is an enforced displacement applied on the upper surface that is representative of real tensile tests. The applied displacement value is based on the range of displacement rates found in the literature for simulations and physical tests [55, 247, 286, 293, 352]. In the framework of this investigation, a displacement rate of 1 mm/min is chosen to justify the assumption of linear strain and, thus, not require non-linear simulations. This value is then translated into a quasi-static tensile load case, which leads to an enforced displacement of 1 mm. The second load introduction type covers the cases of negative pressure applied to the top surface or traction force on the top nodes, which are commonly used in finite element simulations to describe the investigated

load case. In the framework of this investigation, this load introduction type is simulated as negative surface pressure. For comparison purposes, the magnitude of the applied pressure is established in the frame of preliminary studies as equivalent to the applied enforced displacement of the previous load type. The values cover a range between around 0.2 MPa and 1.7 MPa, depending on the stiffness of the investigated target region.

$$load\ type = \begin{cases} 1 \equiv U_z \\ 2 \equiv F_z \end{cases} \tag{C5}$$

The defined goal volume fraction V_f is set to enforce a topology with fewer material in the design space in order to focus on the main load paths while maintaining a certain lightweight grade.

$$0.1 \leq V_f \leq 0.5 \tag{C6}$$

The lower limits of both minimum and maximum member size variables are set to enable thin lattice-like topologies in the design space while their upper limits aim to achieve a minimal topology connection without enforcing too large overhangs.

$$0.5 \cdot t \leq m_{minmem} \leq 2 \cdot t \tag{C7}$$

$$1 \cdot t \leq m_{maxmem} \leq 3 \cdot t \tag{C8}$$

In this study, the suggested range of the parameter $DISCRETE$ of 2 to 3 [390] has been extended. Large values can be used to identify the main load paths, while smaller ones result in more discrete structures.

$$DISCRETE = p - 1 \tag{C9}$$

$$1 \leq DISCRETE \leq 4 \tag{C10}$$

The $TOPDISC$ parameter can be set to either on or off.

$$TOPDISC = \begin{cases} 0 \equiv off \\ 1 \equiv on \end{cases} \tag{C11}$$

The aim of the identified $Constraint/Objective$ variables is to ensure failure in the target region. In addition, in order to ensure mostly tensile stress conditions in this area, the stress constraints for a uniaxial loading have been applied. The uniaxiality condition involves restricting the principal stresses in the plane perpendicular to the loading direction

σ_{II} and σ_{III} by negligible non-zero values $\sigma_{II,max}$ and $\sigma_{III,max}$ determined after the preliminary runs. These constraints can be applied either in the top region or in the centre region, according to the objective. The following three cases are distinguished:

- Minimise the maximum von Mises stress in the top lattice region σ_{VM}^{Top} with the minimum von Mises stress constraint in the centre lattice region σ_{VM}^{Centre} above the corresponding analytical yield stress $\sigma_{y,ana}$ of the considered unit cell (see section 3.2.1).
- Maximise the minimum von Mises stress in the lattice centre region $\sigma_{\mathrm{VM}}^{\mathrm{Centre}}$ with stress constraints for uniaxiality in the top lattice region $\sigma_{II,max}^{Top}$ and σ_{III}^{Top}, max.
- Minimise the compliance of the design space C_{hD} with the stress constraints for uniaxiality in the top lattice region $\sigma_{II,max}^{Top}$ and $\sigma_{III,max}^{Top}$.

$$Constraint/Objective = \begin{cases} 1 \equiv min\left(\sigma_{VM}^{Top}\right); \sigma_{VM}^{Centre} \geq \sigma_{y,ana} \\ 2 \equiv max(\sigma_{VM}^{Centre}); \sigma_{II;III}^{Top} \leq \sigma_{II;III,max}^{Top} \\ 3 \equiv min\left(C_{hD}\right); \sigma_{II;III}^{Top} \leq \sigma_{II;III,max}^{Top} \end{cases} \quad \text{(C12)}$$

Design of experiment

In the framework of this investigation, a numerical design of experiment is conducted in order to reduce the number of time-consuming runs. To do so, a Latin Hypercube Design (LHD) sampling is employed to evenly cover the multi-dimensional parameter space [403, 404]. The input encompasses the range limits described in the previous section. Although eleven sample runs are necessary for the LHD approach, fifteen samples for each lattice type are chosen as a reasonably large sample size. The sample configurations are summed up in AppendixTable C-1. Additionally, this counteracts the restriction of Optistruct to require a maximum member size of at least two times the minimum member size control [390]. Therefore, the runs with too small values have turned off the maximum member size control. In such a case, the concerned variables are marked with *.

AppendixTable C-1: Resulting LHD samples for the DoE study.

Sample run	AR	$n_{cells,xy}$	$n_{cells,z}$	h_D	Load Type	DISCRETE	TOPDISC	V_f	m_{minmem}	m_{maxmem}	Constraint Objective
1	5.12	10	12	1.57 × a	1	2	1	0.31	1.42 × t	1.00 × t *	3
2	7.84	10	8	3.78 × a	1	4	0	0.18	0.82 × t	0.74 × t *	1
3	8.98	6	4	2.18 × a	1	3	1	0.49	0.55 × t	0.77 × t	2
4	9.51	14	14	5.06 × a	2	2	0	0.25	0.27 × t	1.47 × t	3
5	6.94	10	12	0.97 × a	1	3	0	0.22	1.28 × t	2.13 × t	3
6	6.61	12	14	5.58 × a	1	4	0	0.42	0.67 × t	1.81 × t	1
7	8.34	6	18	3.34 × a	1	1	0	0.10	0.80 × t	1.05 × t *	1
8	8.49	14	20	3.96 × a	2	3	0	0.14	0.95 × t	1.50 × t *	2
9	7.56	16	8	5.94 × a	2	1	1	0.36	0.43 × t	1.00 × t	2
10	6.28	16	22	1.92 × a	1	4	1	0.32	0.58 × t	1.30 × t	2
11	9.91	14	20	2.64 × a	2	1	1	0.27	0.60 × t	1.11 × t *	3
12	4.19	12	22	3.14 × a	1	4	0	0.40	1.20 × t	2.16 × t *	2

Sample run	AR	$n_{cells,xy}$	$n_{cells,z}$	h_D	Load Type	DISCRETE	TOPDISC	V_f	m_{minmem}	m_{maxmem}	Constraint Objective
13	4.76	8	16	4.52 × a	2	2	0	0.37	2.04 × t	2.36 × t *	1
14	5.44	8	18	4.88 × a	2	1	1	0.47	1.68 × t	2.40 × t *	1
15	5.96	8	10	0.75 × a	2	3	1	0.19	1.34 × t	1.72 × t *	3

*maximum member size control turned off

Evaluation of results

Correlation matrices are employed to evaluate the results of the DoE study. The following correlation analyses are considered: the Pearson, Kendall and Spearman correlations [403, 405] as well as the Maximal Information Coefficient (MIC) [406]. The Pearson correlation assumes a normal distribution of the values and a linear correlation, whereas Kendall and Spearman do not assume a statistical distribution and use the rank of the values to correlate a monotone behaviour. The rank is determined by sorting the factor values ascending and the values are then replaced by their rank (or position). In Spearman's correlation the direct difference of the ranks is calculated and in Kendall's the ratio of the ranks are used. The MIC correlation method accounts for potential non-linear correlation. Please refer to literature for further details.

In the framework of this investigation, a threshold of significance of the calculated correlation is set for a p-value of 0.07. In order to perform the correlation analyses, a set of score criteria is introduced. The structure score assesses the transferability of the topology design into structural elements (pronounced structure or design patterns). The material distribution score evaluates the allocation of material with respect to both design space and manufacturing constraints such as overhanging structures. Complementary to this, the lightweight score assesses an effective material distribution and aims at minimising the material usage, which can be relevant to the implementation of lattice structures into lightweight components. A proper load introduction is evaluated by the connectivity score, which focuses on the material connection between the transition and target regions. The stress distribution, for which the ideal case is a failure in the centre region under an almost uniaxial loading condition, is evaluated by means of finite element analyses of the resulting design topologies. The z-stress distribution score determines the load distribution in the loading direction and is compared to the xy-stress distribution score, which evaluates the uniaxiality of stresses within the whole structure. The overall score is an independent criterion that takes all the aforementioned features into account and provides an overall impression of the resulting topology on the most intuitive grading of results. These criteria are qualitatively ranked in four levels from bad to very good in order to address any score bias. All the score criteria contribute equally to the evaluation of the best runs, apart from the lightweight score and the z-stress distribution score, for which weighting factors of 0.5 and 1.5, respectively, are introduced due to their respective relevance. The final score biases are then normalised to a range between 0 and 1 in order to ensure comparability between the employed correlation analyses.

DoE results

In the framework of the correlation analysis, the optimisation variables are confronted to score the criteria. A summary of the main findings can be found in AppendixTable C-2. Due to the statistically small number of samples investigated within the framework of this study, the outcomes of the correlation analysis are to be considered as trends rather than results leading to definitive statements. As the correlations are low, with most of the absolute values being below 0.5, particular attention was paid to the related p-values during the analysis of the results. The low correlation scores can be explained by the differences in the behaviours of the unit cells as well as by potential modelling precision or convergence issues, which are due to the arbitrarily broad range of optimisation variables. However, the derived results are deemed sufficient, on the one hand, to give advice on the relevant variables and corresponding ranges for further optimisation studies dealing with lattice structures and, on the other hand, to hint at common relevant structural elements.

The strongest correlations for both lattice types are observed for the number of unit cells in the plane transverse to the load direction $n_{RUC,xy}$ and the type of loading. $n_{RUC,z}$ yields a direct positive correlation, which means that it is suggested to use higher unit cell numbers in the xy-plane, where possible. As discussed in section 4.1, the typical load path in truss lattice structures is three-dimensional. Therefore, an ideal size for the target region can be speculated. The size can be expected to be lattice-structure-dependent and could provide different slenderness ratios for the tensile specimen. The correlation results regarding the load type highlight that a surface pressure loading should be preferred. In the preliminary studies, some displacement loaded optimisation runs failed or had no material connection from the lattice to a top connector, meaning that they were physically meaningless. Additionally, the objective/constraint combination correlates strongly for the bcc lattice structure but also for the f_2cc_z lattice structure. The optimisation towards the minimisation of compliance presents higher scores. This result is in line with the convergences issues of optimisation using enforced displacement addressed in the literature [390, 407-411]. In the frame of the topology optimisation of a design space in the vicinity of thin walled features such as lattice structures, and for one-dimensional loading, it is advisable to use the compliance objective with stress constraints and a loading modelled as negative pressure.

Among the other investigated optimisation variables, the two important design variables that are the aspect ratio AR and the design space height h_D do not reveal clear correlations. For the bcc lattice structure, the study gives an indication of a possible positive correlation with higher aspect ratios towards better stress distribution in the loading direction. As the upper limits are derived by the lattice structures to remain a manufacturable three-dimensional feature, medium to high aspect ratios (e.g., $AR = 8$) are suggested for further investigations. As no correlation for the aspect ratio in the f_2cc_z lattice structure results from the investigations, the advice for the bcc lattice can be followed too, as the results do not

suggest otherwise. For the design space height and, thus, the height of the transition region, an anti-proportional correlation can be perceived for the f_2cc_z lattice structure. This means that lower design space heights should be favoured to achieve an optimised stress layout. Here, it is supposed that the reduced number of design variables for the optimisation decreases the degrees of freedom for the algorithm and can therefore lead to more distinctive results. As a clear optimal design height cannot be obtained and no minimal transition section can be identified. It is suggested to individually adjust the height of the desired transition region of a given sample to a narrow height until a deterioration of the result is observed.

The classical optimisation parameters yield different correlation results. The minimum and maximum member size controls m_{minmem} and m_{maxmem} present a notable anti-proportional correlation for only the f_2cc_z lattice structure. Given the feasible mesh size for the design space, the minimum member size does not necessarily affect the design to an extent that results in a different topology. If the minimum member size control is not used, a checker-board control should be applied to reduce the bad connection of the elements [390]. The maximum member size control can aid in the design but offers no distinct benefit. The suggestion is to exclude these parameters in a first run and enable them only if the specific topology material appears overly localised (enable the maximum member size control) or if no proper connection is created with the lattice (enable the minimum member size control). The $DISCRETE$ penalty factor displays a correlation with the xy-stress distribution score for only the bcc lattice structure. Therefore, it is suggested to use the standard values for structural problems in the case of thin-walled features too. The $TOPDISC$ card in Optistruct shows a similar characteristic, as no considerable correlation is perceivable, and can, therefore, be disabled. The volume fraction V_f shows no correlating behaviour and remains to be determined by the application, as it is mostly influenced by the desired parts weight goal. For independent optimisation, the general value of $V_f = 0.3$ can be used.

A noticeable and important combination of correlations for the following sections is observed for the structure score. This score correlates to a good extent with both the aspect ratio and constraint/objective combination variables. This means that the structural elements should be easily recognisable for the high aspect ratios and are representative of the investigated loading case, which should not encounter the aforementioned convergence problems. This highlights the trustworthiness of the results and the potential to turn the identified features into a realistic and effective design.

AppendixTable C-2: Summary of the main correlations.

RUC	Variable	Correlation outcome	Relevant score criteria
f_2cc_z	$n_{cells,xy}$	High $n_{cells,xy}$	General correlation
	$load\ type$	Negative surface pressure	General correlation
	h_D	Low h_D	Only for the z-stress distribution score
	$Constraint/Objective$	Compliance optimisation with stress constraint	General correlation
	m_{minmem}	Low m_{minmem}	Only for the connectivity score
	m_{maxmem}	Low m_{maxmem}	Only for the connectivity score
	AR	High AR	Not high but indication through the z-stress distribution score
bcc	$n_{cells,xy}$	High $n_{cells,xy}$	General correlation
	$n_{cells,z}$	High $n_{cells,z}$	General correlation, especially for the xy-stress distribution score
	$load\ type$	Negative surface pressure	Structure score and material distribution score
	$DISCRETE$	High $DISCRETE$	Only for the xy-stress distribution score
	$Constraint/Objective$	Compliance optimisation with stress constraint	General correlation
Both	$TOPDISC$	Turned off	No correlation observable
	V_f	Standard value of 0.3	No correlation observable

D Design: notch stress reduction

This section offers complementary data to the investigation of the notch stress reduction methods reported in section 4.3.

Investigated graded configurations

AppendixTable D-1 and AppendixTable D-2 sum up the investigated graded configurations for bcc and f_2cc_z, respectively. Successfully designed and meshed configurations are marked with ticks (✓). Among them, configurations with slight workaround are coloured differently (✓). Performed workarounds consists in applying a correction factor between 1 % and 7 % to the curvature radius γ only. Due to the low level of applied correction factors, the comparability of results is not impacted. Configurations that could not be investigated are marked with a cross, while CAD convergence issues (×) are differentiated from FEM meshing issues (×). Both bcc TTM and f_2cc_z PCM configurations are not listed for the reasons explained in section 4.3.

AppendixTable D-1: Overview of investigated configurations (bcc).

	FRM							PCM					
f/y	0.25	0.50	0.75	1.00	1.25	1.50	f/y	0.25	0.50	0.75	1.00	1.25	1.50
0.81	✓	✓	✓	✓*	✓	×	0.81	×	×	×	✓	✓	✓
0.90	×	×	✓	×	✓	×	0.90	×	×	✓	×	✓*	✓
1.00	✓	×	×	✓	✓	✓*	1.00	×	×	✓	✓	✓	✓
1.10	✓	×	✓	✓	✓	×	1.10	×	×	×	✓*	✓	✓
1.20	✓	×	✓	✓	✓	✓	1.20	×	×	✓*	✓	✓	✓
1.35	✓	✓	✓	✓	✓*	✓	1.35	×	×	✓	×	✓*	✓*

AppendixTable D-2: Overview of investigated configurations (f_2cc_z).

	FRM							TTM					
f/y	0.07	0.14	0.20	0.27	0.34	0.41	f/y	0.07	0.14	0.20	0.27	0.34	0.41
0.81	✓*	✓	✓	✓	✓*	✓*	0.81	✓*	✓	✓	×	×	×
0.90	✓*	×	✓	✓*	✓	✓	0.90	✓	×	×	✓	✓	×
1.00	✓*	×	✓	✓	×	✓	1.00	✓*	✓*	×	✓	×	×
1.10	✓	✓	✓	✓	✓	✓	1.10	✓	✓	×	×	×	×
1.20	×	×	✓	✓	✓	×	1.20	✓*	✓*	×	✓	×	✓
1.35	×	×	×	×	✓	✓	1.35	×	✓*	✓*	✓	×	✓

Results

AppendixTable D-3 presents the results for the bcc configuration along the selected load path depicted in Figure 81, c. AppendixTable D-4, AppendixTable D-5 and AppendixTable D-6 sum up the results for the f_2cc_z configuration for the selected load path depicted in Figure 81, d, respectively. In order to help identifying trends from the table, colour plots

are used. While stress based criteria, i.e. $\sigma_{VM,mean}$, $\sigma_{VM,max}$, K_t, employ standard heat plot, L^* using a middle value of 1, corresponding to the initial, i.e. notched, ungraded configuration. Furthermore, the relative difference in stress concentration factor Δ_{K_t} and in normalised lightweight grade Δ_{L^*} are presented too. They are calculated according to Eq.D1 and Eq.D2, respectively.

$$\Delta_{K_t} = \frac{K_{t,TTM/PCM} - K_{t,FRM}}{K_{t,PCM}} \tag{D1}$$

$$C\Delta_{L^*} = \frac{L^*_{TTM/PCM} - L^*_{FRM}}{L^*_{FRM}} \tag{D2}$$

AppendixTable D-3: Result table (bcc).

Configuration			$\sigma_{VM,mean}$		$\sigma_{VM,max}$		K_t			L^*		
f	t_{graded}	γ	FRM	PCM	FRM	PCM	FRM	PCM	Δ_{K_t}	FRM	PCM	Δ_{L^*}
0.81	300	0.25	41	N/A	128	N/A	3.1	N/A	N/A	1.6	N/A	N/A
		0.50	43	N/A	111	N/A	2.6	N/A	N/A	1.8	N/A	N/A
		0.75	46	N/A	114	N/A	2.5	N/A	N/A	1.8	N/A	N/A
		1.00	50	50	118	110	2.4	2.2	-5.8%	1.8	2.0	12.8%
		1.25	50	50	119	110	2.4	2.2	-6.1%	1.8	1.8	0.3%
		1.50	N/A	55	N/A	117	N/A	2.1	N/A	N/A	1.7	N/A
0.90	333	0.25	N/A	N/A	N/A	N/A	N/A	N/A	N/A	N/A	N/A	N/A
		0.50	N/A	N/A	N/A	N/A	N/A	N/A	N/A	N/A	N/A	N/A
		0.75	47	46	113	99	2.4	2.1	-12.0%	1.7	2.0	13.0%
		1.00	N/A	N/A	N/A	N/A	N/A	N/A	N/A	N/A	N/A	N/A
		1.25	51	58	122	109	2.4	1.9	-20.9%	1.5	1.9	24.1%
		1.50	N/A	59	N/A	116	N/A	1.9	N/A	N/A	1.7	N/A
1.00	370	0.25	45	N/A	132	N/A	2.9	N/A	N/A	1.4	N/A	N/A
		0.50	N/A	N/A	N/A	N/A	N/A	N/A	N/A	N/A	N/A	N/A
		0.75	N/A	53	N/A	93	N/A	1.7	N/A	N/A	2.2	N/A
		1.00	57	58	111	97	1.9	1.7	-14.1%	1.9	2.1	12.5%
		1.25	62	64	116	103	1.9	1.6	-13.7%	1.8	2.0	10.5%
		1.50	69	70	130	110	1.9	1.6	-15.9%	1.6	1.9	16.6%
1.10	407	0.25	48	N/A	139	N/A	2.9	N/A	N/A	1.3	N/A	N/A
		0.50	N/A	N/A	N/A	N/A	N/A	N/A	N/A	N/A	N/A	N/A
		0.75	49	N/A	124	N/A	2.5	N/A	N/A	1.4	N/A	N/A
		1.00	53	55	128	116	2.4	2.1	-11.5%	1.4	1.5	8.4%
		1.25	67	68	132	123	2.0	1.8	-8.5%	1.6	1.6	2.9%
		1.50	N/A	74	N/A	132	N/A	1.8	N/A	N/A	1.5	N/A
1.20	444	0.25	49	N/A	149	N/A	3.0	N/A	N/A	1.1	N/A	N/A
		0.50	N/A	N/A	N/A	N/A	N/A	N/A	N/A	N/A	N/A	N/A
		0.75	60	60	140	124	2.4	2.1	-11.8%	1.3	1.5	14.4%
		1.00	65	66	145	132	2.2	2.0	-11.0%	1.3	1.4	7.7%
		1.25	70	72	152	141	2.2	2.0	-8.9%	1.3	1.3	2.8%
		1.50	77	79	176	151	2.3	1.9	-15.9%	1.1	1.2	9.3%
1.35	500	0.25	54	N/A	162	N/A	3.0	N/A	N/A	1.0	N/A	N/A
		0.50	59	N/A	158	N/A	2.7	N/A	N/A	1.0	N/A	N/A
		0.75	63	70	169	141	2.7	2.0	-24.6%	1.0	1.3	30.7%
		1.00	68	70	179	151	2.6	2.1	-17.7%	1.0	1.1	17.2%
		1.25	73	N/A	190	N/A	2.6	N/A	N/A	0.9	N/A	N/A
		1.50	80	83	203	175	2.5	2.1	-16.8%	0.9	1.2	34.9%

AppendixTable D-4: Result table (f_2cc_z, load path 1).

Configuration			$\sigma_{VM,mean}$		$\sigma_{VM,max}$		K_t			L^*		
f	t_{graded}	γ	FRM	TTM	FRM	TTM	FRM	TTM	Δ_{K_t}	FRM	TTM	Δ_{L^*}
0.81	300	0.07	332	332	823	641	2.5	1.9	-22.1%	1.5	2.0	28.6%
		0.14	338	339	673	543	2.0	1.6	-19.5%	1.9	2.4	24.4%
		0.20	346	347	642	489	1.9	1.4	-24.3%	2.0	2.7	32.2%
		0.27	354	N/A	605	N/A	1.7	N/A	N/A	2.2	N/A	N/A
		0.34	363	N/A	575	N/A	1.6	N/A	N/A	2.3	N/A	N/A
		0.41	373	N/A	562	N/A	1.5	N/A	N/A	2.4	N/A	N/A
0.90	333	0.07	303	305	714	590	2.4	1.9	-17.8%	1.5	1.8	21.4%
		0.14	N/A	N/A	N/A	N/A	N/A	N/A	N/A	N/A	N/A	N/A
		0.20	317	N/A	565	N/A	1.8	N/A	N/A	1.9	N/A	N/A
		0.27	326	332	545	452	1.7	1.4	-18.6%	2.0	2.5	22.5%
		0.34	336	341	534	471	1.6	1.4	-13.1%	2.1	2.4	14.7%
		0.41	346	N/A	520	N/A	1.5	N/A	N/A	2.2	N/A	N/A
1.00	370	0.07	273	273	613	504	2.2	1.8	-17.9%	1.4	1.7	21.7%
		0.14	N/A	281	N/A	428	N/A	1.5	N/A	N/A	2.1	N/A
		0.20	287	N/A	516	N/A	1.8	N/A	N/A	1.8	N/A	N/A
		0.27	295	300	504	423	1.7	1.4	-17.7%	1.8	2.2	21.0%
		0.34	N/A	N/A	N/A	N/A	N/A	N/A	N/A	N/A	N/A	N/A
		0.41	315	N/A	481	N/A	1.5	N/A	N/A	2.0	N/A	N/A
1.10	407	0.07	245	N/A	555	N/A	2.3	N/A	N/A	1.3	N/A	N/A
		0.14	251	252	507	423	2.0	1.7	-16.9%	1.4	1.7	20.3%
		0.20	258	N/A	479	N/A	1.9	N/A	N/A	1.5	N/A	N/A
		0.27	265	N/A	467	N/A	1.8	N/A	N/A	1.6	N/A	N/A
		0.34	274	N/A	448	N/A	1.6	N/A	N/A	1.7	N/A	N/A
		0.41	283	N/A	444	N/A	1.6	N/A	N/A	1.8	N/A	N/A
1.20	444	0.07	N/A	337	N/A	636	N/A	1.9	N/A	N/A	1.4	N/A
		0.14	N/A	226	N/A	380	N/A	1.7	N/A	N/A	1.6	N/A
		0.20	231	N/A	436	N/A	1.9	N/A	N/A	1.4	N/A	N/A
		0.27	238	241	422	343	1.8	1.4	-19.7%	1.5	1.8	24.6%
		0.34	245	N/A	414	N/A	1.7	N/A	N/A	1.5	N/A	N/A
		0.41	N/A	260	N/A	356	N/A	1.4	N/A	N/A	1.8	N/A
1.35	500	0.07	N/A	N/A	N/A	N/A	N/A	N/A	N/A	N/A	N/A	N/A
		0.14	N/A	191	N/A	315	N/A	1.7	N/A	N/A	1.4	N/A
		0.20	N/A	197	N/A	304	N/A	1.5	N/A	N/A	1.5	N/A
		0.27	N/A	203	N/A	296	N/A	1.5	N/A	N/A	1.6	N/A
		0.34	207	N/A	359	N/A	1.7	N/A	N/A	1.3	N/A	N/A
		0.41	214	203	354	318	1.7	1.6	-5.4%	1.3	1.4	5.9%

AppendixTable D-5: Result table (f_2cc_z, load path 3).

Configuration			$\sigma_{VM,mean}$		$\sigma_{VM,max}$		K_t			L^*		
f	t_{graded}	γ	FRM	TTM	FRM	TTM	FRM	TTM	Δ_{K_t}	FRM	TTM	Δ_{L^*}
0.81	300	0.07	209	209	479	405	2.3	1.9	-15.5%	1.7	2.0	18.5%
		0.14	213	213	445	371	2.1	1.7	-16.8%	1.8	2.2	20.3%
		0.20	217	218	409	341	1.9	1.6	-17.1%	2.0	2.4	20.8%
		0.27	222	N/A	396	N/A	1.8	N/A	N/A	2.1	N/A	N/A
		0.34	228	N/A	383	N/A	1.7	N/A	N/A	2.2	N/A	N/A
		0.41	234	N/A	379	N/A	1.6	N/A	N/A	2.3	N/A	N/A
0.90	333	0.07	240	241	543	464	2.3	1.9	-15.0%	1.5	1.8	17.4%
		0.14	N/A	N/A	N/A	N/A	N/A	N/A	N/A	N/A	N/A	N/A
		0.20	250	N/A	464	N/A	1.9	N/A	N/A	1.9	N/A	N/A
		0.27	257	262	458	362	1.8	1.4	-22.3%	1.9	2.5	28.5%
		0.34	264	269	434	362	1.6	1.3	-17.9%	2.1	2.5	21.4%
		0.41	273	N/A	430	N/A	1.6	N/A	N/A	2.1	N/A	N/A
1.00	370	0.07	273	273	608	520	2.2	1.9	-14.6%	1.4	1.7	17.1%
		0.14	N/A	281	N/A	458	N/A	1.6	N/A	N/A	1.9	N/A
		0.20	287	N/A	516	N/A	1.8	N/A	N/A	1.8	N/A	N/A
		0.27	294	300	509	412	1.7	1.4	-20.7%	1.8	2.3	25.6%
		0.34	N/A	N/A	N/A	N/A	N/A	N/A	N/A	N/A	N/A	N/A
		0.41	315	N/A	485	N/A	1.5	N/A	N/A	2.0	N/A	N/A
1.10	407	0.07	N/A	306	N/A	586	N/A	1.9	N/A	N/A	1.5	N/A
		0.14	313	314	625	501	2.0	1.6	-20.1%	1.5	1.8	25.2%
		0.20	322	N/A	590	N/A	1.8	N/A	N/A	1.6	N/A	N/A
		0.27	332	N/A	569	N/A	1.7	N/A	N/A	1.7	N/A	N/A
		0.34	342	N/A	552	N/A	1.6	N/A	N/A	1.8	N/A	N/A
		0.41	354	N/A	539	N/A	1.5	N/A	N/A	1.8	N/A	N/A
1.20	444	0.07	N/A	337	N/A	636	N/A	1.9	N/A	N/A	1.4	N/A
		0.14	N/A	346	N/A	567	N/A	1.6	N/A	N/A	1.6	N/A
		0.20	355	N/A	640	N/A	1.8	N/A	N/A	1.5	N/A	N/A
		0.27	366	370	622	505	1.7	1.4	-19.8%	1.5	1.9	24.6%
		0.34	378	N/A	606	N/A	1.6	N/A	N/A	1.6	N/A	N/A
		0.41	N/A	400	N/A	556	N/A	1.4	N/A	N/A	1.8	N/A
1.35	500	0.07	N/A	N/A	N/A	N/A	N/A	N/A	N/A	N/A	N/A	N/A
		0.14	N/A	390	N/A	634	N/A	1.6	N/A	N/A	1.4	N/A
		0.20	N/A	404	N/A	564	N/A	1.4	N/A	N/A	1.6	N/A
		0.27	N/A	416	N/A	595	N/A	1.4	N/A	N/A	1.6	N/A
		0.34	425	N/A	682	N/A	1.6	N/A	N/A	1.4	N/A	N/A
		0.41	440	451	671	635	1.5	1.4	-7.5%	1.5	1.6	8.3%

AppendixTable D-6: Result table (f_2cc_z, load path 2).

Configuration			$\sigma_{VM,mean}$		$\sigma_{VM,max}$		K_t			L^*		
f	t_{graded}	γ	FRM	TTM	FRM	TTM	FRM	TTM	Δ_{K_t}	FRM	TTM	Δ_{L^*}
0.81	300	0.07	77	79	305	355	4.0	4.5	13.6%	1.9	1.7	-11.8%
		0.14	79	79	260	314	3.3	4.0	20.9%	2.3	1.9	-17.1%
		0.20	79	81	232	281	2.9	3.5	18.6%	2.6	2.2	-15.6%
		0.27	81	N/A	221	N/A	2.7	N/A	N/A	2.7	N/A	N/A
		0.34	82	N/A	209	N/A	2.5	N/A	N/A	2.9	N/A	N/A
		0.41	84	N/A	200	N/A	2.4	N/A	N/A	3.0	N/A	N/A
0.90	333	0.07	83	89	370	400	4.5	4.5	-0.1%	1.5	1.5	0.0%
		0.14	N/A	N/A	N/A	N/A	N/A	N/A	N/A	N/A	N/A	N/A
		0.20	87	N/A	297	N/A	3.4	N/A	N/A	2.0	N/A	N/A
		0.27	87	91	278	322	3.2	3.5	11.2%	2.1	1.9	-10.3%
		0.34	90	91	257	302	2.9	3.3	15.9%	2.4	2.0	-13.9%
		0.41	92	N/A	247	N/A	2.7	N/A	N/A	2.5	N/A	N/A
1.00	370	0.07	87	87	504	519	5.8	6.0	3.4%	1.1	1.1	-3.3%
		0.14	N/A	89	N/A	464	N/A	5.2	N/A	N/A	1.2	N/A
		0.20	92	N/A	372	N/A	4.0	N/A	N/A	1.5	N/A	N/A
		0.27	85	95	338	381	4.0	4.0	0.3%	1.6	1.5	-0.7%
		0.34	N/A	N/A	N/A	N/A	N/A	N/A	N/A	N/A	N/A	N/A
		0.41	100	N/A	290	N/A	2.9	N/A	N/A	2.1	N/A	N/A
1.10	407	0.07	91	93	396	459	4.3	4.9	14.1%	1.3	1.2	-12.3%
		0.14	94	86	350	406	3.7	4.7	26.9%	1.5	1.2	-21.2%
		0.20	96	N/A	321	N/A	3.3	N/A	N/A	1.7	N/A	N/A
		0.27	98	N/A	295	N/A	3.0	N/A	N/A	1.9	N/A	N/A
		0.34	101	N/A	279	N/A	2.8	N/A	N/A	2.0	N/A	N/A
		0.41	104	N/A	267	N/A	2.6	N/A	N/A	2.1	N/A	N/A
1.20	444	0.07	N/A	87	N/A	384	N/A	4.4	N/A	N/A	1.2	N/A
		0.14	N/A	99	N/A	364	N/A	3.7	N/A	N/A	1.4	N/A
		0.20	101	N/A	279	N/A	2.8	N/A	N/A	1.9	N/A	N/A
		0.27	103	104	264	317	2.5	3.0	19.7%	2.0	1.7	-16.5%
		0.34	96	N/A	250	N/A	2.6	N/A	N/A	2.0	N/A	N/A
		0.41	N/A	110	N/A	298	N/A	2.7	N/A	N/A	1.8	N/A
1.35	500	0.07	N/A	N/A	N/A	N/A	N/A	N/A	N/A	N/A	N/A	N/A
		0.14	N/A	105	N/A	335	N/A	3.2	N/A	N/A	1.4	N/A
		0.20	N/A	105	N/A	292	N/A	2.8	N/A	N/A	1.6	N/A
		0.27	N/A	107	N/A	277	N/A	2.6	N/A	N/A	1.7	N/A
		0.34	108	N/A	226	N/A	2.1	N/A	N/A	2.1	N/A	N/A
		0.41	102	104	211	268	2.1	2.6	24.7%	2.1	1.7	-19.7%

E Realisation: lattice structures

This section offers complementary data to the investigation of the reliable manufacturing of lattice structures at submillimetre range reported in section 5.1.

Point exposure

AppendixTable E-1 provides complementary information to Figure 96.

AppendixTable E-1: Manufacturability results for the investigated parameters (point exposure, single struts).

Name	$b_{p,CAD}$ [μm]	$l_{p,CAD}$ [µm]	P [W]	v [mm/s]	E_l [J/m]	Manual	Script	
						t [µm]	t [µm]	C [-]
S_79_125	5	125	175	2200.0	79.5	171.8	216.3±38.2	0.19±0.01
S_100_150	5	150	200	2000.0	100.0	207.8	233.5±1.4	0.15±0.03
S_125_175	5	175	225	1796.6	125.2	218.4	250.2±33.1	0.23±0.09
S_156_200	5	200	250	1593.3	156.9	234.2	259.4±6.7	0.18±0.08
S_222_225	5	225	275	1238.0	222.1	247.6	262.8±17.2	0.27±0.03
S_339_250	5	250	300	882.7	339.9	261.0	284.6±6.4	0.16±0.05
S_447_275	5	275	325	726.8	447.2	272.3	286.4±6.1	0.30±0.11
S_613_300	5	300	350	570.9	613.1	278.6	283.5±4.5	0.53±0.17

Contour exposure

AppendixTable E-2 provides complementary information to Figure 98.

AppendixTable E-2: Manufacturability results for $P = 200\text{W}$ and $v = 2500\text{mm/s}$ (contour exposure, single struts).

$d_{h,c}$ [µm]	t [µm]	t_{hollow} [µm]	b_{SCE} [μm]	OL [%]	$t_{c,calc}$ [μm]	$\Delta t - t_{c,calc}$ [%]	C_{out} [-]	C_{in} [-]
77.5	287.1	N/A	166.1	53	243.7	18	0.45	N/A
102.5	313.5	N/A	166.1	38	268.7	17	0.68	N/A
127.5	322.8	N/A	166.1	23	293.7	10	0.81	N/A
152.5	341.4	N/A	166.1	8	318.7	7	0.82	N/A
177.5	333.6	N/A	166.1	-7	343.7	-3	0.47	N/A
202.5	308.9	N/A	166.1	-22	368.7	-16	0.75	N/A
227.5	305.9	N/A	166.1	-37	393.7	-22	0.70	N/A
252.5	338.4	N/A	166.1	-52	418.7	-19	0.68	N/A
277.5	338.4	N/A	166.1	-67	443.7	-24	0.62	N/A
300.0	372.9	N/A	166.1	-81	466.1	-20	0.56	N/A
325.0	415.4	N/A	166.1	-96	491.1	-15	0.55	N/A
327.5	413.1	N/A	166.1	-97	493.7	-16	0.61	N/A
350.0	421.7	N/A	166.1	-111	516.1	-18	0.57	N/A

$d_{h,c}$ [µm]	t [µm]	t_{hollow} [µm]	b_{SCE} [μm]	OL [%]	$t_{c,calc}$ [μm]	$\Delta t - t_{c,calc}$ [%]	C_{out} [-]	C_{in} [-]
352.5	422.1	N/A	166.1	-112	518.7	-19	0.60	N/A
375.0	442.7	N/A	166.1	-126	541.1	-18	0.53	N/A
377.5	429.2	N/A	166.1	-127	543.7	-21	0.61	N/A
400.0	445.8	N/A	166.1	-141	566.1	-21	0.47	N/A
425.0	477.2	N/A	166.1	-156	591.1	-19	0.47	N/A
450.0	517.0	220	166.1	-171	616.1	-16	0.52	0.14
475.0	540.1	197	166.1	-186	641.1	-16	0.52	0.16
500.0	580.8	187	166.1	-201	666.1	-13	0.55	0.16
525.0	599.8	189	166.1	-216	691.1	-13	0.53	0.11
550.0	625.9	184	166.1	-231	716.1	-13	0.49	0.08
575.0	639.7	186	166.1	-246	741.1	-14	0.55	0.11
600.0	670.8	173	166.1	-261	766.1	-12	0.59	0.16
625.0	684.1	165	166.1	-276	791.1	-14	0.43	0.10
650.0	734.8	175	166.1	-291	816.1	-10	0.54	0.14
675.0	724.4	162	166.1	-306	841.1	-14	0.56	0.12
700.0	774.5	169	166.1	-321	866.1	-11	0.53	0.12
725.0	798.3	166	166.1	-336	891.1	-10	0.54	0.13
750.0	842.0	168	166.1	-351	916.1	-8	0.58	0.13
775.0	853.5	167	166.1	-366	941.1	-9	0.56	0.18
800.0	859.9	166	166.1	-382	966.1	-11	0.54	0.10
825.0	910.2	175	166.1	-397	991.1	-8	0.57	0.07
850.0	927.4	169	166.1	-412	1016.1	-9	0.52	0.08
875.0	956.5	180	166.1	-427	1041.1	-8	0.57	0.05
900.0	976.0	158	166.1	-442	1066.1	-8	0.55	0.15
925.0	1004.6	164	166.1	-457	1091.1	-8	0.54	0.06
950.0	1019.2	154	166.1	-472	1116.1	-9	0.58	0.18
975.0	1062.2	152	166.1	-487	1141.1	-7	0.55	0.15
1000.0	1074.4	160	166.1	-502	1166.1	-8	0.59	0.17

AppendixTable E-3 sums up achieved circularities for representative parameter combinations and for the different identified regions. Data regarding the hollow region are not sufficient to provide representative results of its sub-regions. Low laser power leads to a bigger drop in circularity when entering into the hollow region.

AppendixTable E-3: Roundness results for the investigated parameters (contour exposure, single struts).

P	v	E_l	C_{out} [-]		
[W]	[mm/s]	[J/m]	Full strut (stable)	Full strut (unstable)	Hollow strut
200	3500	57.1	0.71±0.08	0.59±0.10	0.57±0.03
250	3500	71.4	0.71±0.08	0.65±0.05	0.59±0.03
200	2500	80.0	0.69±0.17	0.58±0.08	0.54±0.03
300	2500	120.0	0.75±0.06	0.68±0.07	0.57±0.03
250	1750	142.9	0.70±0.03	0.66±0.08	0.64±0.04
200	1000	200.0	0.73±0.02	0.60±0.07	0.59±0.04

AppendixTable E-4 lists the different thickness ranges and the measured melt pool widths of each identified region for representative parameter combinations. The formation of hollow struts is mostly driven by the laser power while the scanning speed slightly influences it. Low energy inputs lead to sooner hollow strut as the melt pool is narrower, which is mainly driven by the laser scanning speed.

AppendixTable E-4: Thickness ranges for different regions (contour exposure, single struts).

			Full strut				Hollow strut				
P [W]	v [mm/s]	E_l [J/m]	Stable from $d_{h,c}$ [µm]	t [µm]	Unstable from $d_{h,c}$ [µm]]	t [µm]	Unstable from $d_{h,c}$ [µm]	t [µm]	Stable from $d_{h,c}$ [µm]	t [µm]	b_{SCE} [μm]
200	3500	57.1	115	304	190	320	475	525	725	750	154.8
250	3500	71.4	30	308	350	420	500	570	875	950	176.6
200	2500	80.0	80	287	150	340	450	520	600	670	166.1
300	2500	120.0	30	347	300	285	575	700	800	915	223.3
250	1750	142.9	25	331	125	410	525	650	650	780	198.6
200	1000	200.0	50	325	100	350	425	570	550	690	207.0

AppendixTable E-5 provides complementary data to Figure 102. Only successfully printed lattice structures are reported.

AppendixTable E-5: Manufacturability results for the investigated parameters (contour exposure, lattice structures).

Name	P [W]	v [mm/s]	E_l [J/m]	$d_{h,c}$ [µm]	t [µm]	a [mm]	AR [-]	C_{out} [-]
Parameter set 1	200	1000	200.0	99.0	333.8	3	9.0	0.40
Parameter set 1	200	1000	200.0	449.0	612.6	3	4.9	0.33
Parameter set 1	200	1000	200.0	499.0	635.0	3	4.7	N/A
Parameter set 1	200	1000	200.0	549.0	700.5	3	4.3	N/A
Parameter set 2	200	1750	114.3	403.6	577.0	3	5.2	0.62
Parameter set 2	200	1750	114.3	453.6	613.6	3	4.9	0.50
Parameter set 2	200	1750	114.3	503.6	667.8	3	4.5	0.48
Parameter set 3	200	2500	80.0	477.5	540.2	3	5.6	0.64
Parameter set 3	200	2500	80.0	527.5	581.0	3	5.2	0.59
Parameter set 4	200	3500	57.1	515.2	550.5	3	5.4	0.56
Parameter set 4	200	3500	57.1	565.2	587.9	3	5.1	0.41
Parameter set 5	250	1750	142.9	122.9	451.7	3	6.6	0.40
Parameter set 5	250	1750	142.9	172.9	416.5	3	7.2	0.37
Parameter set 5	250	1750	142.9	522.9	695.0	3	4.3	N/A
Parameter set 5	250	1750	142.9	572.9	666.0	3	4.5	N/A
Parameter set 5	250	1750	142.9	622.9	791.0	3	3.8	N/A
Parameter set 5	250	1750	142.9	672.9	817.0	3	3.7	0.36
Parameter set 6	250	2500	100.0	174.1	423.5	3	7.1	0.18
Parameter set 6	250	2500	100.0	224.1	426.2	3	7.0	0.42
Parameter set 6	250	2500	100.0	524.1	637.0	3	4.7	0.51
Parameter set 6	250	2500	100.0	574.1	729.0	3	4.1	N/A
Parameter set 6	250	2500	100.0	624.1	791.0	3	3.8	N/A
Parameter set 7	250	3500	71.4	479.8	546.7	3	5.5	0.33
Parameter set 7	250	3500	71.4	529.8	584.0	3	5.1	0.43

Name	P [W]	v [mm/s]	E_l [J/m]	$d_{h,c}$ [µm]	t [µm]	a [mm]	AR [-]	C_{out} [-]
Parameter set 7	250	3500	71.4	579.8	658.9	3	4.6	0.26
Parameter set 8	300	2500	120.0	159.0	426.5	3	7.0	0.38
Parameter set 9	300	3500	85.7	111.8	413.5	3	7.3	0.44
Parameter set 9	300	3500	85.7	161.8	449.3	3	6.7	0.54
Parameter set 9	300	3500	85.7	461.8	591.8	3	5.1	0.29
Parameter set 9	300	3500	85.7	511.8	645.6	3	4.6	0.41

AppendixFigure E-1 shows the influence of the cell size on the strut thickness of 3x3x3 lattice structures. The strut thickness is not influenced by the cell size and, thus, the nodal area as far as lattice structures are concerned. The only variation occurs for AR of 2.9, for which the investigated structures are considered as porous material (see Figure 22 and Figure 23).

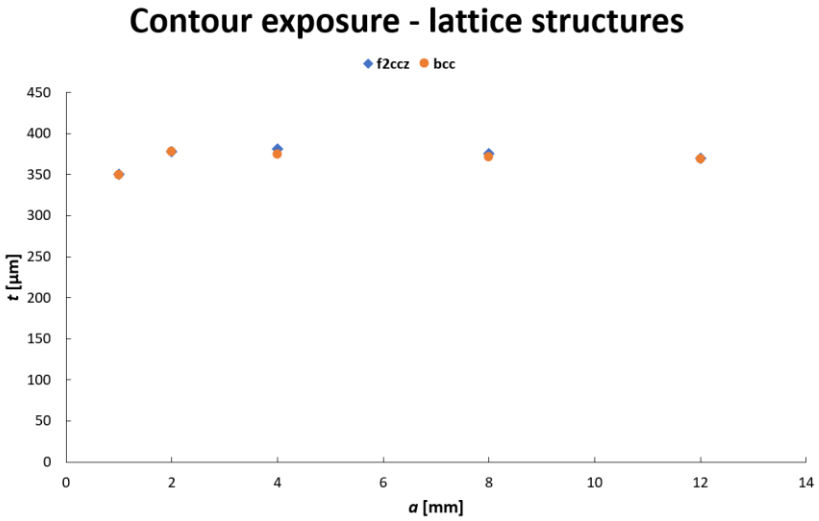

AppendixFigure E-1: Influence of cell size on the diameter of lattice structure struts for $P = 250\text{W}$ and $v = 2500\text{mm/s}$ (contour exposure, lattice structures).

AppendixFigure E-2 reports thickness and circularity results for different build platform temperatures. Few to now influence is noticed as the variations are in the range of order of the observed standard deviations.

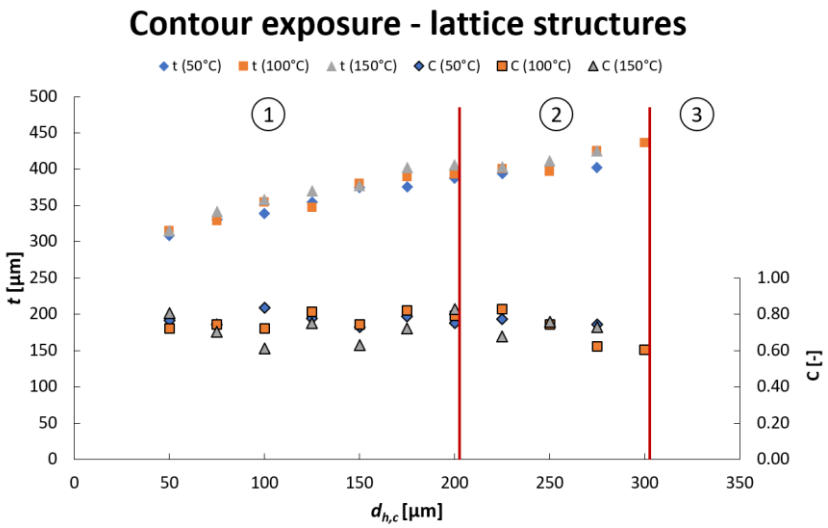

AppendixFigure E-2: Influence of build platform temperature on both diameter and circularity of lattice structure struts for $P = 250\text{W}$ and $v = 2500\text{mm/s}$ (contour exposure, lattice structures).

Hatch exposure

AppendixTable E-6 lists the melt pool width values used for different combinations. They are issued from single track exposure b_{STE} measurements and from the formulation of the multiple track exposure width d_{MTE} (Eq.E1) [57]. $b_{MTE}(n_h = 1)$ can be interpreted as a fictive single track taking the interaction between scanning paths into account.

$$d_{MTE} = 0.77 \cdot d_h \cdot (n_H - 1) + 13.66 \cdot {E_l}^{0.51} \tag{E1}$$

AppendixTable E-6: Used melt pool width values (hatch exposure).

P [W]	v [mm/s]	E_l [J/m]	b_{STE} [μm]	$b_{MTE}(n_h = 1)$ [μm]
200	1500	133.3	115.0	165.6
200	2000	100.0	119.2	143.0
250	2000	125.0	116.0	160.3
200	2500	80.0	96.7	127.7
250	2500	100.0	99.1	143.0
300	2500	120.0	109.6	157.0
250	3000	83.3	N/A	130.3
300	3000	100.0	N/A	143.0
300	3500	85.7	94.1	132.2

Eq.E2 provides the relationship between strut diameter and hatch distance derived from Eq.E1. Due to the linearity of this relationship, which is also confirmed by Figure 106, assessing the hatch distance for one diameter is sufficient for the hole parameter combination. AppendixTable E-7 shows the results obtained for a diameter of 370 μm. The upper limit of hatch distance corresponds to an overlap OL (Eq.59) of -20 % to ensure connection between single tracks while its lower limit is set to an overlap of 30 % to avoid keyhole

porosity [32]. The bold values in AppendixTable E-7 have been selected as corresponding to extremal and mean values of this range. The latter corresponds to the line energy of the parameter set used in further experiments for consistency.

$$d_h = \frac{t - 13.66 \cdot {E_l}^{0.51}}{0.77 \cdot (n_H - 1)} \tag{E2}$$

AppendixTable E-7: Hatch distance value variations for $t = 370\mu m$ (hatch exposure).

P [W]	v [mm/s]	E_l [J/m]	$d_h(n_h = 2)$ [μm]	$d_h(n_h = 3)$ [μm]	$d_h(n_h = 4)$ [μm]	$d_h(n_h = 5)$ [μm]
200.0	1500.0	133.3	265.4	132.7	88.5	66.4
200.0	2000.0	100.0	294.8	147.4	98.3	73.7
250.0	2000.0	125.0	272.4	**136.2**	90.8	68.1
200.0	2500.0	80.0	314.7	157.4	104.9	78.7
250.0	2500.0	83.3	311.3	**155.6**	**103.8**	77.8
300.0	2500.0	100.0	294.8	147.4	98.3	73.7
250.0	3000.0	85.7	308.8	154.4	102.9	77.2

AppendixFigure E-3 and AppendixTable E-8 report quality results of f_2cc_z lattice structures obtained for different values of the beam offset. The beam offset was varied relatively to $b_{MTE}(n_h = 1)$ listed in AppendixTable E-6 for consistency with Eq.E1 and Eq.E2. Values bo corresponding to one fourth of the considered melt pool width lead to the lowest average difference between as-designed and as-built lattice strut diameters. The trends in roundness are not affected by the offset. Therefore, the selected beam offset values are $b_{MTE}(n_h = 1)/4$ for consistency with Eq.E1 and Eq.E2 and $b_{STE}/4$ for consistency with Eq.57 and Eq.58.

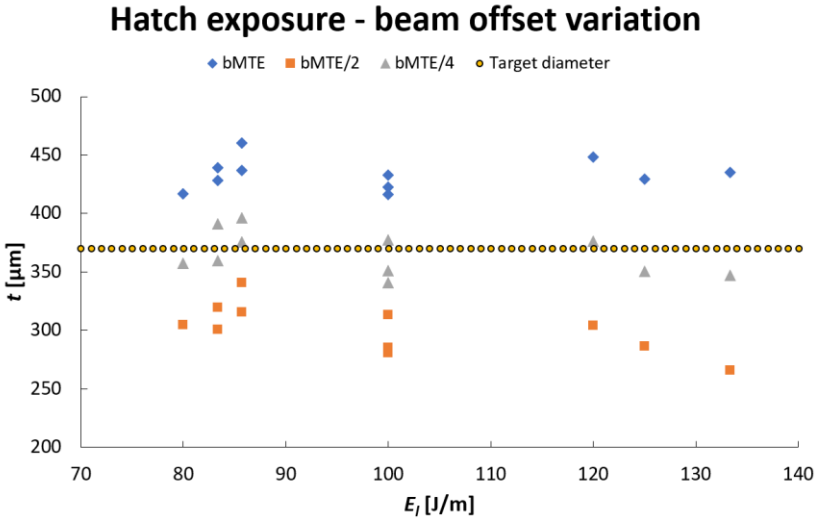

AppendixFigure E-3: Diameters for different beam offset values (hatch exposure, lattice structures).

AppendixTable E-8: Beam offset variations for different parameter combinations (hatch exposure, lattice structures).

t_{CAD} [µm]	P [W]	v [mm/s]	E_l [J/m]	d_h [µm]	$t - t_{CAD}$ ($b_{MTE}/4$) [μm]	C [-]	C ($b_{MTE}/4$) [-]
370	250	3000	83.3	155.6	-2.7	0.38	0.33
370	300	3500	85.7	154.4	1.5	0.37	0.39
370	200	2000	100.0	147.4	-7.8	0.43	0.35
370	250	2500	100.0	147.4	-5.1	0.43	0.46
370	300	3000	100.0	147.4	2.0	0.40	0.44
370	300	2500	120.0	138.3	1.8	0.42	0.46
370	250	2000	125.0	136.2	-5.2	0.44	0.49
370	200	1500	133.3	132.7	-6.3	0.34	0.39
370	200	2500	80.0	104.9	-3.4	0.37	0.43
370	250	3000	83.3	103.8	5.8	0.39	0.39
370	300	3500	85.7	102.9	7.1	0.40	0.37

AppendixTable E-9 and AppendixTable E-10 provide complementary information to Figure 106.

AppendixTable E-9: Investigated parameters (hatch exposure, single struts).

Name	P [W]	v [mm/s]	E_l [J/m]	bo [µm]	d_h [µm]	OL [%]
parameter set 1	250	2000	125.0	29.1	103	10.5
parameter set 2	250	2000	125.0	38.9	103	10.5
parameter set 3	250	2000	125.0	29.1	136	-17.4
parameter set 4	250	2000	125.0	38.9	136	-17.4
parameter set 5	250	2000	125.0	29.1	155	-34.1
parameter set 6	250	2000	125.0	38.9	155	-34.1
parameter set 7	250	2500	100.0	29.1	103	10.5
parameter set 8	250	2500	100.0	38.9	103	10.5

AppendixTable E-10: Results for the investigated parameters (hatch exposure, single struts).

Name	$t - t_{CAD}$ [μm]			C [-]		
	Mean	Min	Max	Mean	Min	Max
parameter set 1	19.5±21.3	-45.86	61.30	0.46±0.07	0.34	0.64
parameter set 2	2.9±13.6	-21.55	30.33	0.45±0.07	0.32	0.65
parameter set 3	-9.2±12.3	-32.15	18.40	0.44±0.05	0.35	0.55
parameter set 4	1.6±10.9	-13.79	30.31	0.47±0.08	0.37	0.68
parameter set 5	-18.3±10.1	-35.91	2.45	0.45±0.07	0.33	0.59
parameter set 6	-23.4±16.8	-41.11	43.55	0.44±0.07	0.34	0.58
parameter set 7	55.4+13.8	71.5	33.6	0.26+0.17	0.61	0.15
parameter set 8	48.7+21.1	69.9	25.7	0.16+0.05	0.26	0.13

AppendixTable E-11 and AppendixTable E-12 show the comparison between as-built diameters and diameters calculated with Eq.57 and Eq.58 for single struts and lattice structures, respectively. It can be observed that $t_{h2,calc}$ can predict accurately diameters for both single struts and f_2cc_z lattice structures while $t_{h1,calc}$ is more precise for bcc, yielding excellent accuracy as well. It is here supposed that these differences in effectiveness are linked to the shape of the melt pool and strut inclination angle. However, there is not enough data available to validate this hypothesis, which is not in focus of the current work.

AppendixTable E-11: Predictability of diameters for $P = 250\text{W}$, $v = 2000\text{mm/s}$, $bo = 29.1\mu\text{m}$ and $d_h = 136.2\mu\text{m}$ (hatch exposure, single strut).

t_{CAD} [μm]	$\Delta t - t_{h1,calc}$ [%]	$\Delta t - t_{h2,calc}$ [%]
300	-14.6	9.2
325	-18.8	2.0
350	-9.7	11.7
375	-10.0	9.8
400	-10.8	7.5
425	-12.8	4.0
450	-13.7	2.0
475	-9.2	6.4
500	-13.1	1.0
525	-12.1	1.4
550	-9.8	3.5
575	-10.4	2.2
600	-12.8	-1.1
625	-9.6	2.1
650	-9.4	1.8
675	-9.1	1.8
700	-7.6	3.0
725	-9.7	0.3
750	-8.2	1.6
775	-7.8	1.7
800	-8.2	0.9
825	-9.2	-0.4
850	-9.3	-0.8
875	-9.6	-1.4
900	-6.2	2.1
925	-7.3	0.6
950	-7.2	0.5
975	-7.6	0.0
1000	-7.4	-0.1

AppendixTable E-12: Predictability of lattice strut diameters for $P = 250\text{W}$, $v = 2000\text{mm/s}$, $bo = 38.9\mu\text{m}$, $d_h = 136.2\mu\text{m}$, $AR = 3.5$ and $\theta_h = 90°$ (hatch exposure, lattice structures).

Lattice	t_{CAD} [μm]	$\Delta t - t_{h1,calc}$ [%]	$\Delta t - t_{h2,calc}$ [%]
f_2cc_z	200	-8.1	3.3
	230	-9.8	0.0
	245	-10.2	-1.0
	260	-14.7	-6.5
	275	-7.2	1.2
	290	-6.6	1.5
	305	-7.6	0.0
	320	-7.7	-0.4
bcc	155	-3.1	12.1
	155	-3.0	12.2
	170	0.9	15.4
	185	0.3	13.7
	185	0.4	13.8
	200	-6.0	5.6
	200	-5.9	5.7
	215	1.9	13.7
	215	2.9	14.7
	230	0.5	11.4
	230	-2.9	7.6
	245	1.1	11.4
	245	-4.4	5.3
	260	-1.2	8.3

Contour-hatch combination

AppendixTable E-13 and AppendixTable E-14 show the selected parameter combinations and corresponding results for single struts. The investigated parameter combinations ensure the comparability with both single contour and hatch exposures. Two contour parameters were selected based on different circularity ranges (see AppendixTable E-3) while the hatch parameter was kept constant (see AppendixTable E-9). The influence of the scanning sequence on strut manufacturability was investigated by either starting from the inner exposure (IN), i.e. the hatch exposure, or from the outer exposure (OUT), i.e. the contour exposure. The beam offset of the contour exposure bo_c corresponds to the half of the average difference between as-built and as-designed struts of the single contour exposure (AppendixTable E-2). The offset of the hatch exposure bo_h of the overlap value of 100 % corresponds to the half of the average difference between as-built and as-designed struts of the single contour exposure (AppendixTable E-9). Offset values of other overlaps further are issued from the combination of the melt pool width of a single contour b_{SCE} and the overlap value (AppendixTable E-4).

AppendixTable E-13: Manufacturability results for the investigated parameters (contour-hatch exposure, single struts).

Name	P_c [W]	v_c [mm/s]	bo_c [µm]	P_h [W]	v_h [mm/s]	bo_h [µm]	d_h [µm]	OL [%]	$t - t_{CAD}$ [μm]	C [-]
CH-1_IN_100	200	3500	17.4	250	2000	38.9	104	100	26.6±15.3	0.39±0.09
CH-1_IN_50	200	3500	17.4	250	2000	121.5	104	50	11.2±19.3	0.52±0.09
CH-1_IN_25	200	3500	17.4	250	2000	162.8	104	25	5.3±15.3	0.46±0.10
CH-1_OUT_100	200	3500	17.4	250	2000	38.9	104	100	25.8±13.2	0.40±0.08
CH-1_OUT_50	200	3500	17.4	250	2000	121.5	104	50	6.2±28.9	0.51±0.10
CH-1_OUT_25	200	3500	17.4	250	2000	162.8	104	25	13.7±20.9	0.50±0.13
CH-1_OUT_0	200	3500	17.4	250	2000	204.1	104	0	8.1±20.5	0.53±0.07
CH-1_OUT_-25	200	3500	17.4	250	2000	245.4	104	-25	10.3±23.9	0.54±0.12
CH-2_IN_100	250	1750	63.5	250	2000	38.9	104	100	7.7±16.1	0.43±0.08
CH-2_IN_50	250	1750	63.5	250	2000	148.2	104	50	-1.8±16	0.57±0.07
CH-2_IN_25	250	1750	63.5	250	2000	202.9	104	25	1.0±10.0	0.49±0.10
CH-2_OUT_100	250	1750	63.5	250	2000	38.9	104	100	22.7±20.4	0.42±0.08
CH-2_OUT_50	250	1750	63.5	250	2000	148.2	104	50	10.3±24.7	0.55±0.10
CH-2_OUT_25	250	1750	63.5	250	2000	202.9	104	25	-6.9±8.3	0.54±0.12
CH-2_OUT_0	250	1750	63.5	250	2000	257.5	104	0	12.4±16.7	0.53±0.08
CH-2_OUT_-25	250	1750	63.5	250	2000	312.2	104	-25	10.2±11.4	0.60±0.11

AppendixTable E-14: Manufacturability results for the investigated parameters per category (contour-hatch exposure, single struts).

Type	$t - t_{CAD}$ [μm]	C [-]
IN	8.3±15.3	0.48±0.09
OUT	11.3±18.9	0.51±0.10
C1	13.4±19.7	0.48±0.10
C2	6.9±15.4	0.52±0.09
OL =100 %	20.7±16.2	0.41±0.08
OL = 50 %	6.4±22.2	0.54±0.09
OL = 25 %	3.3±13.6	0.50±0.11
OL = 0 %	10.2±18.6	0.53±0.08
OL = -25 %	10.2±17.7	0.57±0.11

AppendixTable E-15 reports the manufacturability results of 3x3x3 f_2cc_z lattice structures of a cell width of 3 mm for the contour-hatch exposure.

AppendixTable E-15: Manufacturability results for the investigated parameters (contour-hatch exposure, lattice structures).

Name	t_{CAD} [μm]	$d_{h,c}$ [µm]	Region	t [μm]	t_{strut} [μm]	$t - t_{strut}$ [μm]	C [-]	$t - t_{CAD}$ [μm]	C_{strut} [-]	$C - C_{strut}$ [-]
CH-1_OUT_25	550	515.2	3	527.8	547.0	-19.2	0.31	-22.2	0.54	-0.23
CH-1_OUT_50	550	515.2	3	550.3	562.6	-12.3	0.40	0.3	0.60	-0.19
CH-1_OUT_50	600	565.2	3	610.6	625.0	-14.4	0.40	10.6	0.48	-0.08
CH-1_OUT_50	700	665.2	3	698.7	688.5	10.2	0.35	-1.3	0.60	-0.26
CH-2_OUT_25	800	672.9	4	802.0	815.6	-13.6	0.45	2.0	0.60	-0.15
CH-2_OUT_50	800	672.9	4	805.3	787.9	17.4	0.49	5.3	0.68	-0.18

AppendixTable E-16 shows the single strut manufacturability results for the double contour-hatch exposure (outer diameter first).

AppendixTable E-16: Manufacturability results for the investigated parameters (double contour-hatch exposure, single struts).

t_{CAD} [μm]	P_c [W]	v_c [mm/s]	bo_c [µm]	P_h [W]	v_h [mm/s]	bo_h [µm]	d_h [µm]	OL [%]	$t - t_{CAD}$ [μm]	C [-]
625-1000	250	3500	334.0	250	2000	333.95	104	25	-12.5±12.3	0.63±0.08

Multiple contour combination

AppendixTable E-17 and AppendixTable E-18 show the selected parameter combinations and corresponding results for single struts. The influence of the scanning sequence on strut manufacturability was investigated by either starting from the inner contour (IN) or from the outer contour (OUT). The beam offset of the outer contour exposure bo_c corresponds to the half of the average difference between as-built and as-designed struts of the single contour exposure (AppendixTable E-2). Offset values of other overlaps further consider a value corresponding to the melt pool width of a single contour b_{ScE} factorised by the overlap value (AppendixTable E-4).

AppendixTable E-17: Manufacturability results for the investigated parameters per category (double contour exposure, single struts).

Type	$t - t_{CAD}$ [μm]	C [-]
IN	-14.7±21.7	0.56±0.06
OUT	-11.3±30.3	0.59±0.07
C1	-1.4±36.4	0.57±0.07
C2	-24.6±15.6	0.58±0.05
OL = 50 %	-4.0±35.6	0.57±0.06
OL = 25 %	-13.7±27.6	0.55±0.07
OL = 0 %	-21.3±14.8	0.60±0.06

AppendixTable E-18: Manufacturability results for the investigated parameters (double contour exposure, single struts).

Name	P_c [W]	v_c [mm/s]	bo_c [µm]	OL [%]	Full from $d_{h,c}$ [µm]	Full from t [μm]	Hollow from $d_{h,c}$ [µm]	Hollow from t [μm]	$t - t_{CAD}$ [μm]	C [-]
2C-1_IN_50	250	3500	-133.44 -35.1	50	579.8	643.2	654.8	282.4	13.5±58.6	0.58±0.08
2C-1_IN_25	250	3500	-182.61 -35.1	25	579.8	665.2	754.8	327.1	-13.1±21	0.53±0.08
2C-1_IN_0	250	3500	-231.79 -35.1	0	579.8	779.9	879.8	369.9	-12.4±16.8	0.59±0.06
2C-1_OUT_50	250	3500	-35.1 -133.44	50	579.8	624.4	704.8	290.6	-3.1±42.8	0.58±0.05
2C-1_OUT_25	250	3500	-35.1 -182.61	25	579.8	674.8	804.8	345.0	20.1±59.8	0.55±0.09
2C-1_OUT_0	250	3500	-35.1 -231.79	0	579.8	617.6	854.8	397.3	-13.5±19.5	0.57±0.09
2C-2_IN_50	300	2500	-186.69 -70.52	50	584.0	887.5	759.0	363.7	-11±8.8	0.56±0.04
2C-2_IN_25	300	2500	-244.78 -70.52	25	584.0	881.0	859.0	458.1	-35.4±15	0.50±0.09
2C-2_IN_0	300	2500	-302.87 -70.52	0	584.0	906.4	N/A	N/A	-30±10.1	0.61±0.01
2C-2_OUT_50	300	2500	-70.52 -186.69	50	509.0	857.2	834.0	398.3	-15.5±32.3	0.56±0.06
2C-2_OUT_25	300	2500	-70.52 -244.78	25	584.0	793.0	N/A	N/A	-26.5±14.5	0.62±0.03
2C-2_OUT_0	300	2500	-70.52 -302.87	0	584.0	751.1	N/A	N/A	-29.2±12.8	0.65±0.08
3C-1_OUT_25	250	3500	-35.1 -182.61 -330.1	25	679.8	742.8	N/A	N/A	-10.5±19.6	0.62±0.04
4C-1_OUT_50	250	3500	-35.1 -133.44 -231.8 330.1	50	729.8	771.7	N/A	N/A	-17.1±22.6	0.59±0.05

AppendixTable E-19 reports manufacturability results of 3x3x3 f_2cc_z lattice structures of a cell width of 4.25 mm.

AppendixTable E-19: Manufacturability results for the investigated parameters (double contour exposure, lattice structures).

Name	t_{CAD} [μm]	$d_{h,c,out}$ [µm]	t [μm]	$t - t_{CAD}$ [μm]	$t - t_{strut}$ [μm]	C_{out} [-]
2C-1_OUT_50	800	730	770.3	-29.7	-8.6	0.35
2C-1_OUT_25	800	730	789.4	-10.6	2.3	0.33
2C-2_IN_50	900	759	879.4	-20.6	-8.0	0.35

F Realisation: lattice-to-bulk transition

This section offers complementary data to the investigation the reliable manufacturing of the lattice-to-bulk transition reported in section 5.2.

Modular design

AppendixFigure F-1 provides details on the design of the pocketed bulk region in the context of modular design. A minimum wall thickness of 2 mm for was considered for a stable and precise manufacturing of the pocket. The pocket height was designed as depending on a given number of RUCs (here 3) in order to reflect the design solutions developed in section 4.1. The pocket width considers the width of the lattice structures to be embedded, a side tolerance of 0.1 mm and a shaft angle of 5°.

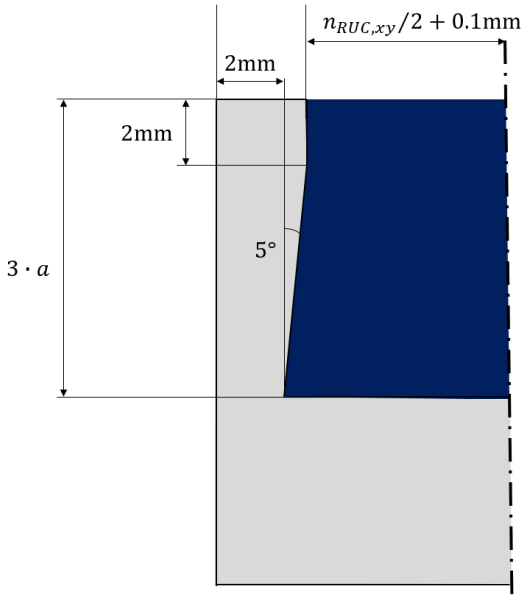

AppendixFigure F-1: Detailed pocket design (modular design).

The mass of required resin for embedment m_{resin} can be derived from Eq.F1 and Eq.F2. The employed epoxy resin is the same one as for the grinding pots described in section 3.4.3, i.e. LY556/HY917/DY070 [382] and has a density ρ_{resin} of 1.1 g/cm³. The volume occupied by the lattice structures can be estimated using the cell volume and the relative density (or averaged relative density) of the RUC $\bar{\rho}$. AppendixTable F-1 reports the resin mass employed for the investigated bcc samples of section 6.3 ($a = 3.5mm$, $V_{tot} = 8689.8mm^3$).

$$m_{resin} = (V_{tot} - V_{lattice}) \cdot \rho_{resin} \tag{F1}$$

$$V_{lattice} = n_{RUC,x} \cdot n_{RUC,y} \cdot n_{RUC,z} \cdot a^3 \cdot \bar{\rho} \tag{F2}$$

AppendixTable F-1: Required resin mass for each bcc configuration.

Aspect ratio	Configuration	m_{resin} [g]
AR06	Ungraded	8.4
AR08	Ungraded	8.9
AR10	Ungraded	9.1
AR06	Graded	7.7
AR08	Graded	8.4
AR10	Graded	8.8

G Validation: tensile specimen design

This section offers complementary data to the validation of the tensile specimen design employing a structural grading reported in section 6.3.

Details on tensile specimens

AppendixFigure G-1 shows schematically the strut thickness distribution in the graded part of a graded sample at a given height, i.e. in the plane perpendicular to the loading direction. Four concentric diameter zones are obtained according to the grading formulation detailed in Figure 35 of section 4.1.1.

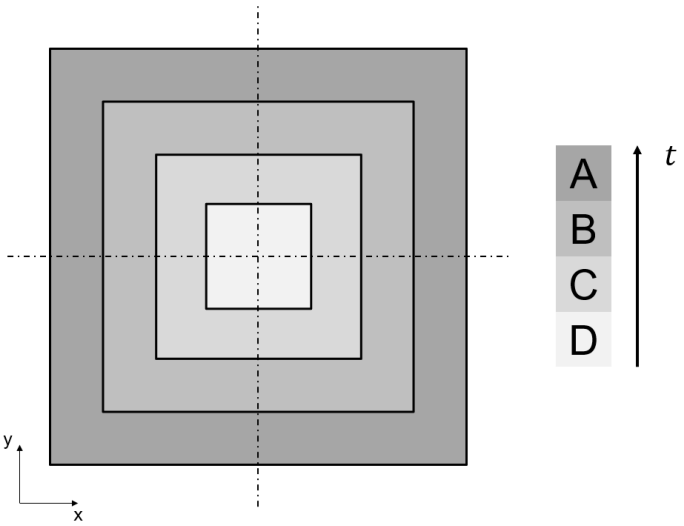

AppendixFigure G-1: Strut thickness distribution in a graded sample part.

AppendixTable G-1 and AppendixTable G-2 report the strut diameters for the graded cells of the bcc and f_2cc_z lattice samples of aspect ratio of 10 considering the grading parameters listed from AppendixTable B-3 to AppendixTable B-6, respectively. According to table Table 3, the transition region of bcc samples consists of eight graded cells while nine graded cells are required in the transition region of f_2cc_z samples. The diameter variation in the vicinity of the ungraded cells is the range of order of the standard deviations listed in Table 8.

AppendixTable G-1: Strut diameters for the graded configuration of bcc AR10.

Zone	t [µm]								
	$z^* = 8$	$z^* = 7$	$z^* = 6$	$z^* = 5$	$z^* = 4$	$z^* = 3$	$z^* = 2$	$z^* = 1$	$z^* = z_0^*$
A	585.9	468.4	449.0	430.1	411.8	394.3	377.6	362.4	350.0
B	399.4	392.3	385.4	378.6	372.1	365.8	359.9	354.4	350.0
C	326.7	330.0	333.3	336.5	339.6	342.5	345.3	347.9	350.0
D	259.0	272.1	284.8	297.3	309.3	320.9	331.8	341.9	350.0

AppendixTable G-2: Strut diameters for the graded configuration of f_2cc_z AR10.

Zone	t [µm]									
	$z^* = 9$	$z^* = 8$	$z^* = 7$	$z^* = 6$	$z^* = 5$	$z^* = 4$	$z^* = 3$	$z^* = 2$	$z^* = 1$	$z^* = z_0^*$
A	594.1	459.0	443.1	427.7	412.6	398.1	384.3	371.3	359.4	350.0
B	389.4	384.3	379.3	374.4	369.7	365.1	360.8	356.7	353.0	350.0
C	321.6	325.3	328.9	332.4	335.8	339.1	342.2	345.2	347.9	350.0
D	259.4	271.1	282.6	293.8	304.7	315.2	325.2	334.6	343.2	350.0

AppendixTable G-3 reports both upper and lower diameter limits for each graded configuration.

AppendixTable G-3: Minimum and maximum strut diameters for each configuration.

RUC	a [mm]	AR6		AR8		AR10	
		t_{min} [µm]	t_{max} [µm]	t_{min} [µm]	t_{max} [µm]	t_{min} [µm]	t_{max} [µm]
bcc	3.0	400.9	805.9	286.4	620.7	222.0	502.2
	3.5	467.8	940.2	334.1	724.1	259.0	585.9
f_2cc_z	3.0	386.0	861.9	282.1	643.6	222.3	509.2
	3.5	450.3	1005.6	329.1	750.8	259.4	594.1

AppendixFigure G-2 provides details on the experimental setup as well as on the design of the bulk region. The total height of the bulk region h_{bulk} was set to 38 mm while its length l_{bulk} depends on the manufacturing approach of the sample. In the case of monolithic samples (see section 5.2.1), the length of the bulk region corresponds to the number of RCUs in one direction of the plane perpendicular to the loading direction. In the case of hybrid samples based on the modular design, the selected length is shown in AppendixFigure F-1. A bolt connection was chosen to avoid any moments while constraining the sample. A bolt diameter $\emptyset_{bolt}$ of 10.5 mm was selected. In order to allow some positioning play, the bore hole diameter $\emptyset_{bolt}$ was set to 11 mm. The distance between the bolt and the lattice structure h_{bolt} was set to 24 mm. This value comes from a parametric FE investigation in order to ensure that the bore hole does not influence the load introduction into the lattice structure. The bore holes were drilled separately to avoid any influencing deviation from the initial design. A centring sleeve was employed to ensure that the sample is positioned upright.

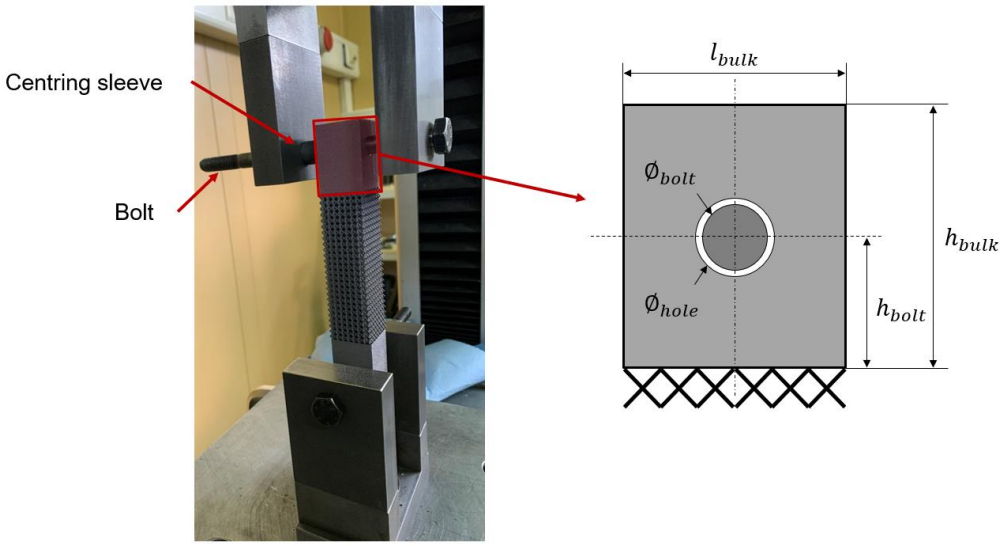

AppendixFigure G-2: Details on the test setup and the design of the bulk region.

Stiffness correction

As mentioned in section 3.4.1, the stiffnesses of both machine and load introduction were considered by correcting the measured displacement of the crosshead. Tensile specimens consisting of the transition regions of the samples investigated in section 4.1 were designed according to the principle of Figure 35. Data from Table 3 and from AppendixTable B-3 to AppendixTable B-6 were used. AppendixFigure G-3 and AppendixFigure G-4 show failed specimen for both f_2cc_z and bcc configurations, respectively. The observed failure modes are in line with the ones reported from Figure 143 to Figure 145 of section 6.3.

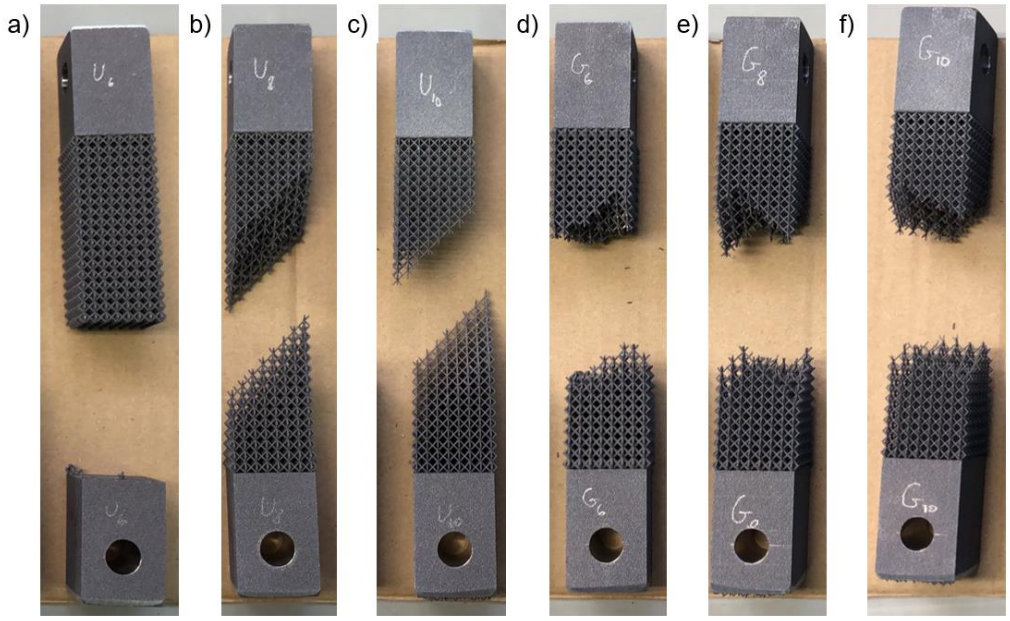

AppendixFigure G-3: Specimen failure in the framework of the stiffness correction investigation (f_2cc_z): AR6 ungraded (a), AR8 ungraded (b), AR10 ungraded (c), AR6 graded (d), AR8 graded (e), AR10 graded (f).

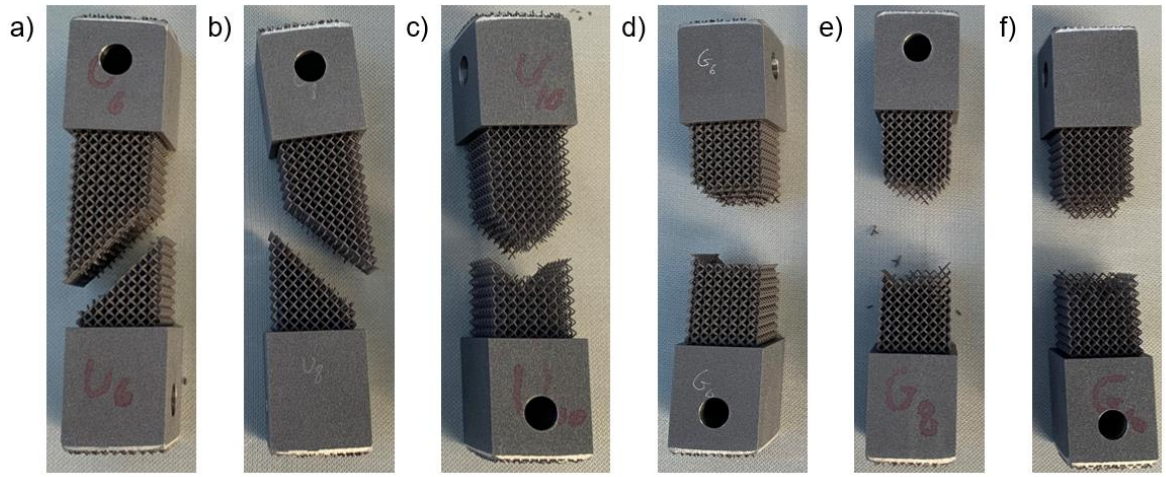

AppendixFigure G-4: Specimen failure in the framework of the stiffness correction investigation (bcc): AR6 ungraded (a), AR8 ungraded (b), AR10 ungraded (c), AR6 graded (d), AR8 graded (e), AR10 graded (f).